Zeitschrift: IABSE publications = Mémoires AIPC = IVBH Abhandlungen
Band: 32 (1972)

Teilband: IABSE Publications = Mémoires AIPC = IVBH Abhandlungen

ASSOCIATION INTERNATIONALE DES PONTS ET CHARPENTES
INTERNATIONALE VEREINIGUNG FÜR BRÜCKENBAU UND HOCHBAU
INTERNATIONAL ASSOCIATION FOR BRIDGE AND STRUCTURAL ENGINEERING

MÉMOIRES
ABHANDLUNGEN
PUBLICATIONS

32-II

1972

PUBLIÉS PAR LE SECRÉTARIAT GÉNÉRAL À ZURICH
HERAUSGEGEBEN VOM GENERALSEKRETARIAT IN ZÜRICH
PUBLISHED BY THE GENERAL SECRETARIAT IN ZURICH

Editeur - Verleger - Publisher

Association Internationale des Ponts et Charpentes
Ecole Polytechnique Fédérale de Zurich

Internationale Vereinigung für Brückenbau und Hochbau
Eidgenössische Technische Hochschule Zürich

International Association for Bridge and Structural Engineering
Swiss Federal Institute of Technology, Zurich

En commission pour la vente en librairie
Kommissionsverlag für den Buchhandel - Copies for sale at

Verlag Leemann Zürich

Printed in Switzerland

Préface

A plusieurs reprises, nous nous sommes posés la question d'éditer nos «Mémoires» sous la forme d'une série de volumes traitant chacun un thème général déterminé. Nous y avons renoncé parce qu'il est nécessaire que les nouvelles connaissances soient diffusées le plus rapidement possible. Comme la créativité peut difficilement être commandée, nous facilitons la qualité des contributions en leur offrant une possibilité régulière de publicité sans autres contingences limitatives. Les dix contributions de ce volume 32/II confirment la justesse de notre philosophie. Les thèmes traités sont fort divers et cette richesse contribue précisément à la qualité du volume. Que tous les auteurs soient ici chaleureusement remerciés.

Une fois de plus, je me permets de faire appel à nos membres de langue française pour qu'ils nous fassent parvenir des contributions. Nous souhaiterions aussi que soient abordés les problèmes d'exécution et de montage, tant il est vrai qu'il y a interaction entre théorie et pratique.

Zurich, octobre 1972

Le Président de l'AIPC:

Prof. Maurice Cosandey
Président de l'Ecole Polytechnique Fédérale de Lausanne

Vorwort

Bereits mehrere Male haben wir uns mit der Frage befasst, die Abhandlungen in Form einer Serie herauszugeben, wovon jede ein allgemeines, bestimmtes Thema behandeln soll. Davon haben wir uns abgewandt, und zwar weil es notwendig ist, die neuesten Erkenntnisse jeweils so rasch als möglich zu verbreiten. Da die schöpferische Leistung nur schwer bestimmbar ist, erleichtern wir die Abfassung der Beiträge insofern, als wir die Möglichkeit einer regelmässigen Veröffentlichung ohne irgendwelche Einschränkungen anbieten. Die zehn Beiträge dieses Bandes bestätigen die Richtigkeit unserer Denkungsart. Die behandelten Themen sind sehr unterschiedlich, und gerade diese Vielfalt ist es, die zum Wert des Bandes beiträgt. An dieser Stelle möchten wir allen Autoren herzlich danken.

Ich gestatte mir noch einmal, an alle Mitglieder französischer Sprache den Aufruf zur Einreichung von Beiträgen zu richten. Wir würden es sehr begrüssen, wenn auch die Probleme der Ausführung und Montage erörtert würden, um so mehr als Theorie und Praxis in Wechselwirkung stehen.

Zürich, Oktober 1972

Der Präsident der IVBH:

Prof. Maurice Cosandey

Präsident der Eidgenössischen Technischen Hochschule Lausanne

Preface

Several times, we have considered to issue our "Publications" in form of a serie of volumes, each of them treating a general determined theme. However, we have thrown it up, because it is necessary that new experiences and knowledge are diffused as quickly as possible. As creativeness can hardly be dictated, we are facilitating the quality of the contributions by offering a regular possibility of publicity, without any other limiting contingencies. The ten reports of this volume 32/II confirm the justness of our philosophy. The themes treated are very different and this richness precisely contributes to the quality of the volume. On this occasion, we should like to thank all authors vividly for their collaboration.

Once more, may I ask all French speaking members to provide some contributions. We would very much appreciate if themes on execution and assembly would be taken up all, the more as there is an interaction between theory and practice.

Zurich, October 1972

The President of IABSE:

Prof. Maurice Cosandey

President of the Swiss Federal Institute of Technology, Lausanne

Leere Seite
Blank page
Page vide

Table des matières - Inhaltsverzeichnis - Table of Contents

Die Methode der finiten Elemente für die Lösung von Torsionsproblemen

The Finite Element Method in Torsion Analysis

La méthode des éléments finis pour la solution de problèmes de torsion

W. A. M. BREKELMANS
Ing.

J. D. JANSSEN
Prof. Dr. Ing.

Laboratorium für Technische Mechanik, Technische Hochschule Eindhoven NL

1. Einleitung

Die Methode der finiten Elemente [2] hat sich für die numerische Analyse von Festigkeits- und Steifigkeitsproblemen als sehr verwendungsfähiges Hilfsmittel erwiesen. Ausserdem ist das nach dieser Methode angewandte Verfahren geeignet, bestimmte Arten partieller Differentialgleichungen zweiter Ordnung einer numerischen Lösung zuzuführen. Es ist somit eine mathematische Arbeitsweise, die unter bestimmten Umständen mit der Differenzmethode identisch ist, aber – zumindest einstweilen – grössere Anwendungsmöglichkeiten bietet [1, 2].

Nachstehend wird das Verfahren anhand der St.-Venantschen Torsionstheorie für prismatische Stäbe erläutert.

Dabei werden drei verschiedene Formulierungen dieser Theorie, die sich zum Entwurf von Näherungsmethoden eignen, betrachtet und die spezifischen Einzelheiten jeder einzelnen Methodik angegeben. Diese Näherungsmethoden bieten die Möglichkeit, die Torsionssteifigkeit zwischen zwei Grenzwerten einzuschliessen. Sie werden durch einige Beispiele erläutert und mit anderen Methoden verglichen.

2. Cie Differentialgleichungen und die Randbedingungen

Wir betrachten einen prismatischen Stab, dessen Querschnitt in Fig. 2.1 gezeichnet ist. Das Koordinatensystem wurde so gewählt, dass die z-Achse parallel zur Stabachse verläuft.

Der Stab wird in den Endquerschnitten mit einem Torsionsmoment M

belastet, derart, dass die Torsionstheorie nach de St.-Venant anzuwenden ist. Dies bedeutet, dass alle Spannungen, mit Ausnahme von τ_{zx} und τ_{zy} (Fig. 2.1), gleich Null sind.

Das Torsionsproblem kann in mehrfacher Weise formuliert werden [4, 7]. Setzt man voraus, dass das Material homogen und isotrop ist mit Schubmodul G

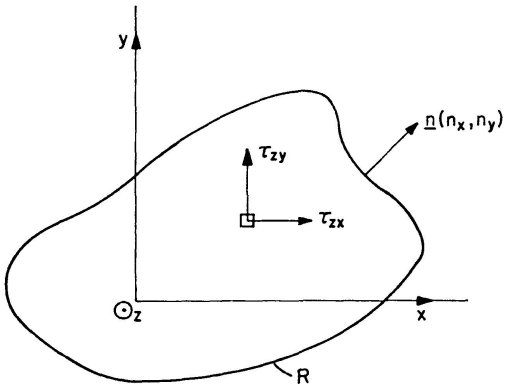

Fig. 2.1. Querschnitt eines Stabes.

und die Drillung β konstant ist und beschränkt man sich vorläufig auf Querschnitte ohne Löcher, so sind die mit a, b und c angegebenen Formulierungen möglich:

a) $\Delta \varphi_0 = 0,$ (2.1)

Randbedingung: $\frac{d\varphi_0}{dn} = (\text{grad}\,\varphi_0) = y\,n_x - x\,n_y.$ (2.2)

b) $\Delta \psi = 0,$ (2.3)

Randbedingung: $\psi = \frac{1}{2}(x^2+y^2).$ (2.4)

c) $\Delta \varphi = -2,$ (2.5)

Randbedingung: $\varphi = 0.$ (2.6)

Für die Schubspannungen τ_{zx} und τ_{zy} und das Torsionsmoment M gilt in den einzelnen Fällen:

a) $$\tau_{zx} = G\beta\left(\frac{\partial \varphi_0}{\partial x} - y\right),$$ (2.7)

$$\tau_{zy} = G\beta\left(\frac{\partial \varphi_0}{\partial y} + x\right),$$ (2.8)

$$M = \left\{I_p - \iint_F \left[\left(\frac{\partial \varphi_0}{\partial x}\right)^2 + \left(\frac{\partial \varphi_0}{\partial y}\right)^2\right] dx\,dy\right\}.$$ (2.9)

b) $$\tau_{zx} = G\beta\left(\frac{\partial \psi}{\partial y} - y\right),$$ (2.10)

$$\tau_{zy} = -G\beta\left(\frac{\partial \psi}{\partial x} - x\right),$$ (2.11)

$$M = G\beta\left[2\iint_F \psi\,dx\,dy - I_p\right].$$ (2.12)

c) $$\tau_{zx} = G\beta\frac{\partial\varphi}{\partial y}, \tag{2.13}$$

$$\tau_{zy} = -G\beta\frac{\partial\varphi}{\partial x}, \tag{2.14}$$

$$M = 2G\beta\iint_F \varphi\,dx\,dy. \tag{2.15}$$

Darin bedeutet F die Querschnittsfläche und I_p das polare Flächenträgheitsmoment:

$$I_p = \iint_F (x^2+y^2)\,dx\,dy. \tag{2.16}$$

Statt der gegebenen partiellen Differentialgleichungen mit Randbedingungen kann man für die Beschreibung des Problems auch von der Behauptung ausgehen, dass die Integralformeln (2.17), (2.18) und (2.19) stationär sind für bestimmte Variationen der gesuchten Funktionen φ_0, ψ und φ.

a) $$I_1(\varphi_0) = \iint_F \frac{1}{2}\left\{\left(\frac{\partial\varphi_0}{\partial x}\right)^2+\left(\frac{\partial\varphi_0}{\partial y}\right)^2\right\}dx\,dy + \oint_R (x\,n_y - y\,n_x)\,\varphi_0\,ds. \tag{2.17}$$

b) $$I_2(\psi) = \iint_F \frac{1}{2}\left\{\left(\frac{\partial\psi}{\partial x}\right)^2+\left(\frac{\partial\psi}{\partial y}\right)^2\right\}dx\,dy. \tag{2.18}$$

c) $$I_3(\varphi) = \iint_F \left\{\frac{1}{2}\left[\left(\frac{\partial\varphi}{\partial x}\right)^2+\left(\frac{\partial\varphi}{\partial y}\right)^2\right]-2\varphi\right\}dx\,dy. \tag{2.19}$$

Auf Grund bekannter Sätze der Variationsrechnung folgt alsdann eine alternative Formulierung für die Gleichungen (2.1) ... (2.6):

a) $\delta I_1 = 0$ für alle $\delta\varphi_0$. (2.20)

b) $\delta I_2 = 0$ für alle $\delta\psi$ mit der Beschränkung

$\psi = \frac{1}{2}(x^2+y^2)$ auf dem Rand des Gebietes F. (2.21)

c) $\delta I_3 = 0$ für alle $\delta\varphi$ mit $\varphi = 0$ auf dem Rand. (2.22)

Interessant ist, dass die Bedingungen (2.20) und (2.22) unmittelbar abgeleitet werden können, wenn man von der potentiellen Energie V bzw. der komplementären Energie V^* für einen durch Torsion beanspruchten Stab mit Länge 1 ausgeht und Minimalprinzipien für diese Formeln verwendet [3, 4].

Für V und V^* gilt:

$$V = \tfrac{1}{2}G\beta^2\iint_F \left\{\left(\frac{\partial\varphi_0}{\partial x}-y\right)^2+\left(\frac{\partial\varphi_0}{\partial y}+x\right)^2\right\}dx\,dy - \beta M, \tag{2.23}$$

$$V^* = \tfrac{1}{2}G\beta^2\iint_F \left\{\left(\frac{\partial\varphi}{\partial x}\right)^2+\left(\frac{\partial\varphi}{\partial y}\right)^2\right\}dx\,dy - 2G\beta^2\iint_F \varphi\,dx\,dy. \tag{2.24}$$

Hieraus kann einfach abgeleitet werden:

$$V = G\beta^2 I_1 + \tfrac{1}{2} G\beta^2 I_p - \beta M, \tag{2.25}$$

$$V^* = G\beta^2 I_3. \tag{2.26}$$

Mit dem Prinzip der minimalen potentiellen Energie ergibt sich:

$$\delta I_1 = 0 \tag{2.27}$$

unter der dynamischen Randbedingung:

$$G\beta(2 I_1 + I_p) = M. \tag{2.28}$$

Es ist nachweisbar, dass diese Formel für M mit (2.9) übereinstimmt. Aus dem Variationsprinzip der komplementären Energie folgt:

$$\delta I_3 = 0. \tag{2.29}$$

Das Vorangehende impliziert, dass für ein gegebenes Torsionsmoment der mit einer Näherung für φ_0 aus (2.20) berechnete Wert von β nicht grösser sein kann als der exakte Wert. Der Wert von β, der mit (2.22) berechnet werden kann, wenn für φ eine Näherungsfunktion genommen wird, ist immer grösser als oder ebenso gross wie der exakte Wert. Auf diese Weise lässt sich der wirkliche Torsionswiderstand zwischen einer oberen und einer unteren Schranke eingrenzen, die entsprechend den Näherungsansätzen beliebig nahe aneinanderrücken können.

3. Näherungslösungen

3.1. Einleitung

Nur für verhältnismässig wenige Querschnittsformen lässt sich die exakte Lösung des Torsionsproblems bestimmen [4, 7]. Manchmal ist es für die Lösung notwendig, unendliche Reihen zu verwenden, wobei die Erzielung numerischer Resultate umfassende Rechenarbeit erfordert.

Für dünnwandige Stäbe sind Näherungsmethoden bekannt, die sich, wenn es sich um Stäbe mit offenem Profil handelt, auf die Lösung für schmale Rechteckquerschnitte stützen, und die für Stäbe mit geschlossenem Profil von der Hypothese ausgehen, dass die Schubspannungen über die Wandstärke hinweg konstant sind. Bisher ist es nicht gelungen, das Anwendungsgebiet dieser Näherungslösungen genau zu begrenzen.

Manchmal können mit Lösungen der Differentialgleichung und einer Umkehrmethode Näherungslösungen konstruiert werden. Für jede lineare Kombination derartiger Lösungen ist die Randkurve bestimmbar, wobei die Randbedingungen erfüllt sind. Gerade diese Kombination ist anzustreben, wobei die wirkliche Randkurve bestens genähert wird.

Wir werden diese Methodik anhand eines Stabes erläutern, dessen Querschnitt von einem regelmässigen Polygon begrenzt wird. Für das angegebene

Verfahren eignet sich am besten die dritte Formulierung des Torsionsproblems (Formel (2.5) und (2.6)).

Ausserdem können mit den Variationsprinzipien Näherungslösungen konstruiert werden. Dieses Verfahren, im allgemeinen als Methode Ritz bekannt, werden wir, ebenfalls in der Formulierung (2.5) und (2.6), für das gleiche Beispiel anwenden.

Die Differenzmethode ermöglicht eine numerische Lösung der Differentialgleichung.

Das nächste Kapitel behandelt die Methode der finiten Elemente, eine Methode, die als Spezialfall der Methode Ritz betrachtet werden kann.

3.2. Umkehrmethode mit Beispiel

Wird der Querschnitt eines durch Torsion beanspruchten prismatischen Stabes von einem regelmässigen Polygon mit n-Eckpunkten (Fig. 3.1) begrenzt, so ergibt sich für die Lösung φ der Differentialgleichung (2.5) mit der Randbedingung (2.6):

$$\varphi = -\tfrac{1}{2} r^2 + C_0 + \sum_{p=1}^{\infty} C_p r^{np} \cos(n p \vartheta). \tag{3.1}$$

Dabei sind r und ϑ die in Fig. 3.1 angegebenen Polarkoordinaten.

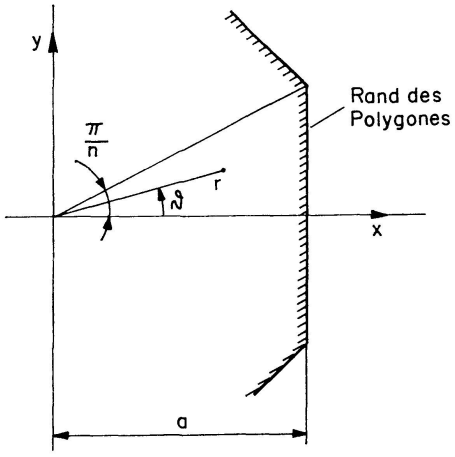

Fig. 3.1. Regelmässiges Polygon mit n-Eckpunkten.

Das Torsionsproblem ist gelöst, wenn die Konstanten $C_0, C_1, \ldots$ derartig bestimmt werden können, dass für $0 \leqq \vartheta \leqq \pi/n$ die Randbedingung $\varphi = 0$ erfüllt ist.

Ein Verfahren, das auch in der Praxis anwendbar ist, erhält man, wenn man nur die ersten j-Glieder der Reihe in (3.1) betrachtet und für die Berechnung der Konstanten $(C_0, C_1, \ldots C_j)$, $j+1$ Bedingungen formuliert.

Für den Fall $j = 2$ wird das Problem weiter ausgearbeitet. Zur Ableitung der Gleichungen für C_0, C_1 und C_2 können viele Kriterien angewandt werden. Nachstehend folgen zwei Beispiele, nämlich:

a)
$$\varphi = 0 \text{ für } \begin{cases} r = a, & \vartheta = 0, \\ r = \dfrac{a}{\cos\frac{\pi}{2n}}, & \vartheta = \dfrac{\pi}{2n}, \\ r = \dfrac{a}{\cos\frac{\pi}{n}}, & \vartheta = \dfrac{\pi}{n}. \end{cases} \tag{3.2}$$

b)
$$\left.\begin{aligned} \varphi &= 0 \\ \frac{d\varphi}{dy} &= 0 \\ \frac{d^2\varphi}{dy^2} &= 0 \end{aligned}\right\} \text{ für } x = a,\ y = 0 \quad \text{(siehe Abb. 3.1).} \tag{3.3}$$

In jedem Kriterium sind selbstverständlich drei Forderungen zur Bestimmung von C_0, C_1 und C_2 gestellt worden.

Wenn daraus φ bestimmt worden ist, kann nachträglich die Randkurve angegeben werden, für welche diese Lösung exakt ist. Im allgemeinen wird diese Kurve dargestellt durch (siehe Fig. 3.1):

$$r(\vartheta) = \frac{a}{\cos\vartheta}[1 + \delta(\vartheta)] \quad (0 \leqq \vartheta \leqq \pi/n). \tag{3.4}$$

Dabei ist $\frac{a}{\cos\vartheta}\delta(\vartheta)$ die Abweichung der erwünschten Kurve. Vergleicht man $|\delta|$ mit 1, so lässt sich ein qualitativer Eindruck vom Wert der Näherungslösung gewinnen.

Für die maximale Schubspannung und die Torsionssteifigkeit kann man dann schreiben:

$$\tau_{max} = \frac{M}{k_1 a^3}, \tag{3.5}$$

$$\frac{M}{G\beta} = k_2 a^4. \tag{3.6}$$

Die dimensionslosen Grössen k_1 und k_2 werden als Vergleichsmassstab angewendet.

Wird das genannte Verfahren auf einen Stab mit einem Querschnitt von der Form eines gleichseitigen Dreiecks angewandt und werden dabei die Kriterien (3.2) oder (3.3) gebraucht, so erhält man für φ das exakte Resultat:

$$\varphi = -\frac{1}{2}r^2 + \frac{2}{3}a^2 - \frac{r^3}{6a}\cos(3\vartheta). \tag{3.7}$$

Für einen Stab von regelmässigem viereckigem Querschnitt kann anhand von (3.2) berechnet werden:

$$\varphi = -\frac{1}{2}r^2 + 0{,}5903\,a^2 - 0{,}0928\frac{z^4}{a^2}\cos 4\vartheta + 0{,}0024\frac{r^8}{a^6}\cos 8\vartheta. \tag{3.8}$$

Dieses Resultat ist nicht exakt, jedoch lässt sich beweisen, dass $|\delta| < 0{,}008$, während τ_{max} um etwa 1% zu niedrig und $\frac{M}{G\beta}$ um etwa 1% zu hoch berechnet werden.

Für einen Stab mit einem Querschnitt in Form eines regelmässigen sechseckigen Polygons sind die mit (3.2) und (3.3) berechneten Resultate in der Tabelle 3.1 gegeben.

Die Resultate, die man mit den Kriterien (3.2) erhält, entsprechen den Resultaten in [6].

Tabelle 3.1. Sechseckiges Polygon

	C_0	C_1	C_2	$\|\delta\|_{max}$	k_1	k_2
Kriterien (3.2)	0,5412	–0,0447	0,0035	0,01	1,511	1,853
Kriterien (3.3)	0,5373	–0,0385	0,0012	0,05	1,497	1,821

3.3. Methode Ritz mit Beispiel

Die Energie I_3 nach (2.19), die in direktem Zusammenhang mit der komplementären Energie V^* nach (2.24) steht, eignet sich für das Entwerfen von Näherungsmethoden. Die in (2.19) einzusetzende Funktion φ wird aus einer Sammlung von Funktionen gewählt, die alle einige unbestimmte Konstanten enthalten. Die Auswahl der Konstanten ist am günstigsten, wenn die Energie I_3 für alle zulässigen Variationen dieser Konstanten stationär ist.

Da im Prinzip der minimalen komplementären Energie im Variationsprozess die Gleichgewichtsforderungen erfüllt sein müssen, muss φ wenigstens zweimal differenzierbar sein. Ferner muss infolge der Bedingung (2.6) an der Randkurve des Querschnitts $\varphi = 0$ gelten. In [4] wird diese Methode u. a. auf einen vierkantigen Stab angewandt. Nimmt man an, dass

$$\varphi = b_0 (x^2 - a^2)(y^2 - a^2) \tag{3.9}$$

so resultiert (2.22) in einer linearen Gleichung für b_0. Hierbei stellt sich heraus, dass die Torsionssteifigkeit um 1,3% zu niedrig ist. Nimmt man zwei Konstanten und berücksichtigt dabei die Symmetrie des Querschnitts, so kann man sich dadurch der richtigen Torsionssteifigkeit bis auf 0,15% nähern. Die berechnete maximale Schubspannung weicht dann aber noch um etwa 4% vom korrekten Wert ab.

Für einen Querschnitt mit einem regelmässigen Sechseck als Randkurve kann man nach einem analogen Verfahren vorgehen. Setzt man z. B.

$$\varphi = (x^2 - a^2)(x^2 + 3y^2 - 2xy\sqrt{3} - 4a^2)(x^2 + 3y^2 + 2xy\sqrt{3} - 4a^2) f(x, y) \tag{3.10}$$

so entspricht φ der Randbedingung. Die Funktion $f(x, y)$ in dieser Formel soll zweimal differenzierbar sein, ist aber im übrigen willkürlich. Da es empfehlens-

wert ist, die Symmetrie des Querschnitts zu berücksichtigen, wählt man

$$f(x,y) = b_0 + b_1(x^2+y^2). \tag{3.11}$$

Mit der Substitution von (3.10) und (3.11) in (2.19) folgt $I_3 = I_3(b_0, b_1)$, worauf die unbekannten Konstanten b_0 und b_1 bestimmt werden können mit Hilfe der Gleichungen:

$$\frac{\partial I_3(b_0, b_1)}{\partial b_i} = 0 \quad (i = 0,1). \tag{3.12}$$

Für b_0, b_1, k_1 und k_2 wurde in [5] abgeleitet:

$$\begin{aligned} b_0 &= -0{,}03264\ G\beta/a^4, \\ b_1 &= -0{,}02621\ G\beta/a^6, \\ k_1 &= 1{,}678 \quad \text{(siehe (3.5))}, \\ k_2 &= 1{,}777 \quad \text{(siehe (3.6))}. \end{aligned}$$

Zu bemerken ist, dass die in dieser Weise für k_1 und k_2 berechneten Werte in bezug auf die exakten Werte um etwa 11% zu hoch, bzw. um etwa 4% zu niedrig sind. Die Tatsache, dass die Torsionssteifigkeit unterschätzt wird, ist, wie schon früher bemerkt, ein allgemein bekanntes Kennzeichen von Näherungslösungen, die sich auf das Prinzip der komplementären Energie stützen.

Es ist klar, dass die genannte Methode sehr arbeitsintensiv und für elektronische Rechenmaschinen nicht einfach und zweckmässig programmierbar ist. Im nächsten Kapitel wird ein Verfahren beschrieben, das sich für elektronische Verarbeitung eignet.

4. Die Methode der finiten Elemente für Torsionsprobleme mit einfach zusammenhängendem Gebiet

Ebenso wie bei den im letzten Kapitel angegebenen Methoden, beruht die Methode der finiten Elemente [1] auf Integralformeln, aus denen mittels Variationsprinzipien die beschreibenden Differentialgleichungen folgen würden, wenn die zu variierenden Funktionen nicht weiter eingeschränkt werden.

In 3.3 wurde für den ganzen Querschnitt eine Funktion φ mit zwei Parametern genommen. In der Methode der finiten Elemente (kurz: Elementenmethode) wird der Querschnitt eingeteilt in eine Anzahl von Teilen (Elemente genannt) mit meist sehr einfacher Begrenzung, wie z. B. Dreiecke, Rechtecke und Trapeze. Beschränkt man sich zunächst auf die Beschreibung des Problems mit Hilfe der Funktion φ, so wird für jedes Element der Verlauf von φ im Inneren des Elementes als gegeben angenommen. Für das Element in Fig. 4.1 kann für φ z. B. die Bedingung gestellt werden:

$$\varphi = c_1 + c_2 x + c_3 y, \tag{4.1}$$

wobei c_1, c_2 und c_3 noch unbekannte Konstanten sind.

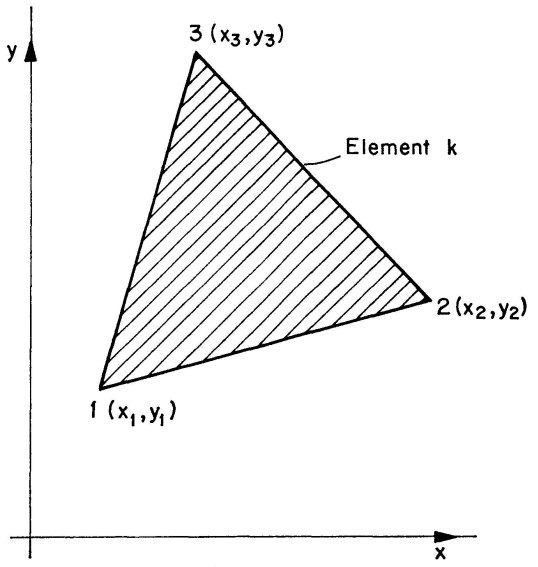

Fig. 4.1. Beispiel eines Elementes.

Werden auf diese Weise Voraussetzungen für jedes Element im beobachteten Querschnitt getroffen, so lässt sich I_3 einfach in einer Anzahl von Konstanten ausdrücken. Der Satz: $\delta I_3 = 0$ ist nicht ohne weiteres anwendbar, da φ beim Variieren dieser Konstanten jedenfalls kontinuierlich sein soll. Durch Ansatz (4.1) ist φ kontinuierlich im Innern des Elementes, während die Kontinuität von φ auf den Grenzen zwischen den Elementen garantiert ist, wenn man, statt c_1, c_2 und c_3 für jedes Element, den Wert von φ in jedem Knotenpunkt des Querschnitts als zu variierende Grösse betrachtet. Deshalb sollen für jedes Element die Unbekannten c_1, c_2 und c_3 im Wert von φ in den Knotenpunkten des Elementes ausgedrückt werden.

Den Wert von φ in den Knotenpunkten 1, 2 und 3 des k-ten Elementes (siehe Fig. 4.1) geben wir mit bzw. φ_1, φ_2 und φ_3 an und definieren den Spaltenvektor φ^k mit:

$$\varphi^k = \begin{bmatrix} \varphi_1 \\ \varphi_2 \\ \varphi_3 \end{bmatrix}.$$

Statt (4.1) ergibt sich für φ im Inneren des Elementes k:

$$\varphi(x,y) = \varphi_1 P_1(x,y) + \varphi_2 P_2(x,y) + \varphi_3 P_3(x,y). \tag{4.3}$$

P_1 ist gegeben durch:

$$P_1 = \frac{1}{2\Delta}[(x_2 y_3 - x_3 y_2) + (y_2 - y_3)\, x + (x_3 - x_2)\, y]. \tag{4.4}$$

Dabei ist Δ die Oberfläche des betrachteten Elementes. P_2 und P_3 folgen aus (4.4), indem man die Indizes zyklisch vertauscht.

Ist die Anzahl von Elementen gleich K, so kann man für I_3 nach (2.19) schreiben:

$$I_3 = \sum_{k=1}^{K} I_3^k, \tag{4.5}$$

wobei für I_3^k gilt:

$$I_3^k = \iint_{\Delta} \left\{ \frac{1}{2} \left[\left(\frac{\partial \varphi}{\partial x} \right)^2 + \left(\frac{\partial \varphi}{\partial y} \right)^2 \right] - 2\varphi \right\} dx\, dy. \tag{4.6}$$

Mit φ nach (4.3) kann mittels (4.4) und (4.6) für I_3^k abgeleitet werden:

$$I_3^k = \tfrac{1}{2} \varphi'^k H^k \varphi^k - \varphi'^k f^k.$$

(Bemerkung: Transponierung einer Matrix oder eines Spaltenvektors A wird mit A' angegeben.)

Für H^k gilt:

$$H^k = \frac{1}{4\Delta} \begin{bmatrix} (y_2-y_3)^2+(x_2-x_3)^2 & (y_3-y_1)(y_2-y_3)+(x_3-x_1)(x_2-x_3) & (y_1-y_2)(y_2-y_3)+(x_1-x_2)(x_2-x_3) \\ (y_2-y_3)(y_3-y_1)+(x_2-x_3)(x_3-x_1) & (y_3-y_1)^2+(x_3-x_1)^2 & (y_1-y_2)(y_3-y_1)+(x_1-x_2)(x_3-x_1) \\ (y_2-y_3)(y_1-y_2)+(x_2-x_3)(x_1-x_2) & (y_3-y_1)(y_1-y_2)+(x_3-x_1)(x_1-x_2) & (y_1-y_2)^2+(x_1-x_2)^2 \end{bmatrix}, \tag{4.8}$$

während f^k definiert ist durch:

$$f'^k = \tfrac{2}{3} \Delta [1 \;\; 1 \;\; 1]. \tag{4.9}$$

Mit I_3^k nach (4.7) kann I_3 aus (4.5) für den ganzen Querschnitt bestimmt werden. Wegen der Randbedingungen des Variationsproblems soll am Rande gelten: $\varphi(x, y) = 0$. Das bedeutet, dass für Knotenpunkte am Rande des Gebietes φ gleich Null sein muss.

Betrachtet man die Werte von φ für alle Knotenpunkte im beobachteten Gebiet als Komponenten eines Spaltenvektors Φ, so kann man für I_3 schreiben:

$$I_3 = \tfrac{1}{2} \Phi' H_3 \Phi - \Phi' f, \tag{4.10}$$

wobei die Matrix H_3 symmetrisch ist, also $H_3' = H_3$. Auf ganz einfache Weise können H_3 und f aus den Matrizen H^k bzw. den Vektoren f^k für alle Elemente zusammengestellt werden.

Aus $\delta I_3 = 0$ folgt für alle Variationen der Komponenten des Vektors Φ ein System linearer Gleichungen für diese Komponenten:

$$H_3 \Phi = f, \tag{4.11}$$

woraus sich ableiten lässt:

$$\Phi = H_3^{-1} f. \tag{4.12}$$

Der Ansatz (4.3) für φ im Inneren des Elementes ist linear in x und y. Die Schubspannungen τ_{zx} und τ_{zy} in jedem Element sind deshalb konstant vorausgesetzt worden.

Aus (2.13) und (2.14) ergibt sich:

$$\tau^k = \begin{bmatrix} \tau_{zx} \\ \tau_{zy} \end{bmatrix} = \frac{G\beta}{2\Delta} \begin{bmatrix} (x_3-x_2) & (x_1-x_3) & (x_2-x_1) \\ (y_3-y_2) & (y_1-y_3) & (y_2-y_1) \end{bmatrix} \varphi^k. \tag{4.13}$$

Ausser den Schubspannungen ist meist auch die Torsionssteifigkeit interessant. Mit (2.15) ergibt sich:

$$J_d = \frac{M}{G\beta} = 2\sum_{k=1}^{K}\{\tfrac{2}{3}\Delta[1\ \ 1\ \ 1]\varphi^k\}. \tag{4.14}$$

Die mit (4.14) berechnete Torsionssteifigkeit ist immer kleiner als oder ebenso gross wie die exakte Torsionssteifigkeit des Querschnitts, da die angewandte Näherungslösung auf dem Prinzip der minimalen komplementären Energie beruht. Man kann die gleiche Folgerung in bezug auf J_d ziehen, wenn man das Prinzip der minimalen potentiellen Energie für die Bestimmung von Näherungslösungen der Seifenhautanalogie anwendet.

Häufig wird der Querschnitt ein- oder mehrfach symmetrisch sein. In Punkten der Symmetrieachse wird die Komponente der Schubspannung dieser Achse entlang gleich Null sein. Das heisst, auf dieser Achse gilt $\frac{d\varphi}{dn} = 0$, wobei $\frac{d}{dn}$ die Differenzierung senkrecht zur Achse bedeutet. Im Kapitel 2 ist dargelegt worden (siehe (2.17)), dass Bedingungen vom Typ $\frac{d\varphi}{dn} = f(x,y)$ am Rande R berücksichtigt werden können, wenn an (2.19) das Linienintegral $-\oint_R f(x,y)\,\varphi\,ds$ hinzugefügt wird. Da auf einer Symmetrieachse $f(x,y)=0$ ist, braucht man kein besonderes Glied an I_3 hinzuzufügen, wenn man einen geeigneten Teil des Querschnitts betrachtet. Für Randpunkte, die auf einer Symmetrieachse liegen, soll φ selbstverständlich – im Gegensatz zur Situation bei einer materiellen Randkurve – frei gelassen werden.

Im vorhergehenden wurde die Arbeitsweise der Elementenmethode mit der Formel (2.19) für $I_3(\varphi)$ als Ausgangspunkt erklärt. In völlig analoger Weise kann man ausgehen von (2.17) für $I_1(\varphi_0)$ oder (2.18) für $I_2(\psi)$. Definiert man, analog (4.2), die Spaltenvektoren φ_0^k und ψ^k und setzt man für φ_0 bzw. ψ einen linearen Verlauf in jedem Element voraus, so ergibt sich für die mit (4.7) übereinstimmenden Formeln:

$$I_1^k = \tfrac{1}{2}\varphi_0'^k H^k \varphi_0^k - \varphi_0'^k f_0^k, \tag{4.15}$$

$$I_2^k = \tfrac{1}{2}\psi'^k H^k \psi^k. \tag{4.16}$$

Die in (4.15) und (4.16) auftretende Matrix H^k ist identisch mit (4.8).

Wenn die Werte von φ_0 in allen Knotenpunkten des Querschnitts, einschliesslich der Randpunkte, im Spaltenvektor Φ_0 geordnet werden, so gilt:

$$I_1 = \tfrac{1}{2}\Phi_0' H_1 \Phi_0 - \Phi_0' f_0. \tag{4.17}$$

Das Glied $\Phi_0' f_0$ stammt von $\oint_R (x n_y - y n_x)\varphi_0\,ds$ (siehe (2.17)). Der Beitrag vom Teil AB des Randes (siehe Fig. 4.2) zu $\Phi_0' f_0$ ist gleich:

$$[\varphi_{0_i}\varphi_{0_j}]\begin{bmatrix} -\frac{1}{3}x_i^2 + \frac{1}{6}x_j^2 + \frac{1}{6}x_i x_j - \frac{1}{3}y_i^2 + \frac{1}{6}y_j^2 + \frac{1}{6}y_i y_j \\ -\frac{1}{6}x_i^2 + \frac{1}{3}x_j^2 - \frac{1}{6}x_i x_j - \frac{1}{6}y_i^2 + \frac{1}{3}y_j^2 + \frac{1}{6}y_i y_j \end{bmatrix}. \tag{4.18}$$

Mit (4.18) kann f_0 berechnet werden.

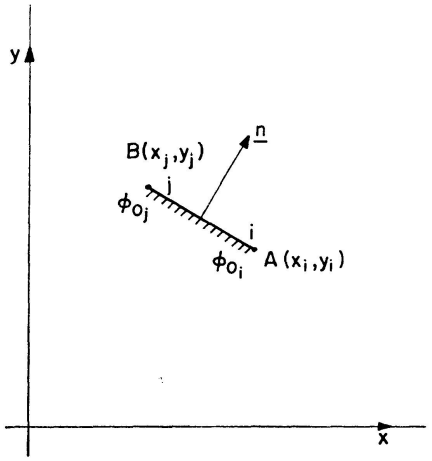

Fig. 4.2. Teil AB des Randes.

Bilden die Werte von ψ in allen Knotenpunkten im Inneren des Gebietes den Spaltenvektor Ψ, und werden die Werte von ψ in den Knotenpunkten am Rande des Gebietes in den Spaltenvektor Ψ_0 geordnet, so kann man für I_2 schreiben:

$$I_2 = \tfrac{1}{2}[\Psi' \Psi_0'] \begin{bmatrix} H_2 & H_{20} \\ H_{20}' & H_{00} \end{bmatrix} \begin{bmatrix} \Psi \\ \Psi_0 \end{bmatrix}. \tag{4.19}$$

Der Spaltenvektor Ψ in (4.19) kann variieren. Dadurch ergibt sich:

$$H_2 \Psi + H_{20} \Psi_0 = 0. \tag{4.20}$$

Die Komponenten von Ψ_0 werden von den Randbedingungen (2.4) bestimmt und die Lösung des Gleichungssystemes (4.20) folgt aus:

$$\Psi = -H_2^{-1} H_{20} \Psi_0. \tag{4.21}$$

Auch wenn das Problem mit φ_0 oder ψ formuliert wird, lassen sich die Schubspannungen und die Torsionssteifigkeit in einfacher Weise bestimmen und kann eine eventuelle Symmetrie des Querschnitts vorteilhaft berücksichtigt werden.

5. Einige Beispiele

5.1. Rechteckquerschnitt

Für St.-Venantsche Torsion von Stäben mit Rechteckquerschnitt sind in [4] einige charakteristische Grössen gegeben worden als Funktion des Verhältnisses b/a (siehe Fig. 5.1).

Durch das im vierten Kapitel dargestellte Verfahren für die Berechnung von φ werden hier dieselbe Charakteristiken bestimmt. Infolge der Symmetrie des Querschnitts braucht man nur den in Fig. 5.1 schraffierten Teil in Elemente einzuteilen. Das Muster der Einteilung in Elemente ist in Fig. 5.2 gezeichnet.

Die Randbedingungen sind:

$$\varphi = 0 \text{ für } \begin{cases} x = a, & 0 \leqq y \leqq b, \\ y = b, & 0 \leqq x \leqq a. \end{cases} \tag{5.1}$$

Als wohl am meisten interessante Charakteristiken wählen wir die zwei Faktoren k und k_1, die entsprechend [4] definiert sind durch:

$$M = k G \beta a^4, \tag{5.2}$$

$$\tau_{max} = k_1 G \beta a. \tag{5.3}$$

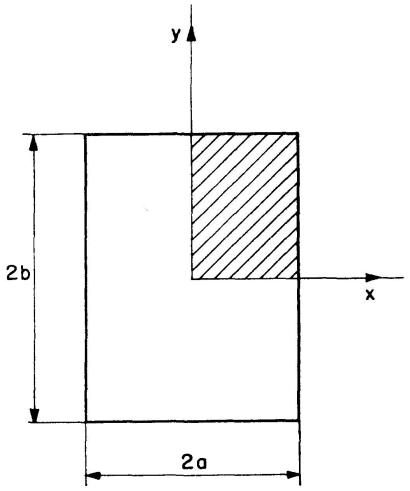

Fig. 5.1. Rechteckquerschnitt.

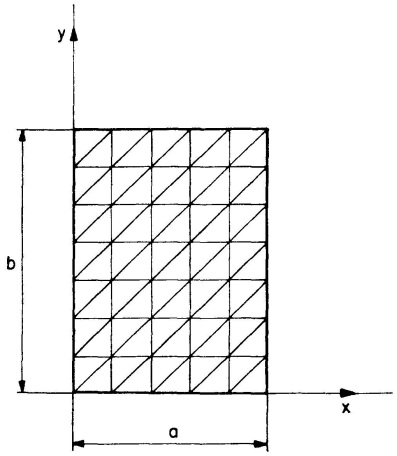

Fig. 5.2. Muster der Einteilung in Elemente.

In der Tabelle 5.1 sind für einige Verhältnisse b/a die Werte von k und k_1 nach [4] und die mit einer Einteilung in 450 Elemente berechneten Werte gegeben worden. Dabei ist zu bemerken, dass k_1 mittels Extrapolation aus den berechneten Resultaten bestimmt werden soll.

Tabelle 5.1. Rechteckquerschnitt

b/a	1,0	1,2	1,5	2,0	2,5	3,0	4,0	5,0	10,0
k (El.meth.)	2,238	3,173	4,674	7,278	9,917	12,560	17,850	23,130	49,410
k (nach [4])	2,248	3,187	4,704	7,328	9,960	12,624	17,984	23,280	49,920
k_1 (El.meth.)	1,345	1,512	1,690	1,856	1,933	1,967	1,991	1,996	1,993
k_1 (nach [4])	1,350	1,518	1,696	1,860	1,936	1,970	1,994	1,998	2,000

Wie schon im dritten Kapitel vorhergesagt, ergibt sich aus dieser Tabelle, dass die Werte von k nach der Elementenmethode kleiner sind als die exakten Werte. Die Unterschätzung der Torsionssteifigkeit variiert von 0,4% für $b/a = 1$ bis 1% für $b/a = 10$. Die Abweichung in der maximalen Schubspannung ist weniger als 0,5%. Durch Verfeinerung der Elementeneinteilung nähert man sich besser der Realität. Wird z.B. für $b/a = 5$ der in Fig. 5.1 schraffierte Teil in 900 Elemente eingeteilt, so ergibt sich: $k = 23{,}230$ und $k_1 = 1{,}996$.

Mit $b/a = 10$ und ebenfalls 900 Elementen folgt: $k = 49{,}770$ und $k_1 = 1{,}997$, während mit 1800 Elementen $k = 49{,}870$ und $k_1 = 1{,}999$ berechnet wird.

5.2. Kreissektor als Querschnitt

Für einen Querschnitt wie in Fig. 5.3 gezeichnet, ist – für den schraffierten Teil – die Elementenmethode für die Berechnung von φ angewandt.

Das Muster der Einteilung in Elemente ist in Fig. 5.4 gezeichnet.

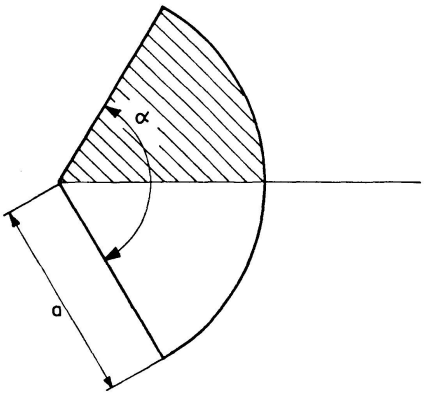

Fig. 5.3. Kreissektor als Querschnitt.

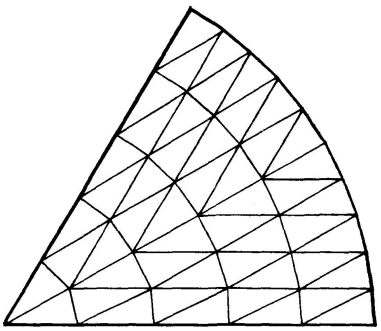

Fig. 5.4. Muster der Einteilung in Elemente.

Entsprechend [4] definieren wir:

$$M = k G \beta a^4, \tag{5.4}$$

$$\tau_{max} = \begin{cases} k_1 G \beta a & \text{auf dem Kreisbogen,} \\ k_2 G \beta a & \text{auf dem geraden Rand.} \end{cases} \tag{5.5}$$

Besonders für grosse Werte von α (z. B. $\alpha > \pi$) lässt sich die maximale Schubspannung am geraden Rand mit dem gewählten Elementenmuster nicht ganz genau berechnen, weil diese Spannungen mittels Extrapolation bestimmt werden sollen.

In der Tabelle 5.2 sind die Resultate, berechnet mit einer Einteilung in 450 Elemente, mit den Resultaten nach [4] verglichen. Daraus ergibt sich eine zufriedenstellende Übereinstimmung.

Tabelle 5.2. Kreissektor als Querschnitt

α	$\pi/4$	$\pi/3$	$\pi/2$	$2\pi/3$	π	$3\pi/2$	$5\pi/3$	2π
k (El.meth.)	0,0179	0,0345	0,0816	0,143	0,295	0,565	0,660	0,852
k (nach [4])	0,0181	0,0349	0,0825	0,148	0,296	0,572	0,672	0,878
k_1 (El.meth.)	0,38	0,45	0,56	0,63	0,73	0,80	0,82	0,84
k_1 (nach [4])	—	0,452	—	0,622	0,719	—	—	—
k_2 (El.meth.)	0,41	0,49	0,60	0,68	0,86	—	—	—
k_2 (nach [4])	—	0,490	—	0,652	0,849	—	—	—

5.3. Regelmässiges Vieleck als Querschnitt

Im dritten Kapitel wurde untersucht, wie mehrere Näherungsmethoden angewandt werden können, falls der Querschnitt ein regelmässiges Vieleck ist (siehe Fig. 3.1). Auch die Elementenmethode kann dabei sehr nützlich sein. Wird die Symmetrie optimal benutzt, so kann das Elementenmuster die in Fig. 5.5 gezeichnete Form haben.

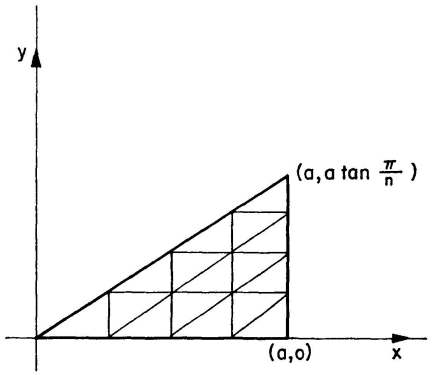

Fig. 5.5. Muster der Einteilung in Elemente.

Am Ende des zweiten Kapitels wurde bewiesen, dass die exakte Torsionssteifigkeit begrenzt werden kann, wenn sowohl eine Berechnung zur Bestimmung von φ_0 wie von φ ausgeführt wird.

a) Die untere Grenze wird bestimmt mittels der Methode zur Berechnung von φ. Die Randbedingung lautet:

$$\varphi = 0 \quad \text{für } x = a,\ 0 \leqq y \leqq a \tan\frac{\pi}{n}, \tag{5.6}$$

wobei n die Anzahl der Eckpunkte ist.

b) Die obere Grenze wird bestimmt mittels der Methode zur Berechnung von φ_0. Nur wenn der Ursprung des Koordinatensystemes mit dem Schnittpunkt der Symmetrieachsen zusammenfällt, gilt als Randbedingung $\varphi_0 = 0$ für die Symmetrieachsen. Mit der Wahl des Koordinatensystemes nach Fig. 5.5 soll gefordert werden:

$$\varphi_0 = 0 \quad \text{für } 0 \leqq x \leqq a \begin{cases} y = 0, \\ y = x \tan\dfrac{\pi}{n} \end{cases} \tag{5.7}$$

Das Vorhergehende soll anhand des regelmässigen Sechseckes demonstriert werden. Dabei werden die Unter- und Obergrenze für k_2 (siehe (3.6)) angegeben mit k_{2a} und k_{2b}.

Wird der Teil in Fig. 5.5 in 324 Elemente aufgeteilt, so findet man:

$$k_{2a} = 1{,}838,$$
$$k_{2b} = 1{,}842.$$

Für die exakte Torsionssteifigkeit k_2 gilt somit:

$$1{,}838 \leqq k_2 \leqq 1{,}848.$$

Für eine Reihe von regelmässigen Polygonen mit variabler Anzahl von Eckpunkten wurden die am meisten interessanten Charakteristiken berechnet. Es ist vorteilhaft, dimensionslose Kenngrössen f^* und τ^*_{max} zu definieren, die für die Flexibilität bzw. die maximale Schubspannung massgebend sind:

$$f^* = \tfrac{1}{2}\pi a^4 \frac{G\beta}{M}, \tag{5.8}$$

$$\tau^*_{max} = \tfrac{1}{2}\pi a^3 \frac{\tau_{max}}{M}. \tag{5.9}$$

Aus den graphischen Darstellungen 5.1 und 5.2 sind die Resultate für f^* und τ^*_{max} ersichtlich. Zum Vergleich sind in diesen Darstellungen auch die entsprechenden Werte für zwei Stäbe mit kreisförmigem Querschnitt gegeben,

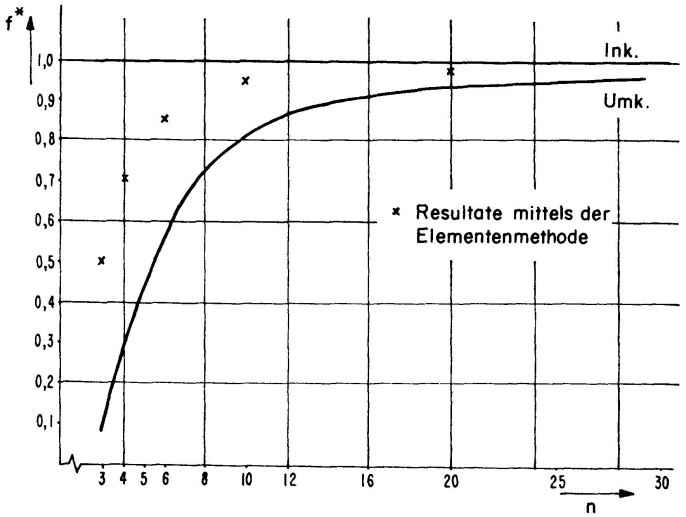

Graphik 5.1. Vergleich der Flexibilität.

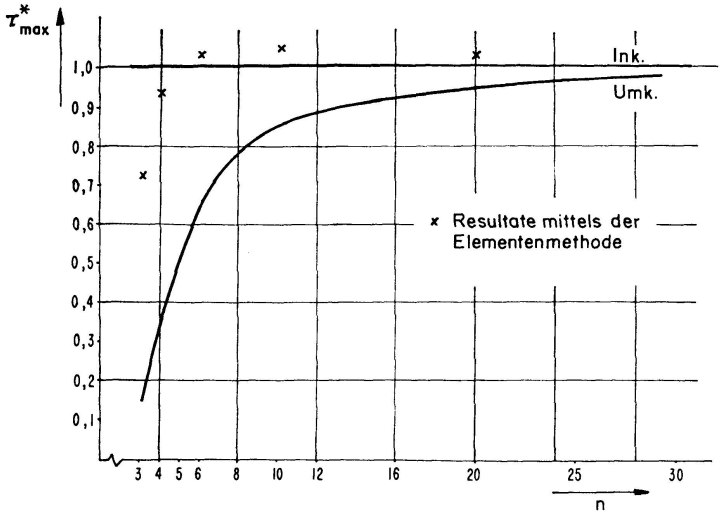

Graphik 5.2. Vergleich der maximalen Schubspannung.

dessen Radius ebenso gross ist wie der Radius des Innenkreises R_i bzw. des Umkreises R_u des betrachteten Querschnitts. Es gilt:

$$R_i = a, \tag{5.10}$$

$$R_u = \frac{a}{\cos\frac{\pi}{n}}. \tag{5.11}$$

6. Mehrfach zusammenhängende Querschnitte

Ist der Querschnitt nicht einfach zusammenhängend (siehe Fig. 6.1), so können die in (2.1) bis einschliesslich (2.6) gegebenen Formulierungen nicht benützt werden.

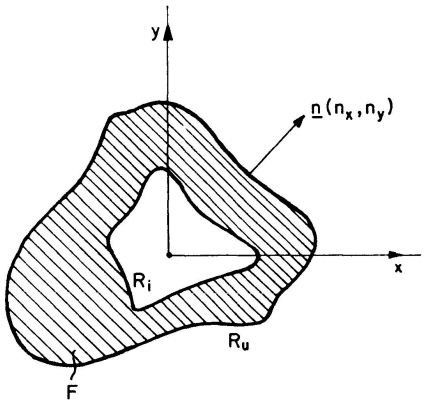

Fig. 6.1. Mehrfach zusammenhängender Querschnitt.

Mit den Buchstaben a, b und c werden die Änderungen angegeben, die für Querschnitte mit nur einem Loch in den Formulierungen a, b und c des zweiten Kapitels angebracht werden müssen. Die Erweiterung nach Querschnitten mit mehreren Löchern bietet keine besonderen Probleme.

a) $\Delta\varphi_0 = 0$ im Gebiet F, (6.1)

$$\frac{d\varphi_0}{dn} = (\text{grad}\,\varphi_0) = y\,n_x - x\,n_y \text{ auf } R_u \text{ und } R_i. \tag{6.2}$$

b) $\Delta\psi = 0$ in F, (6.3)

$$\psi = \tfrac{1}{2}(x^2+y^2) \text{ auf } R_u, \tag{6.4}$$

$$\psi = \tfrac{1}{2}(x^2+y^2) + C_1 \text{ auf } R_i. \tag{6.5}$$

Dabei ist C_1 eine noch unbekannte Konstante, die bestimmt werden kann nach der Bedingung:

$$\oint_{R_i} \frac{d\psi}{dn}\,ds = 0. \tag{6.6}$$

c) $\Delta\varphi = -2$ in F, (6.7)

$$\varphi = 0 \quad \text{auf } R_u, \tag{6.8}$$

$$\varphi = C_2 \text{ auf } R_i. \tag{6.9}$$

Wenn die Oberfläche des Loches A_i ist, kann die unbekannte Konstante C_2 bestimmt werden mittels der Bedingung:

$$\oint_{R_i} \frac{d\varphi}{dn} ds = -2A_i. \tag{6.10}$$

Die Arbeitsweise mit Hilfe der Elementenmethode ändert sich nicht für die Formulierung a.

Die Änderungen in der Arbeitsweise für die Formulierungen b und c werden wir noch näher betrachten.

b) Mit der Elementenmethode kann $\psi(x, y)$ bestimmt werden, wenn die Randbedingungen explizit gegeben sind. Es berechnet sich:

$$\psi_1(x,y) \text{ aus } \begin{cases} \Delta\psi_1 = 0 & \text{in } F, \\ \psi_1 = \frac{1}{2}(x^2+y^2) & \text{auf } R_u, \\ \psi_1 = \frac{1}{2}(x^2+y^2) & \text{auf } R_i, \end{cases}$$

$$\psi_2(x,y) \text{ aus } \begin{cases} \Delta\psi_2 = 0 & \text{in } F, \\ \psi_2 = \frac{1}{2}(x^2+y^2) & \text{auf } R_u, \\ \psi_2 = \frac{1}{2}(x^2+y^2)+A_i & \text{auf } R_i. \end{cases}$$

Die gewünschte Lösung ψ ist eine lineare Kombination von ψ_1 und ψ_2:

$$\psi = p\psi_1 + q\psi_2 \tag{6.11}$$

mit Unbekannten p und q, die bestimmt werden aus:

$$p+q = 1, \tag{6.12}$$

$$p\oint_{R_i} \frac{d\psi_1}{dn} ds + q\oint_{R_i} \frac{d\psi_2}{dn} ds = 0. \tag{6.13}$$

c) Die Arbeitsweise gestaltet sich analog zur Arbeitsweise für Formulierung b und beruht gleichfalls auf Superposition.

Nachdem die verlangten Funktionen ψ und φ berechnet worden sind, lassen sich die Schubspannungen und die Torsionssteifigkeit bestimmen. Die Torsionssteifigkeit für die Formulierung b bzw. c berechnet sich aus den Formeln:

$$M = G\beta\left[I_p - \iint_F \left(y\frac{\partial\psi}{\partial y} + x\frac{\partial\psi}{\partial x}\right) dx\,dy\right], \tag{6.14}$$

$$M = G\beta[2\iint_F \varphi\,dx\,dy + 2\varphi_{R_i}A_i], \tag{6.15}$$

wobei φ_{R_i} und die Konstante C_2 aus Gleichung (6.9) identisch sind.

Das grösste Bedenken gegen die vorgeschlagene Arbeitsweise besteht darin, dass die Berechnungsgenauigkeit der Kreisintegrale entlang R_i beschränkt ist. Die in dieser Weise für einen Querschnitt in der Form eines Kreisringes berechneten Resultate stimmen jedoch mit den exakten Werten sehr gut überein.

Eine völlig andere Möglichkeit zur Berechnung der Torsionsgrössen für mehrfach zusammenhängende Querschnitte ergibt sich, wenn in der Methode für einfach zusammenhängende Querschnitte mit einem variablen Schubmodul gerechnet wird. Ein Loch kann dann simuliert werden, wenn an der Stelle des Loches der Schubmodul viel kleiner gesetzt wird als im übrigen Querschnitt.

Mit den Buchstaben a, b und c werden wir die Änderungen in den Gleichungen für die Formulierung der Theorie mit bzw. φ_0, ψ und φ angeben. Dabei sind namentlich die Gleichungen für I_1, I_2 und I_3 von Bedeutung, weil die Arbeitsweise mittels der Methode der finiten Elemente sich darauf stützt.

a) Die Formeln für τ_{zx} und τ_{zy} wählen wir identisch mit (2.7) und (2.8), damit die Schubspannungen den Kompatibilitätsanforderungen genügen:

$$\tau_{zx} = G\beta\left(\frac{\partial \varphi_0}{\partial x} - y\right), \tag{6.16}$$

$$\tau_{zy} = G\beta\left(\frac{\partial \varphi_0}{\partial y} + x\right). \tag{6.17}$$

Aus der Gleichgewichtsbedingung folgen die Differentialgleichung und die Randbedingung, die das Torsionsproblem völlig beschreiben:

$$\frac{\partial}{\partial x}\left(G\frac{\partial \varphi_0}{\partial x}\right) + \frac{\partial}{\partial y}\left(G\frac{\partial \varphi_0}{\partial y}\right) + x\frac{\partial G}{\partial y} - y\frac{\partial G}{\partial x} = 0 \text{ in } F_t, \tag{6.18}$$

$$\frac{d\varphi_0}{dn} = (\text{grad}\,\varphi_0) = y\,n_x - x\,n_y \text{ auf } R_u, \tag{6.19}$$

wobei F_t die von R_u umschlossene Oberfläche ist.

Wir definieren $I_1(\varphi_0)$ mit:

$$I_1(\varphi_0) = \iint_{F_t} G\left\{\frac{1}{2}\left[\left(\frac{\partial \varphi_0}{\partial x}\right)^2 + \left(\frac{\partial \varphi_0}{\partial y}\right)^2\right] - x\frac{\partial \varphi_0}{\partial y} + y\frac{\partial \varphi_0}{\partial x}\right\} dx\,dy, \tag{6.20}$$

und man kann einfach beweisen, dass für *alle* Variationen $\delta\varphi_0$ gilt $\delta I_1 = 0$, wenn φ_0 die exakte Lösung ist, also den Gleichungen (6.18) und (6.19) genügt.

Die Torsionssteifigkeit kann bestimmt werden aus:

$$M = \beta \iint_{F_t} G\left[-y\frac{\partial \varphi_0}{\partial x} + x\frac{\partial \varphi_0}{\partial y} + x^2 + y^2\right] dx\,dy. \tag{6.21}$$

b) Man wählt derartige Formeln für die Schubspannungen, dass im Inneren der Randkurve R_u das Gleichgewicht garantiert ist:

$$\tau_{zx} = \beta\left(\frac{\partial G\psi}{\partial y} - G^* y\right), \tag{6.22}$$

$$\tau_{zy} = -\beta\left(\frac{\partial G\psi}{\partial x} - G^* x\right). \tag{6.23}$$

G^* ist eine beliebige Konstante von gleicher Dimension wie G.

Mit der Kompatibilitätsbedingung ergibt sich die beschreibende Differentialgleichung:

$$\frac{\partial}{\partial x}\left\{\frac{1}{G}\left(\frac{\partial G\psi}{\partial x}-G^*x\right)\right\}+\frac{\partial}{\partial y}\left\{\frac{1}{G}\left(\frac{\partial G\psi}{\partial y}-G^*y\right)\right\}+2=0 \text{ in } F_t, \tag{6.24}$$

während die Randbedingung in ψ durch das Gleichgewicht am Rande R_u bestimmt wird:

$$G\psi=\tfrac{1}{2}G^*(x^2+y^2) \text{ auf } R_u. \tag{6.25}$$

Wir definieren $I_2(\psi)$ mit:

$$I_2=\iint\limits_{F_t}\left\{\frac{1}{2G}\left[\left(\frac{\partial G\psi}{\partial x}\right)^2+\left(\frac{\partial G\psi}{\partial y}\right)^2\right]+G\psi\left[\frac{\partial}{\partial x}\left(\frac{G^*}{G}x\right)+\frac{\partial}{\partial y}\left(\frac{G^*}{G}y\right)-2\right]\right\}dx\,dy. \tag{6.26}$$

Wenn $\delta I_2=0$ für alle zulässigen Variationen $\delta\psi$ einer Funktion ψ mit $G\psi=\frac{1}{2}G^*(x^2+y^2)$ auf R_u – also differenzierbare Variationen sind und die Bedingung $\delta\psi=0$ auf R_u genügen –, so ist diese Funktion ψ die exakte Lösung des Problems. Für die Berechnung der Torsionssteifigkeit soll die nächste Formel benutzt werden:

$$M=2\beta\iint\limits_{F_t}G\psi\,dx\,dy-G^*\beta I_p. \tag{6.27}$$

Zwar ist hinzuzufügen, dass für diese Arbeitsweise Differenzierbarkeit von G erforderlich ist.

c) In Abweichung von (2.13) und (2.14) wird eine andere Spannungsfunktion φ definiert, woraus die Schubspannungen τ_{zx} und τ_{zy} folgendermassen abgeleitet werden können:

$$\tau_{zx}=\beta\frac{\partial\varphi}{\partial y}, \tag{6.28}$$

$$\tau_{zy}=-\beta\frac{\partial\varphi}{\partial x}. \tag{6.29}$$

Die weitere Berechnung vollzieht sich analog mit der unter b).

Differentialgleichung:

$$\frac{\partial}{\partial x}\left(\frac{1}{G}\frac{\partial\varphi}{\partial x}\right)+\frac{\partial}{\partial y}\left(\frac{1}{G}\frac{\partial\varphi}{\partial y}\right)+2\beta=0 \text{ in } F_t. \tag{6.30}$$

Randbedingung:

$$\varphi=0 \text{ auf } R_u. \tag{6.31}$$

Definiert man $I_3(\varphi)$ mit:

$$I_3=\iint\limits_{F_t}\left\{\frac{1}{2G}\left[\left(\frac{\partial\varphi}{\partial x}\right)^2+\left(\frac{\partial\varphi}{\partial y}\right)^2\right]-2\beta\varphi\right\}dx\,dy, \tag{6.32}$$

so gilt, dass $\delta I_3=0$ für alle zulässigen Variationen $\delta\varphi$ (mit $\delta\varphi=0$ auf R_u) der Funktion φ, die die exakte Lösung des Problems ist.

Die Torsionssteifigkeit kann bestimmt werden durch:

$$M = 2\beta \iint_{F_t} \varphi \, dx \, dy . \tag{6.33}$$

Sowohl die Formulierung a wie c ist für mehrfach zusammenhängende Querschnitte sehr anwendungsfähig, da eine Diskontinuität in G keine besondern Probleme mit sich bringt.

Schliesslich geben wir einige Resultate für einen Kastenträger mit Querschnitt nach Fig. 6.2.

Auf Grund der Symmetrie des Querschnitts braucht man nur den in Fig. 6.2 schraffierten Teil zu betrachten. Das gewählte Elementenmuster ist in Fig. 6.3 gezeichnet; die Anzahl der Elemente war insgesamt 700.

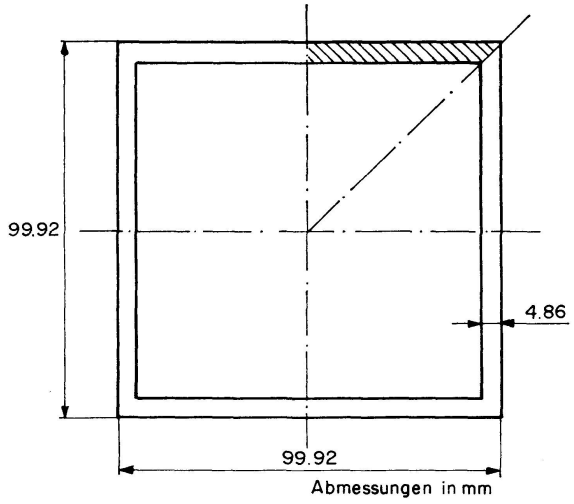

Fig. 6.2. Beispiel eines Querschnitts.

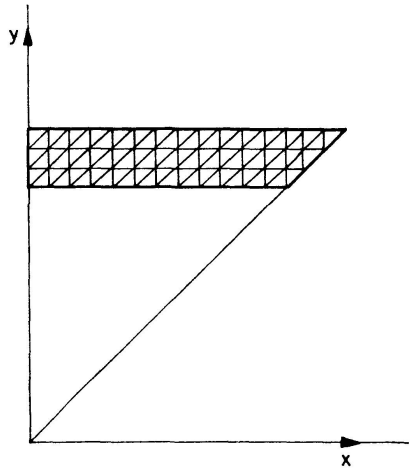

Fig. 6.3. Muster der Einteilung in Elemente.

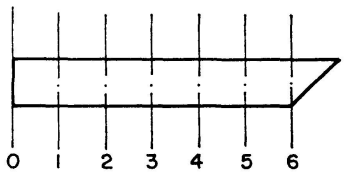

Fig. 6.4. Geraden durch die Wand.

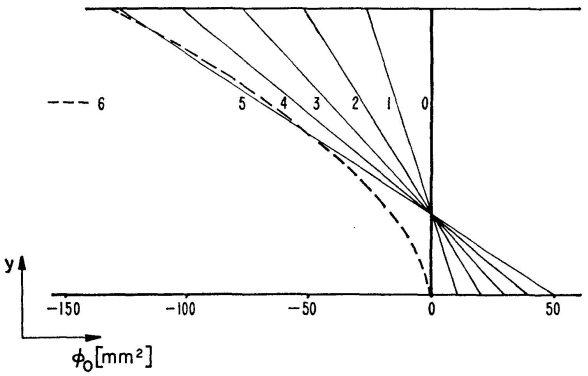

Graphik 6.1. Verwölbung des Querschnitts.

Für dieses Problem wurde zunächst die Arbeitsweise zur Berechnung von φ_0 gewählt. In einem physischen Modell charakterisiert φ_0 die Verwölbung des Querschnitts. In der Graphik 6.1 ist die Verwölbung für die in Fig. 6.4 gezeichneten Geraden durch die Wand des Trägers entlang dieser Geraden angegeben. Der Verlauf der Schubspannung τ_{zx} über der Wand, ein wenig von der Ecke entfernt, ist linear, wie deutlich aus der Darstellung 6.2 hervorgeht.

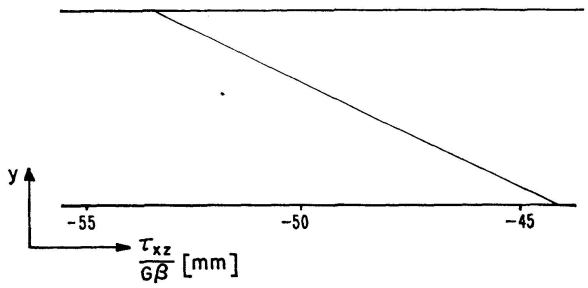

Graphik 6.2. Verlauf der Schubspannungen.

Mit der Torsionstheorie nach Bredt, die sich auf die Hypothese stützt, wonach die Schubspannung über die Wandstärke hinweg konstant ist, findet man für die Torsionssteifigkeit:

$$\frac{M}{G\beta} = 4{,}175 \cdot 10^6 \text{ [mm}^4\text{]},$$

während mit der Methode der finiten Elemente (Formulierung mit φ_0)

$$\frac{M}{G\beta} = 4{,}284 \cdot 10^6 \text{ [mm}^4\text{]}$$

berechnet wird.

Eine weitere Berechnung der Torsionssteifigkeit mittels der Elementenmethode mit bestimmender Grösse φ ermöglicht eine Einschränkung von $\frac{M}{G\beta}$:

$$4{,}268 \cdot 10^6 \text{ [mm}^4\text{]} \leqq \frac{M}{G\beta} \leqq 4{,}284 \cdot 10^6 \text{ [mm}^4\text{]}.$$

Für den Querschnitt nach Fig. 6.2 ist die Torsionssteifigkeit nach Bredt also um etwa 2,5% zu niedrig.

7. Schlussbemerkungen

In dieser Arbeit wurde versucht zu zeigen, dass die Methode der finiten Elemente für eine bestimmte Art von Problemen, nämlich Potentialprobleme, bestens geeignet ist. Als Beispiel wurde die Torsionstheorie nach de St.-Venant gewählt, doch eignet sich die Methode auch z. B. zur Berechnung von Temperaturverteilungen oder zur Bestimmung des Geschwindigkeitsprofils in Strömungsproblemen.

Es sei darauf hingewiesen, dass nicht alle Aspekte der Methode untersucht wurden. Die Genauigkeit der Resultate in Abhängigkeit vom Elementenmuster und von der Anzahl ist kaum erwähnt. Es wäre interessant, noch zu prüfen, ob über die Genauigkeit qualitative Entscheidungen gefällt werden können.

Das Vorhergehende behandelt nur ein dreieckiges Element mit linearer Verteilung der interessanten Funktion (φ_0, ψ oder φ) im Inneren des Elementes. Bemerkt sei auch, dass es ohne Schwierigkeiten möglich ist, statt des linearen

Verlaufes für φ_0, ψ oder φ einen quadratischen Verlauf anzunehmen. Mit dem gleichen Elementenmuster und der gleichen Anzahl von Elementen sind beim Element mit quadratischem Verlauf viel bessere Resultate zu erwarten als mit dem verwendeten Element.

Bezeichnungen

β	Verdrehung des Querschnitts pro Längeneinheit.
φ_0	Verwölbungsfunktion.
φ	Spannungsfunktion.
ψ	nach den Cauchy-Riemannschen Differentialgleichungen an φ_0 hinzugefügte Funktion.
τ_{zx}, τ_{zy}	Schubspannungen.
r, ϑ	Polarkoordinaten.
x, y, z	Kartesische Koordinaten.
F	Querschnittsfläche.
G	Schubmodul.
I_1, I_2, I_3	Integralformel in bzw. φ_0, ψ und φ.
I_p	polares Flächenträgheitsmoment.
M	Torsionsmoment.
R	Rand des Gebietes F.
V	potentielle Energie.
V^*	komplementäre Energie.

Literaturverzeichnis

1. Zienkiewics, O. C. and Cheung, Y. K.: Finite elements in the solution of field problems. The Engineer 220 (1965) September, p. 507–510.
2. Visser, W.: The finite element method in deformation and heat conduction problems. Proefschrift Technische Hogeschool Delft (1968).
3. Krahula, J. L. and Lauterbach, G. F.: A finite element solution for Saint-Venant torsion. AAIA Journal 7 (1969) December, p. 2200–2203.
4. Timoshenko, S. and Goodier, J. N.: Theory of elasticity. McGraw-Hill Book Company Inc., New York, Toronto, London (1951).
5. Brekelmans, W. A. M.: Torsie van een cilindrische balk met een dwarsdoorsnede, begrensd door een regelmatige veelhoek. Intern rapport groep "Technische Mechanica" van de Technische Hogeschool Eindhoven (1967).
6. Huette, des Ingenieurs Taschenbuch. I. Theoretische Grundlagen. Verlag von Wilhelm Ernst & Sohn, Berlin (1955).
7. Weber, C. und Günther, W.: Torsionstheorie. Friedrich Vieweg & Sohn, Braunschweig (1958).

Zusammenfassung

Die Methode der finiten Elemente ist für die numerische Lösung von Potentialgleichungen vorzüglich geeignet. Das Verfahren wird anhand verschiedener Formulierungen der St.-Venantschen Torsionstheorie für prismatische Stäbe mit einfach und mehrfach zusammenhängenden Querschnitten erläutert. Die Methode bietet die Möglichkeit, die Torsionssteifigkeit zwischen zwei Grenzwerten einzuschliessen. Für einige klassische Beispiele werden die Resultate mit den bei anderen Methoden berechneten Ergebnissen verglichen.

Summary

The finite element method is very suitable for the analytical solution of potential equations. It is explained by several different formulations of the St-Venant torsion theory of prismatic bars with simple or multiple connected sections. The method offers the possibility to find two treshold values for the torsional stiffness. For some classical examples the results are compared with the solutions of other methods.

Résumé

La méthode des éléments finis convient très bien à la solution numérique des équations potentielles. Elle est illustrée au moyen de différentes formulations de la théorie de torsion de St-Venant pour des barres prismatiques à sections tubulaires simples ou multiples. La méthode offre la possibilité de trouver deux valeurs limites pour la rigidité torsionnelle. Les résultats sont comparés pour quelques exemples classiques avec ceux trouvés par d'autres méthodes.

Inelastic Analysis of Reinforced Concrete Panels: Experimental Verification and Application[1])

Analyse non-élastique de plaques acier-béton: Vérification expérimentale et application

Unelastische Analyse von Stahlbetonscheiben: Experimentelle Nachprüfung und Anwendung

VLADIMIR CERVENKA
Structural Engineer, Building Research Institute, T. U. Prague, formerly, Research Assistant, University of Colorado, Boulder

KURT H. GERSTLE
Professor of Civil Engineering, University of Colorado, Boulder

Introduction

The analysis described in a previous paper [1] provides an approximate solution for the inelastic response of reinforced concrete panels. This analysis is based on the incremental finite element method and includes two types of material nonlinearities, namely, crack propagation and plasticity.

Two kinds of unavoidable approximations were introduced in this analysis, namely, material behavior idealization and discrete numerical solution. The effect of these approximations is studied here by means of analytical and experimental results.

Two test series were used for this purpose in this investigation. The first test series, intended to simulate the action of shear walls, was conducted by the authors, the second test series was performed by T. PAULAY [2] in connection with an investigation of the coupling of shear walls. The full description of the comparative study is given in Ref. [3]. Here, only representative results are shown to illustrate the conclusions.

---

[1]) This material is presented in two parts. The first paper published in Vol. 31-II describes the theoretical aspects. This is the second paper which presents experimental verification and application to shear walls.

The specimens used in both studies were deep beams subjected to the maximum moment M and shear force V. Such a loading can be characterized by the shear span ratio r defined by $r = \frac{M}{Vd}$, where d is the depth of the beam. The shear span ratio in the first test series was approximately $r = 1$, and the shear span ratio in Paulay's coupling beams was $r = 0.5$. Both of these ratios indicate relatively large shear loading.

In practical structural design, wall elements such as shear walls or deep beams are often treated by methods developed for ordinary beams. Results of these beam solutions will be compared with the finite element analysis and experiments, in order to judge their validity.

Authors' Tests

The purpose of the experimental program was to provide data on the real behavior of reinforced concrete panels under in-plane loads which could be compared with the analytical results. The following aspects were mainly investigated:

1. The load-displacement response of panels.
2. The crack patterns and crack propagation.
3. Failure mechanisms.

The test panels were orthogonally reinforced square plates 30×30 in., 2 or 3 inches in thickness, reinforced as indicated in Fig. 1. Two panels were combined to form one beam-like specimen as shown in Fig. 1; this arrangement enabled testing of the beam specimen as a simply supported beam with midpoint load. Thus, two square panels were always tested simultaneously, though each panel acted independently of the other because of the statically determinate supports. The concentrated forces at the supports and at the load point were transmitted to the panels by three vertical ribs as shown in Fig. 1. These ribs also helped to maintain the lateral stability of the specimens during the testing.

The testing arrangement allowed application of monotonic as well as cyclic load histories.

Horizontal and vertical displacements were measured at the bottom point of the outside ribs. Direct relative displacements of the panel corners with respect to the top of the center rib were obtained.

The cracks were continuously observed, and new cracks were marked. Pictures of the entire crack propagation were taken by two cameras, one for each panel. For easier identification of the crack location from the pictures, a mesh coinciding with the finite element mesh considered in the analysis was drawn on the surface of the panel.

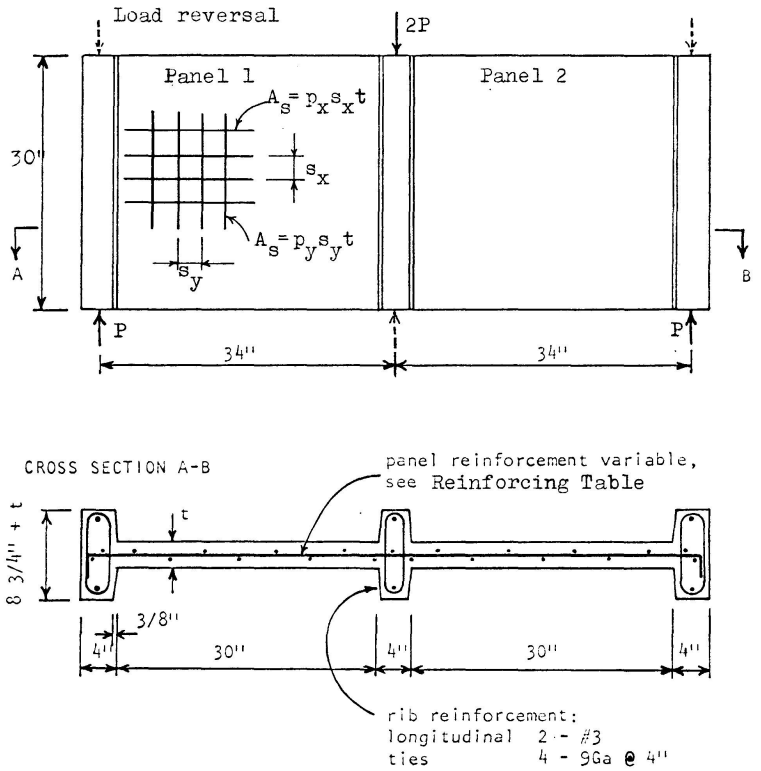

Panel	Thick-ness t, in.	Reinforcing					
		Type	s_x, in.	p_x	s_y, in.	p_y	
W 2	3	#3	4 2	0.00916 0.01832	4	0.00916	Top. 24″ Bot. 6″
W 3–2	2	¼″ Rod	2	0.00785	–	–	
W 4	3	#3	3	0.0122	3	0.0122	

Fig. 1. Test Specimen.

Analytical Models

The test specimens were analyzed by the finite element method described in a previous paper [1]. The idealization of the panel shown in Fig. 1, for the finite element analysis is shown in Fig. 2. Three types of finite element meshes, Mn, with $n=5$, 8, and 10 were used. All supports are located along the right vertical boundary line where all but the topmost nodal point are constrained horizontally and free vertically; the topmost nodal point is constrained in both directions. The actual single load P, acting on each panel, is substituted by two equivalent loads $P/2$.

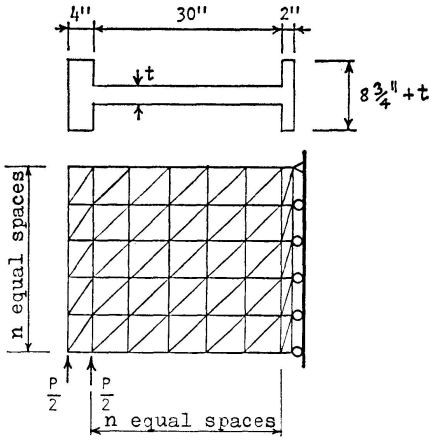

n	Designation	Number of Elements
5	M 5	70
8	M 8	160
10	M 10	240

Fig. 2. Finite Element Model.

Analytical and Experimental Results

Specimen W 2

Experimental load-displacement diagrams for both panels of specimen $W\,2$ are shown in Fig. 3. The load P on the panel is plotted versus the vertical displacement of the outside rib at the point of load P.

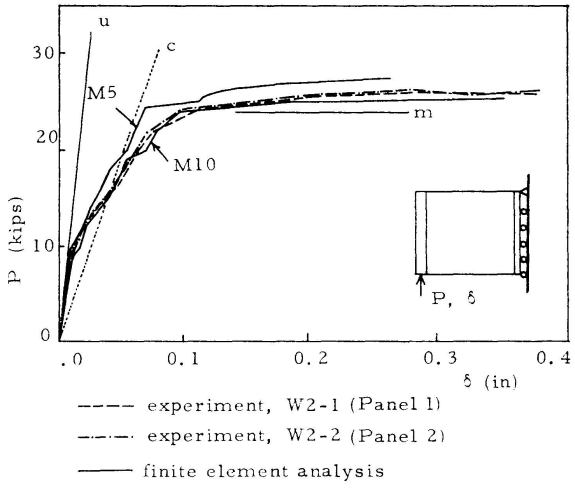

Fig. 3. Comparison of Analytical and Experimental Load-Displacement Diagrams for Specimen W 2.

The finite element analysis of this specimen was performed for two kinds of meshes, $M\,5$ and $M\,10$, to show the effect of the size of finite element. The load-displacement diagrams for both meshes are also shown in Fig. 3. As expected from the bound principles of the displacement method, the finer grid results in increased deformations. Both analyses were terminated by specifying limit displacements. At these points the load-displacement diagrams were almost horizontal and no further increase of load was expected.

Fig. 3 also shows lines representing predictions based on beam theory.

Experiment Analysis

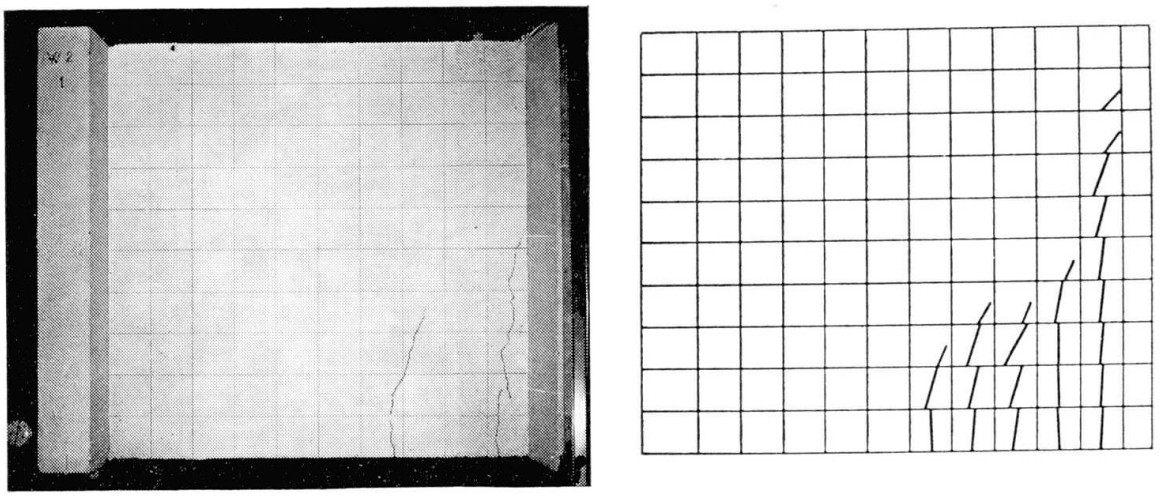

a) $P = 14.0$ Kips

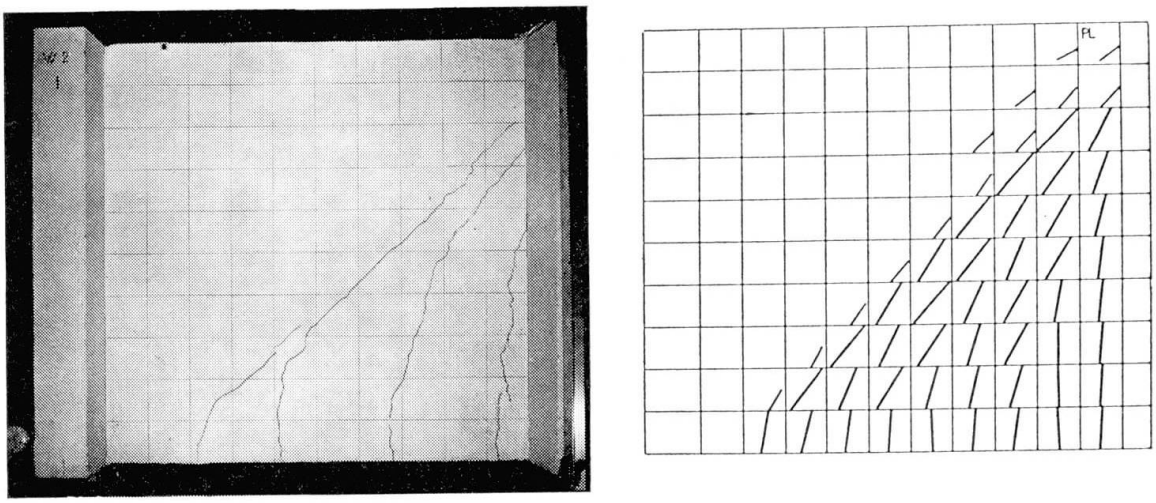

b) $P = 24.0$ Kips

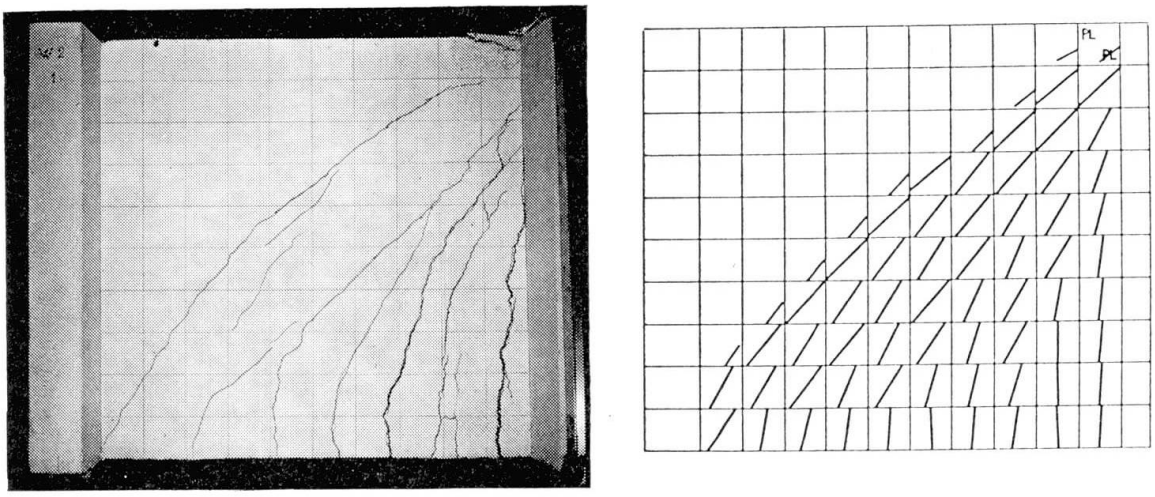

c) $P = 25.5$ Kips

Fig. 4. Comparison of Analytical and Experimental Crack Patterns for Panel W 2.

Lines u and c represent elastic beam behavior based, respectively, on uncracked and cracked section properties. Line m represents ultimate load due to attainment of the ultimate bending moment at the critical section. It can be observed here that beam theory yields reasonably good results.

Analytical and experimental crack patterns for three load levels are shown in Figs. 4a to c. The agreement between analytical M 10 and experimental results is excellent for load-displacement relationship as well as for crack locations and crack directions.

From the test it was observed that the flattening of the load-displacement diagram was initiated by yielding of the reinforcement which was indirectly evident from the wide opening of the cracks at $P = 24\,K$ and $\delta = 0.1$ inch. The failure of the test specimen was caused by crushing of the concrete at $P = 27\,K$ and $\delta = 0.45$ inch. This type of failure was very well predicted by the analysis. The maximum concrete compression strain in the plastic zone (designated by PL in Fig. 4c) at the last calculated load stage $P = 25.5\,K$ and $\delta = 0.35$ in. was $\epsilon^c = 0.0087$. If the limit concrete strain is assumed $\epsilon_u \leqq 0.008$ the analysis would predict crushing of the concrete and consequent failure of the panel at that stage. The failure of the test panel was observed under slightly higher load and greater displacement at $P = 26.5\,K$ and $\delta = 0.45$, which is considered to be in a good agreement with analytical values.

Specimen W 3

This specimen contained panels with different reinforcement. Panel W 3–1 was reinforced orthogonally and panel W 3–2 had only horizontal reinforcement. Failure of the specimen was caused by the weaker panel W 3–2. Only results for this panel will be presented here.

Three different analyses were performed and compared with the experimental behavior.

In the first analysis the force increments were specified. The load-displacement diagrams of this analysis and experiment are compared in Fig. 5 and the final crack patterns are compared in Fig. 6. Good agreement between analytical and experimental behavior is found over the entire load range except in the limit stage.

The failure mechanism observed from the experiment was of a typical shear type, characterized by opening of one diagonal crack, as shown in Fig. 6. It can be seen from the relative displacements of the mesh lines crossing the cracks that the diagonal crack opened in the vertical direction. This phenomenon can be also observed from the analysis as shown in Fig. 7. In this figure the analytical distribution of the strains ϵ_y along the vertical lines of the panel is shown; the points of maximum ϵ_y are connected to show the course of the predicted major diagonal crack, whose location agrees well with the observed crack. However, there is considerable difference between the mechanisms of

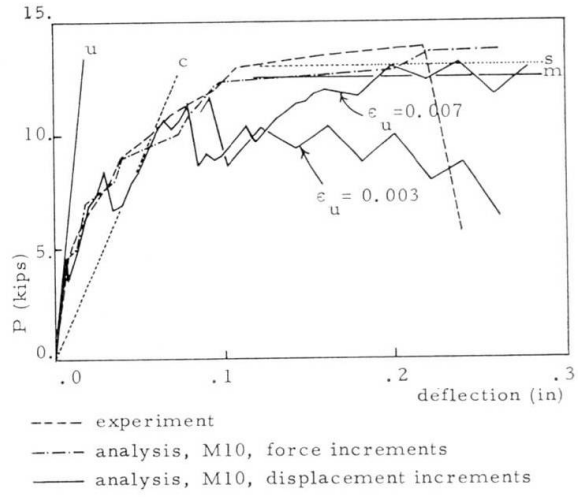

Fig. 5. Comparison of Analysis with Experiment for Panel W 3–2.

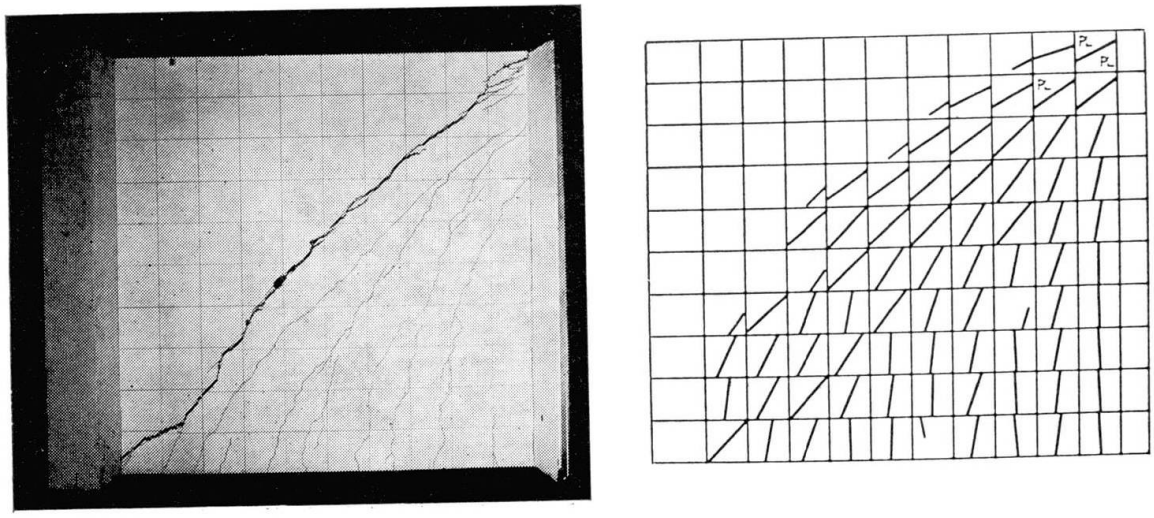

Experiment Analysis

Fig. 6. Comparison of Final Analytical and Experimental Crack Patterns for Panel W 3–2.

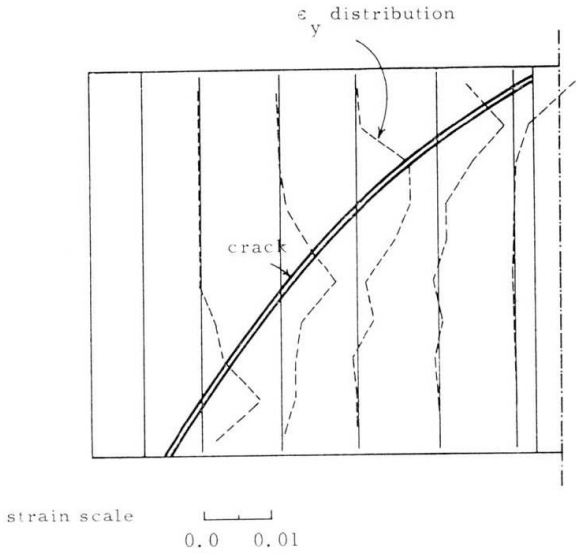

Fig. 7. Panel W 3–2. Diagonal Crack Location from the Distribution of Anlytical Strains ϵ_y.

failure. While in the experiment the opening of the diagonal crack leads to an abrupt instability failure, the analysis shows plasticity of the cracked concrete in the vicinity of the diagonal crack which gives some additional displacement capacity to the panel.

The difference between the experimental and analytical failure mechanisms is caused mainly by the deficiency of the finite element representation of the cracked concrete. The analytical mechanism naturally results from the fact that the cracks are not smoothly continuous from one element to another, but form a sawtooth pattern; thus a continuous diagonal crack can form only if the concrete adjacent and parallel to the crack discontinuity is crushed.

Further analyses of the panel were performed for specified displacement increments. This type of analysis permits all instability regions characterized by drops of the load to be obtained. The resulting load-displacement diagrams for two values of compressive limit strain, $\epsilon_u = 0.003$ in/in and $\epsilon_u = 0.007$ in/in, are also shown in Fig. 5.

In these analyses the formation of diagonal cracks is accompanied by a big drop at $\delta = 0.08$ and 0.10 inches, respectively. A similar load drop due to diagonal crack opening in the experiment caused the failure at $\delta = 0.22$. It is seen that the analysis is indeed able to represent the loss of strength of the elements adjacent to the diagonal crack, if a sufficiently low ultimate concrete strain is assumed.

Fig. 5 also shows the lines u and c corresponding to the stiffnesses according to elastic, uncracked and cracked, beam theory with shear distortions included. The horizontal lines m and s indicate the ultimate beam strength in moment and shear, respectively. In this case also, beam theory can give reasonable results.

Specimen W 4

This specimen was subjected to cyclic loading. The comparison of analytical and experimental results is presented for the first four load cycles. One cycle includes loading and unloading in one direction. The load cycle in the positive direction was always followed by a load cycle in the reversed direction.

The magnitude of the cyclic load was $P = 12.0\,K$ which is 0.46 of the monotonic limit load. The analysis of this cyclic loading is based on Mesch M 8. The comparison of analytical and experimental load-displacement diagrams for elastic cycling is shown in Fig. 8.

The analytical diagram indicates changes due to crack formation only in the first two cycles. In all following cycles with the same magnitude of load no other changes take place and the diagram is formed by the line connecting the origin and maximum load points. Hence, the analysis indicates elastic behavior of the cracked panel in the cycles following the first and second cycles. The experimental diagram shows some residual displacements even

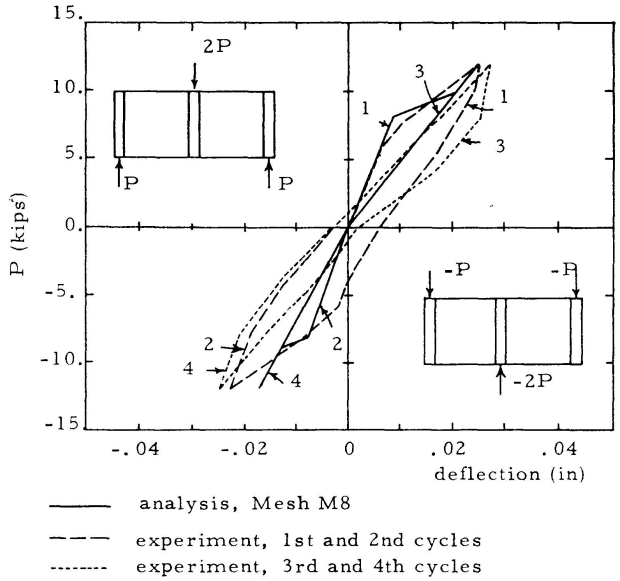

Fig. 8. Comparison of Analysis with Experiment for Specimen W 4 under Elastic Cycling. Numbers Indicate Cycles.

under this low load. These residual displacements are probably caused by bond slip and by imperfect crack closing caused by crack surface damage. All these effects are neglected in the analysis.

After completion of these four cycles the magnitude of load was increased and the specimen was subjected to cyclic loading of magnitude close to the limit monotonic load. Very large plastic deformations occurred during this loading and failure occurred in the sixth cycle. Clearly, a realistic analysis for cyclic loads in plastic range must include representation of bond slip and the crack mode with two sets of cracks opened simultaneously.

The crack patterns in both ranges of cyclic loading, which are not presented here, showed very good comparison between analysis and experiment.

Paulay's Tests

Two coupling beams were selected from (2) and used in the investigation. Here only one of them, Beam 391, is presented.

Test specimens were of the form shown in Fig. 9. The tested beam was connected with end blocks which simulated the real boundary conditions likely to occur in shear wall structures.

For purpose of the analysis the shape of the specimen was idealized as shown in Fig. 10. The stiffness of the end blocks was chosen such as to match the experimental stiffness in the elastic *uncracked* state. The analytical end rotations of beams are considered as rotations of the vertical line connecting the points 1 and 2 of Fig. 10. The experimental rotations were measured in the middle of the end blocks of the specimen shown in Fig. 9.

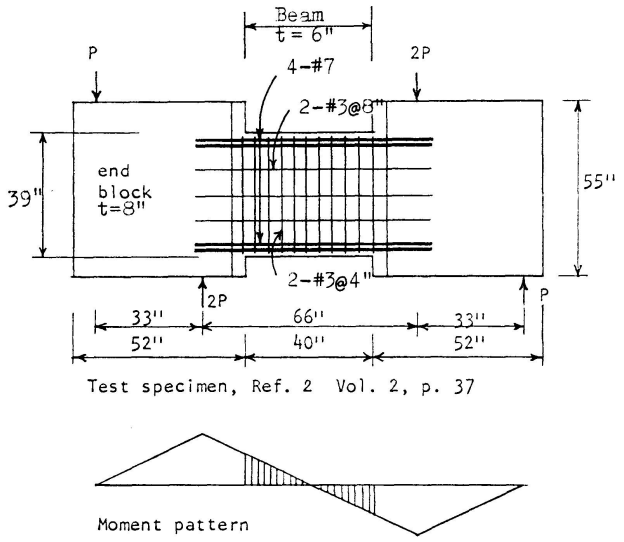

Fig. 9.

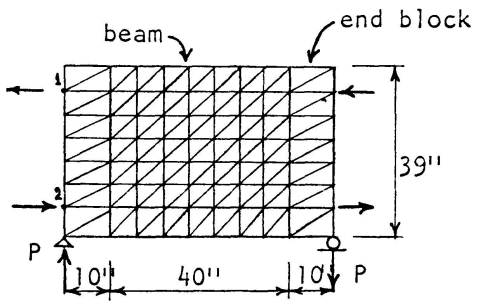

Fig. 10. Analytical Beam and Mesh Layout.

Beam 391

This beam was subjected to monotonically increasing load leading to failure. Two analytical solutions were performed, differing only in the tensile strength of concrete. The load-rotation diagrams of both solutions are compared with experimental results in order to show the effect of tensile strength on the solution. Two analytical curves, one using the modulus of rupture as a measure of the tensile strength, and the other using the splitting strength, are compared with experiment in Fig. 11. The analytical solutions differ only under low load when crack propagation takes place.

The analytical and experimental load-rotation diagrams indicate the overestimation of the real stiffness and of the real limit load by the analysis. This is partly caused by the coarseness of the finite element mesh. However, the main cause is probably the large bond slip of the main bending reinforcement

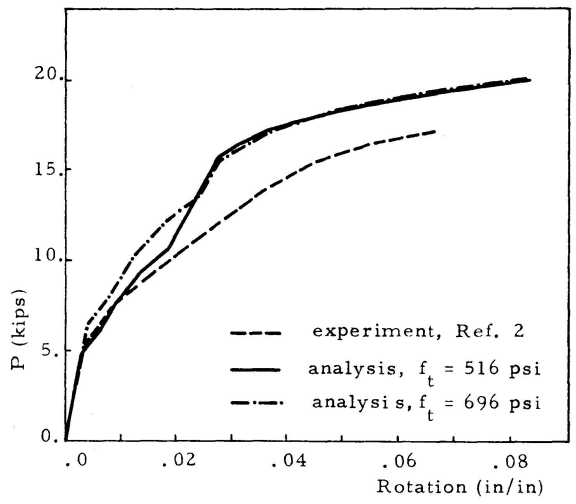

Fig. 11. Comparison of Analysis with Experiment for Beam 391.

(# 7 bars), particularly in the anchorage regions, which is not included in the analysis. Again it appears that inclusion of this effect in the analysis is necessary.

The comparison of the final analytical and experimental crack patterns is shown in Fig. 12.

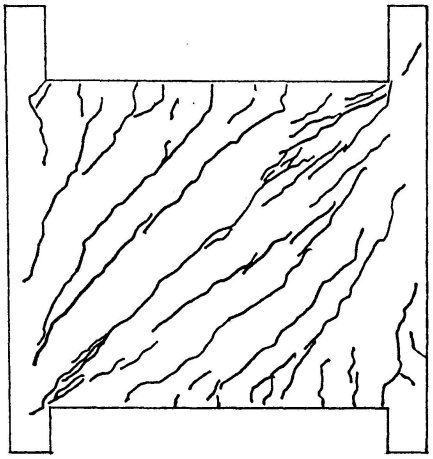

Experimental Crack Pattern from Ref. 2, Vol. 2, p. 128.

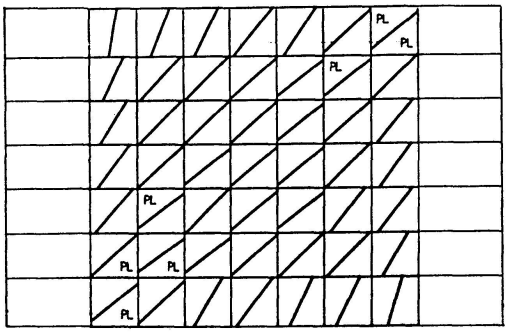

Analysis

Fig. 12. Comparison of Analytical and Experimental Crack Patterns at Failure for Beam 391.

The experimental beam failed in shear when a major crack formed along the diagonal of the beam. Similarly to the case of Panel *W* 3–2, a discrepancy was found between analytical and experimental failure mechanisms. The continuous diagonal crack cannot form in the analytical solution due to the basic assumption of the method which considers every element separately. Instead, the analysis shows concrete plasticity in the vicinity of the beam diagonal, as indicated in Fig. 12.

The analytical and experimental strains in the top longitudinal steel are compared in Fig. 13 at two load stages, showing good agreement between analysis and experiment. The analysis verified the experimentally observed fact that the longitudinal reinforcement is in tension throughout the whole length of the beam (even in the so-called compression zones) as soon as the beam is cracked.

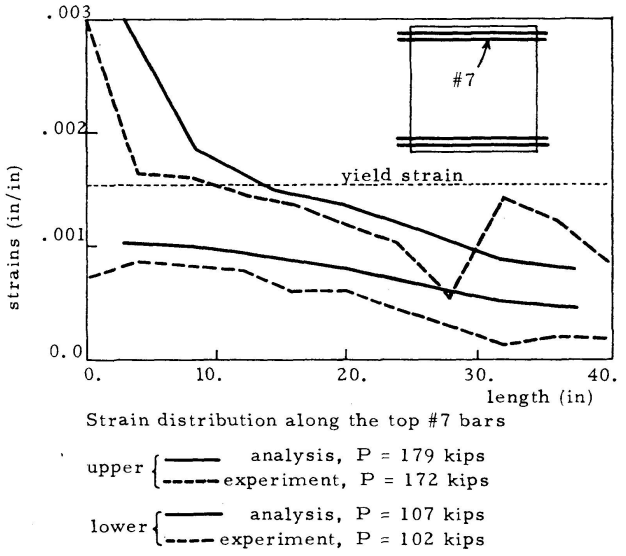

Fig. 13. Comparison of Analytical and Experimental Strains in Main Reinforcement.

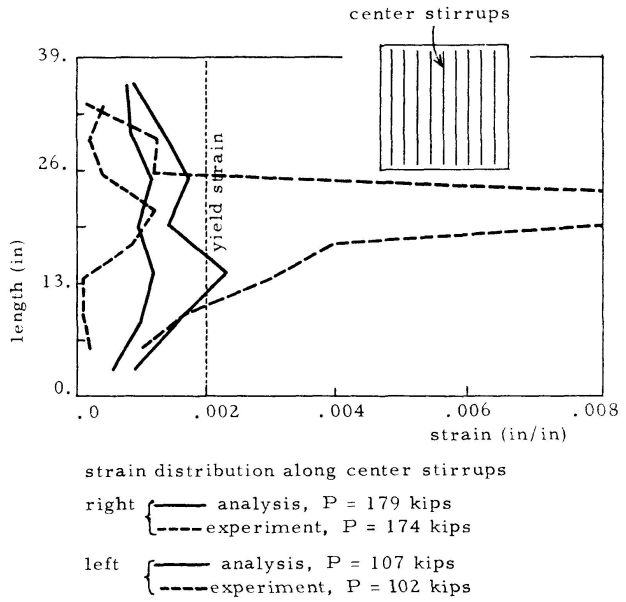

Fig. 14. Comparison of Analytical and Experimental Strains in Vertical Reinforcement.

The analytical and experimental strain distributions in the center stirrup are compared in Fig. 14 in two load stages. Here again, the discrepancy caused by different failure mechanisms is observed. The strain distribution in the analysis is much more uniform. The large strains which occur in the experimental beam at the point where the stirrup crosses the main diagonal crack do not occur in the analysis; nevertheless, the analysis indicates strains above the yield level of 0.002 in the vicinity of the diagonal crack

Conclusions

Applicability of the Finite Element Analysis

On the basis of the results presented, the following conclusions can be drawn:

1. The material stiffnesses given in an earlier paper [1] correctly represented the behavior of the reinforced concrete in a class of cases characterized by large crack regions. A comparative study confirmed that crack propagation and plasticity of materials are the most important non-linear effects in the problems with monotonically increasing load. Load-displacement relations can be accurately predicted in such cases.
2. The analysis can well predict crack locations and crack directions either by fine or by coarse mesh analyses. The crack modes used in the analysis [1] are sufficient for the monotonic loading cases and for cyclic loading cases without occurrence of plastic deformations.
3. Bending type of failure mechanism characterized by formation of plastic regions in the reinforcement and the compression concrete is well predicted by the analysis. The shear type failure mechanism characterized by opening of a large diagonal crack is not properly reproduced by the analysis.
4. For the prediction of the response to cyclic load histories, bond slip and crack surface deterioration should be included in the analysis. For cyclic loading involving yielding of the steel, an additional crack mode representing simultaneous occurrence of two cracks in different directions is necessary.

Simplification of Analysis of Planar Elements

On the basis of the limited amount of comparisons of the simplified beam analysis with the experimental and analytical results, the following conclusions can be drawn:

1. Beam analysis overestimates the stiffness of the uncracked panel. This only confirms the already well-known fact that the linear strain distribution is not applicable to deep beams.
2. Beam analysis of the cracked panel based on elastic transformed cross section excluding tension concrete well represents the average stiffness of a cracked panel.
3. Beam analysis only slightly underestimates the ultimate load of panels and can serve as a conservative estimate of panel strength for both bending and shear failures.

The conclusions imply some practical suggestions for the analysis of structures containing walls or panels. First, an elastic analysis including the cracked concrete by means of the transformed cracked section would apparently give a good estimate of the real stiffness of the cracked structure. Secondly, the

plastic hinge theory appears to be applicable to the limit analysis of wall structures (frame-shear wall systems) subject to the same limitations used in frames (shear failure must be avoided by sufficient transverse reinforcement and rotational capacity must not be exceeded).

These conclusions are made only on the basis of three panels and thus do not cover a wide range of other practical cases with various shear spans and reinforcing. Therefore, they must be considered as tentative.

The finite element analysis used in this investigation can be eventually used for a more detailed study of this problem which would lead to more conclusive suggestions for design of reinforced concrete walls.

Acknowledgement

This paper is based on part of a Ph. D. thesis by the senior author submitted to the Department of Civil Engineering, University of Colorado. Thanks are expressed to the University's Council on Research and Creative Work for financial support, to the Computing Center for computation time, and to the Department for use of the laboratory facilities. The authors also appreciate the help of Professors Paul P. Lynn and Leonard G. Tulin, University of Colorado, and of Professor Thomas Paulay, University of Canterbury.

Keywords

Cyclic load; experiment; finite element method; limit analysis; reinforced concrete; shear wall; stress analysis; structural analysis; panels; plasticity; cracking.

References

1. CERVENKA, V., and K. H. GERSTLE: Inelastic Analysis of Reinforced Concrete Panels, Part I: Theory. IABSE Publications Vol. 31-II, 1971.
2. PAULAY, T.: The Coupling of Shear Walls. Ph. D. Thesis, Department of Civil Engineering, University of Canterbury, Christchurch, New Zealand, 1969.
3. CERVENKA, V.: Inelastic Finite Element Analysis of Reinforced Concrete Panels Under In-Plane Loads. Ph. D. Thesis, Department of Civil Engineering, University of Colorado, 1970.

Summary

Inelastic finite element analysis of reinforced concrete panels is compared with experimental results. Load-displacement diagrams, crack patterns and failure mechanisms of shear wall specimens are examined under monotonic

as well as cyclic load histories. Load-displacement relations and crack patterns can be accurately predicted by the analysis for the case with monotonically increased load.

Résumé

L'analyse inélastique d'éléments finis de plaques en acier-béton est comparée aux résultats expérimentaux. Des diagrammes de déplacement de la charge, des épreuves de rupture et influences de défauts aux épreuves de cisaillement sont examinées sous charge monotonique et sous les conformités de charges cycliques. Des relations de déplacement de la charge et des épreuves de rupture se laissent prédire exactement par l'analyse pour le cas de charges uniformément élevées.

Zusammenfassung

Die unelastische Analyse endlicher Elemente von Stahlbetonscheiben wird mit den experimentellen Ergebnissen verglichen. Lastverschiebungsdiagramme, Bruchproben und Brucheinflüsse von Schubwandproben werden sowohl unter gleichförmiger wie unter den Gesetzmässigkeiten zyklischer Belastungen untersucht. Lastverschiebungs-Beziehungen und Bruchproben lassen sich durch die Analyse für den Fall einer gleichförmig zunehmenden Belastung genau vorhersagen.

Leere Seite
Blank page
Page vide

Free Vibration of Curved and Straight Beam-Slab or Box-Girder Bridges

Vibrations de ponts à section en T ou en caisson, courbes ou droits

Schwingungen gekrümmter oder gerader Plattenbalken- oder Kastenträgerbrücken

Y. K. CHEUNG
Professor, Department of Civil Engineering, The University of Calgary, Calgary, Alberta, Canada

M. S. CHEUNG
Post Doctoral Fellow, Department of Civil Engineering, The University of Calgary, Calgary, Alberta, Canada

Introduction

This paper describes the application of a finite strip method to the determination of the natural frequencies and modal shapes of undamped vibration of curved or straight singel-spanned bridges (Fig. 1a) made up of thin plates connected together along circumferential (longitudinal) edges.

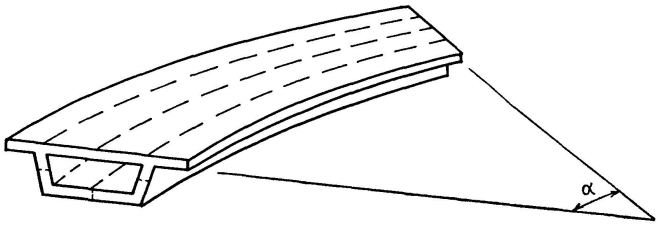

Fig. 1a. A Curved Box Bridge and It's Idealization into Strips.

The static analysis of such right bridges has been presented by CHU and DUDNIK [6], using the elasticity theory developed by GOLDBERG and LEVE [7], and by CHEUNG [3], using the finite strip approach, and very good accuracy has been demonstrated in all the numerical examples.

The static analyses of curved girder bridges have been presented by BELL and HEINZ [1], using a slope-deflection Fourier series method. However, an approximation has been introduced since the torsional and bending rigidities of each girder must be assigned somehow to account for the composite action of the plate and girder. Furthermore, the method presented is unsuitable for the analysis of box girders. Recently, the writers [2] have successfully applied

the finite strip method to the static analysis of curved box girder bridges. In the present paper, the dynamic analysis of such bridges will be dealt with.

In this method, the plates are divided into strips extending from one support to the other. Displacement functions given in the form of the product of a Fourier series in the circumferential (longitudinal) direction and a simple polynomial in the transverse direction can be chosen for the displacements u, v and w and the stiffness and mass matrices of a strip can be formulated according to the usual finite element procedure. By virtue of the orthogonality of the Fourier series, all the terms of the series uncouple and only small matrices are needed for the eigenvalue solutions of each term.

The general formulation of stiffness and mass matrices has been presented in detail elsewhere [4], [5], and shall not be repeated here. Also the straight strip will simply be interpreted as a special case of the curved strip, in which the radius of curvature r is infinitely large, the subtended angle α infinitely small, and the product $r\alpha$ is equal to the span of a straight strip.

In a paper by WITTRICK and WILLIAMS [8], a similar approach is used to obtain the natural frequencies of *rectangular* stiffened plates. However, since the governing differential equations (for simply-supported case only) were solved exactly, the resulting stiffness matrix contains transcendental terms and therefore, a complicated eigenvalue solution had to be used.

Stiffness and Mass Matrices

A. Curved Interior and Exterior Webs of Box Girder

Each web is in general a part of a conical frustum (Fig. 1b), but becomes a cylindrical panel when it is in a vertical position. For such a curved surface the membrane and bending actions are coupled, and the stiffness matrix is of the sixe 8×8.

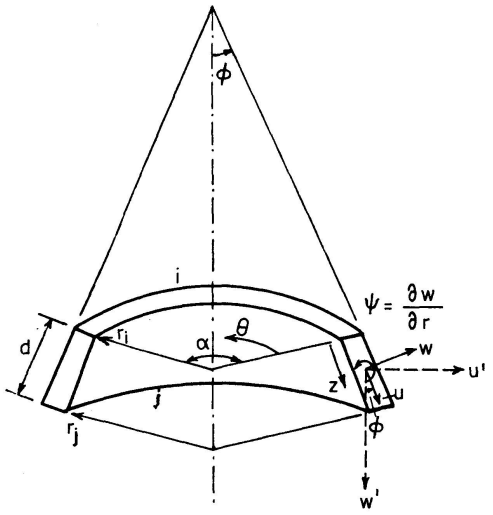

Fig. 1b. A Conical Web Strip.

Displacement functions:

$$
\begin{aligned}
u_m &= \left[\left(1-\frac{z}{d}\right)u_{im}+\left(\frac{z}{d}\right)u_{jm}\right]\sin\frac{m\pi\theta}{\alpha},\\
v_m &= \left[\left(1-\frac{z}{d}\right)v_{im}+\left(\frac{z}{d}\right)v_{jm}\right]\cos\frac{m\pi\theta}{\alpha},\\
w_m &= \left[\left(1-\frac{3z^2}{d^2}+\frac{2z^3}{d^3}\right)w_{im}+\left(z-\frac{2z^2}{d}+\frac{z^3}{d^2}\right)\psi_{im}\right.\\
&\quad\left.+\left(\frac{3z^2}{d^2}-\frac{2z^3}{d^3}\right)w_{jm}+\left(\frac{z^3}{d^2}-\frac{z^2}{d}\right)\psi_{jm}\right]\sin\frac{m\pi\theta}{\alpha}
\end{aligned}
\tag{1}
$$

or

$$f=[N_m]\{\delta_m\}. \tag{1a}$$

Strain displacement relationship:

$$
\begin{Bmatrix}\epsilon_z\\ \epsilon_\theta\\ \gamma_{z\theta}\\ \chi_z\\ \chi_\theta\\ \chi_{z\theta}\end{Bmatrix}_m
=
\begin{Bmatrix}
\dfrac{\partial u}{\partial z}\\[2ex]
\dfrac{1}{r}\dfrac{\partial v}{\partial\theta}+\dfrac{w\cos\phi+u\sin\phi}{r}\\[2ex]
\dfrac{1}{r}\dfrac{\partial u}{\partial\theta}+\dfrac{\partial v}{\partial z}-\dfrac{v\sin\phi}{r}\\[2ex]
-\dfrac{\partial^2 w}{\partial z^2}\\[2ex]
-\dfrac{1}{r^2}\dfrac{\partial^2 w}{\partial^2\theta}+\dfrac{\cos\phi}{r^2}\dfrac{\partial v}{\partial\theta}-\dfrac{\sin\phi}{r}\dfrac{\partial w}{\partial z}\\[2ex]
2\left(-\dfrac{1}{r}\dfrac{\partial^2 w}{\partial z\,\partial\theta}+\dfrac{\sin\phi}{r^2}\dfrac{\partial w}{\partial\theta}+\dfrac{\cos\phi}{r}\dfrac{\partial v}{\partial z}-\dfrac{\sin\phi\cos\phi}{r^2}v\right)
\end{Bmatrix}_m
=[B_m]\{\delta_m\}, \tag{2}
$$

where $\{\delta_m\}$ is equal to $\{u_{im}, v_{im}, w_{im}, \psi_{im}, u_{jm}, v_{jm}, w_{jm}, \psi_{jm}\}^T$.

Property matrix:

$$
[D]=\begin{bmatrix}
K_z & K_2 & 0 & 0 & 0 & 0\\
K_2 & K_\theta & 0 & 0 & 0 & 0\\
0 & 0 & K_{z\theta} & 0 & 0 & 0\\
0 & 0 & 0 & D_z & D_2 & 0\\
0 & 0 & 0 & D_2 & D_\theta & 0\\
0 & 0 & 0 & 0 & 0 & D_{z\theta}
\end{bmatrix}, \tag{3}
$$

in which

$$
K_z=\frac{E_z t}{1-\nu_z\nu_\theta},\qquad K_2=\nu_\theta K_z,\qquad K_\theta=\frac{E_\theta t}{1-\nu_z\nu_\theta},\qquad K_{z\theta}=G_{z\theta}t,
$$

$$
D_z=\frac{E_z t^3}{12(1-\nu_z\nu_\theta)},\qquad D_2=\nu_\theta D_z,\qquad D_\theta=\frac{E_\theta t^3}{12(1-\nu_z\nu_\theta)},\qquad D_{z\theta}=\frac{G_{z\theta}t^3}{12}.
$$

The strain matrix $[B_m]$ and stiffness $[S_m]$ can be found in reference [2], while the corresponding mass matrix $[m_m]$ (8×8) is given in Appendix I.

B. Top and Bottom Flanges

The top and bottom flanges of the box girder are flat plates which are curved in plan (Fig. 1c), and therefore the membrane and bending actions can actually be uncoupled and treated separately first and then subsequently combined together. Such a formulation has been attempted and the stiffness matrix can be found in reference [2].

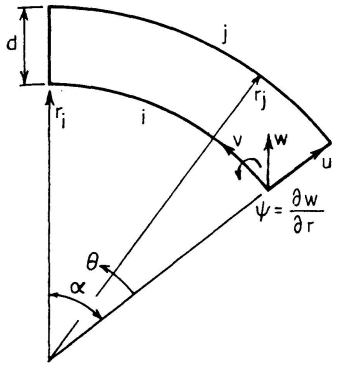

Fig. 1c. A Flange Strip.

However, it is much easier, from the programming point of view, to compute the flange strip stiffness and mass matrices directly from those of the web strip. In such cases, the angle ϕ (Fig. 1b) would be simply taken as equal to 90°.

The stiffness matrix and mass matrix of a strip are given by the following well-known relationships:

$$[S_m] = \int_A [B_m]^T [D] [B_m] \, dA \,, \tag{4}$$

$$[m_m] = \int_A \rho h [N_m]^T [N_m] \, dA \,. \tag{5}$$

Eqs. (4) and (5) refer to matrices for the local coordinate system, and such matrices must be transformed to the global coordinate system before assemblage.

The transformation matrix for a strip can be given in terms of the angle of inclination ϕ, such that

$$\{\delta_m\} = [R] \{\delta'_m\}, \tag{6a}$$

where

$$[R] = \begin{bmatrix} \sin\phi & 0 & \cos\phi & 0 \\ 0 & 1 & 0 & 0 \\ \cos\phi & 0 & -\sin\phi & 0 \\ 0 & 0 & 0 & -1 \end{bmatrix} \tag{6b}$$

and $\{\delta_m\}$, $\{\delta'_m\}$ are the displacements in the local and global coordinates respectively.

The transformed stiffness and mass matrices will have the form of

$$[S'_m] = [R]^T [S_m] [R] \tag{7}$$

and

$$[m'_m] = [R]^T [m_m] [R]. \tag{8}$$

Once the transformed matrices of a strip have been computed, they are assembled into overall stiffness and mass matrices in the same way as for those of a plane frame, and the resulting equation

$$\{[S'_m] - \omega^2 [M'_m]\}\{\Delta'_m\} = 0 \tag{9}$$

solved by any eigenvalue solution.

Some Illustrative Numerical Examples

To illustrate the application of the preceding theory and to demonstrate its accuracy, a selection of numerical examples for both straight and curved bridges will now be presented.

Table 1. Natural Frequencies of a Stiffened Panel ($l = 6b'$) in the Range $0 < \bar{n} \leqq 0.1$

Section of the panel	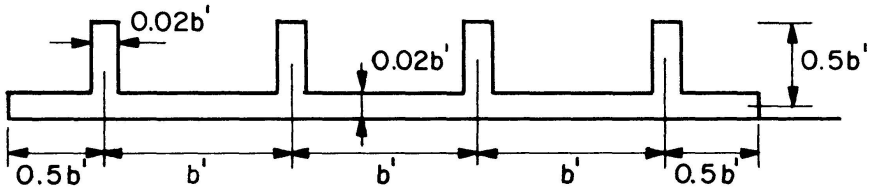			
Mode Number	$\bar{n} = \frac{\omega l}{\sqrt{E/\rho}}$		Wave Number m	Type of Symmetry
	Finite Strip	Reference (8)		
1	0.0287	0.0286	1	*A*
2	0.0292	0.0291	1	*S*
3	0.0365	0.0359	1	*S*
4	0.0366	0.0362	1	*A*
5	0.0394	0.0391	1	*S*
6	0.0396	0.0395	2	*S*
7	0.0411	0.0410	2	*A*
8	0.0504	0.0504	3	*S*
9	0.0521	0.0519	3	*A*
10	0.0557	0.0555	2	*S*
11	0.0639	0.0636	1	*A*
12	0.0643	0.0641	4	*S*

In Table 1, the natural frequencies of a rectangular simply supported stiffened panel have been computed (using rectangular strips) and compared against the results of WITTRICK and WILLIAMS [8], and the two sets of results are found to be nearly identical. A total of 12 strips is used for this problem, although if symmetrical and antisymmetrical conditions were used, it would only be necessary to use 6 strips in the computation.

The circular frequencies of a curved box girder bridge (Fig. 2a) were computed by the curved strip program and the frequencies are presented in Table 2.

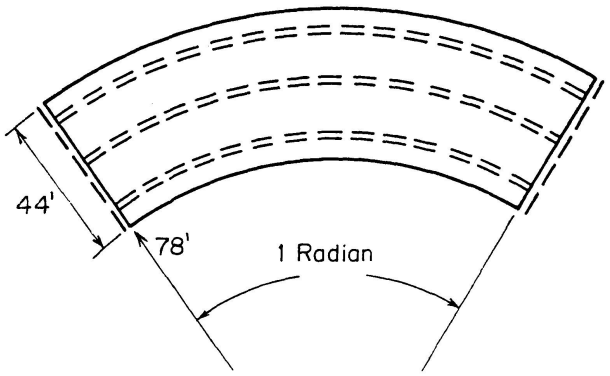

Fig. 2a. Plan of a Curved Box Girder Bridge.

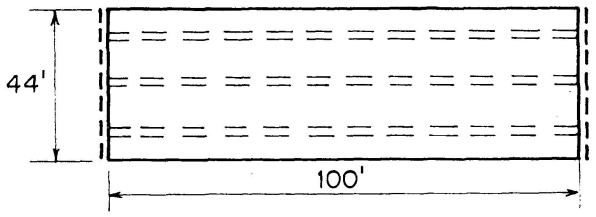

Fig. 2b. Plan of a Straight Box Girder Bridge.

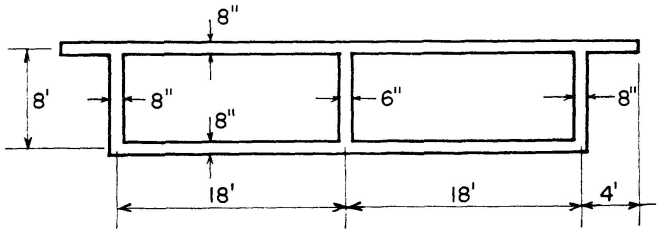

Fig. 2c. Section of the Box Girder Bridges.

Table 2. Circular Frequencies of a Curved Box Girder Bridge ($E=1$, $\nu=0.16$, $\rho=1$)

Longitudinal Mode	Circular Frequencies				
	ω_1	ω_2	ω_3	ω_4	ω_5
$m = 1$	0.002620	0.004249	0.008066	0.008501	0.008553
$m = 2$	0.008002	0.008605	0.009107	0.011427	0.013644
$m = 3$	0.009436	0.010257	0.011821	0.012246	0.020046
$m = 4$	0.010608	0.011556	0.013459	0.013523	0.025243

The modal shapes corresponding to the given frequencies are sketched in Fig. 3.

Each sketch is prepared directly from the eigenvector output which includes all the nodal displacement parameters of the box girder.

Table 3. Circular Frequencies of a Rectangular Box Girder Bridge ($E=1$, $\nu=0.16$, $\rho=1$)

Circular Frequencies (radian/sec.)	ω_1		ω_2		ω_3		ω_4		ω_5	
Longitudinal Mode	Straight Strip	Curved Strip	Straight Strip	Curved Strip	Straight Strip	Curved Strip	Straight Strip	Curved Strip	Straight Strip	Curved Strip
$m = 1$	0.003264	0.003261	0.004070	0.004067	0.007958	0.007958	0.008427	0.008425	0.009733	0.009733
$m = 2$	0.008430	0.008430	0.008531	0.008531	0.008879	0.008879	0.011322	0.011322	0.014782	0.014783
$m = 3$	0.009347	0.009347	0.010356	0.010356	0.011732	0.011732	0.012097	0.012097	0.022693	0.022693
$m = 4$	0.010585	0.010585	0.011641	0.011641	0.013183	0.013183	0.013362	0.013362	0.026011	0.026011

Table 4. Circular Frequencies of a Curved Box Girder Bridge with Concentrated Mass at Midsection of Outer Web ($E=1$, $\nu=0.16$, $\rho=1$)

Circular Frequencies	ω_1		ω_2		ω_3		ω_4		ω_5	
Longitudinal Mode	With Concentrated Mass	Without Concentrated Mass	With Concentrated Mass	Without Concentrated Mass	With Concentrated Mass	Without Concentrated Mass	With Concentrated Mass	Without Concentrated Mass	With Concentrated Mass	Without Concentrated Mass
$m = 1$	0.002283	0.002620	0.003742	0.004249	0.007965	0.008066	0.008073	0.008501	0.008503	0.008553
$m = 2$	0.008002	0.008002	0.008605	0.008605	0.009107	0.009107	0.011427	0.011427	0.013644	0.013644
$m = 3$	0.009434	0.009436	0.010016	0.010257	0.011700	0.011821	0.012240	0.012246	0.015050	0.020046
$m = 4$	0.010608	0.010608	0.011556	0.011556	0.013459	0.013459	0.013523	0.013523	0.025243	0.025243

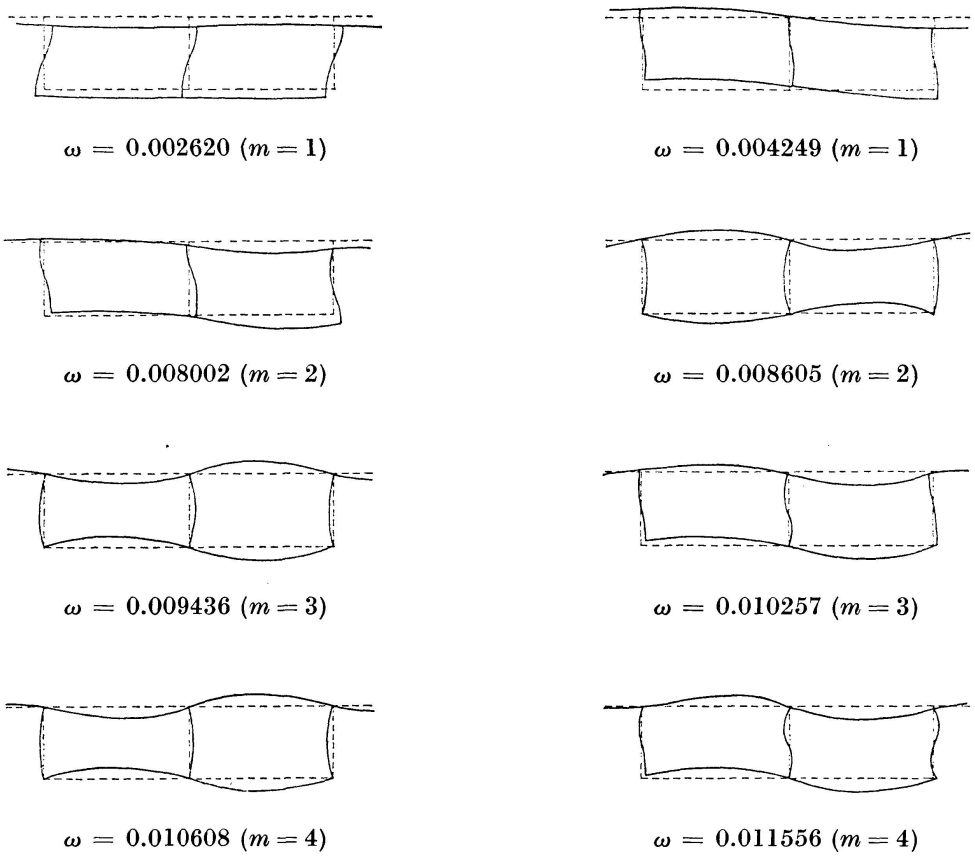

Fig. 3. Modal Shapes of a Curved Box Girder Bridge ($E = 1$, $\nu = 0.16$, $\rho = 1$).

Since the writers are unaware of any previous work on this type of structure, no comparison is offered. However, in order to test the correctness of the curved strip program, it was used to analyze a straight bridge (Fig. 2b) by assuming the subtended angle to be 0.005 radian and the mid-radius of the bridge to be 20 000 feet, so that the mid-circumferential span works out to be 100 feet. The results are then compared with those obtained from the proven straight strip program in Table 3 and the agreement has been found to be excellent for all the frequencies.

The fourth example involves the frequency analysis of the same curved box girder bridge (Example 2) with a concentrated mass attached to the top of the mid-section of the outer web. This concentrated mass, which can be due to presence of a heavy stationary vehicle, is assumed to be equal to one eighth of the total mass of the structure. From Table 4 it is possible to conclude that the additional mass will, in general, lower the natural frequencies of the bridge. However, if the concentrated mass is placed near or on a nodal line, there will be little or no effect on the frequencies. For example, no change can be observed for the frequencies which correspond to the antisymmetric modes.

Notations

a	length of the strip.
[B]	strain matrix.
d	width of the strip.
$[D]$	property matrix.
E_z, E_θ, ν_z $\nu_\theta, G_{z\theta}$	orthotropic material properties.
$[m]$	strip mass matrix.
$[R]$	transformation matrix.
r, θ	polar coordinates.
r_i, r_j	inner and outer radius of a strip.
$[S]$	strip stiffness matrix.
u, v, w	displacement functions.
α	subtended angle
$\{\delta\}$	displacement parameters.
ω	circular frequencies.
ρ	mass density.

Acknowledgement

The financial assistance given by the National Research Council of Canada is gratefully acknowledged.

References

1. Bell, L. C. and Heinz, C. P.: Analysis of Curved Girder Bridges. Journ. of Struct. Div., Proc. ASCE, Vol. 96, No. ST 8, August 1970.
2. Cheung, M. S. and Cheung, Y. K.: Analysis of Curved Box Girder Bridges by Finite Strip Method. IABSE publication, Vol. 31/I, 1971.
3. Cheung, Y. K.: Analysis of Box Girder Bridges by Finite Strip Method. Paper presented at the 2nd Int. Sym. on Concrete Bridge Design, Chicago, March 1969.
4. Cheung, Y. K.: Folded Plate Structures by the Finite Strip Method. Journ. of Struct. Div., Proc. ASCE, Vol. 95, No. ST 12, December 1969.
5. Cheung, Y. K. and Cheung, M. S.: Flexural Vibrations of Rectangular and Other Polygonal Plates. Journ. of Eng. Mech. Div., Proc. ASCE, Vol. 98, No. EM 2, April 1971.
6. Chu, K. H. and Dudnik, E.: Concrete Box Girder Bridges Analysed as Folded Plates. Proc. Int. Sym. on Concrete Bridge Design, Toronto, April 1967.
7. Goldberg, J. E. and Leve, H. L.: Theory of Prismatic Plate Structures. IABSE, Zurich, Switzerland, No. 87, pp. 71–72.
8. Wittrick, W. H. and Williams, F. W.: Natural Vibration of Thin, Prismatic Flat-Walled Structures. Paper presented at IUTAM Sym. on High Speed Computing of Elastic Structures, Liege, August 24–28, 1970.

Appendix I

Mass Matrix of a Curved Strip

$$[m_m] = \rho t \frac{\alpha}{2}$$

$d\left(\frac{d}{12} S\phi + \frac{r_i}{3}\right)$			
	$d\left(\frac{d}{12} S\phi + \frac{r_i}{3}\right)$		
		$d\left(\frac{6d}{70} S\phi + \frac{13}{35} r_i\right)$	
		$d^2\left(\frac{d}{60} S\phi + \frac{11}{210} r_i\right)$	$d^3\left(\frac{d}{280} S\phi + \frac{1}{105} r_i\right)$
$d\left(\frac{d}{12} S\phi + \frac{r_i}{6}\right)$			
	$d\left(\frac{d}{12} S\phi + \frac{r_i}{6}\right)$		
		$d\left(\frac{9d}{140} S\phi + \frac{9}{70} r_i\right)$	$d^2\left(\frac{d}{60} S\phi + \frac{13}{420} r_i\right)$
		$-d^2\left(\frac{d}{70} S\phi + \frac{13}{420} r_i\right)$	$-d^3\left(\frac{d}{280} S\phi + \frac{1}{140} r_i\right)$

$S\phi = \sin\phi$.

	symmetrical		
$d\left(\frac{d}{4}S\phi+\frac{r_i}{3}\right)$			
	$d\left(\frac{d}{4}S\phi+\frac{r_i}{3}\right)$		
		$d\left(\frac{2\,d}{7}S\phi+\frac{13}{35}r_i\right)$	
		$-d^2\left(\frac{d}{28}S\phi+\frac{11}{210}r_i\right)$	$d^3\left(\frac{d}{168}S\phi+\frac{1}{105}r_i\right)$

Summary

The natural frequencies of curved and straight beam-slab or box girder bridges have been computed by the finite strip method. The bridge plates are divided into a number of curved or straight strips extending from one support to the other. By assuming suitable displacement functions for the u, v and w displacements it is possible to formulate the stiffness and mass matrices of a strip. An eigenvalue solution of the assembled overall dynamic stiffness equations will produce the desired frequencies. The stiffness and mass matrices of the straight strip can be obtained directly from those of the curved strip by changing certain variables.

Résumé

Les oscillations propres de ponts à section en T ou en caisson, courbes et droits, ont été calculées par la méthode des bandes finies. Partant d'un appui, les dalles du pont sont divisées en un nombre de bandes courbes ou droites. En supposant des fonctions de déplacement convenables pour les déplacements u, v et w on arrive à formuler les matrices de rigidité et de masse d'une bande. Une solution des valeurs propres des équations dynamiques de rigidité produit les fréquences désirées. Les matrices de rigidité et de masse des bandes droites peuvent être obtenues directement de celles des bandes courbes en changeant certaines variables.

Zusammenfassung

Die Eigenschwingungen gekrümmter und gerader Plattenbalken- oder Kastenträgerbrücken wurden mittels der Methode der finiten Elemente berechnet. Ausgehend von einem Auflager werden die Brückenplatten in eine Anzahl gekrümmter oder gerader Streifen unterteilt. Unter der Annahme passender Verschiebungsansätze für die u-, v- und w-Verschiebungen ist es möglich, die Steifigkeits- und Massmatrizen eines Streifens zu bilden. Eine Eigenwertlösung der dynamischen zusammengesetzten Steifigkeitsgleichungen liefern die Nutzfrequenzen. Die Steifigkeits- und Massmatrizen der geraden Streifen können durch Austausch gewisser Variabler direkt aus denen der gekrümmten Elemente gewonnen werden.

The Flexural Ductility of Reinforced Concrete Sections

La capacité de déformation de sections en béton armé due à l'effort de flexion

Die Verformungsfähigkeit armierter Betonquerschnitte infolge Biegung

M. Z. COHN
Professor of Civil Engineering

S. K. GHOSH
Research Assistant
Department of Civil Engineering

University of Waterloo, Waterloo, Ontario, Canada

Introduction

While the inelastic flexural behaviour of reinforced concrete members and structures has been recognized for a long time [1], its adoption in design practice is still a controversial matter: some codes allow for plastic redistribution of up to 30% of the elastic stress distribution [2], some codes do not recognize plastic action at all [3]. Between these two extremes, some other codes allow an arbitrary degree of redistribution varying from 0 to 30% [4], [5].

In a debate initiated by the Joint ACI-ASCE Committee 428, Limit Design, a few years ago, some basic questions on the admissibility and features of non-linear analysis and design were investigated [6], [7]. From that debate and other similar discussions in the literature, it became obvious that the role, nature and extent of ductility in flexural concrete structures is not fully understood and that some tentative conclusions on the subject were based on insufficient factual data.

It was suggested that high grade steels were not suitable for inelastic design, that the use of compression reinforcement (to increase ductility) eliminates the economic advantages of inelastic design, and that elastic action should not be allowed in reinforced concrete members subject to combined bending and axial loads.

Some years ago one of the authors remarked [7]:

... "It would be ignoring reality to neglect the existence of strength reserve due to the inelasticity of reinforced concrete and not to take advantage of it only because imperfect rather than ideal plasticity is proper to this material. The problem raised by the

particular type of concrete ductility is not *whether* but *how* it should be considered. That concrete, unlike steel, displays only a limited adaptability does not preclude its exploitation, but rather requires a deeper study of its physical significance and limitations." ...

This paper is an attempt in this direction, and has the following objectives:

1. A proper definition of flexural ductility for reinforced concrete sections.
2. An exhaustive study of the main variables affecting ductility.
3. Some conclusions on conditions and limitations of plastic adaptability in structural concrete.
4. Possible practical guidelines on the applicability of limit design to reinforced concrete structures.

The approach used in this analytical investigation is a computer simulation of the behaviour of over 1700 reinforced concrete section specimens under pure and combined bending. Starting from reliable stress-strain characteristics for steel and concrete [8], moment-curvature relationships and ductility factors are derived for an extensive range of variable combinations. Results obtained justify a more positive view of the potential use of inelastic design methods, when their limitations and the effects of major variables are well understood.

Definition of Ductility

Ductility is recognized as a factor governing the rotation capacity of hinging zones and the redistribution of moments in a structure [9]; the adaptability of structures to foundation settlements and volume changes [6]; and the energy absorption capacity of structures subject to dynamic (wind, earthquake, blast) loads [10], [11], [12]. Ductility safeguards a structure against sudden overloads, impact and load reversals. For this reason it is desirable that structures be capable of mobilizing a reasonable amount of ductility whenever actions such as those mentioned above are foreseen. Experience shows that the members of a structure are sufficiently ductile, for all practical purposes, when they resist only transverse loads, are moderately reinforced in tension, moderately to heavily reinforced in compression and shear, use mild or intermediate grade steels, and high grade concretes. It is also an established fact that careful joint detailing and a high standard of execution in the field contribute to the achievement of high degrees of ductility [13].

Beyond these general qualitative facts and except for some attempts to study the ductility of reinforced concrete sections [10], [11], [14], [15], [16], [17], there is only a limited knowledge of the problem.

In a broad sense, ductility is taken to be the ability to sustain deformations beyond the elastic range without a significant variation of the resistance capacity. Such a qualitative description of ductility is broad enough to accom-

modate the response of plastic, strain-hardening or strain-softening materials, as long as precise limits of deformation and strength variations are not specified.

More precise definitions of ductility have to be dependent on at least the following: a) level of study – material, sectional and structural ductility should be defined in terms of strains, curvatures, and rotations or deflections, respectively; b) type of stress – ductility under axial loading, flexure, shear and torsion should be defined in terms of longitudinal strains, curvatures, shearing strains, and angles of twist, respectively; c) nature of study – depending upon which, it may be more or less suitable to define ductility in terms of limiting deformations (e. g. ϵ_u, ϕ_u), differences or ratios between limiting and idealized elastic limit deformations (e. g. $\epsilon_u - \epsilon_y$, $\phi_u - \phi_y$, ϵ_u/ϵ_y, ϕ_u/ϕ_y), or areas under load-deformation diagrams up to limiting deformations or between limiting and idealized elastic limit deformations. While the second alternative may be satisfactory in the limit analysis and design of concrete structures, the last may be more meaningful in earthquake engineering; d) nature of loading (static, dynamic).

Some possible and serious confusions may arise from an interchange of ductility definitions. Here are two typical examples:

a) The effect of high grade concrete is favorable on *sectional* ductility, [14], [15] but is unfavorable on *material* ductility [8].

b) Lateral reinforcement is more efficient than compression reinforcement in increasing the *material* ductility (of concrete), [18]; compression reinforcement is more efficient than lateral reinforcement in increasing *sectional* ductility [19].

This study is concerned with the ductility of reinforced concrete sections, on the assumption that the properties of steel and concrete are known. The investigation is limited to pure and combined bending, because these are the most common cases when a designer faces inelastic action in structural concrete. Further studies should provide similar data on r. c. ductility in shear and torsion. As an index of sectional ductility, the *ductility factor* is defined as the ratio of ultimate to yield curvatures, ϕ_u/ϕ_y. It is found that this definition is the most widely used for evaluating ductility under static loads and is equally significant for both steel [20] and reinforced concrete [21], [22]. In brief, this investigation is concerned with the ductility (a) of reinforced concrete sections, (b) under flexural action, (c) defined as a ratio of curvatures, (d) for static loading only.

Having defined the meaning of the ductility factor in the context of this paper it is necessary to further define the curvatures, ϕ_u and ϕ_y. The current practice is to assume that the ultimate curvature is associated with a conventional limiting value of the concrete strain at the extreme fibre i. e. $\epsilon_u = 0.3\%$, $\epsilon_u = 0.35\%$ and $\epsilon_u = 0.38\%$ according to the ACI Code [23], CEB Recommendations [4] and some earlier investigations at the University of Illinois [14], [24], respectively. These ϵ_u values are considered to be independent

of such factors as the longitudinal and lateral reinforcement, strain-hardening, strain gradient, etc. A more satisfactory definition of the ultimate strain, proposed by RÜSCH [25] is adopted in this study: since the primary function of a structure is to carry loads, ϵ_u is defined as the strain corresponding to the ultimate stage, i. e. at which the section reaches its maximum load or moment carrying capacity. Similarly, the ultimate curvature, ϕ_u, is the one associated with the strain, (ϵ_u), load, (P_u), or moment, (M_u), at the ultimate stage.

The yield curvature, ϕ_y, is defined as the curvature at which the tension steel reaches its yield point stress. The stress-strain relationships used for steel in the present investigation are characterized by well defined yield points. Thus, when the tension steel in a section does not yield before the section reaches its ultimate stage, it is either because the section is highly over-reinforced or because it carries a heavy axial load. Instead of attempting to arbitrarily define an idealized yield stage, the ductility factors of such sections, possessing very little ductility, are assumed to be equal to unity in the present study.

Factors Affecting Ductility

The major factors affecting the ductility of a reinforced concrete section can be classified as follows:

1. Material Variables:
   a) Concrete quality.
   b) Grades of tension and compression reinforcement.
   c) Grade of lateral reinforcement.
   d) Strain-hardening of steel.
   e) Bond.
   f) Tensile strength of concrete.

2. Geometric Variables:
   a) Shape and size of sections.
   b) Amount of tension reinforcement.
   c) Amount of compression reinforcement.
   d) Amount and spacing of lateral reinforcement.
   e) Cover thickness.

3. Loading Variables:
   a) Duration of loading.
   b) Axial loading.
   c) Prestressing.
   d) Repetition of loading.
   e) Loading reversal.

The effects of the above factors on sectional ductility were investigated by using a nonlinear sectional theory, realistic stress-strain relationships for concrete and steel and a numerical method of computation developed in [8]. These have been described in a recent paper by the authors [26] and are briefly reviewed in the next section.

Sectional Analysis

a) Stress-Strain Relationship for Concrete in Compression

The main factors affecting concrete behaviour are: concrete strength, lateral reinforcement, creep, strain gradient, size of specimen and type of loading. A stress-strain relationship for concrete in compression, proposed by SARGIN [8], takes all these factors into account by a proper choice of five governing parameters: the concrete cylinder strength, f'_c; the initial Young modulus, E_c; the ratio of maximum stress to cylinder strength, k_3; the strain corresponding to maximum stress, ϵ_0; and a parameter, D, which mainly affects the descending branch of the stress-strain curve. By denoting $A = E_c \epsilon_0 / k_3 f'_c$ and $x = \epsilon/\epsilon_0$, Sargin's relationship can be expressed as:

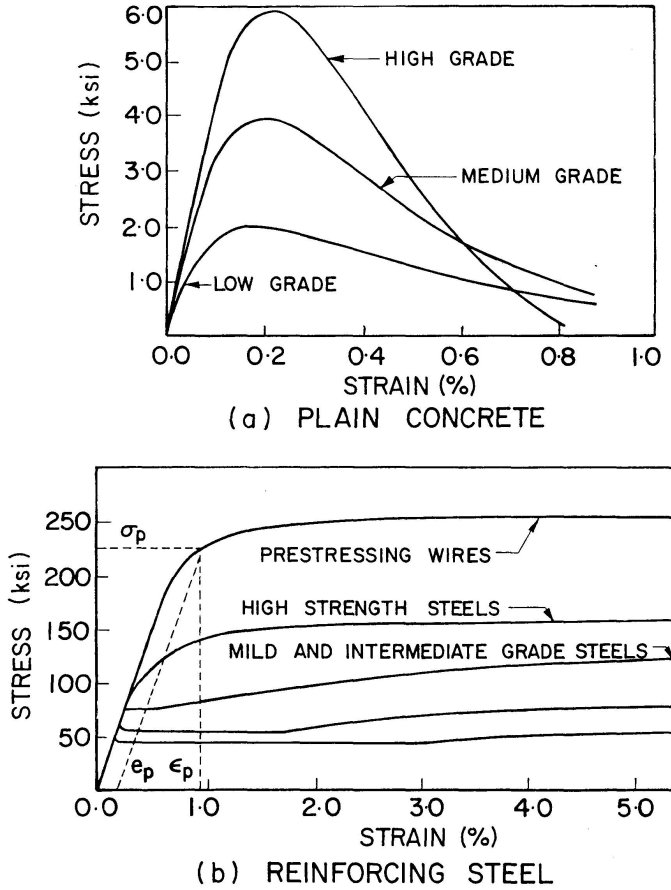

Fig. 1. Typical stress-strain curves for (a) concrete in compression and (b) reinforcing steel.

$$\sigma = k_3 f'_c \frac{A x + (D-1) x^2}{1 + (A-2) x + D x^2}. \tag{1}$$

Equations expressing E_c, k_3, ϵ_0 and D in terms of the factors affecting them are given in [8] and are used in numerical calculations. For the sake of brevity, these are not reproduced here. Typical stress-strain curves for concrete in compression, Eq. (1), are illustrated in Fig. 1 (a).

b) Stress-Strain Relationship for Concrete in Tension

The behaviour of concrete in tension is assumed to be elastic-brittle and can be expressed by the following equations:

$$\begin{aligned} \sigma_t &= E_c \epsilon_t \quad (\text{for } \epsilon_t \leqq \epsilon_{tr}), \\ \sigma_t &= 0 \qquad (\text{for } \epsilon_t > \epsilon_{tr}), \end{aligned} \tag{2}$$

where $\epsilon_{tr} = \sigma_{tr}/E_c$ is the cracking strain and σ_{tr} is the modulus of rupture of concrete. An equation expressing σ_{tr} in terms of the factors governing it is also given in [8].

c) Stress-Strain Relationships for Reinforcing Steels

The following idealized relationships, consisting of three parts corresponding to the elastic, yield and strain-hardening ranges, and considered applicable to most American steel grades with yield limits not in excess of 75 ksi, are adopted in this study:

$$\begin{aligned} \sigma_s &= E_s \epsilon_s \quad (\text{for } 0 \leqq \epsilon_s \leqq \epsilon_y), \\ \sigma_s &= f_y \qquad (\text{for } \epsilon_y < \epsilon_s \leqq \epsilon_{sh}), \\ \sigma_s &= f_y + E_{sh} (\epsilon_s - \epsilon_{sh}) \, 1 - \frac{E_{sh} (\epsilon_s - \epsilon_{sh})}{4 (\sigma_{su} - f_y)} \quad (\text{for } \epsilon > \epsilon_{sh}), \end{aligned} \tag{3}$$

where E_s is the Young modulus for steel, f_y is the yield limit, ϵ_{sh} is the strain at the onset of hardening, E_{sh} is the strain-hardening modulus and σ_{su} is the ultimate stress.

Typical stress-strain curves for steel, Eq. (3), are illustrated in Fig. 1 (b), along with stress-strain curves for high strength steels (proof stress > 75 ksi) and prestressing wires, which are not used in the present investigation.

d) Nonlinear Sectional Theory

With the notations and assumptions of Fig. 2, the force and moment equilibrium equations for a reinforced concrete section, symmetrical about

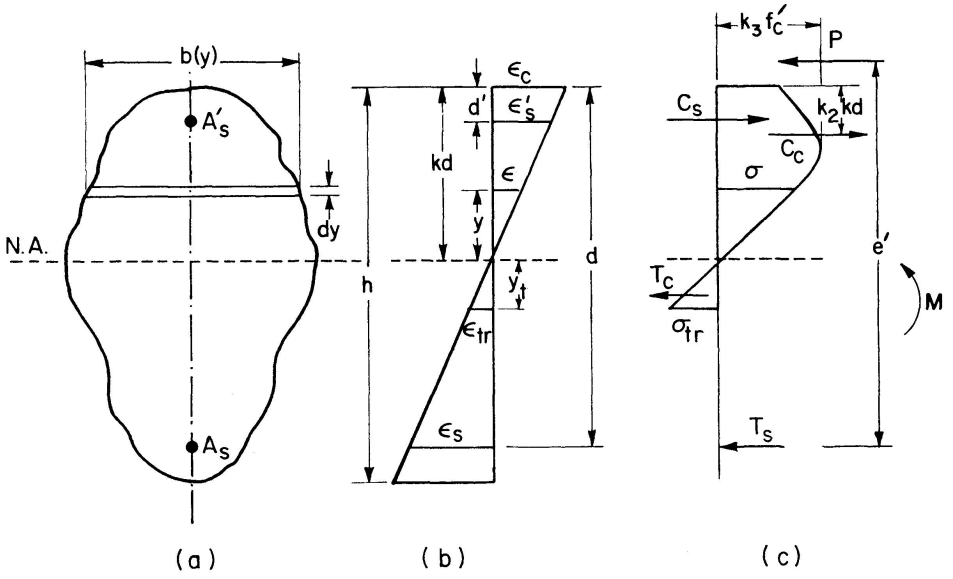

Fig. 2. Basic notations in the flexural analysis of reinforced concrete sections.

one axis and loaded in the plane of symmetry, can be expressed as follows:

$$\int_0^{kd} \sigma(\epsilon)\, b(y)\, dy + A'_s \sigma'_s - \int_0^{y_t} \sigma_t(\epsilon_t)\, b(y)\, dy - A_s \sigma_s = P, \tag{4}$$

$$\int_0^{kd} \sigma(\epsilon)\, b(y)\, (d - k\,d + y)\, dy + A'_s \sigma'_s (d - d') - \int_0^{y_t} \sigma_t(\epsilon_t)\, b(y)\, (d - k\,d - y)\, dy = P\,e' + M. \tag{5}$$

The assumption of linear strain distribution implies:

$$\frac{\epsilon_c}{k\,d} = \frac{\epsilon'_s}{k\,d - d'} = \frac{\epsilon_s}{d - k\,d} = \frac{\epsilon}{y} = \frac{\epsilon_{tr}}{y_t}. \tag{6}$$

Eqs. (1), (2) and (3) are used to eliminate σ, σ_t and σ_s, σ'_s, respectively, and Eq. (6) to eliminate y and y_t from Eqs. (4) and (5).

e) Numerical Method of Solution

A numerical method is developed to solve Eqs. (4) and (5) simultaneously in the following steps (Fig. 3):

a) Starting from zero, increase ϵ_c at some chosen interval.
b) For any given value of ϵ_c, find a value of k by successive approximation such that Eq. (4) is satisfied with a specified tolerance.
c) Solve Eq. (5) for M with the known values of ϵ_c, k and the given P.
d) Calculate all other behaviour parameters: ϕ, EI (flexural rigidity), etc.
e) Continue to increase ϵ_c up to and beyond the value ϵ_u at which the moment reaches a maximum. ϵ_u corresponds to the ultimate state of the section.

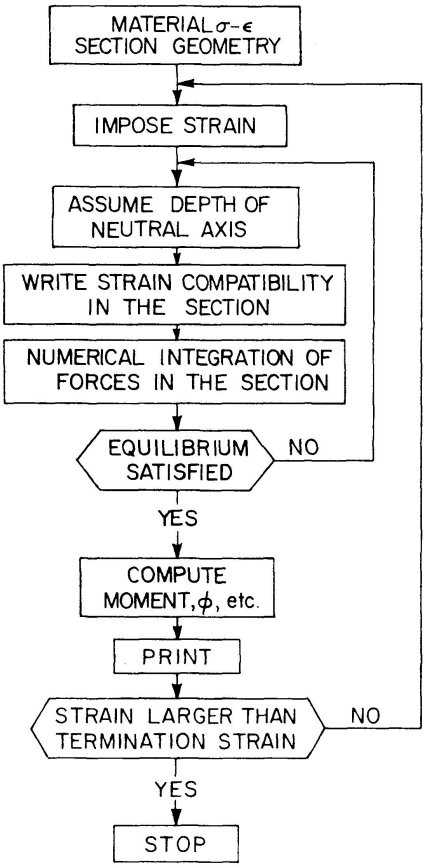

Fig. 3. Flow diagram for numerical analysis.

Using the above method of sectional analysis, 1734 sections were analyzed under various combinations of the factors enumerated in the preceding section (Tables 1 and 2). Some of the results of this investigation are presented herein. The effects of the various factors on the ductility of the sections analyzed are discussed in the next three sections.

Material Variables

The effects of *concrete and tension reinforcement qualities* on the $M-\phi$ relationships of reinforced concrete sections are shown in Fig. 4. This figure shows that, irrespective of the reinforcement percentage p, sectional ductility increases with increasing concrete and decreasing tension reinforcement strengths. This can be seen more clearly in Fig. 5, in which the ductility ratio ϕ_u/ϕ_y is plotted against the reinforcement percentage p for various grades of concrete and tension reinforcement. Each curve has a little arrowhead attached to it, which corresponds to the maximum percentage of tension reinforcement, p_{max}, that can be used in sections designed according to the ACI ultimate strength theory [23]. Fig. 5 shows that although for low reinforcement percentages fairly high ductility ratios are available for most grades of concrete and steel, this ratio may be as low as 2.5 for some steel and concrete grades,

Table 1. Variable combinations for various sections investigated

SECTION #	T	P/P_u =0.0	P/P_u =0.1	P/P_u =0.2	P/P_u =0.3	P/P_u =0.4	P/P_u =0.45	P/P_u =0.5	P/P_u =0.6	P/P_u =0.8	f'_c ksi	f_y ksi	p %	p'/p	E_{sh} $\times 10^3$ksi	d'' in.	s in.	t min.	c in.	F	σ_t
1	57												0.5								
2	58																	30			
3																		10			
4																		10^2			
5													1.0					10^3			
6														0				10^4			
7																		10^5			
8																		10^6			
9	59												1.5								
10	60												2.0					30			
11													2.5								
12	61																				
13																		10			
14																		10^2			
15													3.0					10^3			
16																		10^4			
17																		10^5			
18																		10^6			C
19													3.5								O
20	62												4.0								N
21													0.5								S
22													1.0								I
23											3	45	1.5		1.25	1/4	9		2	1.0	D
24	63												2.0								E
25													2.5	0.25							R
26													3.0								E
27													3.5								D
28	64												4.0								
29	65												1.5	0.33							
30	66												3.0								
31													0.5								
32	67	73	83	93	103	113	123	133	143				1.0								
33													1.5								
34	68	74	84	94	104	114	124	134	144				2.0	0.5				30			
35													2.5								
36		75	85	95	105	115	125	135	145				3.0								
37													3.5								
38	69												4.0								
39	70	76	86	96	106	116	126	136	146				1.5	0.67							
40	71	77	87	97	107	117	127	137	147				3.0								
41													0.5								
42													1.0								
43													1.5								
44													2.0	0.75							
45													2.5								
46													3.0								
47													3.5								
48													4.0								
49		78	88	98	108	118	128	138	148				0.5								
50	72	79	89	99	109	119	129	139	149				1.0								
51		80	90	100	110	120	130	140	150				1.5								
52		81	91	101	111	121	131	141	151				2.0	1.00							
53													2.5								
54		82	92	102	112	122	132	142	152				3.0								
55													3.5								
56													4.0								

Sections 153-204, 205-456, 457-608, 1127-1278, 1279-1430, 1431-1582, and 1583-1734 correspond to sections 1-152 for f'_c, f_y = 3,60; 3,75; 4,45; 4,75; 5,45; 5,60; and 5,75 ksi, respectively.

as p approaches p_{max}. It must be remembered, however, that Fig. 5 is for singly reinforced sections containing nominal amounts of lateral reinforcement (No. 2 ties at 9″ spacing). Ductility can be increased somewhat by reducing the spacing and increasing the diameter of the ties. It an be improved considerably by the addition of suitable amounts of compression reinforcement.

Sectional behaviour is affected much more by the spacing and cross-sectional area of lateral reinforcement than by its grade. The latter was, therefore, not studied in the present investigation.

Table 2 · Variable combinations for various sections investigated

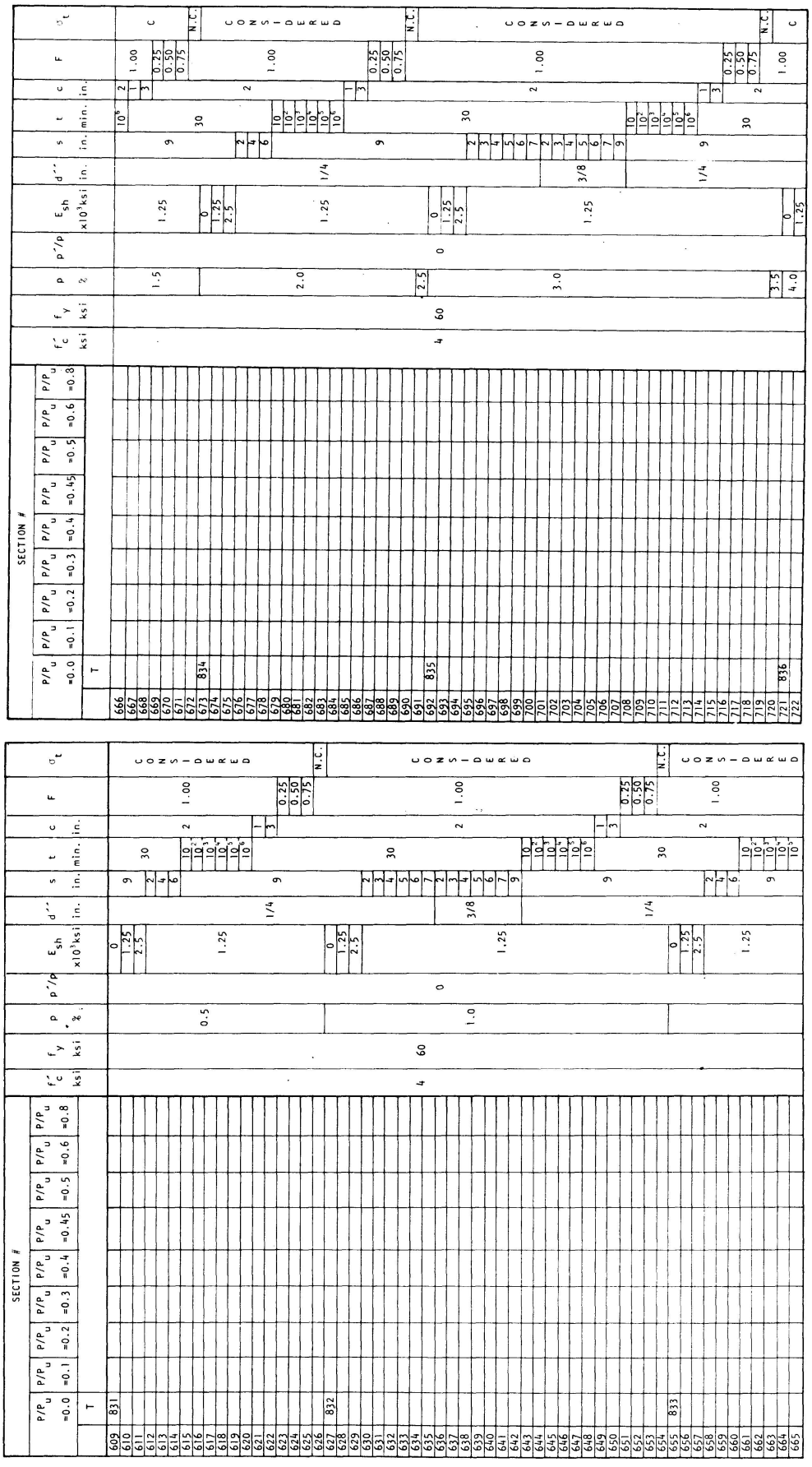

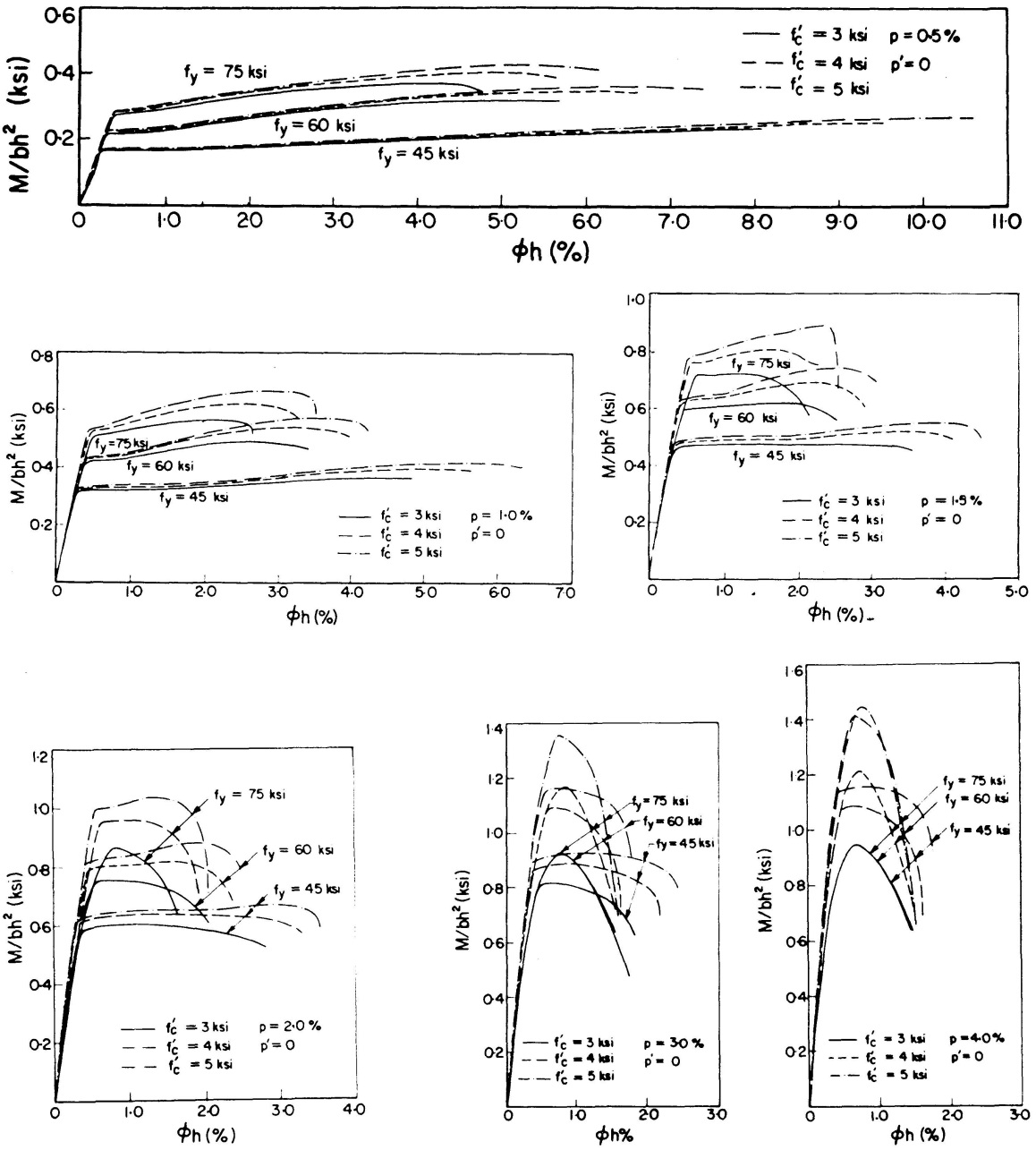

Fig. 4. Effect of concrete and steel grades and of steel percentages on ductility: M-ϕ diagrams.

Fig. 6 shows the effects of *strain-hardening* of steel on the $M-\phi$ relationships of singly reinforced sections. All reinforcing steels had the same modulus of elasticity, yield strength and strain at the onset of hardening; only the strain-hardening modulus E_{sh} was varied. The ductility ratio ϕ_u/ϕ_y is plotted against p for three different E_{sh} in Fig. 7. It can be seen that strain-hardening of steel improves the ductility of lightly reinforced sections, but has a negligible effect on heavily reinforced sections. Fig. 7 also shows that ductility increases as E_{sh} is increased from 0 to 1.25×10^3 ksi, but then it decreases as E_{sh} is further increased to 2.5×10^3 ksi. This would suggest that there is an optimal values of E_{sh} that maximizes the sectional ductility.

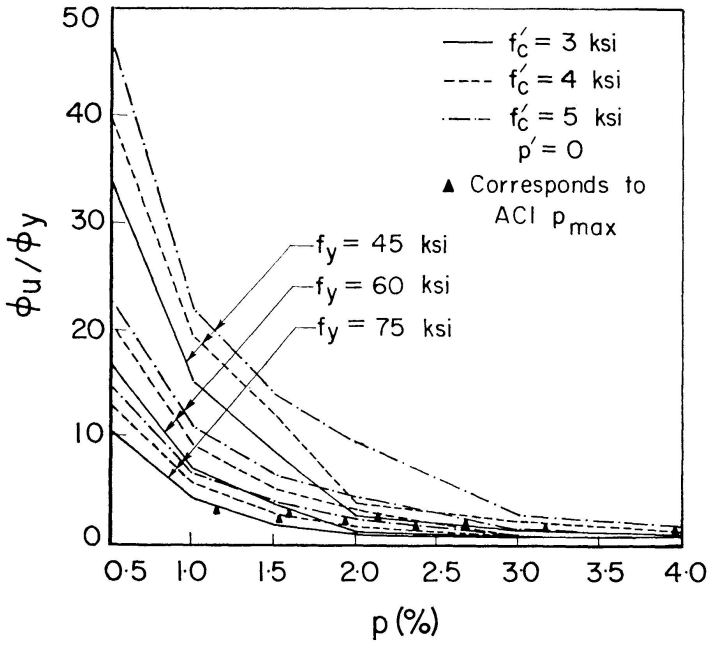

Fig. 5. Effect of concrete and steel grades and of steel percentages on ductility: ϕ_u/ϕ_y-p diagrams.

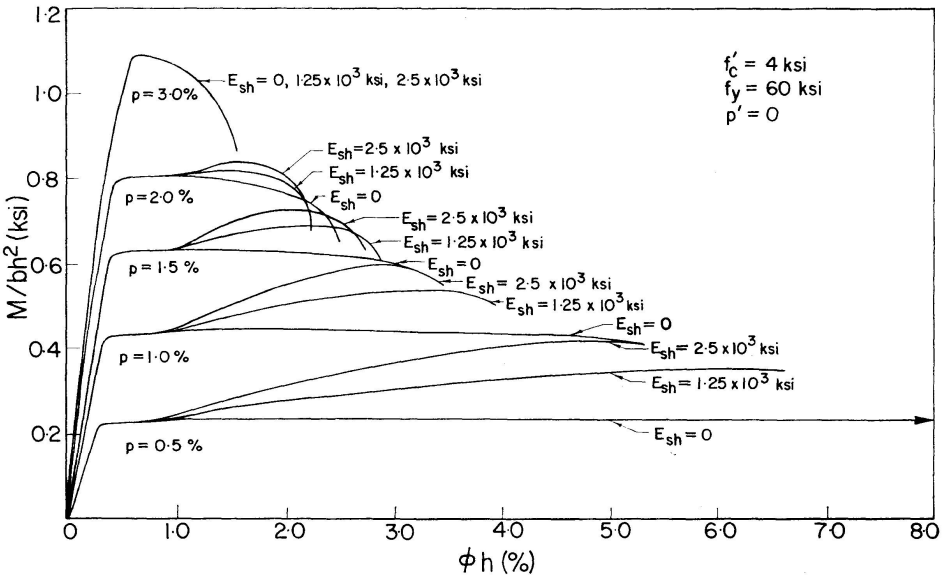

Fig. 6. Effect of strain-hardening of steel on ductility: M-ϕ diagrams.

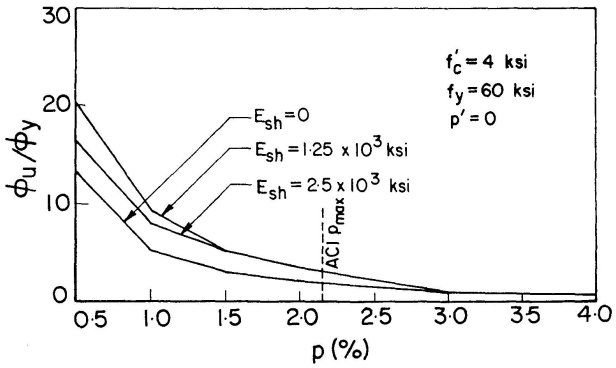

Fig. 7. Effect of strain-hardening of steel on ductility: ϕ_u/ϕ_y-p diagrams.

The effect of *bond* was investigated through BAKER's [26] bond factor F, which is defined as the ratio of steel and virtual concrete strains at the same level, i. e.

$$F = \frac{\epsilon_s k}{\epsilon_c (1-k)}. \tag{7}$$

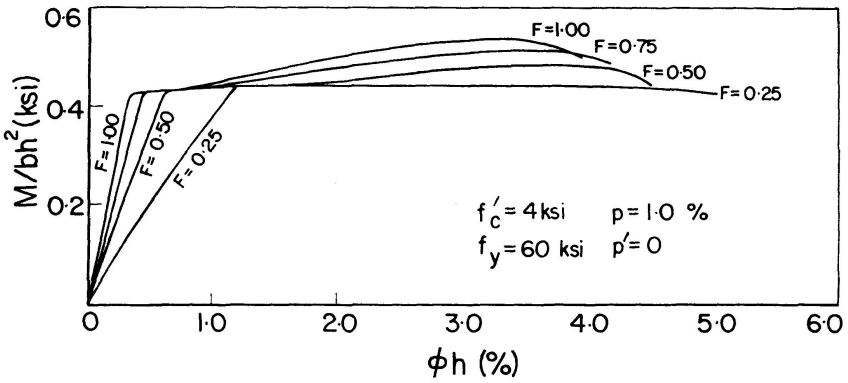

Fig. 8. Effect of bond on ductility: M-ϕ diagrams.

Fig. 8 shows the $M-\phi$ relationships of four singly reinforced sections with $F=0.25$, 0.50, 0.75 and 1.00, respectively, and identical in all other respects. The ductility ratios of these sections are plotted in Fig. 9, which shows that ductility is the highest for the section with full bond ($F=1.00$) and that it decreases steadily as F is reduced from 1.00 to 0.25.

$M-\phi$ relationships for sections in which the *tensile strength of concrete* was totally neglected and in which it was accounted for were found to be nearly identical. It was, therefore, concluded that the tensile strength of concrete has no significant effect on the sectional behaviour.

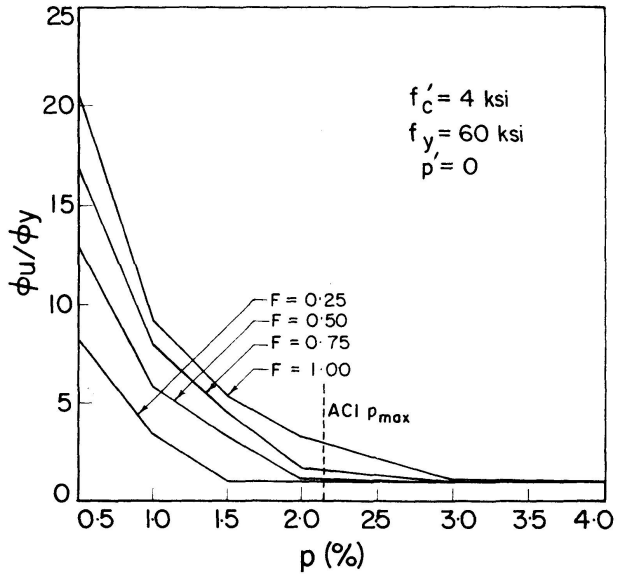

Fig. 9. Effect of bond on ductility: ϕ_u/ϕ_y-p diagrams.

Geometric Variables

NEWMARK and HALL [10] studied the effect of variations in depth on the ductility of rectangular sections and concluded that ductility was unaffected by such variations. The effects of sectional width and effective depth variations on the rotation capacity (hence ductility) of rectangular sections were investigated by CORLEY [28]. He concluded that ductility was not significantly affected either by depth or by width. These conclusions, based on reliable experimental evidence, are accepted in this study; the effects of *sectional size* on ductility are not investigated.

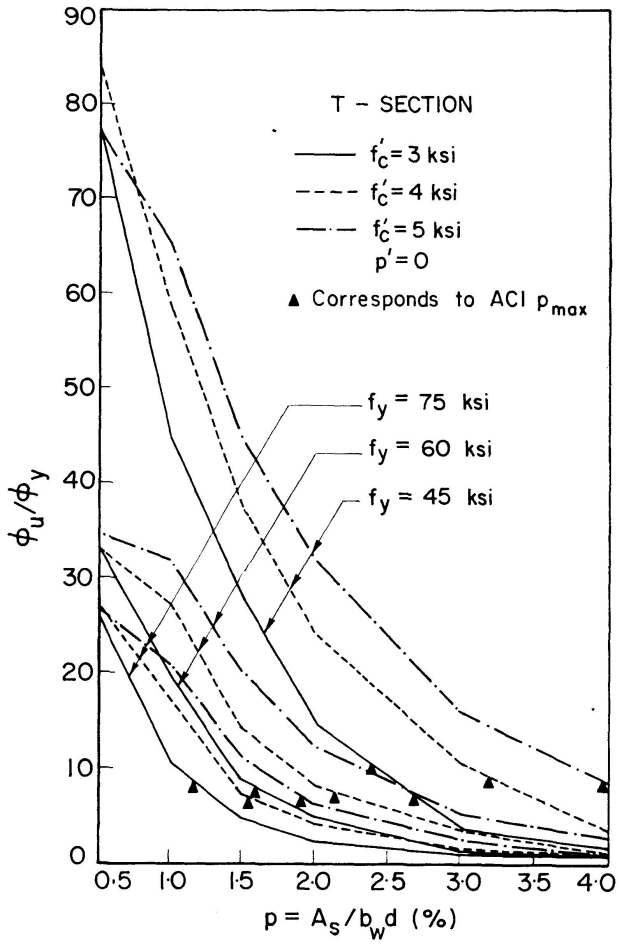

Fig. 10. Effect of sectional shape on ductility: ϕ_u/ϕ_y-p diagrams for T-sections.

Fig. 10 shows $\phi_u/\phi_y - p$ (with $p = A_s/b_w d$, and b_w = web width) diagrams for T-sections, the overall depth, effective depth and web width of which were equal to the corresponding depths and width (20″, 18″ and 10″, respectively) of the rectangular sections studied so far. The flange width and thickness were 30″ and 2.5″, respectively. It can be seen by comparison with Fig. 5 that the overhanging flanges provide a substantial improvement in ductility. This is not surprising in view of the fact that the overhanging flange area can be considered as an equivalent compression steel area and compression reinforce-

ment is known to have a favourable effect on ductility. *Sectional shapes* other than rectangle and T were not investigated.

The effect of the *amount of tension reinforcement* on ductility can be observed in Figs. 4 and 5. Fig. 11 illustrates sectional $M-\phi$ relationships for various amounts of tension steel, corresponding to a particular quality of concrete

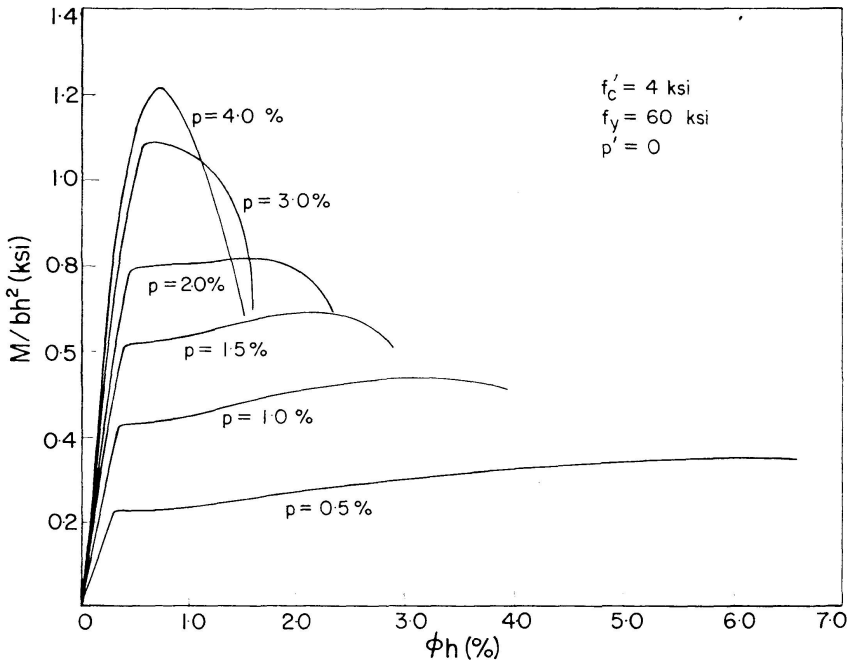

Fig. 11. Effect of tension steel percentage on ductility: M-ϕ diagrams.

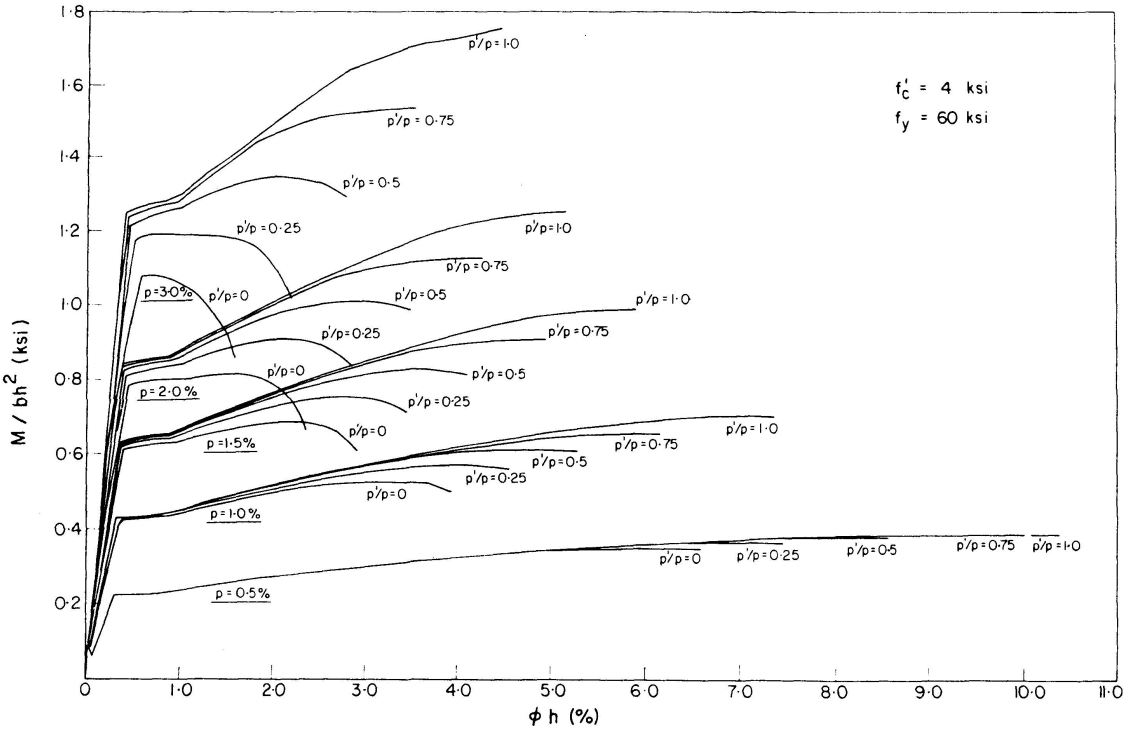

Fig. 12. Effect of compression reinforcement on ductility: M-ϕ diagrams.

and of tension reinforcement. Figs. 4, 5 and 11 confirm that ductility decreases with increasing amounts of tension reinforcement, and that very little or no ductility is available for sections with very high steel percentages (e.g. 4%). This is why most codes of practice [23] impose an upper limit on the amount of tension reinforcement that should be used in design.

Fig. 12 shows the effect of *compression reinforcement* on sectional $M-\phi$ relationships. For a particular quality of concrete and of reinforcing steel, $M-\phi$ diagrams are drawn for various percentages of tension reinforcement and for various ratios of compression and tension steel areas. ϕ_u/ϕ_y-p diagrams for various p'/p ratios and for various qualities of concrete and steel are plotted in Fig. 13. These figures show clearly that sectional ductility can be improved considerably by the addition of suitable amounts of compression reinforcement. This is also evident from Table 3, in which ϕ_u/ϕ_y values are tabulated for different concrete and steel qualities, various amounts of tension

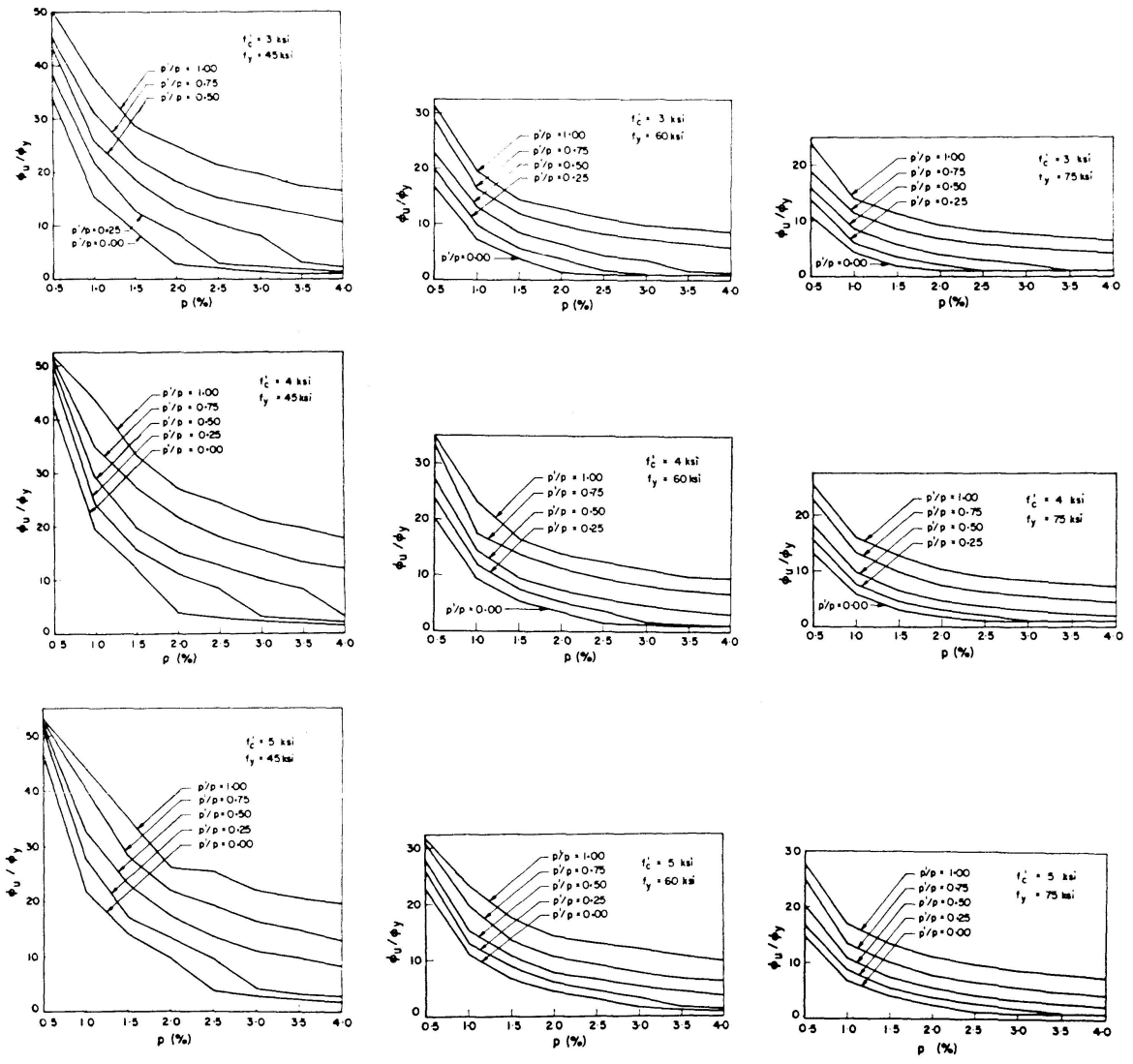

Fig. 13. Effect of compression reinforcement on ductility: ϕ_u/ϕ_y-p diagrams.

reinforcement and various p'/p ratios. For flexural members, the ductility of support sections is usually more critical than that of span sections [22], because span sections very often act as T-sections, so that their ductility is improved considerably by the overhanging flange areas (Fig. 10). However, support sections usually contain an amount of compression reinforcement. In flexural members, the amount of positive moment steel is usually about 75 to 80% of the tension steel provided for negative moments. If half of the steel for positive moments is bent up, the other half automatically provides compression steel in the amount $A_s' = 0.5 \times 0.8\, A_s = 0.4\, A_s$, where A_s' is the tension steel for negative moments. This amount of compression steel can considerably improve the ductility of a section. Table 3 shows that the ductility ratio of a section with $p = 1.5\%$, $f_c' = 4$ ksi and $f_y = 60$ ksi nearly doubles from 5.35 to 9.48 when compression steel in the amount $A_s' = 0.5\, A_s$ is added. Incidentally, Table 3 also indicates that sections reinforced with usual, economic percentages of high grade steel, when made of commensurately high grades of concrete, are capable of mobilizing reasonable levels of ductility. For instance, a section with $f_c' = 5$ ksi, $f_y = 75$ ksi, $p = 1.5\%$, and $p' = 0.25\, p$, has a ductility factor of 5.48. This would appear to suggest that inelastic design is not necessarily unsuitable for structures made of high grade steels, as has sometimes been claimed in the past. Table 3 also indicates that the unfavourable effect of an increase in steel strength on sectional ductility is usually more pronounced than the favourable effect of an increase in concrete strength.

The effect of *tie spacing* on sectional $M - \phi$ relationships is illustrated in Fig. 14. Fig. 15 shows ϕ_u/ϕ_y variation with p for different tie spacings. It can be seen that ductility increases somewhat as tie spacing is reduced, but that

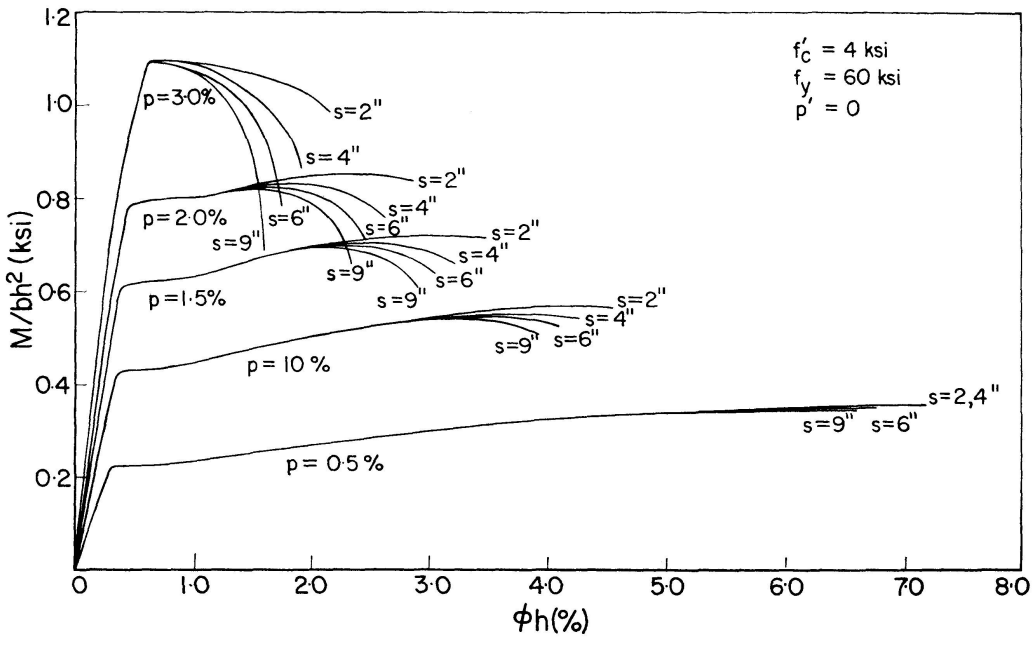

Fig. 14. Effect of tie spacing on ductility: M-ϕ diagrams.

Table 3. Ductility factor, ϕ_u/ϕ_y, for sections with various steel and concrete strengths and tension and compression reinforcement areas

f'_c ksi	f_y ksi	p %	p′/p=0	p′/p=0.25	p′/p=0.5	p′/p=0.75	p′/p=1.0
			ϕ_u/ϕ_y				
3	45	0.5	33.80	38.20	43.70	45.20	50.30
		1.0	15.20	21.80	25.80	31.00	37.60
		1.5	8.75	12.60	18.60	22.80	28.50
		2.0	2.78	8.63	13.20	18.25	25.00
		2.5	2.00	2.89	10.20	15.25	21.00
		3.0	1.39	2.32	8.18	13.90	19.70
		3.5	1.00	1.76	3.00	12.10	17.45
		4.0	1.00	1.33	2.47	10.65	16.60
	60	0.5	16.75	19.95	22.90	28.60	31.40
		1.0	7.10	9.61	12.95	16.20	19.40
		1.5	3.77	5.52	8.30	11.70	14.30
		2.0	1.42	3.74	6.43	9.65	12.70
		2.5	1.00	1.10	4.40	8.30	11.05
		3.0	1.00	1.00	3.54	7.32	9.85
		3.5	1.00	1.00	1.64	6.52	9.38
		4.0	1.00	1.00	1.33	5.92	8.59
	75	0.5	10.60	13.70	15.85	18.60	23.90
		1.0	4.25	5.83	8.39	11.30	13.88
		1.5	1.90	3.41	5.60	8.41	11.10
		2.0	1.00	2.00	3.89	6.77	9.12
		2.5	1.00	1.00	2.90	5.85	8.12
		3.0	1.00	1.00	2.28	5.21	7.61
		3.5	1.00	1.00	1.00	4.72	7.00
		4.0	1.00	1.00	1.00	4.30	6.47
4	45	0.5	42.40	48.10	50.10	51.20	51.80
		1.0	19.40	24.10	29.30	34.60	43.80
		1.5	12.13	15.65	19.80	27.30	33.40
		2.0	3.94	11.12	15.05	21.60	27.00
		2.5	2.89	8.37	12.60	17.95	24.40
		3.0	2.21	3.06	10.10	15.55	21.05
		3.5	1.72	2.61	8.35	13.20	19.80
		4.0	1.5	2.10	3.17	12.10	17.64
	60	0.5	20.30	23.70	27.20	33.40	34.70
		1.0	9.22	11.80	14.35	17.35	23.00
		1.5	5.35	7.42	9.48	13.70	16.40
		2.0	3.26	5.05	7.15	11.16	13.65
4	60	2.5	1.50	3.56	5.67	9.50	12.48
		3.0	1.10	1.64	4.59	8.34	11.05
		3.5	1.00	1.33	3.66	7.41	9.95
		4.0	1.00	1.03	3.08	6.65	9.53
	75	0.5	13.05	15.50	18.30	22.60	25.45
		1.0	5.82	7.50	9.68	13.20	15.95
		1.5	2.96	4.48	6.46	9.70	12.60
		2.0	1.77	3.00	4.65	7.44	10.20
		2.5	1.00	2.03	3.61	6.27	9.00
		3.0	1.00	1.00	2.97	5.52	8.44
		3.5	1.00	1.00	2.39	4.97	7.69
		4.0	1.00	1.00	2.00	4.48	7.07
5	45	0.5	46.40	51.00	52.00	52.50	53.00
		1.0	21.80	27.70	32.60	40.40	44.30
		1.5	14.00	17.10	23.00	28.20	35.20
		2.0	9.60	13.30	17.20	21.90	26.10
		2.5	3.82	9.56	13.50	19.20	25.40
		3.0	2.84	4.06	10.90	16.20	21.90
		3.5	2.32	3.30	9.70	14.80	20.50
		4.0	1.86	2.72	8.18	12.70	19.50
	60	0.5	22.60	25.90	27.90	30.90	31.80
		1.0	10.95	12.90	15.25	19.60	23.40
		1.5	6.53	8.73	10.80	13.33	17.50
		2.0	4.43	6.05	8.21	10.50	14.30
		2.5	3.13	4.57	6.60	9.15	13.00
		3.0	1.60	3.48	5.38	7.80	12.10
		3.5	1.14	1.83	4.50	6.71	10.85
		4.0	1.00	1.46	3.74	6.24	9.85
	75	0.5	14.73	16.70	20.20	25.00	27.60
		1.0	6.64	8.56	10.70	13.30	16.95
		1.5	3.96	5.48	7.30	10.00	13.20
		2.0	2.48	3.76	5.50	7.67	11.10
		2.5	1.19	2.61	4.23	6.52	9.75
		3.0	1.00	1.87	3.39	5.73	8.72
		3.5	1.00	1.09	2.79	4.96	8.28
		4.0	1.00	1.00	2.37	4.54	7.57

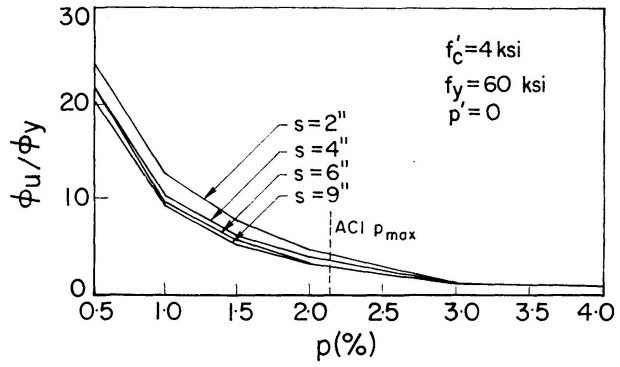

Fig. 15. Effect of tie spacing on ductility: ϕ_u/ϕ_y-p diagrams.

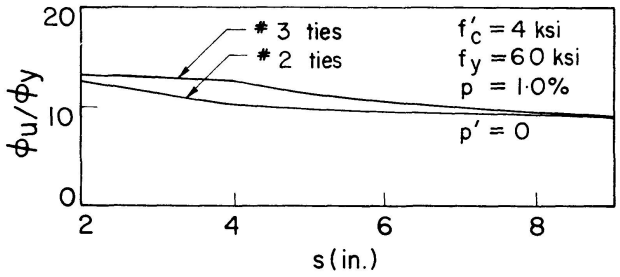

Fig. 16. Effect of tie size on ductility: ϕ_u/ϕ_y-p diagrams.

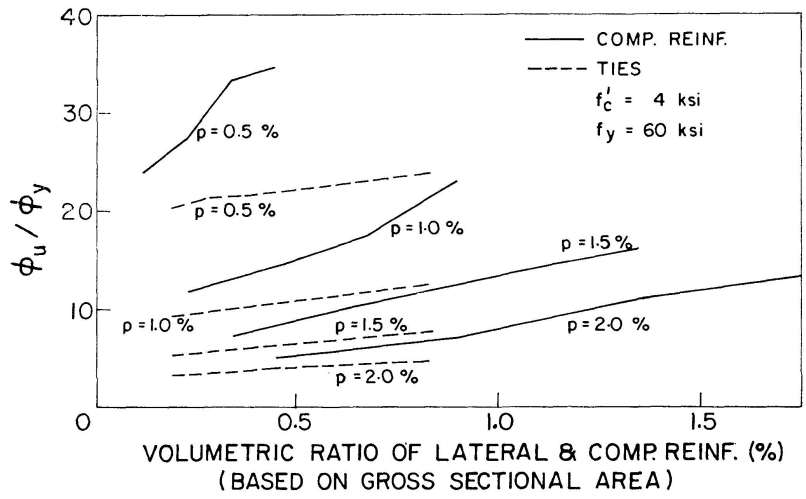

Fig. 17. Relative effect of compression and lateral reinforcements on ductility.

this is not a very effective way to improve ductility. Fig. 16 shows that ductility increases slightly with an increase in the cross-sectional area of lateral reinforcement, at all tie spacings.

Fig. 17 illustrates the relative efficiency of compression and lateral reinforcements in improving the ductility of reinforced concrete sections. It can be seen clearly that compression reinforcement is considerably more efficient than ties at all percentages of tension reinforcement. In a recent investigation, [18] Shah and Vijay Rangan studied the relative efficiency of compression

reinforcement, rectangular ties and randomly oriented short steel fibres in improving the ductility of compression concrete in flexural members. Rectangular ties were found to be by far the most efficient among the three. This conclusion may seem to be contradictory to that suggested by Fig. 17. It has been pointed out, however, that this is not the case [19]. As has been mentioned while discussing various ductility definitions, the ductility of steel and concrete as materials is very different from the ductility of a reinforced concrete section.

Fig. 18 shows the effect of cover thickness on sectional $M-\phi$ relationships. $\phi_u/\phi_y - p$ diagrams for different thicknesses of cover are plotted in Fig. 19. It can be seen that the influence of cover thickness on sectional ductility is negligible.

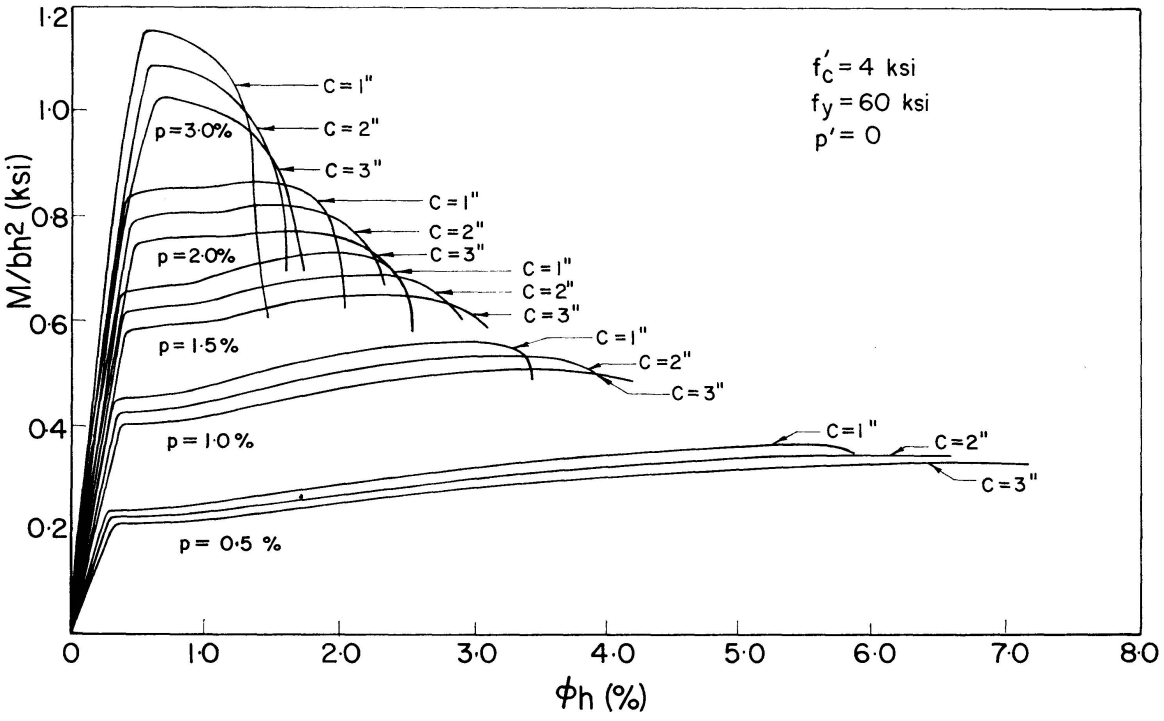

Fig. 18. Effect of concrete cover on ductility: M-ϕ diagrams.

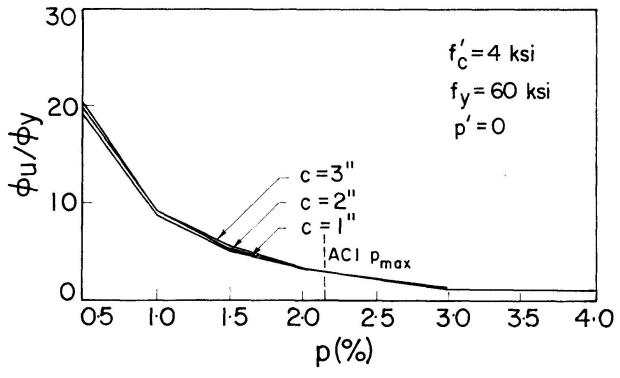

Fig. 19. Effect of concrete cover on ductility: ϕ_u/ϕ_y-p diagrams.

Loading Variables

In creep analysis, the major factors are the rate of loading, loading duration and the age of concrete at the time of loading. Since control of the rate of loading is difficult in actual structures, a conventional loading rate should be adopted. A practical proposal, due to RÜSCH [25] and adopted in this study, is to assume that the load is applied in about 20 minutes at constant rates and sustained subsequently up to failure. The age of concrete at the time of loading was assumed to be 28 days for all the sections studied. Fig. 20 illustrates $M-\phi$ relationships for different *durations of loading*, corresponding to various percentages of tension reinforcement. ϕ_u/ϕ_y-p diagrams are plotted for different loading durations in Fig. 21. It can be seen that the effect of creep

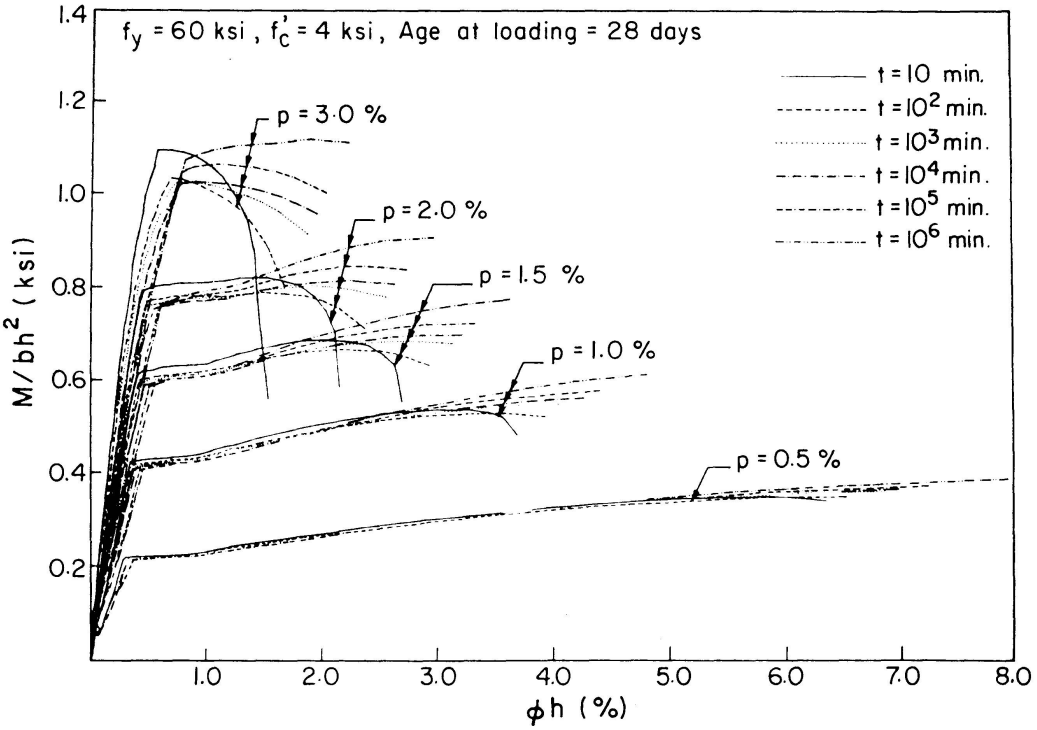

Fig. 20. Effect of loading duration on ductility: M-ϕ diagrams.

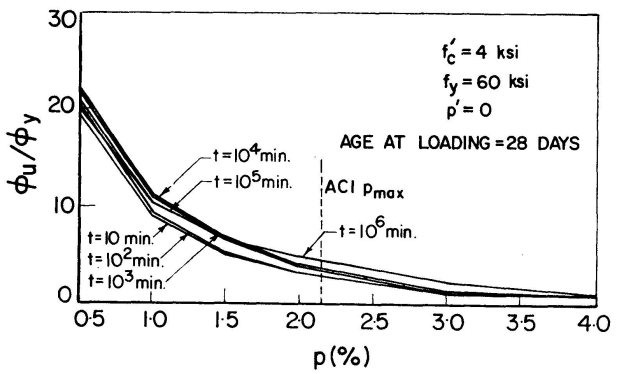

Fig. 21. Effect of loading duration on ductility: ϕ_u/ϕ_y-p diagrams.

on ductility is, in general, favourable, although for low reinforcement percentages, ductility drops a little when loading duration exceeds 10^4 min. ($\doteq$ 1 week). On the whole, the effect of loading duration on ductility is found not to be very significant.

Fig. 22 shows the effect of *axial loading* on sectional $M-\phi$ relationships for a particular quality of concrete and of reinforcing steel and for various amounts of reinforcement. $\phi_u/\phi_y - p\,(=p')$ diagrams for various levels of axial load and various qualities of steel and concrete are plotted in Fig. 23 for symmetrically reinforced rectangular sections. Load-moment interaction diagrams for sections with $f'_c = 4$ ksi, $f_y = 60$ ksi and different $p = p'$ are illustrated

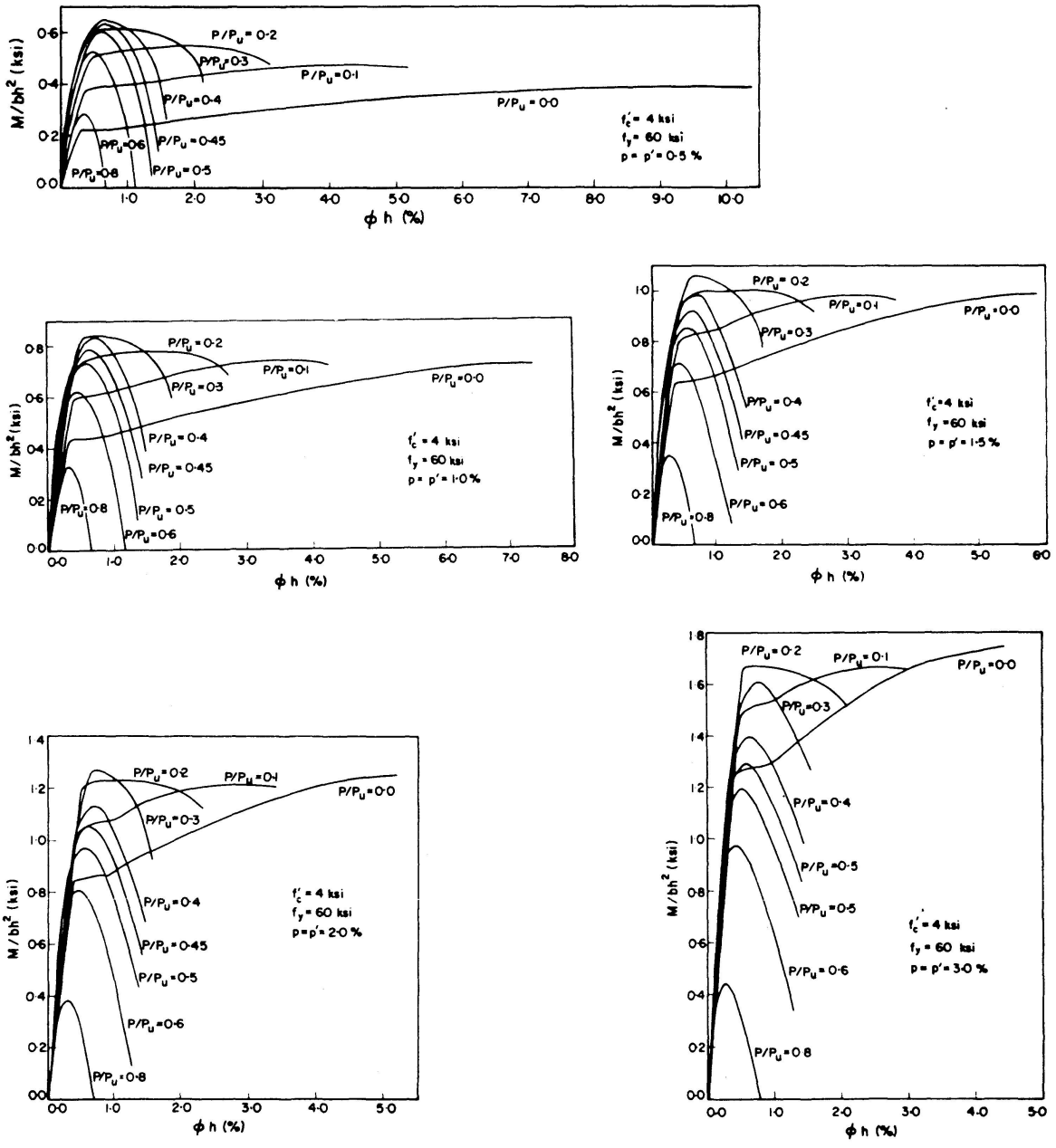

Fig. 22. Effect of axial loads on ductility: M-ϕ diagrams.

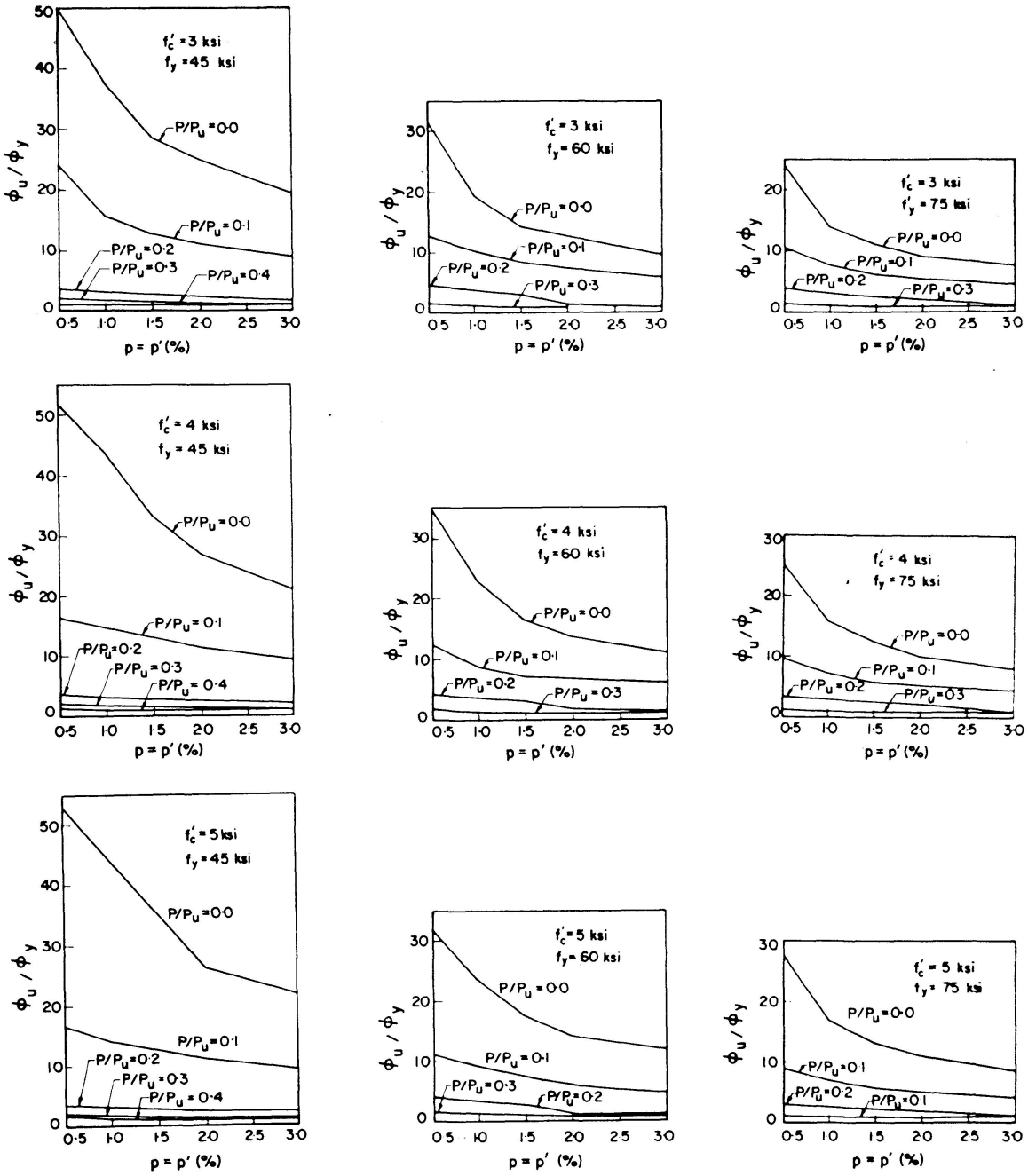

Fig. 23. Effect of axial loads on ductility: ϕ_u/ϕ_y-p diagrams.

(in full lines) in Fig. 24. The shape of these diagrams in the region which corresponds to tension failure is to be noted. This shape is a consequence of the ultimate stage definition adopted in this study. The interaction diagrams drawn in full lines change to those indicated by dotted lines when the ultimate stage is defined by the extreme compression fibre strain reaching a value of 0.3%. Fig. 24 indicates that sectional behaviour is governed by tension only as long as axial load levels do not exceed 20 to 35% (depending upon the amount of reinforcement) of the axial load carrying capacity of the section. Fig. 23 indicates that as long as failure is governed by tension, a section is

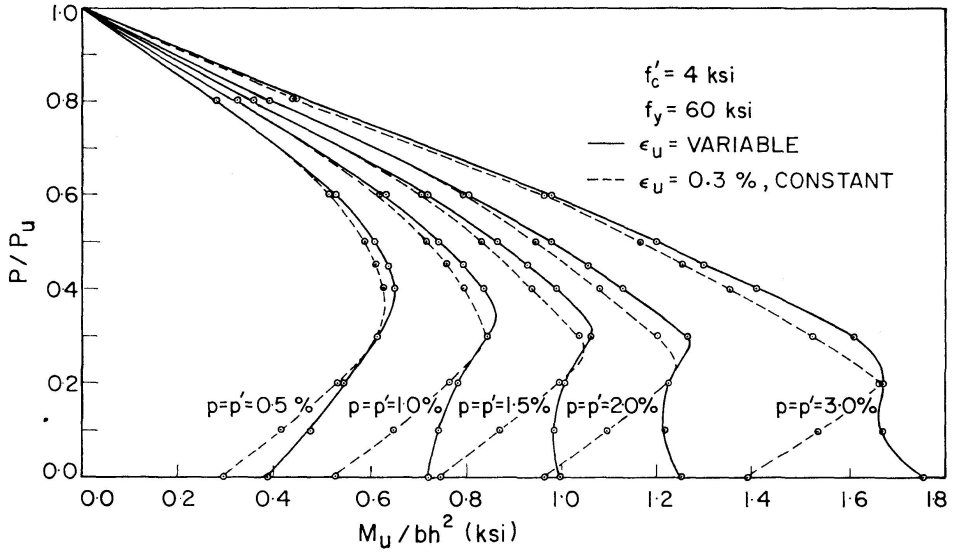

Fig. 24. Interaction diagrams for symmetrically reinforced sections.

capable of mobilizing a certain amount of ductility, although this decreases drastically as the axial load on the section approaches the level corresponding to balanced failure. Fig. 23 also indicates that for the low levels of axial load usually carried by flexural members in reinforced concrete frames (not exceeding 10–15% of the axial load carrying capacity), fairly high amounts of sectional ductility are always available.

The effects of *repeated loading and load reversals* were not investigated by the authors. They would like, however, to refer here to an experimental investigation into these effects carried out by NEWMARK and HALL [10]. Several singly and doubly reinforced beams were tested such that the load on each beam was removed completely and then reapplied at several stages during a test. The results indicated that the removal and reapplication of load had little or no effect on either the load carrying capacity or the ductility. A few symmetrically reinforced beams were tested under repeated reversals of load. There were some indications that while load carrying capacity remained unchanged, ductility was impaired, albeit only slightly, by such repeated load reversals.

Summary and Conclusions

The findings of the present investigation can be summarized as follows:

1. The various factors affecting the ductility of a reinforced concrete section can be divided into three groups: material, geometric and loading variables.

2. a) Among the material factors, the quality of concrete and the grade of reinforcement appear to be the most important. Sectional ductility increases with higher concrete grades and lower tension reinforcement strengths.

b) Sectional ductility increases as the strain-hardening modulus of tension

reinforcement, E_{sh}, is increased from zero to a certain value, but then decreases as E_{sh} is further increased.

c) Ductility is the highest for sections with full bond.

d) The tensile strenght of concrete does not appreciably affect sectional ductility.

3. a) Among the geometric variables, sectional width and depth do not appear to affect sectional ductility.

b) The overhanging flange areas of T-sections improve sectional ductility considerably.

c) The ductility of a section decreases as the amount of tension reinforcement increases, very little ductility being available as p approaches the balanced steel percentage.

d) Sectional ductility can be improved by decreasing the spacing and increasing the amount of lateral reinforcement, and also by the addition of suitable amounts of compression reinforcement. The latter is found to be much more efficient than the former in providing sectional ductility. When an improved ductility is desired, the addition of suitable amounts of compression reinforcement seems to be the best way to provide it.

e) The influence of cover thickness on sectional ductility appears to be negligible.

4. Among the loading factors, only the effects of duration of loading and of axial loading are studied in detail.

a) The effect of loading duration on sectional ductility is found not to be very significant.

b) A section is found capable of mobilizing some ductility as long as failure is governed by tension, although the amount of this available ductility decreases drastically as the level of axial load approaches that corresponding to balanced failure. However, fairly high amounts of sectional ductility are found to be available for sections subject to axial loads in the order of 10–15% of their carrying capacities.

The following conclusions can be drawn from this study:

1. The ductility of reinforced concrete sections in bending is primarily influenced by p, p', f'_c and f_y. Other variables have a secondary effect. (However, the amount and distribution of lateral reinforcement have an essential role in improving shear behaviour and preventing premature shear failure.)

2. The ductility factor is significantly reduced for high grade steels. However, when such steels are combined with relatively high grade concretes, the ductility factor is sufficiently large to accommodate plastic redistribution for usual, economical steel percentages. (For $\phi_u/\phi_y \geqq 5$ with $f_y = 75\,\text{ksi}$, $f'_c = 5\,\text{ksi}$ and $p' = 0$, $p \doteq 1.4\%$ follows.)

3. Since most reinforced concrete sections contain some compression rein-

forcement (because of construction or code requirements), the available ductility is usually adequate and larger than it would appear.

4. If a minimum value of $\phi_u/\phi_y = 5$ is accepted as a prerequisite for practical inelastic design, plastic action can be permitted in reinforced concrete columns, provided that the sections fail in tension under combined bending and compression.

Notations

A $E_c \epsilon_0 / k_3 f'_c$.
A_s area of tension steel.
A'_s area of compression steel.
b width of section.
c thickness of cover.
C_c resultant force in compression concrete.
C_s resultant force in compression steel.
d effective depth or depth of tension steel from extreme compression fibre.
d' depth of compression steel from extreme compression fibre.
d'' tie diameter.
D parameter of compression concrete stress-strain relationship.
e' eccentricity of external load from centroid of tension steel.
e_p proof strain of high strength steel.
E_c initial tangent modulus of elasticity of concrete.
E_s modulus of elasticity of steel.
E_{sh} strain-hardening modulus of steel.
EI $dM/d\phi = \Delta M/\Delta \phi$, flexural rigidity of section.
f'_c standard cylinder strength of concrete.
f_y yield strength of steel.
F $\epsilon_s k/\epsilon_c (1-k)$, bond factor.
h total depth of section.
k relative depth of neutral axis.
k_2 parameter indicating position of resultant compression concrete force.
k_3 ratio of maximum stress to cylinder strength.
M sectional moment.
M_u ultimate moment.
p A_s/bd, tension reinforcement ratio.
p' A'_s/bd, compression reinforcement ratio.
p_{max} maximum permissible tension reinforcement ratio.
P axial load on section.
P_u ultimate load.
s spacing of lateral reinforcement.
t loading duration in minutes.
T_c resultant force in tension concrete.
T_s resultant force in tension steel.

x ϵ/ϵ_0.
y distance of a sectional fibre away from neutral axis.
y_t depth of uncracked area in tension from neutral axis.
ϵ longitudinal strain, specifically compressive strain in concrete.
ϵ_0 compression concrete strain corresponding to maximum stress.
ϵ_p $e_p + \sigma_p/E_s$.
ϵ_s strain in tension steel.
ϵ'_s strain in compression steel.
ϵ_{sh} steel strain at the onset of strain-hardening.
ϵ_t tensile strain in concrete.
ϵ_{tr} cracking strain of concrete.
ϵ_u ultimate strain, specifically in compression concrete.
ϵ_y yield strain, specifically in compression concrete.
σ compressive stress in concrete.
σ_p proof stress of high strength steel.
σ_s stress in tension steel.
σ'_s stress in compression steel.
σ_t tensile stress in concrete.
σ_{tr} modulus of rupture of concrete.
ϕ sectional curvature.
ϕ_u curvature corresponding to ultimate moment.
ϕ_y curvature corresponding to yield moment.

Acknowledgments

This paper is part of an investigation on the "Inelastic Behaviour of Reinforced Concrete Structures" in progress in the Solid Mechanics Division and the Department of Civil Engineering, University of Waterloo, Waterloo, Ontario, Canada.

The financial support of the National Research Council of Canada, under Grants A-4789 and D-10, is gratefully acknowledged.

References

1. Bach, C., and Graf, O.: Investigations on Reinforced Concrete Beams Concerning the Moment-Curvature Relation. Parts I and II, Deutscher Ausschuss für Eisenbeton, Hefte 38 und 45, Verlag W. Ernst & Sohn, Berlin, 1917 und 1920 (in German).
2. Provisions for the Analysis of Redundant Reinforced Concrete Structures Allowing for the Redistribution of Stresses. 2nd Edition, Gosstrojizdat, Moscow, 1961 (in Russian); translation of the 1st Edition, Bulletin d'Information du CEB, No. 28, Paris, 1960.

3. Deutscher Normenausschuss für Stahlbeton: Specifications for the Construction of Reinforced Concrete Structures. DIN 1045, 4th Ed., Verlag W. Ernst & Sohn, Berlin, November 1959 (in German).
4. CEB-FIP Joint Committee: International Recommendations for the Design and Construction of Concrete Structures. Cement and Concrete Association, London, June 1970.
5. British Standards Institution: Draft British Standard Code of Practice for the Structural Use of Concrete. BSI, London, 1969.
6. Winter, G.: Whither Inelastic Concrete Design? Proceedings of the International Symposium on the Flexural Mechanics of Reinforced Concrete, Miami, Fla., November 1964, pp. 581–585.
7. Cohn, M. Z.: Why Nonlinear Analysis and Design. Proceedings of the International Symposium on the Flexural Mechanics of Reinforced Concrete, Miami, Fla., November 1964, pp. 591–594.
8. Sargin, M.: Stress-Strain Relationship for Concrete and the Analysis of Structural Concrete Sections. Study No. 4, Solid Mechanics Division, University of Waterloo, Waterloo, Ontario, Canada, 1971, 167 p.
9. Roy, H. E. H., and Sozen, M. A.: Ductility of Concrete. Proceedings of the International Symposium on the Flexural Mechanics of Reinforced Concrete, Miami, Fla., November 1964, pp. 213–224.
10. Newmark, N. M., and Hall, W. J.: Dynamic Behavior of Reinforced and Prestressed Concrete Buildings under Horizontal Forces and the Design of Joints (Incl. Wind, Earthquake, Blast Effects). Preliminary Publication, 8th Congress, International Association for Bridge and Structural Engineering, New York, September 1968, pp. 585–613.
11. Blume, J. A., Newmark, N. M., and Corning, L. H.: Design of Multistory Reinforced Concrete Buildings for Earthquake Motions. Portland Cement Association, Skokie, Illinois, 1961, 318 p.
12. Blume, J. A.: Design of Earthquake-Resistant Poured-in-Place Concrete Structures. Ch. 18 of "Earthquake Engineering", Wiegel, R. L., ed., Prentice-Hall, Inc., Edgewood Cliffs, N.J., 1970, pp. 449–474.
13. Entrican, G. C.: Detailing for Ductility in Reinforced Concrete Frames Subject to Earthquake Forces. The Structural Engineer, Vol. 43, No. 8, August 1965, pp. 249–254.
14. Pfrang, E. O., Siess, C. P., and Sozen, M. A.: Load-Moment-Curvature Characteristics of Reinforced Concrete Cross Sections. ACI Journal, Proceedings Vol. 61, No. 7, July 1964, pp. 763–778.
15. Park, R.: Ductility of Reinforced Concrete Frames under Seismic Loading. New Zealand Engineering, Vol. 23, No. 11, Wellington, November 15, 1968, pp. 427–435.
16. Sampson, R. A.: Ductility of Reinforced Concrete Columns. M. Eng. thesis, University of Canterburry, Christchurch, N.Z., 1971.
17. Abbasi, A. F., and Siess, C. P.: Effect of Stress-Strain Characteristics of High-Strength Reinforcement on the Behavior of Reinforced Concrete Beam-Columns. Structural Research Series No. 354, Civil Engineering Studies, University of Illinois, Urbana, September 1969, 374 p.
18. Shah, S. P., and Vijay Rangan, B.: Effects of Reinforcements on Ductility of Concrete. Journal of the Structural Division, ASCE, Vol. 96, No. ST 6, Proc. Paper 7366, June 1970, pp. 1167–1183.
19. Ghosh, S. K.: Discussion of Ref. 18, Journal of the Structural Division, ASCE, Vol. 97, No. ST 3, Proc. Paper 7944, March 1971, pp. 988–989.

20. Americal Society of Civil Engineers: Plastic Design in Steel. A Guide and Commentary. ASCE Manual No. 41, New York, 1971.
21. Cohn, M. Z., and Petcu, V. A.: Moment Redistribution and Rotation Capacity of Plastic Hinges in Redundant Reinforced Concrete Beams. Indian Concrete Journal, Vol. 37, No. 8, Bombay, August 1963, pp. 282–290.
22. Cohn, M. Z.: Rotation Compatibility in the Limit Design of Reinforced Concrete Continuous Beams. Proceedings of the International Symposium on the Flexural Mechanics of Reinforced Concrete, Miami, Fla., November 1964, pp. 359–382.
23. American Concrete Institute: Building Code Requirements for Reinforced Concrete. ACI 318-71, Detroit, Mich., November 1971.
24. Hognestad, E.: A Study of Combined Bending and Axial Load in Reinforced Concrete Members. Bulletin No. 399, Engineering Experiment Station, University of Illinois, Urbana, November 1951, 128 p.
25. Rüsch, H.: Researches Toward a General Flexural Theory for Structural Concrete. ACI Journal, Proceedings Vol. 57, No. 1, July 1960, pp. 1–28.
28. Ghosh, S. K., and Cohn, M. Z.: Effect of Creep on the Flexural Strength and Deformation of Structural Concrete. Preliminary Publication, IABSE Symposium on the Design of Concrete Structures for Creep, Shrinkage and Temperature Changes, Madrid, September 1970, pp. 207–216.
27. Baker, A. L. L.: Limit-State Design of Reinforced Concrete. Cement and Concrete Association, London, 1970.
28. Corley, W. G.: Rotational Capacity of Reinforced Concrete Beams. Journal of the Structural Division, ASCE, Vol. 92, No. ST 5, Proc. Paper 4939, October 1966, pp. 121–146.

Summary

An analytical investigation simulating tests on some 1700 specimens is performed, in order to evaluate the effect of a large number of factors on the ductility of reinforced concrete sections in pure and combined bending.

The analysis is based on reliable stress-strain characteristics for steel and concrete and enables moment-curvature and ductility factor-steel percentage diagrams to be prepared for a broad range of combinations of the variables.

The study demonstrates that reinforced concrete sections possess a significant amount of ductility which can be used advantageously within a wide spectrum of design variables.

Résumé

Une étude analytique simulant environ 1700 essais est effectuée afin de trouver l'influence d'un grand nombre de facteurs sur la capacité de déformation des sections en béton armé sous flexion pure et composée.

L'analyse est basée sur des diagrammes contraintes-déformations éprouvés pour l'acier et le béton. Elle offre la possibilité de trouver pour beaucoup de combinaisons de variables les diagrammes moments-courbures et les diagrammes capacité de déformation-pourcentage d'acier.

L'étude montre que les sections en béton armé possèdent une capacité de déformation accentuée dont on peut profiter dans un large spectre des variables.

Zusammenfassung

Es wird eine analytische Untersuchung, die Versuche an ungefähr 1700 Proben simuliert, durchgeführt, um den Einfluss einer Grosszahl von Faktoren auf die Verformungsfähigkeit armierter Betonquerschnitte unter reiner sowie zusammengesetzter Biegung zu ermitteln.

Die Berechnung beruht auf zuverlässigen Spannungs-Dehnungs-Diagrammen für Stahl und Beton und ermöglicht das Erstellen der Momenten-Krümmungs- sowie der Verformungsfaktor-Stahlgehalt-Diagramme für viele Kombinationsmöglichkeiten der Variablen.

Die Studie zeigt, dass armierte Betonquerschnitte eine ausgeprägte Verformungsfähigkeit besitzen, welche innerhalb eines breiten Spektrums von konstruktiven Annahmen vorteilhaft ausgenützt werden kann.

Leere Seite
Blank page
Page vide

Über die Stärke und Steifigkeit von Kastenträgern mit Rechteckquerschnitt

About Strength and Stiffness of Rectangular Box-Girders

Résistance et rigidité de poutres en caisson rectangulaire

J. D. JANSSEN
Prof. Dr. Ing.

F. E. VELDPAUS
Ing.

Laboratorium für Technische Mechanik, Technische Hochschule Eindhoven NL

1. Einleitung

Das mechanische Verhalten (dünnwandiger) Kastenträger lässt sich in bestimmten Fällen – wovon Fig. 1.1 einige Beispiele gibt – mit Hilfe der elementaren Bernoullischen und Bredtschen Biegungs- und Torsionstheorie nicht genügend exakt beschreiben.

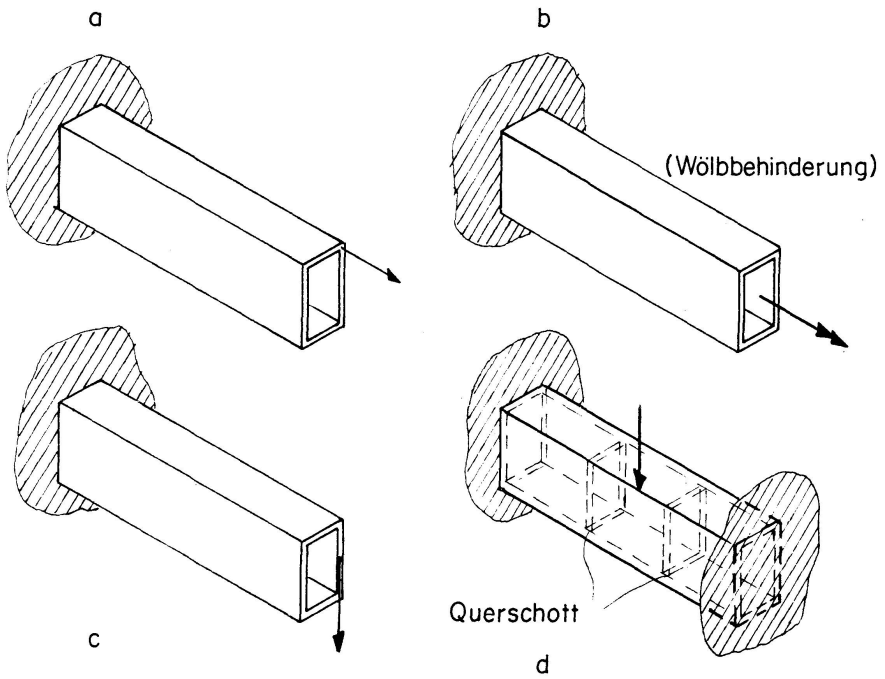

Fig. 1.1. Beispiele für welche die Theorien von Bredt und Bernoulli nicht genügen.

Nach der Bredtschen Theorie treten axiale Verschiebungen des Querschnitts auf, wenn der Träger mit einem Torsionsmoment (Fig. 1.1b) belastet wird. Behinderung dieser Verwölbung wird u. a. das Auftreten axialer Normalspannungen und zusätzlicher Schubspannungen zur Folge haben.

In bestimmten Belastungssituationen – siehe z. B. Fig. 1.1c und Fig. 1.1d – wird ausserdem eine Änderung der Form des Querschnitts stattfinden: das Schiefziehen der Profillinie.

Es gibt eine ganze Reihe eindimensionaler Theorien für dünnwandige Kastenträger, bei denen man den Einfluss der Querschnittsverwölbung berücksichtigt. Oft lässt man dabei die Wirkung des Schiefziehens ausser Betracht, siehe z. B. D. WILLIAMS [1], W. FLÜGGE und K. MARGUERRE [2], R. HEILIG [3], C. KOLLBRUNNER und N. HAJDIN [4]. Experimentell kann klargestellt werden, dass dies öfters nicht den Tatsachen entspricht [5]. Selbstverständlich wäre es möglich, die Wirkung des Schiefziehens hinreichend zu reduzieren, wenn man genügend Querschotte im Träger einbaut. Diese Situation wird aber nicht immer auftreten.

Zwar ist u. a. von JANSSEN [5], DABROWSKI [6], VLASOV [7], LACHER [8], RESINGER [9] und CSONKA [10] eine Theorie angegeben worden, bei der sowohl die Wirkung der Verwölbung als des Schiefziehens des Querschnitts wohl berücksichtigt wird. Ein Vergleich dieser Theorien ist jedoch nicht Zweck dieser Arbeit.

Mit Hilfe der klassischen Theorie für Plattenbiegung und durch genaue Experimente hat JANSSEN [5] bewiesen, dass die in [5] präsentierte Modifikation der Vlasovschen Theorie [7] die Realität zur Genüge darstellt. Aus dieser modifizierten Vlasov-Theorie ergibt sich u. a., dass eine bessere Beschreibung der Biegespannungen möglich ist als mit [7]. Deshalb beschränkt sich diese Arbeit auf die von Janssen aufgestellte Theorie. Wendet man seine auf dem Prinzip der minimalen potentiellen Energie basierte Arbeitsweise an, so bleiben die Berechnungen übersichtlich und systematisch. Wir werden danach streben, die wichtigsten Ergebnisse in eine für den Praktiker nutzbare Form darzustellen.

Hierbei werden wir uns auf zylindrische Kastenträger mit Rechteckquerschnitt und zwei Symmetrieachsen beschränken. Obwohl diese Beschränkungen nicht wesentlich sind, so sind sie doch mehr oder weniger notwendig, um zu einer Theorie zu gelangen, die auch analytisch handlich ist. Bei einem beliebigen Querschnitt ist es zweckmässiger, einem numerischen Weg zu folgen, etwa mit Hilfe der Methode der finiten Elemente [11].

Der Belastungszustand in einem Endquerschnitt des Trägers ist in den Theorien nach Bernoulli-Navier und Bredt völlig charakterisiert durch die Normalkraft, die Querkräfte, die biegenden Momente und das Torsionsmoment. Berücksichtigt man aber die Verwölbung und das Schiefziehen des Querschnitts, so werden auch die in Fig. 1.2 gezeichneten Gleichgewichtssysteme von grosser Wichtigkeit sein.

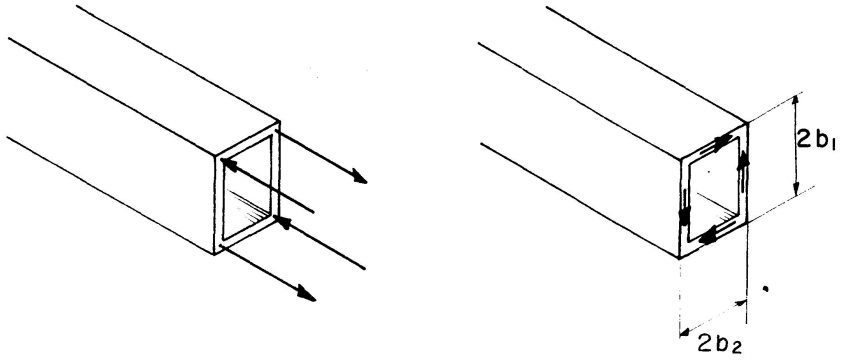

Fig. 1.2. Gleichgewichtssysteme.

In dieser Arbeit werden für einige spezifische Belastungen die Differenzen untersucht, die zwischen der Theorie für Träger mit starrem Querschnitt einerseits und mit verformbarem Querschnitt anderseits auftreten. Dabei möchten wir uns auf Belastungssysteme beschränken, die hinsichtlich der beiden Symmetrieflächen des Trägers antimetrisch sind, wie z. B. ein Torsionsmoment oder die in Fig. 1.2 gezeichneten Kräftesysteme. Eine eventuelle Belastung der zylindrischen Oberfläche des Trägers bleibt ausser Betracht, es sei vielmehr auf die in [5], [7] und [8] präsentierten Arbeitsweisen hingewiesen.

2. Bezeichnungen

2.1. Koordinaten (siehe Fig. 2.1)

x	Längsachse.
y, z	Querschnittshauptachsen.
s	Konturordinate.

2.2. Geometrische Daten (siehe Fig. 2.1)

b_1, b_2	halbe Höhe, bzw. halbe Breite.
$t_1, t_2, t(s)$	Wandstärke.

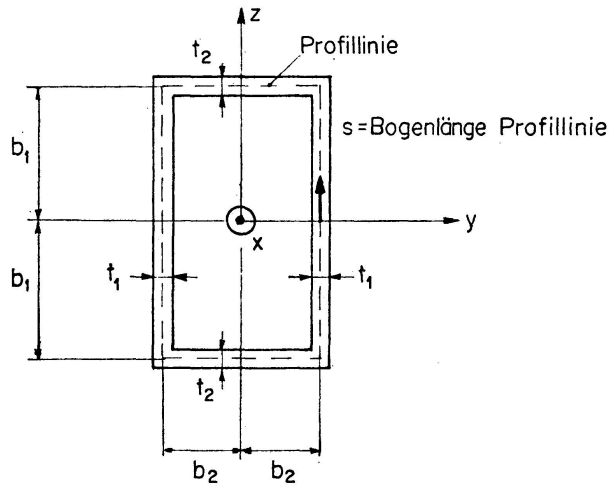

Fig. 2.1. Querschnitt des Trägers; Koordinatensystem.

l Länge des Trägers.
F Querschnittsfläche; $F = 4(b_1 t_1 + b_2 t_2)$.

2.3. *Werkstoffdaten*

E Elastizitätsmodul.
G Schubmodul.
ν Querdehnungszahl.

2.4. *Verschiebungsfunktionen (siehe Fig. 2.2)*

$u(x, s)$ Verschiebung in axialer Richtung.
$v(x, s)$ Verschiebung in Richtung der Konturordinate.
$\beta(x)$ Verwölbungsfunktion.
$\theta(x)$ Verdrehung des Querschnitts.
$\kappa(x)$ Verformungswinkel der Profillinie.
$\phi(s)$ Verschiebung u wenn $\beta(x) = 1$.
$h(s)$ Verschiebung v wenn $\theta(x) = 1$, $\kappa(x) = 0$.
$m(s)$ Verschiebung v wenn $\theta(x) = 0$, $\kappa(x) = 1$.

2.5. *Spannungen und Kraftgrössen (siehe Fig. 2.2)*

$\sigma(x, s)$ axiale Membrannormalspannung.
$\tau(x, s)$ Membranschubspannung.
$\tau_1(x, s), \tau_2(x, s)$ Membranschubspannungen in Platte 1, bzw. Platte 2.
$\sigma_s(x, s)$ Biegespannung.
$\sigma_{id}(x, s)$ Vergleichsspannung.
$\bar{\sigma}(s), \bar{\tau}(s)$ vorgeschriebene Spannungen im Endquerschnitt.
$M(x)$ Torsionsmoment.
$B(x), Q(x)$ axiales, bzw. transversales Bimoment.
$\bar{B}, \bar{M}, \bar{Q}$ vorgeschriebene Belastung im Endquerschnitt.
$M_{1x}(x, s)$ Biegemoment pro Längeneinheit im Querschnitt.
$M_{1s}(x, s)$ Biegemoment pro Längeneinheit im Längsschnitt.

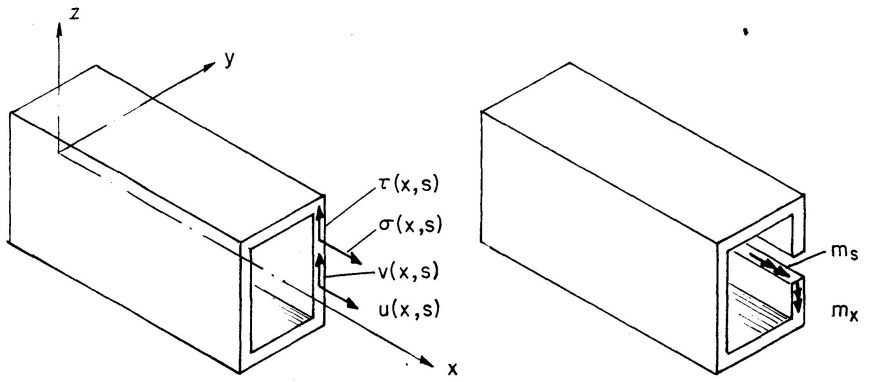

2.2. Spannungen und Verschiebungen.

2.6. Steifigkeitsdaten

a_1, a_2, a_3, a_4		Steifigkeiten nach (3.13), (3.14), (3.15), (3.21).
c		Steifigkeit nach (4.4).
α_0^4	=	$\frac{1}{4}\frac{c}{a_1}$.
ϵ^2	=	$\frac{1}{16}\frac{a_1 c}{a_4^2}$.
λ^2	=	$\frac{a_4}{a_1}$.
μ	=	$\frac{a_3}{a_2}$.
α^2	=	$\alpha_0^2(1+\epsilon)$.
γ^2	=	$\alpha_0^2(1-\epsilon)$.
δ^2	=	$1-\epsilon^2$.

2.7. Indizien

s	für Theorie mit starrer Profillinie.
f	für Theorie mit verformbarer Profillinie.
b	für Theorie nach Bredt.

2.8. Sonstige Symbole

V		potentielle Energie.
l_0		charakteristische Länge des Trägers nach (6.1) und (6.2).
ϕ_1	=	$\cosh(\alpha x)\sin(\gamma x)$.
ϕ_2	=	$\cosh(\alpha x)\cos(\gamma x)$.
ϕ_3	=	$\sinh(\alpha x)\cos(\gamma x)$.
ϕ_4	=	$\sinh(\alpha x)\sin(\gamma x)$.
$(\,)'$		$\frac{d}{dx}(\,)$.

3. Träger mit starrer Profillinie

Analog [5] stützt sich die Theorie auf das Prinzip der minimalen potentiellen Energie, mit der ein übersichtliches, gut fundiertes und konsistentes Näherungsverfahren entsteht, das mit dem u. a. in [3] präsentierten Verfahren übereinstimmt.

Um nicht nur kinematische, sondern auch dynamische Randbedingungen mit einzubeziehen, betrachten wir einen Träger, der bei $x=0$ starr eingespannt ist und bei $x=l$ durch die Normalspannungen $\bar{\sigma}(s)$ und die Schubspannungen $\bar{\tau}(s)$, die gleichmässig über die Wandstärke verteilt sind, belastet ist. Selbstverständlich sollen $\bar{\sigma}$ und $\bar{\tau}$ den in der Einleitung erwähnten Antimetriebedingungen genügen, also:

$$\int_F \bar{\sigma}\, dF = 0, \qquad \int_F \bar{\sigma}\, y\, dF = \int_F \bar{\sigma}\, z\, dF = 0, \tag{3.1}$$

$$\int_F \bar{\tau} \frac{dy}{ds} dF = \int_F \bar{\tau} \frac{dz}{ds} dF = 0. \tag{3.2}$$

Die Theorie wird eindimensional, wenn das Modell der Verschiebungen im Querschnitt als bekannt vorausgesetzt wird. Für die Verschiebung in Richtung der Konturordinate, $v(x, s)$, setzen wir Unverformbarkeit der Profillinie voraus, wogegen das Modell für die axialen Verschiebungen sich auf die Bredtsche Torsionstheorie stützt. Dann gilt (siehe Fig. 2.2):

$$u(x, s) = \beta(x)\, \phi(s), \tag{3.3}$$

$$v(x, s) = \theta(x)\, h(s) \tag{3.4}$$

mit (siehe Fig. 3.1):

$$\phi(s) = y(s)\, z(s) \tag{3.5}$$

$$h(s) = \begin{cases} b_2 \text{ für } y = \pm b_2, \\ b_1 \text{ für } z = \pm b_1. \end{cases} \tag{3.6}$$

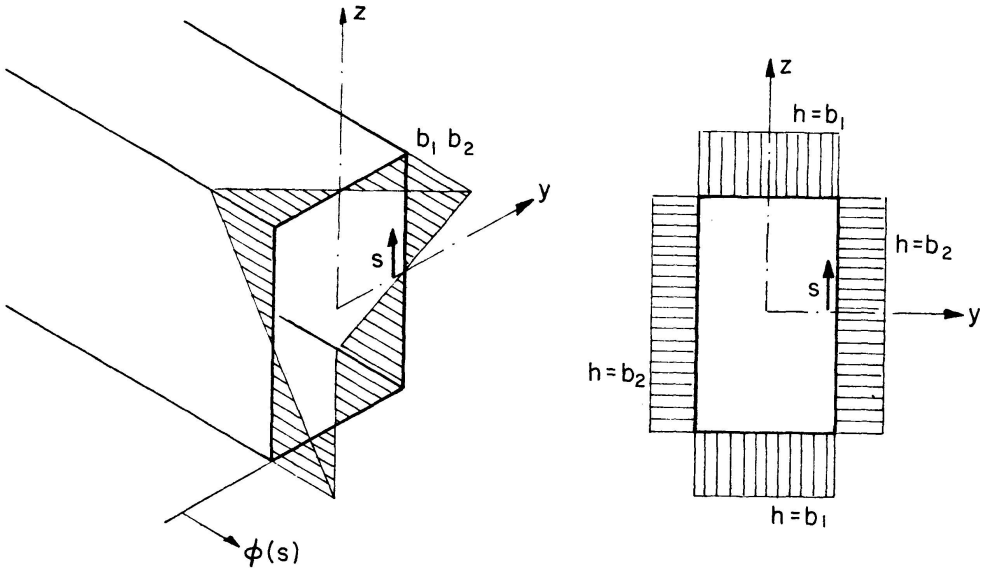

Fig. 3.1. Graphische Darstellung $\phi(s)$ und $h(s)$.

Da nur Membranspannungen auftreten, folgt mit der angegebenen Belastung für die potentielle Energie V des Trägers:

$$V = \frac{1}{2} \int_0^l \int_F \left\{ E \phi^2 (\beta')^2 + G \left(\beta \frac{\partial \phi}{\partial s} + h\, \theta' \right)^2 \right\} dF\, dx - \beta(l) \int_F \bar{\sigma}\, \phi\, dF - \theta(l) \int_F \bar{\tau}\, h\, dF. \tag{3.7}$$

Hieraus ergeben sich das axiale Bimoment $\overline{B}$ und das Torsionsmoment $\overline{M}$ als wichtige Spannungsresultanten der Belastung im Querschnitt $x = l$:

$$\overline{B} = \int_F \bar{\sigma}(s)\, \phi(s)\, dF, \tag{3.8}$$

$$\overline{M} = \int_F \bar{\tau}(s)\, h(s)\, dF. \tag{3.9}$$

Analog (3.8) und (3.9) definieren wir das axiale Bimoment $B(x)$ und das Torsionsmoment $M(x)$ in einem beliebigen Querschnitt:

$$B(x) = \int_F \sigma(x,s)\,\phi(s)\,dF, \tag{3.10}$$

$$M(x) = \int_F \tau(x,s)\,h(s)\,dF. \tag{3.11}$$

Mit der Substitution von (3.1) und (3.2) in (3.7) ergibt sich:

$$V = \tfrac{1}{2}\int_{x=0}^{l} [a_1(\beta')^2 + a_2\{\beta^2 + (\theta')^2\} + 2a_3\beta\theta']\,dx - \overline{B}\,\beta(l) - \overline{M}\,\theta(l), \tag{3.12}$$

wobei die Steifigkeitskonstanten a_1, a_2 und a_3 definiert werden durch:

$$a_1 = E\int_F \phi^2\,dF = \frac{4}{3}E\,b_1^2 b_2^2 (b_1 t_1 + b_2 t_2), \tag{3.13}$$

$$a_2 = G\int_F \left(\frac{d\phi}{ds}\right)^2 dF = G\int_F h^2\,dF = 4\,G\,b_1 b_2 (b_1 t_2 + b_2 t_1), \tag{3.14}$$

$$a_3 = G\int_F h\frac{d\phi}{ds}\,dF = 4\,G\,b_1 b_2(-b_1 t_2 + b_2 t_1). \tag{3.15}$$

Nach dem Prinzip der minimalen potentiellen Energie ist $\delta V = 0$ für alle zulässigen Variationen von β und θ, und hieraus folgen die Differentialgleichungen für $\beta(x)$ und $\theta(x)$:

$$-a_1\beta'' + a_2\beta + a_3\theta' = 0, \tag{3.16}$$

$$a_3\beta' + a_2\theta'' = 0 \tag{3.17}$$

und zwei dynamische Randbedingungen für $x = l$:

$$\overline{B} = a_1\beta'(x=l), \tag{3.18}$$

$$\overline{M} = a_2(\theta' + \mu\beta)_{x=l} = a_4\theta'(x=l) + \mu\,a_1\beta''(x=l), \tag{3.19}$$

wobei die dimensionslose Konstante μ angegeben wird durch:

$$\mu = \frac{a_3}{a_2} \tag{3.20}$$

und a_4 die spezifische Torsionssteifigkeit nach Bredt ist:

$$a_4 = \frac{a_2^2 - a_3^2}{a_2}. \tag{3.21}$$

Die Formeln (3.18) und (3.19) kann man auf jeden beliebigen Querschnitt x erweitern; sie stellen dann den Zusammenhang dar zwischen den Schnittgrössen $B(x)$ und $M(x)$ einerseits und den Verschiebungsgrössen $\beta(x)$ und $\theta(x)$ andererseits:

$$B(x) = a_1\beta'(x), \tag{3.22}$$

$$M(x) = a_4\theta'(x) + \mu\,a_1\beta''(x) = a_4\theta'(x) + \mu\,B'(x). \tag{3.23}$$

Im Zusammenhang mit den Berechnungen des vierten Kapitels für Träger mit verformbarem Querschnitt ist es angebracht, ausser $B(x)$ und $M(x)$, als dritte Schnittgrösse das transversale Bimoment $Q(x)$ zu definieren:

$$Q(x) = B'(x) = a_1 \beta'' = a_2 (\beta + \mu \theta'). \tag{3.24}$$

Aus (3.16) und (3.17) lässt sich eine Differentialgleichung in $\beta(x)$ ableiten:

$$\beta''' - \lambda^2 \beta' = 0, \tag{3.25}$$

wobei

$$\lambda^2 = \frac{a_4}{a_1}. \tag{3.26}$$

Die allgemeinen Lösungen für β, θ, B und M sind lineare Kombinationen der Funktionen 1, x, $\cosh(\lambda x)$ und $\sinh(\lambda x)$. Es gilt:

$$\beta(x) = -\mu c_2 + \lambda \{c_3 \cosh(\lambda x) + c_4 \sinh(\lambda x)\}, \tag{3.27}$$

$$\theta(x) = c_1 + c_2 x - \mu \{c_3 \sinh(\lambda x) + c_4 \cosh(\lambda x)\}, \tag{3.28}$$

$$B(x) = a_4 \{c_3 \sinh(\lambda x) + c_4 \cosh(\lambda x)\}, \tag{3.29}$$

$$M(x) = a_4 c_2. \tag{3.30}$$

In dieser letzten Gleichung kommt selbstverständlich zum Ausdruck, dass das Torsionsmoment M konstant ist, wenn der Träger nur im Endquerschnitt $x = l$ belastet ist. Die Integrationskonstanten c_1, c_2, c_3 und c_4 ergeben sich aus den Randbedingungen $\theta = 0$, $\beta = 0$ für $x = 0$ und $B = \bar{B}$, $M = \bar{M}$ für $x = l$.

Wenn der Trägerquerschnitt quadratisch ist (also $b_1 = b_2$, $t_1 = t_2$ und deshalb $a_3 = 0$), erhält man die Torsionstheorie nach Bredt. Diese Theorie erfolgt auch, wenn die Verwölbung in den Endquerschnitten $x = 0$ und $x = l$ nicht behindert wird (also $B(0) = B(l) = 0$).

Nach Berechnung von $B(x)$, $M(x)$ und $Q(x)$ können die damit zusammenhängenden Spannungen festgestellt werden. Mit dem Hookeschen Gesetz resultiert für die Normalspannung $\sigma(x, s)$ und die Schubspannung $\tau(x, s)$ in den Platten (siehe Fig. 2.2):

$$\sigma(x, s) = E \beta'(x) \phi(s) = \frac{E}{a_1} B(x) \phi(s), \tag{3.31}$$

$$\tau_1(x) t_1 = \frac{M + B'(x)}{8 b_1 b_2} = \frac{M + Q(x)}{8 b_1 b_2}, \tag{3.32}$$

$$\tau_2(x) t_2 = \frac{M - B'(x)}{8 b_1 b_2} = \frac{M - Q(x)}{8 b_1 b_2}. \tag{3.33}$$

JANSSEN [5] hat durch seine Forschung bewiesen, dass man eine bessere Verteilung der Schubspannungen erhält, wenn man axiales Gleichgewicht eines Elementes $t(s)\,dx\,ds$ aus den Trägerplatten voraussetzt. Dann ist das Resultat eine quadratische Verteilung der Schubspannungen für jede Platte. Die Spannungen nach (3.32) und (3.33) soll man als Mittelwerte über die diesbezügliche Platte betrachten. Was den Zweck dieser Arbeit betrifft, so sind die Resultate nach (3.32) und (3.33) hinreichend genau.

4. Träger mit deformierbarer Profillinie

Die Theorie im dritten Kapitel beruht auf der Voraussetzung, dass die Profillinie unverformbar ist. Wie aus (3.32) und (3.33) hervorgeht, treten ausser den Bredtschen Schubspannungen $\frac{M}{8b_1b_2t}$ noch zusätzliche Schubspannungen $\frac{Q}{8b_1b_2t}$ auf.

In Fig. 4.1 sind diese zusätzlichen Schubspannungen angegeben in den Querschnitten zur Stelle x_1 und x_1+dx.

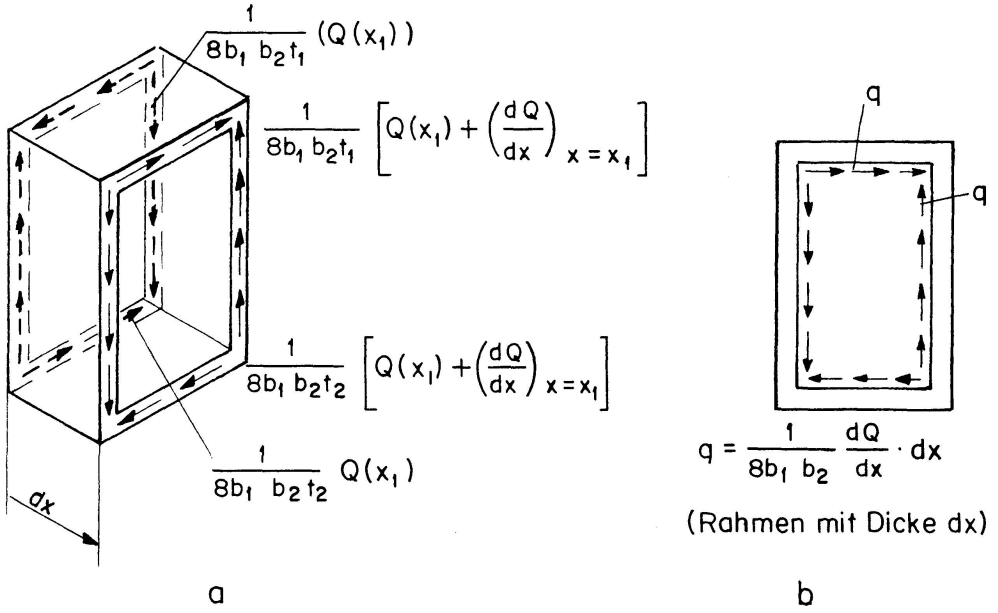

Fig. 4.1. Zusätzliche Schubspannungen.

Betrachtet man das Körperelement dx des Trägers als einen Rahmen, so wird dieser Rahmen infolge der zusätzlichen Schubspannungen belastet (siehe Fig. 4.1b). Nur wenn sich im diesbezüglichen Querschnitt ein Querschott befindet, das in seiner Ebene verhältnismässig steif ist, wird keine Verformung der Profillinie auftreten.

Es liegt nahe, das Deformationsmodell der Formänderung der Profillinie unter der skizzierten Belastung (Fig. 4.1b) zugrunde zu legen. Berücksichtigt man nur die Biegungsenergie, so nimmt die Profillinie die in Fig. 4.2 dargestellte Form an, die vom Winkel κ charakterisiert werden kann.

Für die Verschiebung in s-Richtung folgt dann:

$$v(x,s) = \theta(x)\,h(s) + \kappa(x)\,m(s) \tag{4.1}$$

mit:

$$m(s) = \begin{cases} b_2 & \text{für } y = \pm b_2, \\ -b_1 & \text{für } z = \pm b_1. \end{cases} \tag{4.2}$$

Überall wo $\phi(s)$ differenzierbar ist, zeigt sich:

$$m(s) = \frac{d\phi}{ds}. \tag{4.3}$$

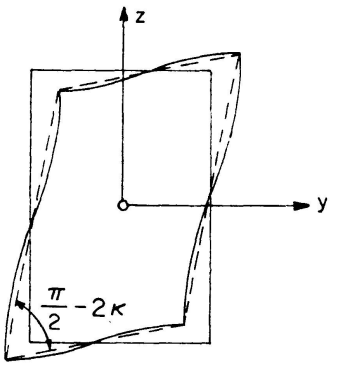

Fig. 4.2. Formänderung des Rahmens (schiefziehen).

Die Profilverformung kann in mehrfacher Weise berücksichtigt werden (siehe z. B. [5, 6, 7, 8]).

Dabrowski teilt die Berechnung auf. Mit der Hypothese, wonach κ gleich null ist, wird zunächst – in einem ganz anderen Verfahren als im dritten Kapitel – das transversale Bimoment $Q = Q(x)$, das die Querschnittstreue gewähren soll, bestimmt. Nachher wird die Verformbarkeit des Querschnitts wiederhergestellt und eine Differentialgleichung vierter Ordnung für den Verformungswinkel κ infolge der Belastung $-Q(x)$ abgeleitet.

Man wendet hier dasselbe Verfahren an wie in [5] und stützt sich deshalb auf das Prinzip der minimalen potentiellen Energie. Die interessanten Differentialgleichungen und die dynamischen Randbedingungen können dann leicht bestimmt werden.

Die axiale Verschiebung $u(x, s)$ wird in dieser Methode, wie auch im dritten Kapitel, durch (3.3) gegeben, während für die Verschiebung in s-Richtung (4.1) statt (3.4) benutzt wird. Dem Integral in (3.12), das die Formänderungsenergie im Träger angibt, soll jetzt ein Glied hinzugefügt werden, das von der mit κ charakterisierten Plattenbiegung stammt. Dazu berechnet man die Biegungsenergie in einem Rahmen, der sich in der Art und Weise deformiert, wie in Fig. 4.2 angegeben.

Die Integration dieser Energie der Länge des Trägers entlang zeigt, dass das zusätzliche Glied in (3.12) gleich $\frac{1}{2}\int_{x=0}^{l} c\,\kappa^2\,dx$ ist.

Unter Annahme der Behinderung der Querkontraktion im Falle einer Plattenbiegung ergibt sich für c:

$$c = \frac{4E}{1-\nu^2}\,\frac{t_1^3 t_2^3}{b_1 t_2^3 + b_2 t_1^3}. \tag{4.4}$$

Nach [5] führt diese Annahme zu hinreichend genauen Ergebnissen.

Ausser dem Torsionsmoment $M(x)$ und dem axialen Bimoment $B(x)$ tritt in dieser Theorie eine dritte Schnittgrösse auf: das transversale Bimoment $Q(x)$, das folgendermassen definiert wird:

$$Q(x) = \int_F \tau(x, s)\, m(s)\, dF. \tag{4.5}$$

Nachher wird es klar, dass diese Definition mit (3.24) konsistent ist. Als wichtige Belastungsgrösse im Endquerschnitt $x=l$ tritt, ausser $\overline{M}$ und $\overline{B}$, auch das transversale Bimoment $\overline{Q}$ auf:

$$\overline{Q} = \int_F \bar{\tau}(s)\, m(s)\, dF. \tag{4.6}$$

Die Formel für die potentielle Energie für einen bei $x=0$ eingespannten und bei $x=l$ von $\overline{M}$, $\overline{B}$ und $\overline{Q}$ belasteten Träger lautet:

$$\begin{aligned} V = \tfrac{1}{2}\int_{x=0}^{l} &[a_1(\beta')^2 + a_2\{(\beta+\kappa')^2 + (\theta')^2\} + 2a_3(\beta+\kappa')\theta' + c\kappa^2]\, dx \\ &-\beta(l)\,\overline{B} - \theta(l)\,\overline{M} - \kappa(l)\,\overline{Q}. \end{aligned} \tag{4.7}$$

Neben den schon im dritten Kapitel eingeführten Steifigkeitsgrössen a_1, a_2 und a_3 spielt in dieser Formel auch die Biegungssteifigkeit c eine Rolle. Aus $\delta V = 0$ für alle zulässigen Variationen von β, θ und κ folgen drei Differentialgleichungen und drei dynamische Randbedingungen für $x=l$:

$$-a_1\beta'' + a_2\beta + a_3\theta' + a_2'\kappa = 0, \tag{4.8}$$

$$a_3\beta' + a_2\theta'' + a_3\kappa'' = 0, \tag{4.9}$$

$$a_2\beta' + a_3\theta'' + a_2\kappa'' - c\kappa = 0, \tag{4.10}$$

$$\overline{B} = a_1\beta'(x=l), \tag{4.11}$$

$$\overline{M} = (a_3\beta + a_2\theta' + a_3\kappa')_{x=l}, \tag{4.12}$$

$$\overline{Q} = (a_2\beta + a_3\theta' + a_2\kappa')_{x=l}. \tag{4.13}$$

Für die Schnittgrössen $B(x)$, $M(x)$ und $Q(x)$ können analoge Gleichungen abgeleitet werden, wenn man einen Träger mit Länge x betrachtet. Es gilt:

$$B(x) = a_1\beta'(x), \tag{4.14}$$

$$M(x) = a_3\beta(x) + a_2\theta'(x) + a_3\kappa'(x), \tag{4.15}$$

$$Q(x) = a_2\beta(x) + a_3\theta'(x) + a_2\kappa'(x). \tag{4.16}$$

Die Differentialgleichungen können mit diesen Schnittgrössen auch folgendermassen geschrieben werden:

$$B'(x) - Q(x) = 0, \tag{4.17}$$

$$M'(x) = 0, \tag{4.18}$$

$$Q'(x) - c\kappa = 0. \tag{4.19}$$

Wenn $\theta(x)$ und $\kappa(x)$ aus (4.8), (4.9) und (4.10) eliminiert werden, ergibt sich für β eine Differentialgleichung fünfter Ordnung.

Mit der Lösung $\beta=\beta(x)$ können $\theta=\theta(x)$ und $\kappa=\kappa(x)$ einfach bestimmt werden. Für die allgemeine Lösung folgt:

$$\begin{aligned} \beta(x) = &-\mu c_2 - (\gamma\phi_2 - \alpha\phi_4)c_3 + (\gamma\phi_1 + \alpha\phi_3)c_4 \\ &+ (\alpha\phi_2 + \gamma\phi_4)c_5 + (\alpha\phi_1 - \gamma\phi_3)c_6, \end{aligned} \tag{4.20}$$

$$\theta(x) = c_1 + c_2 x - 2\epsilon\mu(\phi_1 c_3 + \phi_2 c_4 + \phi_3 c_5 + \phi_4 c_6), \tag{4.21}$$

$$\kappa(x) = (\epsilon\phi_1 + \delta\phi_3)c_3 + (\epsilon\phi_2 - \delta\phi_4)c_4 - (\delta\phi_1 - \epsilon\phi_3)c_5 + (\delta\phi_2 + \epsilon\phi_4)c_6, \tag{4.22}$$

mit

$$\phi_1 = \cosh(\alpha x)\sin(\gamma x), \tag{4.23}$$

$$\phi_2 = \cosh(\alpha x)\cos(\gamma x), \tag{4.24}$$

$$\phi_3 = \sinh(\alpha x)\cos(\gamma x), \tag{4.25}$$

$$\phi_4 = \sinh(\alpha x)\sin(\gamma x), \tag{4.26}$$

während die Konstanten α, γ, ϵ und δ definiert sind mit:

$$\alpha^2 = \alpha_0^2(1+\epsilon), \quad \alpha > 0, \tag{4.27}$$

$$\gamma^2 = \alpha_0^2(1-\epsilon), \quad \gamma > 0, \tag{4.28}$$

$$\epsilon = \frac{1}{2}\alpha_0^2\frac{a_1}{a_4} = \frac{1}{2}\left(\frac{\alpha_0}{\lambda}\right)^2, \tag{4.29}$$

$$\delta^2 = 1-\epsilon^2, \quad \delta > 0 \tag{4.30}$$

und

$$\alpha_0^4 = \frac{1}{4}\frac{c}{a_1}, \quad \alpha_0 > 0. \tag{4.31}$$

Mit (4.14), (4.15), (4.16), (4.20), (4.21) und (4.22) ergibt sich für $B(x)$, $M(x)$ und $Q(x)$:

$$B(x) = 2\alpha_0^2 a_1(\phi_1 c_3 + \phi_2 c_4 + \phi_3 c_5 + \phi_4 c_6), \tag{4.32}$$

$$M(x) = a_4 c_2 = \text{konstant}, \tag{4.33}$$

$$\begin{aligned} Q(x) = {} & 2\epsilon a_4\{(\alpha\phi_4 + \gamma\phi_2)c_3 + (\alpha\phi_3 - \gamma\phi_1)c_4 \\ & + (\alpha\phi_2 - \gamma\phi_4)c_5 + (\alpha\phi_1 + \gamma\phi_3)c_6\}. \end{aligned} \tag{4.34}$$

Da in (4.20), (4.21) und (4.22) und in (4.32), (4.33) und (4.34) die Funktionen $\sin(\gamma x)$ und $\cos(\gamma x)$ auftreten, wird die Lösung einen «schwankenden» Charakter haben. In den graphischen Darstellungen des fünften Kapitels wird dies klar zum Ausdruck kommen.

Die Spannungen σ, τ_1 und τ_2 in einem Querschnitt können nach der in 3. erwähnten Art und Weise bestimmt werden. Dann ergeben sich wieder die Beziehungen (3.31), (3.32) und (3.33). Für die Berechnung der Schubspannungen kann natürlich auch das schon im dritten Kapitel genannte, genauere Verfahren nach [5] angewendet werden.

Ausser diesen Membranspannungen treten Biegespannungen auf, deren Grösse vom Biegemoment pro Längeneinheit im Querschnitt, $M_{1x}(x,s)$, und vom Biegemoment pro Längeneinheit in Längsschnitten, $M_{1s}(x,s)$, bestimmt ist. Wegen der Behinderung der Querkontraktion bei Biegung gilt:

$$M_{1x} = \nu M_{1s}. \tag{4.35}$$

Die maximale Biegespannung σ_b infolge M_{1s} tritt in den Eckpunkten des Trägers auf.

Es gilt

$$M_{1s\,max} = M_{1s}(y = \pm b_2, z = \pm b_1) = \tfrac{1}{8} c\kappa \tag{4.36}$$

und deshalb

$$\sigma_{b\,max} = \frac{6 M_{1s}}{t_{min}^2}, \tag{4.37}$$

wobei t_{min} die kleinste der Wandstärke t_1 und t_2 ist.

5. Vergleich der Theorien mittels eines konkreten Beispiels

Die ausgeführten Theorien werden an Hand eines konkreten Beispiels miteinander verglichen. Dabei ergeben sich interessante Differenzen, die sodann für beliebige Kastenträger mit Rechteckquerschnitt erläutert werden. Grössen die berechnet werden mit Hilfe der Bredtschen Theorie, der Theorie nach 3 und der Theorie nach 4, werden bezeichnet mit Oberindex ^{b}, bzw. ^{s} und ^{f}. In Fig. 5.1 ist der Träger gezeichnet, dem wir unsere Aufmerksamkeit widmen wollen. Alle wichtigen Daten sind in der Abbildung angegeben worden.

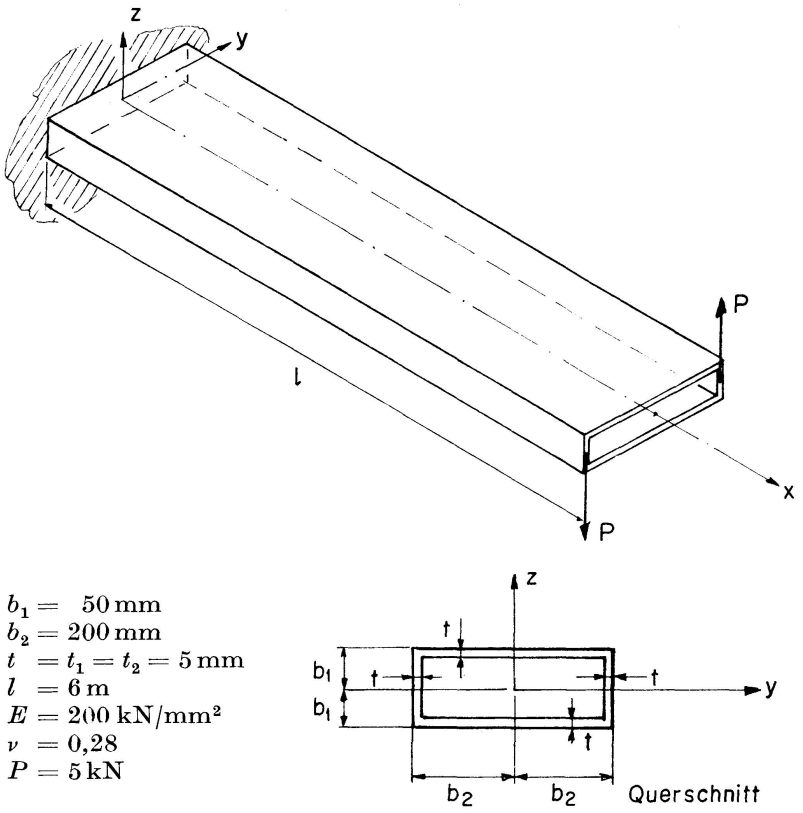

Fig. 5.1. Beispiel.

In Fig. 5.2 bis Fig. 5.5 wurden die interessantesten Spannungs- und Verformungsdaten angegeben. Es zeigt sich sofort, dass die beiden Theorien hinsichtlich der Spannungen und des Verformungswinkels κ quantitativ und qualitativ ganz verschieden sind. Nur die Verdrehung θ des Querschnitts stimmt in den beiden Theorien gut überein. Experimente zeigen, dass die Theorie, gestützt auf die Hypothese der verformbaren Profillinie, der Wirklichkeit sehr nahe kommt. In einer nächsten Veröffentlichung wird noch der Fall erörtert, in dem eine bestimmte Zahl gut aufgestellter Querschotten im Träger eine Situation hervorrufen, wobei der Theorie der starren Profillinie gefolgt werden kann.

Infolge der Wölbbehinderung im Querschnitt $x = 0$ entstehen in beiden

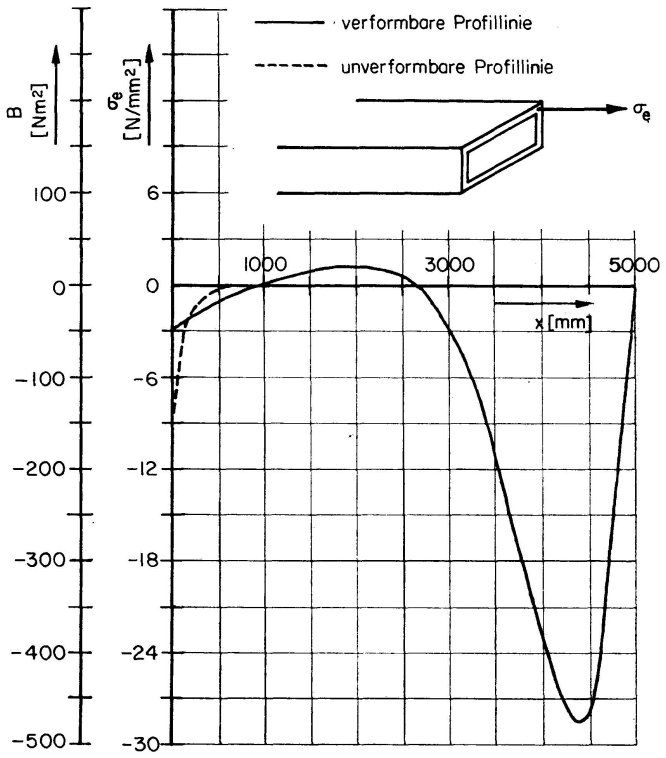

Fig. 5.2. B und σ_e Funktionen von x.

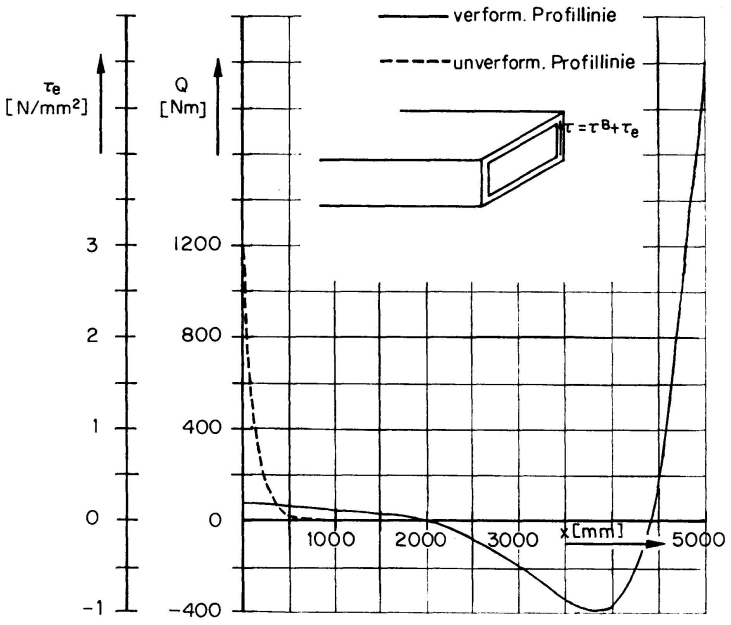

Fig. 5.3. Q und τ_e Funktionen von x.

Theorien Störspannungen, die man hinsichtlich der Bredtschen Schubspannung ($\tau^b = 5\,\mathrm{N/mm^2}$) als gross bezeichnen kann.

Für die maximale Vergleichspannung nach Mohr-Guest ($\sigma_{id\,max}$) in der Einspannstelle gilt:

$$\frac{\sigma^f_{id\,max}}{\sigma^b_{id\,max}} = 1{,}07, \tag{5.1}$$

$$\frac{\sigma^s_{id\,max}}{\sigma^b_{id\,max}} = 1{,}80. \tag{5.2}$$

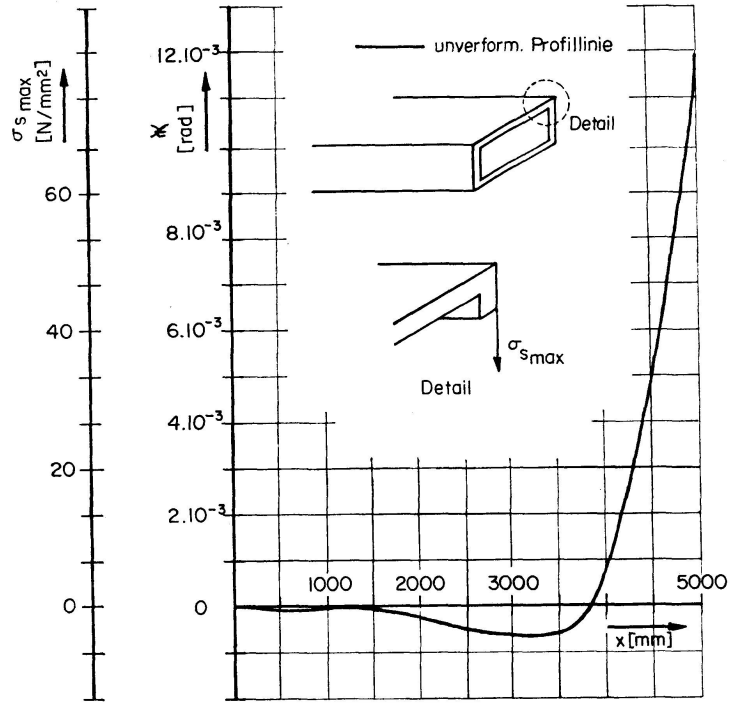

Fig. 5.4. κ und $\sigma_{e\,max}$ Funktionen von x.

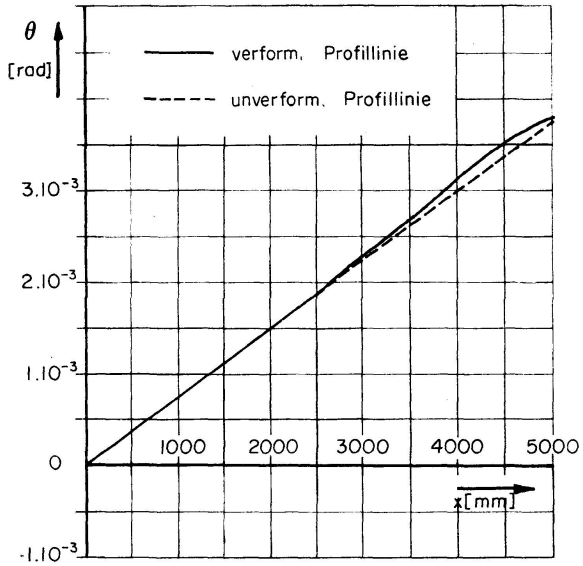

Fig. 5.5. θ Funktion von x.

Ausserdem ist auf die Biegespannungen Rücksicht zu nehmen, die, nach der Theorie der flexiblen Profillinie, bei einem Abstand von ungefähr 500 mm der Einspannstelle maximal sind. Diese Spannungen kann man aber bestimmt nicht vernachlässigen.

Die Störung hinsichtlich der Bredtschen Theorie ist in einer bestimmten Distanz der Einspannstelle verschwunden. In der Theorie mit verformbarer Profillinie ist diese Entfernung viel grösser als in der Theorie mit starrem Querschnitt (2300 mm bzw. 360 mm).

Im Gegensatz zur Theorie für starre Querschnitte gibt die Verformbarkeit der Profillinie auch in der Gegend der Einleitungsstelle des Torsionsmomentes Abweichungen der Bredtschen Theorie. Diese Abweichungen treten auf, weil

die Belastung mit zwei Kräften P nach Abb. 5.1 nicht nur ein Torsionsmoment $\overline{M}$, sondern auch ein transversales Bimoment $\overline{Q}$ verursacht, das in seinem Absolutwert ebenso gross ist wie $\overline{M}$. Die dadurch hervorgerufenen Biegespannungen in den Platten sind, zusammen mit den Schubspannungen, verantwortlich für eine grosse Zunahme der maximalen Vergleichsspannung im Querschnitt $x=l$ hinsichtlich $\sigma^b_{id\,max}$:

$$\frac{\sigma^f_{id\,max}}{\sigma^b_{id\,max}} = 2{,}00. \tag{5.3}$$

In einer Entfernung von etwa 500 mm des belasteten Querschnitts $x=l$ treten sehr grosse axiale Membranspannungen auf (siehe Fig. 5.2). In bezug auf die Störung beim Rande $x=l$ kann man schliessen, dass diese auf 2300 mm des Randes keinen merkbaren Einfluss mehr ausübt.

Im nächsten Kapitel wird näher auf die anhand des gegebenen Beispiels festgestellten Erscheinungen eingegangen. Ausserdem wird eine in der Praxis brauchbare Form der wichtigsten Ergebnisse angestrebt.

6. Allgemeiner Vergleich der Theorien

6.1. Die Störungslänge

Wie aus den im vorigen Kapitel aufgeführten Abbildungen hervorgeht, haben die Störungen hinsichtlich der Bredtschen Theorie einen «dämpfenden» Charakter. In einer Entfernung x von der Einleitungsstelle der Störung wird die Grösse der Störung in der Theorie mit starrer Profillinie bestimmt vom Wert $e^{-\lambda x}$ und in der Theorie mit verformbarer Profillinie vom Wert $e^{-\alpha x}$. Da $e^{-\pi}=0{,}04$, wird die Störungslänge l_0 – ziemlich arbiträr – definiert durch:

$$l^s_0 = \frac{\pi}{\lambda} = \frac{\pi}{\alpha_0}\sqrt{2\epsilon}, \tag{6.1}$$

$$l^f_0 = \frac{\pi}{\alpha_0}. \tag{6.2}$$

Man beachte, dass in (6.2) α_0 statt α benutzt wurde; weil $\epsilon \ll 1$ (siehe Fig. 6.3) sind α und α_0 nahezu gleich.

Wenn $\nu=0{,}28$, so ergibt sich mit den Formeln für α_0 und λ:

$$l^s_0 = 1{,}45\sqrt{\frac{1}{t_1 t_2}(b_1 t_1 + b_2 t_2)(b_1 t_2 + b_2 t_1)}, \tag{6.3}$$

$$l^f_0 = 3{,}31\sqrt[4]{\frac{1}{t_1^3 t_2^3} b_1^2 b_2^2 (b_1 t_1 + b_2 t_2)(b_1 t_2^3 + b_2 t_1^3)} = \frac{l^s_0}{\sqrt{2\epsilon}} \tag{6.4}$$

und für den Spezialfall $t_1=t_2=t$ erhält man:

$$l^s_0 = 1{,}45\,(b_1+b_2), \tag{6.5}$$

$$l^f_0 = 3{,}31\sqrt{\frac{1}{t} b_1 b_2 (b_1+b_2)}. \tag{6.6}$$

Für das Beispiel im fünften Kapitel gilt somit: $l_0^s = 362$ mm und $l_0^f = 2310$ mm. Das Gebiet, in dem die Effekte der Randstörung merkbar sind, ist für Träger mit starrem Querschnitt erheblich kleiner als für Träger mit verformbarem Querschnitt.

Für $t_1 = t_2 = t$ gilt:

$$\frac{l_0^s}{l_0^f} = \sqrt{2\epsilon} = 0{,}439\sqrt{\frac{1}{b_1 b_2}(b_1+b_2)\,t}. \tag{6.7}$$

In Fig. 6.1, 6.2 und 6.3 sind l_0^s/b_1, l_0^f/b_1 und ϵ dargestellt in Abhängigkeit von b_2/b_1 und t/b_2, unter der Bedingung $t_1 = t_2 = t$. Aus Fig. 6.3 geht hervor, dass $\epsilon \ll 1$ für reelle Massen des Trägers.

Wenn die Länge l des Trägers grösser ist als l_0, werden der Spannungs- und Deformationszustand an einem Rand des Trägers nicht oder nur sehr wenig

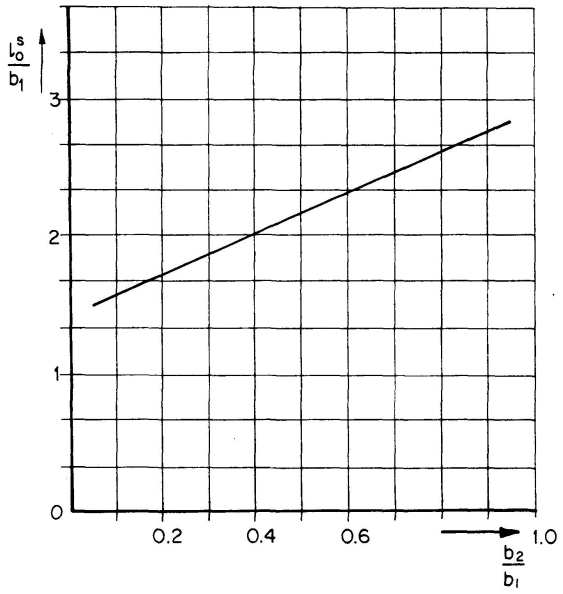

Fig. 6.1. l_0^s/b_1 Funktion von b_2/b_1.

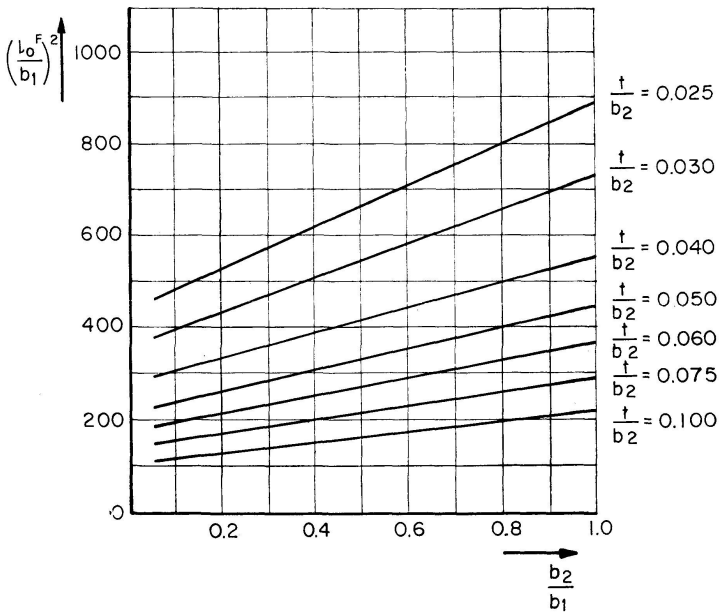

Fig. 6.2. $(l_0^f/b_1)^2$ Funktion von b_2/b_1.

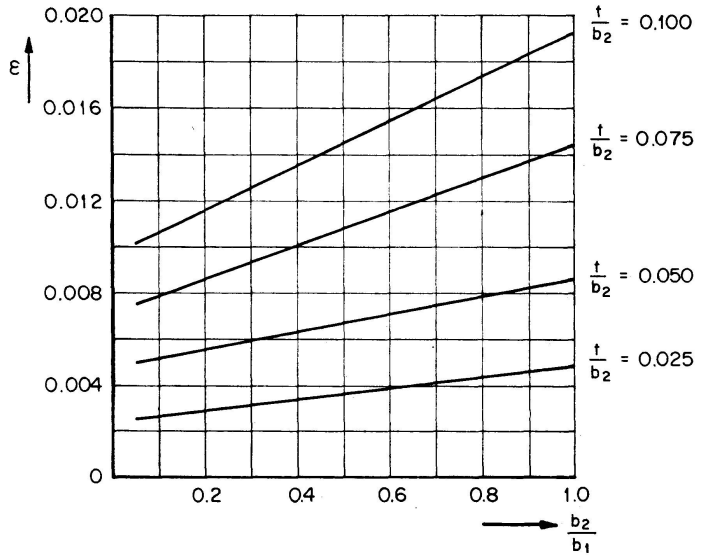

Fig. 6.3. ϵ Funktion von b_2/b_1.

von den Bedingungen am anderen Rand beeinflusst. Ein Träger mit $l > l_0$ wird als «unendlich lang» bezeichnet.

6.2. Das axiale Bimoment B bei Wölbbehinderung

Wird ein Träger, der sich als unendlich lang betrachten lässt, im Querschnitt $x = l$ mit einem Torsionsmoment $\overline{M}$ belastet, so wird im allgemeinen eine Verwölbung der Querschnitte auftreten. Wird die Verwölbung im Querschnitt $x = 0$ völlig behindert (siehe Fig. 5.1), so wird bei $x = 0$ ein axiales Bimoment $B(0)$ auftreten. Annäherungsweise gilt:

$$B^s(0) = -\frac{\mu}{\lambda}\overline{M} = -\frac{\mu}{\alpha_0}\sqrt{2\epsilon}\,\overline{M}, \tag{6.8}$$

$$B^f(0) = -4\frac{\mu}{\alpha_0}\epsilon\,\overline{M} \tag{6.9}$$

und deshalb:

$$\frac{B^f(0)}{B^s(0)} = 2\sqrt{2\epsilon}. \tag{6.10}$$

Aus Fig. 6.3 und Gleichung (6.10) geht klar hervor, dass bei Behinderung der Verwölbung zwischen den axialen Bimomenten $B^s(0)$ und $B^f(0)$ grosse Unterschiede auftreten können. Diese Behauptung ist augenfällig, wenn man (6.8), (6.9) und (6.10) spezifiziert für $t_1 = t_2 = t$:

$$B^s(0) = 0{,}462\,(b_1 - b_2)\,\overline{M}, \tag{6.11}$$

$$B^f(0) = 0{,}405\,(b_1 - b_2)\sqrt{\frac{1}{b_1 b_2}(b_1 + b_2)\,t}\,\overline{M}, \tag{6.12}$$

$$\frac{B^f(0)}{B^s(0)} = 0{,}877\sqrt{\frac{1}{b_1 b_2}(b_1 + b_2)\,t}. \tag{6.13}$$

Man kann darlegen, dass $|B(0)|$ im vorliegenden Fall den Maximalwert von $|B(x)|$ darstellt.

Die infolge $B(0)$ auftretende maximale axiale Normalspannung in den Eckpunkten des Trägers, $\sigma_{ax}(0)$, kann mit der Schubspannung τ^b nach Bredt verglichen werden.

Da
$$\sigma_{ax}(0) = -\frac{3}{4}\frac{B(0)}{b_1 b_2 (b_1 t_1 + b_2 t_2)} \tag{6.14}$$

wird für einen Träger mit konstanter Wandstärke gelten:

$$\frac{\sigma^s_{ax}(0)}{\tau^b} = -2{,}77\,\mu, \tag{6.15}$$

$$\frac{\sigma^f_{ax}(0)}{\tau^b} = -7{,}84\,\mu\sqrt{\epsilon} \tag{6.16}$$

und deshalb:

$$\frac{\sigma^f_{ax}(0)}{\sigma^s_{ax}(0)} = 2{,}83\sqrt{\epsilon}\,. \tag{6.17}$$

6.3. Das transversale Bimoment Q bei Wölbbehinderung

Wenn im Querschnitt $x=0$ die Verwölbung behindert ist, so treten hinsichtlich der Theorie nach Bredt zusätzliche Schubspannungen τ_e auf, deren Grösse durch das transversale Bimoment $Q(0)$ bestimmt ist. Die nähere Untersuchung ergibt:

$$Q^s(0) = \mu\,\overline{M}, \tag{6.18}$$

$$Q^f(0) = 4\,\epsilon\,\mu\,\overline{M}, \tag{6.19}$$

$$\frac{Q^f(0)}{Q^s(0)} = 4\,\epsilon. \tag{6.20}$$

Die Schubspannungsverteilung im Querschnitt lässt sich mit (3.32) und (3.33) einfach bestimmen.

6.4. Die Vergleichsspannung σ_{id} bei Wölbbehinderung

Wir erwähnen die Ergebnisse für die Vergleichsspannung σ_{id} nach Mohr-Guest im Querschnitt in dem die Verwölbung behindert ist und beschränken uns dabei auf Träger mit konstanter Wandstärke $t_1 = t_2 = t$. Wenn $b_1 \geqq b_2$ (und deshalb $\mu \geqq 0$) und $\nu = 0{,}28$, dann ergibt sich:

$$\frac{\sigma^s_{id}}{\tau^b} = 2\sqrt{1 + 2\,\mu + 2{,}92\,\mu^2}, \tag{6.21}$$

$$\frac{\sigma^f_{id}}{\tau^b} = 2\sqrt{1 + (8 + 15{,}36\,\mu)\,\mu\,\epsilon + 16\,\mu^2\,\epsilon^2}. \tag{6.22}$$

6.5. Die Plattenbiegung bei Wölbbehinderung

Aus den graphischen Darstellungen in Kapitel 5 geht hervor, dass bei Wölbbehinderung für Träger mit verformbarer Profillinie in einer Entfernung

von etwa $x_0 = \frac{1}{4} l_0$ von der Einspannstelle maximale Biegespannungen σ_b in den Platten auftreten. Wenn $t_1 = t_2 = t$ und $b_1 > b_2$ gilt:

$$\frac{\sigma_b^f(x_0)}{\tau^b} = -15{,}5\,\mu\,\epsilon\,\alpha_0 \frac{b_1 b_2}{t} = -48{,}7\,\mu\,\epsilon \frac{b_1 b_2}{t\,l_0^f}. \tag{6.23}$$

Wie aus (6.23) ersichtlich sein wird, sind diese Biegespannungen sicherlich nicht immer vernachlässigbar.

6.6 Effekte infolge eines transversalen Bimomentes $\bar{Q}$

Aus dem Beispiel im fünften Kapitel folgt, dass die Beanspruchung durch ein transversales Bimoment $\bar{Q}$ für Träger mit verformbarer Profillinie zu einer ganz anderen Spannungsverteilung Anlass gibt als von der Bredtschen Theorie vorausgesagt wird. Wenn der Querschnitt starr ist, gibt eine Belastung $\bar{Q}$ keine zusätzlichen Spannungen.

Für die Belastungslage in Fig. 5.1 ist $\bar{Q}$ dem Torsionsmoment $\bar{M}$ gleich. Für Träger mit $t_1 = t_2 = t$ gilt für die maximale Biegespannung σ_b in Längsflächen bei $x = l$:

$$\left|\frac{\sigma_b^f(l)}{\tau^b}\right| = 12\,\alpha_0 \frac{b_1 b_2}{t} = 37{,}7 \frac{b_1 b_2}{t\,l_0^f}. \tag{6.24}$$

Die im Querschnitt $x = l$ auftretenden maximalen Schubspannungen sind ihrem Absolutwert nach zweimal so gross wie τ^b.

Die axialen Membranspannungen, die für $x = l$ gleich null sind, erreichen ihren Maximalwert in einer Entfernung von etwa $x_0 = \frac{1}{4} l_0$ vom belasteten Rand her. Für diese Spannungen gilt:

$$\frac{\sigma_{ax}^f(x = l - x_0)}{\tau^b} = -1{,}08\,\alpha_0 \frac{b_1 b_2}{t} = -3{,}39 \frac{b_1 b_2}{t\,l_0^f}. \tag{6.25}$$

6.7. Die Torsionssteifigkeit

Auch die Torsionssteifigkeit ist von den Randbedingungen und der angewandten Theorie abhängig. Zur Berechnung der Steifigkeit betrachten wir einen Träger mit Länge l grösser als l_0, der belastet ist wie in Fig. 6.4 angegeben ist.

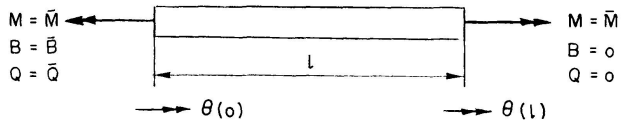

Fig. 6.4. Träger mit Länge $l > l_0$.

Für Träger mit starrer Profillinie ergibt sich:

$$\theta(l) - \theta(0) = \frac{\bar{M}}{a_4} l + \mu\,(1 - e^{-\lambda l})\,\bar{B}, \tag{6.26}$$

während für Träger mit verformbarer Profillinie gilt:

$$\theta(l)-\theta(0)=\frac{\overline{M}}{a_4}l+\mu(1-\psi_1-\psi_2)\,\overline{B}-\frac{\mu}{\alpha_0}\psi_1\,\overline{Q}, \tag{6.27}$$

mit

$$\psi_1=e^{-\alpha_0 l}\sin(\alpha_0 l), \tag{6.28}$$

$$\psi_2=e^{-\alpha_0 l}\cos(\alpha_0 l). \tag{6.29}$$

7. Schlussbemerkungen

Der Vergleich von Ergebnissen, unter Zuhilfenahme zwei verschiedener Theorien für dünnwandige Träger, zeigt klar, dass das Deformieren oder nicht Deformieren der Profillinie grundsätzliche Unterschiede mit sich bringt. Manchmal wird fälschlich die Theorie für Träger mit unverformbarem Querschnitt angewandt.

In der Praxis ist Unverformbarkeit der Profillinie nur annähernd herstellbar, wenn genügend viele Querschotte angebracht worden sind. Die obige Darstellung zeigt, dass derartige Querschotte nicht immer unbedingt eine Besserung des Spannungszustandes mit sich bringen. Die in 5. studierte Konstruktion zeigt zum Beispiel, dass die Spannungen in der Nähe der Wölbbehinderungsstelle bei einem Träger mit unverformbarem Querschnitt (also mit vielen Querschotten) um etwa 70% höher sind als bei einem Träger mit verformbarer Profillinie (also ohne Querschotte). Das Beispiel zeigt auch, dass ein Querschott beim Einführen einer Torsionsbelastung einen positiven Effekt hat.

Mit der Theorie für Träger mit verformbarer Profillinie kann die Wirkung von Querschotten auf die Spannungen und Verformungen analysiert werden. In einer folgenden Veröffentlichung soll darauf näher eingegangen werden.

Literatur

1. Williams, D.: Torsion of a rectangular tube with axial constraints. R.A.E. Report, Reports and Memoranda no. 1619, March, 1934.
2. Flügge, W. und Marguerre, K.: Wölbkräfte in dünnwandigen Profilstäben. Ingenieur-Archiv, XVIII. Band, 1950.
3. Heilig, R.: Beitrag zur Theorie der Kastenträger beliebiger Querschnittsform. Der Stahlbau, 1961, Heft 11, S. 333.
4. Kollbrunner, C. und Hajdin, N.: Wölbkrafttorsion dünnwandiger Stäbe mit geschlossenem Profil. Mitteilungen der Technischen Kommission der Schweizer. Stahlbau-Vereinigung, Heft 32 (Juni 1966).
5. Janssen, J.: Over de torsietheorie van Vlasov voor dunwandige rechthoekige kokers. Dissertatie, Technische Hogeschool Eindhoven (1967).
6. Dabrowski, R.: Der Schubverformungseinfluss auf die Wölbkrafttorsion der Kastenträger mit verformbarem biegesteifem Profil. Der Bauingenieur, Band 40, 1965, Heft 11.

7. VLASOV, V.: Thin-walled elastic beams. 2nd. ed., Israel Program for Scientific Translations, Jerusalem (1961).
8. LACHER, G.: Zur Berechnung des Einflusses der Querschnittsverformung auf die Spannungsverteilung bei durch elastische oder starre Querschotte versteiften Tragwerken mit prismatischem, offenem oder geschlossenem biegesteifem Querschnitt unter Querlast. Der Stahlbau, 1962, Heft 10, S. 299, Heft 11, S. 325.
9. RESINGER, F.: Der dünnwandige Kastenträger. Forschungsheft aus dem Gebiet des Stahlbaues, Nr. 13, Stahlbau-Verlag G.m.b.H., Köln.
10. CSONKA, P.: Torsion of a square-shaped tube clamped in at both ends. Hungarian Academy of Sciences, Budapest Acta Technica XXIV (1959), H. 3, S. 379, H. 4, S. 90.
11. JANSSEN, J.: De mogelijkheden van de methode der eindige elementen bij de berekening van de sterkte en stijfheid van dunwandige balken. De Ingenieur, 1970, jaargang 82, nr. 43, S. O121.

Zusammenfassung

Mit zwei verschiedenen Gruppen von Voraussetzungen über die Verschiebungen ergeben sich zwei Torsionstheorien für dünnwandige Kastenträger mit Rechteckquerschnitt, nämlich eine Theorie, bei der die Profillinie als starr angenommen wird, und eine Theorie, wobei eine gewisse Verformung der Profillinie möglich ist. Die Analysen beruhen auf dem Prinzip der minimalen potentiellen Energie. Anhand eines konkreten Beispiels werden die charakteristischen Unterschiede zwischen diesen Theorien untersucht. Die Ergebnisse werden auf Träger mit willkürlichem Rechteckquerschnitt verallgemeinert.

Summary

From two different groups of conditions about displacements, two torsion theories of thin-walled box-girders of rectangular section are resulting. In one theory the profile-curve is assumed to be fixed, in the other a certain deformation is possible. The analyses are based on the principal of minimum potential energy. The characteristic differences between both theories are demonstrated by an example. The results are generalized for girders with arbitrary rectangular sections.

Résumé

Avec deux groupes différents de conditions de déplacement on obtient deux théories de torsion pour les poutres en caisson à sections rectangulaires: une première dans laquelle la ligne du profil est considérée comme fixe, et une seconde où une certaine déformation est possible. Les analyses se basent sur le principe de l'énergie potentielle minimale. Un exemple concret illustre les différences caractéristiques entre les deux théories. Les résultats sont généralisés pour des poutres à sections rectangulaires arbitraires.

Nonlinear Buckling of Lattice Domes

Stabilité non-linéaire de coupoles à treillis

Nichtlineare Stabilität von Gitterkuppeln

JAYME MASON

Professor of Applied Mechanics and Civil Engineering, Consulting Engineer, Pontifícia Universidade Católica and Universidade Federal do Rio de Janeiro, Rio de Janeiro, Brazil

1. Introduction

In the design of modern large span geodesic domes, the determination of the buckling load is a problem of primary importance, normally the decisive factor in the whole design. In a previous publication [2], the problem of edge disturbances in lattice domes with triangular meshes has been studied. It is the aim of the present paper, to suplement the previous stress problem by means of a buckling theory, simple enough to be used in effective design. For the theory to give realistic results, it must be based on a nonlinear post-buckling approach, in the spirit of KÁRMÁN and TSIEN's pioneering work [1].

The structural behaviour of the shell lattice will be dealt with by means of a continuous analogue model, which will conveniently replace the discrete lattice members.

Both simple and double-layer lattice domes can be analysed by means of the intended theory. It should be particularly emphasized that, as it was already remarked for the stress problem [2], it may be dangerous to use simple analogies, obtained from the theory of isotropic shells. The bending and the membrane stiffness may differ considerably in the lattice model, whereas they bear a definite relationship to each other in the case of uniform shells.

We shall first review briefly some basic results for the analogue model. Next, the relevant equilibrium and kinematical equations including nonlinear terms will be stated. Appropriate expressions for the compatibility condition and the potential energy will also be derived.

Finally, an approximate solution for the nonlinear buckling problem of

lattice domes will be proposed. The method of solution is similar to the one used by WOLMIR [6], for the non linear buckling problem in uniform shells.

The theory will be applied to a concrete example and the results will be compared with other formulas in the literature.

2. Analogue Model

Let us imagine a sphere (Fig. 1) made of a triangular lattice of stiff members. The lattice voids are closed by a continuous skin, so that the sphere can

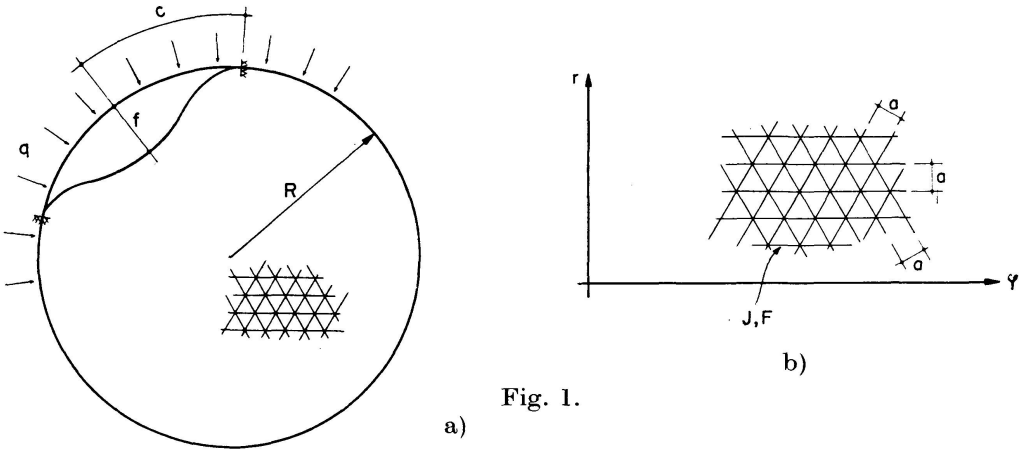

Fig. 1.

support an external pressure q. It is the aim of the present analysis, to determine the value of the external pressure, for which a portion of the sphere of radius c will "snap through" to a new buckled position, determined by the deflection f of its mid-point. We assume that the buckled zone behaves as a shallow shell. The lattice details are reproduced in Fig. 1b, the meshes being equilateral triangles of height a. The properties of lattice members are defined through the cross-sectional area F and the moment of inertia J. Members may be simple bars or trusses. The above lattice will be referred to a polar system of coordinates r, φ, which will be used in the subsequent analysis.

The continuum properties of the lattice model are obtained by subjecting the lattice to generalized unit deformations, as unit elongations and shears and unit changes of curvature and twist.

The contributions of different bars to the shell stress resultants and stiffness will be refered to the unit length of the shell middle surface.

We refer to [3] and [4] for detailed demonstrations. By neglecting the coupling between in-plane and bending contributions (see Fig. 2), the interesting constitutive equations can be written as

$$M_r = d_r^r k_r + d_r^\varphi k_\varphi, \qquad M_\varphi = d_r^\varphi k_r + d_\varphi^\varphi k_\varphi, \tag{1}$$

$$\epsilon_r = \Delta_r^r N_r + \Delta_r^\varphi N_\varphi, \qquad \epsilon_\varphi = \Delta_r^\varphi N_r + \Delta_\varphi^\varphi N_\varphi. \tag{2}$$

In the above relationships, k_r and k_φ are changes of curvatures and ϵ_r and ϵ_φ, membrane strains of the shell middle surface. It has been shown in [3] and [4] that the coefficients d_r^r, $d_r^\varphi \cdots \Delta_r^\varphi$, Δ_φ^φ in (1) and (2) are given by

$$\begin{aligned} d_r^r &= d_\varphi^\varphi = \frac{3EJ}{8a}(3+\mu), & d_r^\varphi &= \frac{3EJ}{8a}(1-\mu), \\ \Delta_r^r &= \Delta_\varphi^\varphi = \frac{a}{EF}, & \Delta_r^\varphi &= -\frac{a}{EF}, \end{aligned} \tag{3}$$

in which

$$\mu = \frac{GJ_d}{EJ} \tag{4}$$

and GJ_d and EJ are respectively Saint-Venant's torsional stiffness and the bending stiffness of a lattice member.

3. Equilibrium and Kinematical Relations for Rotationally Symmetric Bending of Shallow Spherical Shells with Large Deflections

With the notations of Fig. 2, the equilibrium equations of the symmetrically loaded spherical shell, by accounting for the influence of deflections on the

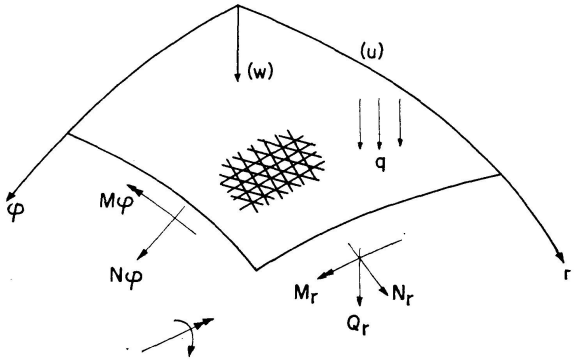

Fig. 2.

geometry are given by

$$\begin{aligned} &\frac{d}{dr}(r N_r) - N_\varphi = 0, \\ &\frac{d}{dr}(r Q_r) + r\left(k + \frac{d^2 w}{dr^2}\right) N_r + r\left(k + \frac{1}{r}\frac{dw}{dr}\right) N_\varphi + q r = 0, \\ &\frac{dM_r}{dr} + \frac{M_r - M_\varphi}{r} = Q_r, \end{aligned} \tag{5}$$

where

$$k = \frac{1}{R}. \tag{6}$$

By eliminating Q_r from the second of (5) by means of the third,

$$\frac{d^2 M_r}{dr^2} + \frac{2}{r}\frac{dM_r}{dr} - \frac{1}{r}\frac{dM_\varphi}{dr} + \left(k + \frac{d^2 w}{dr^2}\right) N_r + \left(k + \frac{1}{r}\frac{dw}{dr}\right) N_\varphi + q = 0. \tag{7}$$

The first equation of (5) will be satisfied identically by assuming

$$N_r = \frac{1}{r}\frac{d\Phi}{dr}, \qquad N_\varphi = \frac{d^2\Phi}{dr^2}, \tag{8}$$

in which Φ is a stress function. On the other hand, the well known formulas for rotationally symmetric in-plane strains are

$$\begin{aligned} \epsilon_r &= \frac{du}{dr} - k\,w + \frac{1}{2}\left(\frac{dw}{dr}\right)^2, \\ \epsilon_\varphi &= \frac{u}{r} - k\,w, \end{aligned} \tag{9}$$

from which we can eliminate the tangential displacement u to obtain

$$\frac{d\,(r\,\epsilon_\varphi)}{dr} - \epsilon_r + k\,r\frac{dw}{dr} + \frac{1}{2}\left(\frac{dw}{dr}\right)^2 = 0. \tag{10}$$

By accounting for (3) and (8), the constitutive Eqs. (2) for the extensional strains are rewritten as

$$\begin{aligned} \epsilon_r &= \frac{a}{E\,F}\left(\frac{1}{r}\frac{d\Phi}{dr} - \frac{1}{3}\frac{d^2\Phi}{dr^2}\right), \\ \epsilon_\varphi &= \frac{a}{E\,F}\left(\frac{d^2\Phi}{dr^2} - \frac{1}{3}\frac{d\Phi}{dr}\right). \end{aligned} \tag{11}$$

If we substitute (11) in (10), the new form of the compatibility relation will be

$$\frac{d}{dr}\left(r\frac{d^2\Phi}{dr^2}\right) - \frac{1}{r}\frac{d\Phi}{dr} + \frac{E\,F}{a}\left[k\,r\frac{dw}{dr} + \frac{1}{2}\left(\frac{dw}{dr}\right)^2\right] = 0,$$

which can be rewritten as

$$\frac{d}{dr}(\nabla^2\Phi) = -\frac{E\,F}{a}\left[\frac{1}{2\,r}\left(\frac{dw}{dr}\right)^2 + k\frac{dw}{dr}\right] \tag{12}$$

by introducing the Laplacian operator

$$\nabla^2(\cdots) = \frac{d^2(\cdots)}{dr^2} + \frac{1}{r}\frac{d(\cdots)}{dr}. \tag{13}$$

By means of (1) and the well known formulas for the changes of curvature

$$k_r = -\frac{d^2w}{dr^2}, \qquad k_\varphi = -\frac{1}{r}\frac{dw}{dr} \tag{14}$$

the equation of equilibrium (7) can be also rewritten as

$$d_r^r\,\nabla^2\nabla^2 w - \left(k + \frac{d^2w}{dr^2}\right)\frac{d^2\Phi}{dr^2} - \left(k + \frac{1}{r}\frac{dw}{dr}\right)\frac{1}{r}\frac{d\Phi}{dr} = q. \tag{15}$$

Eqs. (12) and (15) are no-linear and direct methods of solution have slim chances of success. We supplement the above derivations by including an

expression for the total potential energy of the buckled area in the shell, which will be helpful in obtaining approximate solutions.

4. Potential Energy

If the shell is deformed, it will store potential energy, which can be recovered upon unloading. The potential energy is made up partly of the strain energy and partly of the potential energy of the external loading.

The strain energy arises from two components, membrane effect and bending, which are given respectively by

$$U_m = \tfrac{1}{2}\iint (N_r \epsilon_r + N_\varphi \epsilon_\varphi)\, dS = \tfrac{1}{2}\iint (\Delta_r^r N_r^2 + 2\Delta_r^\varphi N_r N_\varphi + \Delta_\varphi^\varphi N_\varphi^2)\, dS \tag{16}$$

and

$$U_b = \tfrac{1}{2}\iint (M_r k_r + M_\varphi k_\varphi)\, dS. \tag{17}$$

By substituting above (3), (8), (1) and (14) these formulas change into

$$\begin{aligned} U_m &= \frac{a}{2EF}\iint \left[(\nabla^2\Phi)^2 - \frac{8}{3}\frac{1}{r}\frac{d\Phi}{dr}\frac{d^2\Phi}{dr^2}\right] dS, \\ U_b &= \frac{3EJ}{16a}(3+\mu)\iint \left[(\nabla^2 w)^2 - 4\frac{(1+\mu)}{(3+\mu)}\frac{1}{r}\frac{dw}{dr}\frac{d^2w}{dr^2}\right] dS. \end{aligned} \tag{18}$$

We next evaluate the potential energy of the external loading. The displacement pattern of the shell is sketched in Fig. 3.

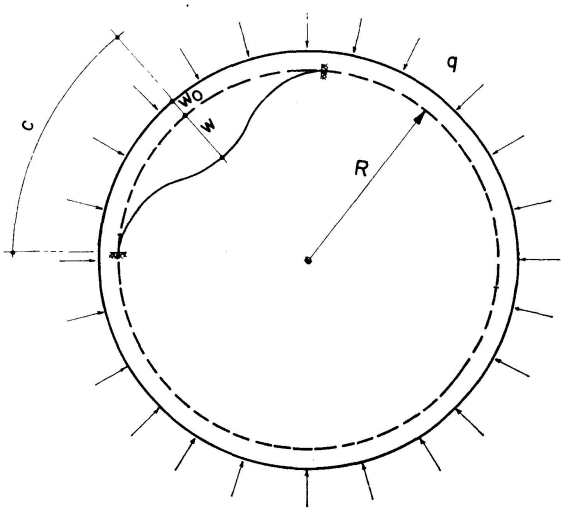

Fig. 3.

In the pre-buckling stage, the lattice sphere will be compressed by an amount w_0 and, in the buckling stage, an area of radius c will experience an additional deflection. Since, before buckling we have a uniform compression $N_r = N_\varphi = -\frac{qR}{2}$, the pre-buckling deflection is easily seen to be $w_0 = \epsilon_r R = \frac{1}{3}\frac{qa}{kEF}$, by using (2). We include the effect of this deflection in the potential energy W of the external loading. The strain energy in the pre-buckling stage will be accounted for later.

Then $$W = -\int\int q\,(w+w_0)\,dS \tag{19}$$

and the total potential energy of the buckled shallow shell will be

$$\Pi = U_m + U_b + W\,. \tag{20}$$

5. Boundary Conditions

We state the boundary conditions which are usually assumed for the buckled shallow shell (Fig. 4):

$$\text{In } r = c, \qquad w = 0, \qquad \frac{dw}{dr}, \tag{21}$$

which is a perfect restraint. Two other boundary conditions must be added for Φ. By assuming that the tangential displacement u vanishes in $r=c$, we

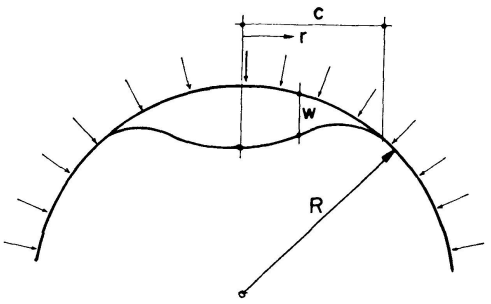

Fig. 4.

conclude from the second of (9) that $r\epsilon_\varphi + k r w = 0$, for $r=c$. On account of (21), this is the same as $\epsilon_\varphi = 0$ for $r=c$, so that

$$\frac{d^2\Phi}{dr^2} - \frac{1}{3}\frac{d\Phi}{dr} = 0 \tag{22}$$

by considering (11). The other condition on Φ is obtained by demanding that N_r be finite for $r=0$, i.e.,

$$\frac{d\Phi}{dr} = 0 \tag{23}$$

[see (8)].

In reality, we have an elastic restraint in $r=c$, which tends to decrease the buckling load based on the assumed conditions.

6. An Approximate Solution of the Buckling Problem

As the integration of the non-linear differential Eqs. (12) and (15) is difficult, we shall develop an approximate energy solution.

We assume for the normal deflection the expression

$$w = f\left(1 - \frac{r^2}{c^2}\right)^2, \tag{24}$$

in which f is the deflection at the mid-point and c the radius. The parameters f and c will be determined later, in such a way that the potential energy be a minimum.

We can make sure that (24) satisfies the boundary conditions (21) Next we insert (24) in the compatibility Eq. (12) and integrate for Φ and then substitute both w and Φ in the expression (20) for the potential energy. The constants c and f which define the shape and the size of the buckled region will be determined from the condition that the potential energy be a minimum.

In a second stage, we could improve the expression for w, by putting Φ in (15), and integrating for w, but the present approximation is considered satisfactory.

By putting now (24) in (12),

$$\frac{d}{dr}(\nabla^2\Phi) = -\frac{8EF}{a}\frac{f}{c^2}\left(\frac{r}{c^2} - 2\frac{r^3}{c^4} + \frac{r^5}{c^6}\right) + \frac{EF}{a}\frac{4fk}{c}\left(\frac{r}{c} - \frac{r^3}{c^3}\right),$$

from which, after two integrations and by accounting for the identify

$$\nabla^2\Phi = \frac{1}{r}\frac{d}{dr}\left(r\frac{d\Phi}{dr}\right)$$

we find

$$\frac{d\Phi}{dr} = -\frac{8EF}{a}\frac{f^2}{c^2}\left(\frac{r^3}{8c^2} - \frac{r^5}{12c^4} + \frac{r^7}{48c^6}\right) + \frac{4EF}{a}\frac{fk}{c}\left(\frac{r^3}{8c} - \frac{r^5}{24c^3}\right) + C_1 r + \frac{C_2}{r}. \quad (25)$$

The constants of integration C_1 and C_2 are determined from the boundary conditions (22) and (23):

$$C_1 = \frac{EF}{a}f\left(2\frac{f}{c^2} - \frac{5}{3}k\right), \qquad C_2 = 0. \quad (26)$$

The expression (25) must be completed, by adding the influence of the membrane stresses $N_r = N_\varphi = -\frac{q}{2k}$ in the pre-buckling stage. This will automatically account for the strain energy in the pre-buckling stage.

From the first of (8), we see that the above effect on $\frac{d\Phi}{dr}$ is given by $-\frac{q}{2k}r$.

Thus, the complete expression of (25) with (26) will be

$$\frac{d\Phi}{dr} = \frac{EF}{6a}\frac{f^2}{c}\left(6\frac{r}{c} - 6\frac{r^3}{c^3} + 4\frac{r^5}{c^5} - \frac{r^7}{c^7}\right) - \frac{EF}{6a}fck\left(5\frac{r}{c} - 3\frac{r^3}{c^3} + \frac{r^5}{c^5}\right) - \frac{qr}{2k}. \quad (27)$$

We also record the expressions for the membrane stresses:

$$\frac{1}{r}\frac{d\Phi}{dr} = N_r = \frac{EF}{6a}\frac{f^2}{c^2}\left(6 - 6\frac{r^2}{c^2} + 4\frac{r^4}{c^4} - \frac{r^6}{c^6}\right) - \frac{EF}{6a}fk\left(5 - 3\frac{r^2}{c^2} + \frac{r^4}{c^4}\right) - \frac{q}{2k}, \quad (28)$$

$$\frac{d^2\Phi}{dr^2} = N_\varphi = \frac{EF}{6a}\frac{f^2}{c^2}\left(6 - 18\frac{r^2}{c^2} + 20\frac{r^4}{c^4} - 7\frac{r^6}{c^6}\right) - \frac{EF}{6a}fk\left(5 - 9\frac{r^2}{c^2} + 5\frac{r^4}{c^4}\right) - \frac{q}{2k}.$$

We see that $\nabla^2\Phi = N_r + N_\varphi$ and now we are in a position to evaluate the potential energy.

We first introduce (27) and (28) in the first of (18) and, after some tedious but simple algebraic manipulations, we find

$$U_m = \frac{5\pi}{21}\frac{EF}{a}\frac{f^4}{c^2} - \frac{4\pi}{9}\frac{EF}{a}kf^3 - \frac{\pi}{3}q\frac{f^2}{k} + \frac{19\pi}{60}\frac{EF}{a}c^2k^2f^2 + \frac{\pi}{3}qc^2f + \frac{\pi}{6}\frac{a}{EF}\frac{q^2}{k^2}c^2. \tag{29}$$

The strain energy of bending is found by inserting (24) in the second of (18):

$$U_b = \frac{4EJ}{a}(3+\mu)\frac{f^2}{c^2}. \tag{30}$$

The potential energy W of the external pressure is, with (19), (24) and $w_0 = \frac{1}{3}\frac{qa}{kEF}$.

$$W = -\frac{\pi}{3}qfc^2 - \frac{\pi}{3}\frac{q^2ac^2}{k^2EF}. \tag{31}$$

If, for greater facility in manipulations we introduce the dimensionless quantities

$$\chi = \frac{kc^2a}{F}, \qquad \sigma = \frac{qa^2}{2k^2EF^2}, \qquad \tau = \frac{af}{F}, \qquad \lambda = \frac{Ja^2}{F^3}. \tag{32}$$

The expression (20) for the total potential energy Π can be written as

$$\Pi = \frac{\pi}{3}\frac{kEF^4}{a^4}\left(\frac{5}{7}\frac{\tau^4}{\chi} - \frac{4}{3}\tau^3 - 2\tau^2\sigma + \frac{19}{30}\chi\tau^2 - 2\sigma^2\chi + 12(3+\mu)\frac{\lambda\tau^2}{\chi}\right). \tag{33}$$

The conditions for a minimum of Π are obviously

$$\frac{\partial\Pi}{\partial\tau} = 0, \qquad \frac{\partial\Pi}{\partial\chi} = 0$$

with a result that

$$\sigma = \frac{5}{7}\frac{\tau^2}{\chi} - \tau + \frac{19}{60}\chi + 6(3+\mu)\frac{\lambda}{\chi},$$
$$\sigma = \tau\left[\frac{19}{60} - \frac{5}{14}\frac{\tau^2}{\chi^2} - 6(3+\mu)\frac{\lambda}{\chi^2}\right]^{1/2}. \tag{34}$$

The above conditions must be satisfied simultaneously. The parameters τ, χ and λ depend on the geometry of the buckled region of the lattice. The parameter σ defines the buckling pressure through (32).

Eqs. (34) must be solved by trial and error. The parameter λ depends entirely on the mesh size a of the lattice and the cross sectional properties F and J of the lattice members. Hence it is given for a shell under consideration. We next choose values for τ and χ and obtain σ from both formulas (34). If σ

happens to have the same value from both formulas, τ and χ determine a possible buckled shape of the shell. The parameter σ will define the corresponding buckling pressure.

In reality, there are many pairs of values for τ and χ which will give the same values for σ, i. e., there are many possible buckling shapes corresponding to different buckling pressures.

The interesting solution will be the one which yields the smallest value for the buckling pressure.

Once the minimum value for σ is known, the buckling pressure q_{cr} and the associated shape of the buckled region are found from (32):

$$q_{cr} = \sigma_{min} \frac{2 k^2 E F^2}{a^2}, \qquad c = \sqrt{\frac{\chi F}{k a}}, \qquad f = \frac{\tau F}{a}. \tag{35}$$

The process of determining σ_{min} is well fitted for a computer program, involving the simultaneous Eqs. (34).

Graphs of solution of (34), from which we may obtain immediately the relavant buckling parameters are not feasible, since the solution depends heavily on the lattice properties, through λ and μ. These constants change in wide ranges for different lattices and a higher degree of precision is required in the calculations.

On these grounds, an elementary FORTRAN IV program was written for (34), in which associated values of σ were printed in table form. An inspection of the table would supply the wanted solution.

7. Stress Resultants in the Post-Buckling Stage

In order to assess the value of forces in the lattice members in the post-buckling stage, we shall derive formulas for the stress resultants for the buckled shallow shell of radius c.

Formulas for the shearing forces Q_r are particularly important for double-layer lattice domes, because they are determinant for estimating the cross-sections of the diagonal bars in the truss lattice members.

A formula for Q_r is found from the third equation of equilibrium (5) along with (1), (3) and (14). The result is

$$Q_r = -\frac{3 E J (3+\mu)}{8 a} \frac{d}{dr} (\nabla^2 w)$$

and, by substituting (24),

$$Q_r = -\frac{12 (3+\mu) E J}{a} \frac{f r}{c^4} \tag{36}$$

the maximum of which ($r = c$)

$$Q_r = -12 (3+\mu) \frac{E J f}{c^3}. \tag{37}$$

A similar calculation would give for the bending moments,

$$M_r = M_\varphi = 6\frac{EJ}{a}\frac{f}{c^2}, \qquad (r = 0),$$
$$M_r = -9\frac{EJ}{a}\frac{f}{c^2}, \qquad M_\varphi = -3\frac{EJ}{a}\frac{f}{c^2} \quad (r = c). \tag{38}$$

8. A Numerical Application

We shall now apply the preceding theory to the double-layer lattice dome of Fig. 5.

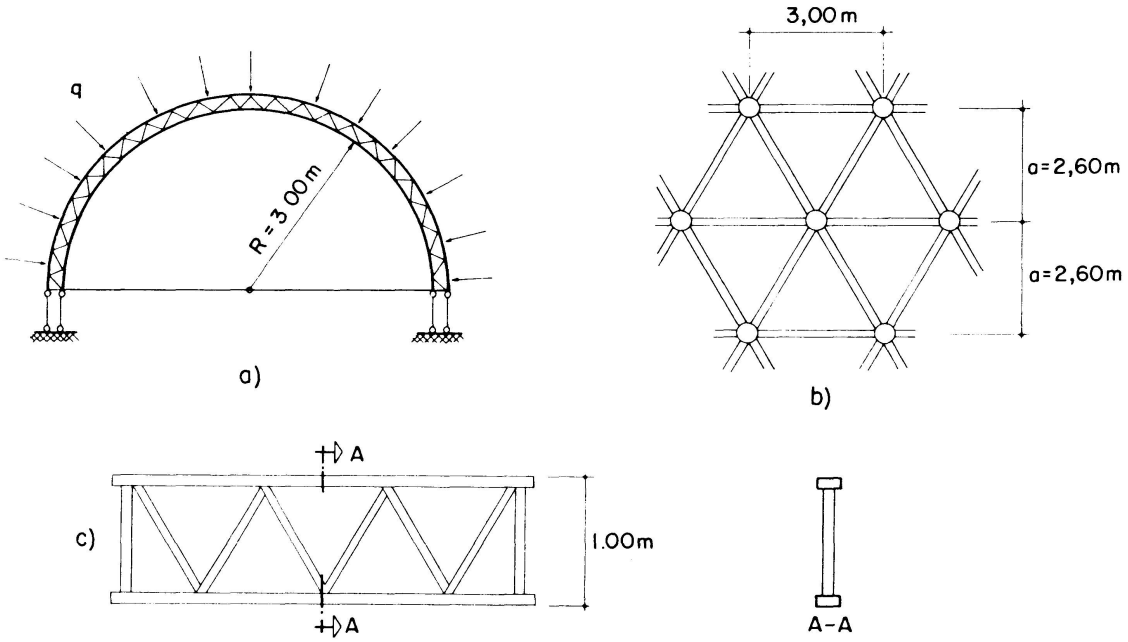

Fig. 5.

It is a dome of 300 m in diameter, whose members are steel trusses with 1 m depth.

The properties of the lattice in the upper region of the dome are found to be

$$F = 40\ \text{cm}^2, \qquad J = 81{,}000\ \text{cm}^4, \qquad a = 260\ \text{cm},$$

$$\lambda = \frac{Ja^2}{F^3} = 85000.$$

If $E = 2.1 \times 10^6\ \text{kg/cm}^2$, the solution of (34), by means a FORTRAN IV program gives, for the minimum of σ,

$$\chi = 14400, \qquad \tau = 13400, \qquad \sigma_{min} = 170.$$

With the above numerical values in (35), we obtain

$$q_{cr} = \sigma_{min} \frac{2 E F^2}{R^2 a^2} = 170 \frac{2 \times 2.1 \times 10^6 \times 40^2}{15000^2 \times 260^2} = 7.6 \times 10^{-2} \text{ kg/cm}^2 = 760 \text{ kg/m}^2,$$

$$f = \frac{\tau F}{a} = \frac{13400 \times 40}{260} = 2050 \text{ cm} = 20.5 \text{ m},$$

$$c = \sqrt{\frac{14400 \times 40 \times 15000}{260}} = 5800 \text{ cm} = 58 \text{ m}.$$

We next use these results in order to evaluate the stress resultants in the post-buckling stage, by means of (37) and (38) ($\mu \cong 0$)

$$Q_{r(r=c)} = -36 \frac{2.1 \times 10^6 \times 8.1 \times 10^4 \times 2.05 \times 10^3}{5.8^3 \times 109 \times 2.6 \times 10^2} = -246 \text{ kg/cm} = 24.6 \text{ t/m},$$

$$M_{r(r=c)} = -9 \frac{2.1 \times 10^6 \times 8.1 \times 10^4 \times 2.05 \times 10^3}{2.6 \times 10^2 \times 5.8^2 \times 10^6} =$$

$$-1.74 \times 10^5 \text{ kgcm/cm} = -174 \text{ tm/m}.$$

The above value of Q_r would make an estimate of the diagonal bars in the trusses possible. We can see that the radial bending moment M_r would bring about plastic deformations.

9. Comparison with Other Theories

In order to check the results of the proceding theory, we compare it with approximate formulas proposed by other authors.

SCHÖNBACH [11] and WRIGHT [8] recommended the formula

$$q_{cr} = \frac{k E F J_x}{l r^2}, \tag{39}$$

in which
- k = 1,25 (SCHÖNBACH) or $k = 1{,}6$ (WRIGHT)
- F cross-section of lattice members (40 cm²)
- J_x = moment of inertia of lattice members
- l = length of lattice members = 300 cm
- r = radius of the dome = 15000 cm

By inserting the appropriate numerical values in (39) we would obtain

$$q_{cr} = 700 \text{ kg/m}^2 \quad \text{for } k = 1.25 \quad \text{and} \quad q_{cr} = 890 \text{ kg/m}^2 \quad \text{for } k = 1.6.$$

BUCKERT [9], [10] in his buckling analysis of orthotropic shells proposed the formula

$$q_{cr} = 0.366\, E \left[\frac{t_m}{R}\right]^2 \left|\frac{t_B}{t_m}\right|^{3/2}, \tag{40}$$

in which

t_m = membrane thickness
t_B = bending thickness
R = radius of dome = 15000 cm

The membrane and the bending thickness will be obtained presently from the analogue model of the lattice shell, i.e., we assume

$$t_m = \frac{F}{a} \quad \text{and} \quad \frac{E\, t_B}{12} = \frac{3\,(3+\mu)\, E\, J}{8\, a}.$$

Then, $t_B = 2.38 \sqrt[3]{\frac{J}{a}}$ and, by inserting the numerical values,

$$t_m = \frac{40}{260} = 0.153 \text{ cm}, \qquad t_B = 2.38 \sqrt[3]{\frac{81{,}000}{260}} = 16.2 \text{ cm}. \tag{41}$$

By substituting all numerical values in (40), we would find

$$q_{cr} = 940 \text{ kg/m}^2.$$

We thus made sure that the present theory is in reasonable agreement with other theories and gives also the shape of the buckled zone.

10. Concluding Remarks

An important conclusion of the present study is that we should avoid applying buckling formulas derived from the theory of uniform shells to lattice domes.

For isotropic shells, membrane and bending thickness are identical. From (41), we can see that, for double-layer lattice domes, the difference between membrane and bending thickness may be considerable. The bending thickness for the above numerical example is larger than the membrane thickness by a factor of a hundred.

We should be also cautious in the choice of the safety factor for the determination of the permissible pressure.

The imperfections in geometry and boundary conditions, as well as the post-buckling deviations in the directions of the external pressure, tend to decrease the theoretical buckling load.

11. References

1. Th. von Kármán, H. S. Tsien: The buckling of spherical shells by external pressure. J. of Aero. Sci., Vol. 7, No. 2, 1939.
2. J. Mason: On the problem of edge disturbances in lattice domes. Abh. der IVBH, Vol. 30, II, 1970.

3. K. KLÖPPEL, R. SCHARDT: Systematische Ableitung von Differentialgleichungen für ebene, anisotrope Flächentragwerke. Stahlbau 2, 1960.
4. J. MASON: Contribuição à Teoria das Estruturas em Superfície Anisótropa. Rio de Janeiro, 1963.
5. K. KLÖPPEL, O. JUNGBLUTH: Beitrag zum Durchschlagproblem dünnwandiger Kugelschalen. Stahlbau 22, Nr. 6, 1953.
6. A. S. WOLMIR: Biegsame Platten und Schalen. Verlag für Bauwesen, Berlin 1962.
7. A. KAPLAN, Y. C. FUNG: A nonlinear theory of bending and buckling of thin elastic shallow spherical shells. NACA, Technical Note 32/2, 1954.
8. D. T. WRIGHT: Membrane forces and buckling in reticulated shells. J. of the St. Div. ASCE, 1965, p. 173–201.
9. K. P. BUCHERT: Zur Stabilität grosser, doppelt gekrümmter und versteifter Schalen. Stahlbau 1965, p. 55–62.
10. K. P. BUCHERT: Buckling considerations in the design and construction of doubly curved space structures. Space Structures, edited by R. M. Davies. Blackwell Scientific Publications, Oxford 1967.
11. W. SCHÖNBACH: Netzkuppeln als Radome. Stahlbau 1969.

Summary

The nonlinear buckling problem of lattice domes with triangular meshes is investigated. The buckled zone is treated as a shallow shell, by accounting for nonlinear terms in the kinematic relations.

The lattice properties are simulated by means of a continuous analogue model.

Results of the theory are compared with approximate formulas in the literature.

Résumé

Le problème du flambage non-linéaire des coupoles à treillis à subdivision triangulaire est étudié. La zone d'instabilité est traitée comme coque surbaissée, en considérant des termes non-linéaires dans les rélations cinématiques.

Les propriétés du treillis sont simulées par un modèle continu. Les résultats de la théorie sont comparés à d'autres formules existant dans la littérature.

Zusammenfassung

Das nichtlineare Stabilitätsproblem der Gitterkuppeln mit dreieckiger Ausfachung wird untersucht. Die Beulfläche wird als flache Schale behandelt, in dem nichtlineare Glieder in den kinematischen Beziehungen berücksichtigt werden.

Das Verhalten des Gitters wird mit einem kontinuierlichen Modell nachgebildet.

Die Ergebnisse der Theorie werden mit anderen Näherungsformeln in der Literatur verglichen.

Leere Seite
Blank page
Page vide

Finite Element Stability Analysis of Thin Shells

Analyse de stabilité de coques minces au moyen de la méthode des éléments finis

Stabilitätsanalyse dünner Schalen mittels der endlichen Elemente-Methode

C. I. MATHEW
B.E., D.I.C., M.Sc. (Eng.) (Lond.), M.ASCE., Principal, Government Polytechnic, Kalamassery, Kerala, India

Introduction

Although the problem of elastic stability belongs inherently to the domain of nonlinear theory of elasticity, important results may be obtained from a linearized theory. The general theory assumes that the loads are conservative and the external loads on the structure are specified as the product of a unit load system and a single load parameter f. A potential energy then exists for the mechanical system consisting of the elastic structure and the external loads. The potential energy has a proper minimum in the stable part but only a stationary value in the unstable part. The critical point may now be characterised by a positive semi-definite second variation of the energy. Two types of singular behaviour due to the loss of stability may now occur characterised by the limit point or the bifurcation point.

Thus although all critical points are characterised by similar Eigenvalue problems, the actual behaviour of the structure at loads in the vicinity of the critical load may vary widely. For Example, flat plates can support loads in their plane far in excess of the critical load. On the other hand, some shell structures fail at loads which are only fraction of the critical loads predicted by the linear theory.

Basic Theory

In a mathematical sense, stability implies a configuration where infinitesimal disturbances will cause only infinitesimal departures from the given equilibrium configuration. In the system investigated here, it is assumed that the stresses

in the model subjected to a conservative set of inplane loads do not change during buckling deformation. This is consistent with the theory of elastic stability.

Thus if T represents the change in potential energy during the buckling deformation, we can write

$$T = U + V, \tag{1}$$

where U is the strain energy caused by the buckling deformation and V is the potential energy of the external loads measured from the unbuckled position.

For structural systems made up of linear elastic material, the change in potential energy T is a quadratic function of the generalised displacements that describe the buckled deformation. Since the first variation of T must vanish to satisfy equilibrium, a sufficient condition that T be a relative minimum is $T \geqq 0$ for all possible buckling deformation configurations. A criterion for determining the critical load can then be that $T = 0$ for some configuration. This is the familiar TIMOSHENKO [1] criterion for stability of elastic systems.

Let
$$U = \tfrac{1}{2} r^T K r \tag{2}$$

and
$$V = -\tfrac{1}{2} r^T f K_s r, \tag{3}$$

where r represents collectively the generalised nodal displacements, K is the flexural stiffness matrix of the model, and K_s is the stability matrix of the model.

Then
$$T = \tfrac{1}{2} r^T (K - f K_s) r = 0. \tag{4}$$

As $T = 0$ for $r \neq 0$, the matrix of the quadratic form $(K - f K_s)$ is positive semidefinite; therefore the critical load is obtained as the lowest root of the determinant equation

$$|K - f K_s| = 0. \tag{5}$$

Stiffness Matrix

The shell is considered as an assemblage of flat elements connected to each other at the nodal points. The stiffness matrix for the element is derived by allowing for three displacements and two rotations at each node.

For a typical rectangular element $ijkl$ shown in Fig. 1 the generalised displacements at the ith node are

$$d_i = \begin{Bmatrix} u_i \\ v_i \\ w_i \\ w_{i,y} \\ -w_{i,x} \end{Bmatrix}. \tag{6}$$

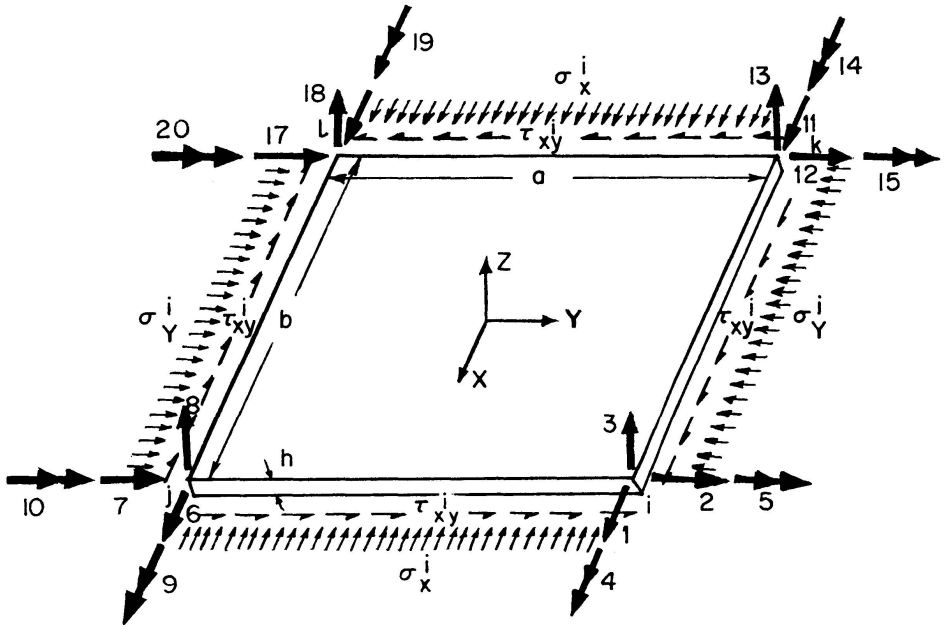

Fig. 1.

Here u_i, v_i, w_i are the displacements along the X, Y, Z directions respectively at the node i.

Selecting the MELOSH-ZIENKIEWICZ [2], [3] displacement functions we have,

$$\begin{aligned} u &= a_1 + a_2 x + a_3 y + a_4 x y, \\ v &= a_5 + a_6 x + a_7 y + a_8 x y, \\ w &= a_9 + a_{10} x + a_{11} y + a_{12} x^2 + a_{13} x y + a_{14} y^2 + a_{15} x^3 \\ &\quad + a_{16} x^2 y + a_{17} x y^2 + a_{18} y^3 + a_{19} x^3 y + a_{20} x y^3 . \end{aligned} \tag{7}$$

Here u, v, w describe displacements along X, Y, Z directions of a point (x, y) in the plate in terms of the constants Eq. (7) may now be written in short form as

$$\begin{Bmatrix} u \\ v \\ w \end{Bmatrix} = P a . \tag{8}$$

Here P is a 3×20 matrix in terms of the variables x, y. a is a 20×1 vector of constants $a_1 \ldots a_{20}$.

Considering all four nodes, the nodal deformation vector of the element is written in the matrix form as

$$r^e = G a . \tag{9}$$

Here, G is a 20×20 matrix in terms of the coordinates of the nodes, and r^e is a 20×1 vector of generalised displacements of the nodes of the element.

The unknown constants a are given by

$$a = G^{-1} r^e . \tag{10}$$

The generalised strains at any point is given by

$$e = \begin{Bmatrix} \dfrac{\partial u}{\partial x} \\ \dfrac{\partial v}{\partial y} \\ \dfrac{\partial u}{\partial y} + \dfrac{\partial v}{\partial x} \\ -\dfrac{\partial^2 w}{\partial x^2} \\ -\dfrac{\partial^2 w}{\partial y^2} \\ 2\dfrac{\partial^2 w}{\partial x\, \partial y} \end{Bmatrix} \tag{11}$$

or
$$e = C a = C G^{-1} r^e. \tag{12}$$

The stress at any point is given by

$$\sigma = D e = D C G^{-1} r^e. \tag{13}$$

For an isotropic material, the 6×6 matrix of elastic constants D is given by

$$D = \begin{bmatrix} D_1 & & & & & \\ D_1 & D_1 & & & & \\ 0 & 0 & (1-\mu) D_1/2 & & & \\ 0 & 0 & 0 & D_2 & & \\ 0 & 0 & 0 & D_2 & D_2 & \\ 0 & 0 & 0 & 0 & 0 & (1-\mu) D_2/2 \end{bmatrix}. \tag{14}$$

Here
$$D_1 = E h/(1-\mu^2);\ D_2 = E h^3/12(1-\mu^2),$$
E = Modulus of Elasticity,
μ = Poisson's Ratio,
h = Thickness of the plate element.

Now the strain energy of the element

$$U^e = \tfrac{1}{2} e^T D e\, dv,$$
$$= \tfrac{1}{2} r^{eT} G^{-1\,T} \int_v C^T D C\, dv\, G^{-1} r^e$$

or
$$U^e = \tfrac{1}{2} r^{eT} k^e r^e, \tag{15}$$

where
$$k^e = G^{-1\,T} \int_v C^T D C\, dv\, G^{-1} \tag{16}$$

represents the 20×20 stiffness matrix of the element.

The stiffness matrix of the element as obtained in Eq. (16) is with respect to the element co-ordinate axes $X Y Z$. This matrix is transformed into the

global co-ordinate system PQR to form the cylindrical shell element stiffness matrix k^s so that

$$k^s = T^T k^s T. \tag{17}$$

The 20×20 transformation matrix is given by

$$T = \begin{bmatrix} t_r & & & & \\ & t_1 & & 0 & \\ & & t_r & & \\ & 0 & & t_1 & \end{bmatrix} \tag{18}$$

and the 5×5 matrix t_1 is given by

$$t_1 = \begin{bmatrix} 1 & 0 & 0 & 0 & 0 \\ 0 & \operatorname{Cos} M & -\operatorname{Sin} M & 0 & 0 \\ 0 & \operatorname{Sin} M & \operatorname{Cos} M & 0 & 0 \\ 0 & 0 & 0 & 1 & 0 \\ 0 & 0 & 0 & 0 & \operatorname{Cos} M \end{bmatrix}. \tag{19}$$

The t_r matrix is obtained by substituting $-N$ for M in Eq. (19). The angles M and N are defined in Fig. 2. The stiffness matrix of the shell element is given in appendix 1.

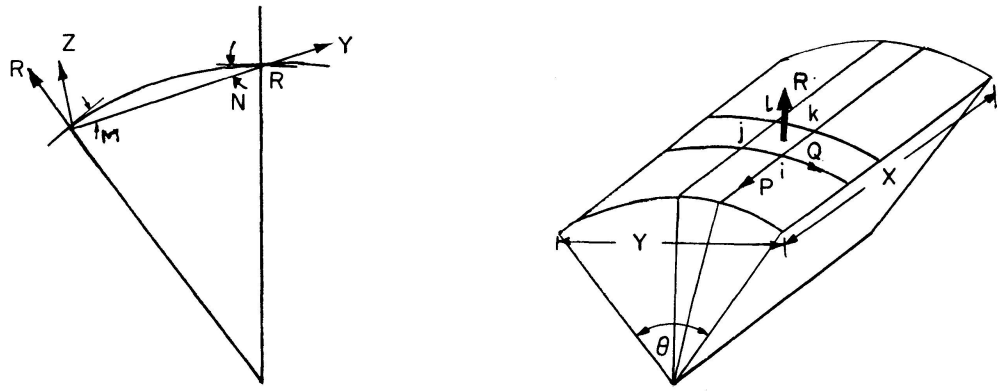

Fig. 2.

Stability Matrix

The potential energy of loads of the element shown in Fig. 1, measured from the unbuckled state is

$$V = -\frac{h}{2} \int_{-a/2}^{a/2} \int_{-b/2}^{b/2} \left[\sigma_x^i \left(\frac{\partial v}{\partial x} \right)^2 + \sigma_y^i \left(\frac{\partial u}{\partial y} \right)^2 + \sigma_x^i \left(\frac{\partial w}{\partial x} \right)^2 + \sigma_y^i \left(\frac{\partial w}{\partial y} \right)^2 + 2 \tau_{xy}^i \frac{\partial w}{\partial x} \frac{\partial w}{\partial y} \right] dx\, dy. \tag{20}$$

Here σ_x^i, and σ_y^i are the initial direct stresses in the x and y directions and τ_{xy}^i is the initial shear stress. In matrix form Eq. (20) may be written as

$$V = -\frac{h}{2}\int_{-a/2}^{a/2}\int_{-b/2}^{b/2} \begin{Bmatrix} \frac{\partial v}{\partial x} \\ \frac{\partial u}{\partial y} \\ \frac{\partial w}{\partial x} \\ \frac{\partial w}{\partial y} \end{Bmatrix}^T \begin{bmatrix} \sigma_x^i & 0 & 0 & 0 \\ 0 & \sigma_y^i & 0 & 0 \\ 0 & 0 & \sigma_x^i & \tau_{xy}^i \\ 0 & 0 & \tau_{xy}^i & \sigma_y^i \end{bmatrix} \begin{Bmatrix} \frac{\partial v}{\partial x} \\ \frac{\partial u}{\partial y} \\ \frac{\partial w}{\partial x} \\ \frac{\partial w}{\partial y} \end{Bmatrix} dx\,dy. \tag{21}$$

Now

$$\begin{Bmatrix} \frac{\partial v}{\partial x} \\ \frac{\partial u}{\partial y} \\ \frac{\partial w}{\partial x} \\ \frac{\partial w}{\partial y} \end{Bmatrix} = Ba = BG^{-1}r^e, \tag{22}$$

where B is a 4×20 matrix in variables x and y.

Thus Eq. (21) reduces to

$$V = -\frac{h}{2}\int_{-a/2}^{a/2}\int_{-b/2}^{b/2} r^{eT} G^{-1\,T} B^T \sigma^i B G^{-1} r^e\,dx\,dy. \tag{23}$$

Here σ^i is the initial stress matrix given in Eq. (21).

The stability matrix for the element is thus obtained as

$$k_s = -h\int_{-a/2}^{a/2}\int_{-b/2}^{b/2} G^{-1\,T} B^T \sigma^i B G^{-1}\,dx\,dy. \tag{24}$$

The reoriented shell element stability matrix is obtained by the same transformation used in the stiffness matrix. Thus

$$k_s^s = T^T k_s T.$$

For buckling under axial loads

$$\sigma_y^i = \tau_{xy}^i = 0.$$

The shell stability matrix under uniform axial compression for a rectangular element is given in appendix I.

Analysis

The general stiffness matrix K and the general stability matrix K_s are assembled using the code number technique [4]. The critical load is determined as the lowest Eigenvalue of the determinant Eq. (5). The standard computer program is capable of handling shells having various boundary conditions, varying thickness, openings and anisotropic material. Plate stability [5], [7] is only a special case of shell stability [6] problem in which M and N are zero.

To find the critical stress intensity on the structure, Eq. (5) is divided by f and brought to the form

$$\frac{1}{f} K r_i = K_s r, \tag{25}$$

in which both r_i and r represent the mode of the first buckling failure. An arbitrary normalised vector is assumed for r and r_i is determined. The coefficient $1/f$ of r_i when it is normalised represents the reciprocal of the first approximation of the lowest critical intensity. The normalised vector r_i thus found is used for r in Eq. (25) and the operation is repeated as the successive Eigenvalues converge. To facilitate faster convergence, and to determine the true mode shape a modification in the procedure is introduced, when two successive approximations of f come within about one percent.

The sought Eigenvalue f of Eq. (25) is replaced by

$$f = m f_1 + f_2, \tag{26}$$

where f_1 is the already found approximation, and m is the coefficient somewhat smaller than unity, such as 0.9, and f_2 – the required addition to be found.

Eq. (25) is then brought to the form,

$$\frac{1}{f_2} (K - m f_1 K_s) r_i = K_s r. \tag{27}$$

The matrix $(K - m f_1 K_s)$ is known and Eq. (27) is solved for f_2 to the required accuracy in the way, in which the Eq. (25) has just been used. The mode of failure is described closely by the eigen vector r_i found from Eq. (27). The subsequent eigenvalues may be found by the same procedure after sweeping the eigen-vectors found from the trial vector r.

The critical loads of curved panels and cylindrical shells simply supported on all edges under uniform axial compression are determined and are compared with the theoretical results [1]. In all the examples the Young's Modulus is unity and Poisson's ratio 1/3.

The critical loads of curved panels $12'' \times 12'' \times 1''$ subtending angles 0° (plate), 10°, 20°, and 30° at centre, simply supported on all edges, for various element sizes are tabulated in Table 1. The critical load of a cylindrical shell

is determined by analysing a 90° sector of the shell with appropriate boundary conditions. Table 2 gives the critical load on a shell simply supported on both edges. The sector has a height of 12″, thickness of 1″, and a quadrant length of 54″. In general the values obtained by the finite element method show good agreement with the existing theoretical results.

Cylindrical shells of medium length under axial compression have a large number of simultaneous buckling modes. Table 3 which gives the first five Eigenvalues of a matrix of order 383 and half band width 31, illustrates the effectiveness of the method adopted to isolate the close Eigenvalues. Analysis of a 90° sector of a simply supported shell with 36×8 elements involved a matrix of order 1485 and half band width of 51. A similar shell with 18×12 elements involved a matrix of order and half band width 1111×71. The critical load in each case was determined in about 450 seconds on IBM 360.

Table 1. Unit Stress at Critical Load

Elements	0°	10°	20°	30°
3×3	0.023065	0.023775	0.025894	0.029388
4×4	0.024120	0.024805	0.026850	0.030234
6×6	0.024947	0.025623	0.027610	0.030910
8×8	0.025267	0.025933	0.027900	0.031177
Elastic Solution	0.025702	0.026373	0.028755	0.032646

Table 2. Unit Stress at Critical Load

Elements	90° Shell $54'' \times 12'' \times 1''$
2×9	0.015658
4×18	0.017085
8×36	0.017503
Elastic Solution	0.017813

Table 3. Eigenvalues 90° Shell $54'' \times 12'' \times 1''$ 4×18 Elements

1	0.017085
2	0.017474
3	0.018425
4	0.022983
5	0.028683

Table 4. Unit Stress at Critical Load

Full Circle Solution	90° Shell $72'' \times 96'' \times 1''$	90° Shell $72'' \times 48'' \times 1''$
Fixed at both Ends	0.012858	0.013467
Simply supported at both ends	0.012561	0.012561
Elastic Solution Simply supported Shell	0.013359	0.013359

The effect of edge conditions on the critical load was also studied by doubling the length of the shell. Table 4 indicates that the critical load of a shell of length equal to its diameter, is that of a simply supported shell irrespective of the boundary conditions.

Conclusions

1. Finite element solutions on subdivision of elements converge monotonically to the theoretical values providing a lowerbound on the theoretical solutions.

2. The results confirm the general validity of the finite element technique in problems of buckling of cylindrical shells.

3. The usefulness of the method lies largely in its applicability to problems for which theoretical solutions are not available. The finite element method overcomes the problem of irregular boundary conditions, nonuniform thickness, segmentation of shells and openings in the shell.

4. To obtain meaningful results, the model should have sufficient number of elements to describe the buckling mode. Thus any shell buckling problem involves determination of Eigenvalues of large matrices. This is overcome by the new method devised in the paper.

5. The presence of imperfections in the shape and properties of the shell make the theory inapplicable.

Acknowledgements

The invaluable assistance of Dr. A. Hrennikoff, Professor Emeritus, University of British Columbia, Vancouver, and the free computer facilities received from the university of British Columbia computing center are gratefully acknowledged.

Appendix I

Table 5 gives the 20×20 stiffness, or stability matrix for a general rectangular cylindrical shell element. Entries of the stiffness matrix are obtained by substituting Table 6 in Table 5 and those of the stability matrix by substituting Table 7 in Table 5.

Table 5

Symmetrical

	1	2	3	4	5
1	X_{11}				
2	$Y_{11}\,\mathrm{Cos}\,N$	$Y_{12}\,\mathrm{Cos}^2 N + F_{13}\,\mathrm{Sin}^2 N$			
3	$Y_{11}\,\mathrm{Sin}\,N$	$(Y_{12}-F_{13})\,\mathrm{Cos}\,N \cdot \mathrm{Sin}\,N$	$Y_{12}\,\mathrm{Sin}^2 N + F_{13}\,\mathrm{Cos}^2 N$		
4	—	$-m^x_{13}\,\mathrm{Sin}\,N$	$m^x_{13}\,\mathrm{Cos}\,N$	m^x_{14}	
5	—	$-m^y_{13}\,\mathrm{Cos}\,N\,\mathrm{Sin}\,N$	$m^y_{13}\,\mathrm{Cos}^2 N$	$m^y_{14}\,\mathrm{Cos}\,N$	$m^y_{15}\,\mathrm{Cos}^2 N$
6	X_{21}	$X_{22}\,\mathrm{Cos}\,N$	$X_{22}\,\mathrm{Sin}\,N$	—	—
7	$Y_{21}\,\mathrm{Cos}\,M$	$Y_{22}\,\mathrm{Cos}\,N\,\mathrm{Cos}\,M - F_{23}\,\mathrm{Sin}\,N\,\mathrm{Sin}\,M$	$Y_{22}\,\mathrm{Cos}\,M\,\mathrm{Sin}\,N + F_{23}\,\mathrm{Cos}\,N\,\mathrm{Sin}\,M$	$F_{24}\,\mathrm{Sin}\,M$	$F_{25}\,\mathrm{Cos}\,N\,\mathrm{Sin}\,M$
8	$-Y_{21}\,\mathrm{Sin}\,M$	$-Y_{22}\,\mathrm{Cos}\,N\,\mathrm{Sin}\,M - F_{23}\,\mathrm{Cos}\,M\,\mathrm{Sin}\,N$	$-Y_{22}\,\mathrm{Sin}\,N\,\mathrm{Sin}\,M + F_{23}\,\mathrm{Cos}\,N\,\mathrm{Cos}\,M$	$F_{24}\,\mathrm{Cos}\,N$	$F_{25}\,\mathrm{Cos}\,N\,\mathrm{Cos}\,M$
9	—	$-m^x_{23}\,\mathrm{Sin}\,N$	$m^x_{23}\,\mathrm{Cos}\,N$	m^x_{24}	$m^x_{25}\,\mathrm{Cos}\,N$
10	—	$-m^y_{23}\,\mathrm{Cos}\,M\,\mathrm{Sin}\,N$	$m^y_{23}\,\mathrm{Cos}\,N\,\mathrm{Cos}\,M$	$m^y_{24}\,\mathrm{Cos}\,M$	$m^y_{25}\,\mathrm{Cos}\,N\,\mathrm{Cos}\,M$
11	X_{31}	$X_{32}\,\mathrm{Cos}\,N$	$X_{32}\,\mathrm{Sin}\,N$	—	—
12	$Y_{31}\,\mathrm{Cos}\,N$	$Y_{32}\,\mathrm{Cos}^2 N + F_{33}\,\mathrm{Sin}^2 N$	$(Y_{32}-F_{33})\,\mathrm{Cos}\,N \cdot \mathrm{Sin}\,N$	$-F_{34}\,\mathrm{Sin}\,N$	$-F_{35}\,\mathrm{Cos}\,N\,\mathrm{Sin}\,N$
13	$Y_{31}\,\mathrm{Sin}\,N$	$(Y_{32}-F_{33})\,\mathrm{Cos}\,N \cdot \mathrm{Sin}\,N$	$Y_{32}\,\mathrm{Sin}^2 N + F_{33}\,\mathrm{Cos}^2 N$	$F_{34}\,\mathrm{Cos}\,N$	$F_{35}\,\mathrm{Cos}^2 N$
14	—	$-m^x_{33}\,\mathrm{Sin}\,N$	$m^x_{33}\,\mathrm{Cos}\,N$	m^x_{34}	$m^x_{35}\,\mathrm{Cos}\,N$
15	—	$-m^y_{33}\,\mathrm{Cos}\,N\,\mathrm{Sin}\,N$	$m^y_{33}\,\mathrm{Cos}^2 N$	$m^y_{34}\,\mathrm{Cos}\,N$	$m^y_{35}\,\mathrm{Cos}^2 N$
16	X_{41}	$X_{42}\,\mathrm{Cos}\,N$	$X_{42}\,\mathrm{Sin}\,N$	—	—
17	$Y_{41}\,\mathrm{Cos}\,M$	$Y_{42}\,\mathrm{Cos}\,N\,\mathrm{Cos}\,M - F_{43}\,\mathrm{Sin}\,N\,\mathrm{Sin}\,M$	$Y_{42}\,\mathrm{Cos}\,M\,\mathrm{Sin}\,N + F_{43}\,\mathrm{Cos}\,N\,\mathrm{Sin}\,M$	$F_{44}\,\mathrm{Sin}\,M$	$F_{45}\,\mathrm{Cos}\,N\,\mathrm{Sin}\,M$
18	$-Y_{41}\,\mathrm{Sin}\,M$	$-Y_{42}\,\mathrm{Cos}\,N\,\mathrm{Sin}\,M - F_{43}\,\mathrm{Cos}\,M\,\mathrm{Sin}\,N$	$-Y_{42}\,\mathrm{Sin}\,N\,\mathrm{Sin}\,M + F_{43}\,\mathrm{Cos}\,N\,\mathrm{Cos}\,M$	$F_{44}\,\mathrm{Cos}\,M$	$F_{45}\,\mathrm{Cos}\,N\,\mathrm{Cos}\,M$
19	—	$-m^x_{43}\,\mathrm{Sin}\,N$	$m^x_{43}\,\mathrm{Cos}\,N$	m^x_{44}	$m^x_{45}\,\mathrm{Cos}\,N$
20	—	$-m^y_{43}\,\mathrm{Cos}\,M\,\mathrm{Sin}\,N$	$m^y_{43}\,\mathrm{Cos}\,N\,\mathrm{Cos}\,M$	$m^y_{44}\,\mathrm{Cos}\,M$	$m^y_{45}\,\mathrm{Cos}\,N\,\mathrm{Cos}\,M$

6	X_{11}				
7	$-Y_{11}\,\mathrm{Cos}\,M$	$Y_{12}\,\mathrm{Cos}^2 M + F_{13}\,\mathrm{Sin}^2 M$	Symmetrical		
8	$Y_{11}\,\mathrm{Sin}\,M$	$(F_{13}-Y_{12})\,\mathrm{Cos}\,M \cdot \mathrm{Sin}\,M$	$Y_{12}\,\mathrm{Sin}^2 M + F_{13}\,\mathrm{Cos}^2 M$		
9	—	$-m^x_{13}\,\mathrm{Sin}\,M$	$-m^x_{13}\,\mathrm{Cos}\,M$	m^x_{14}	
10	—	$m^y_{13}\,\mathrm{Cos}\,M\,\mathrm{Sin}\,M$	$m^y_{13}\,\mathrm{Cos}^2 M$	$-m^y_{14}\,\mathrm{Cos}\,M$	$m^y_{15}\,\mathrm{Cos}^2 M$
11	X_{41}	$-X_{42}\,\mathrm{Cos}\,M$	$X_{42}\,\mathrm{Sin}\,M$	—	—
12	$-Y_{41}\,\mathrm{Cos}\,N$	$Y_{42}\,\mathrm{Cos}\,N\,\mathrm{Cos}\,M - F_{43}\,\mathrm{Sin}\,N\,\mathrm{Sin}\,M$	$-Y_{42}\,\mathrm{Cos}\,N\,\mathrm{Sin}\,M - F_{43}\,\mathrm{Cos}\,M\,\mathrm{Sin}\,N$	$F_{44}\,\mathrm{Sin}\,N$	$-F_{45}\,\mathrm{Cos}\,M\,\mathrm{Sin}\,N$
13	$-Y_{41}\,\mathrm{Sin}\,N$	$Y_{42}\,\mathrm{Cos}\,M\,\mathrm{Sin}\,N + F_{43}\,\mathrm{Cos}\,N\,\mathrm{Sin}\,M$	$-Y_{42}\,\mathrm{Sin}\,N\,\mathrm{Sin}\,M + F_{43}\,\mathrm{Cos}\,N\,\mathrm{Cos}\,M$	$-F_{44}\,\mathrm{Cos}\,N$	$F_{45}\,\mathrm{Cos}\,N\,\mathrm{Cos}\,M$
14	—	$-m^x_{43}\,\mathrm{Sin}\,M$	$-m^x_{43}\,\mathrm{Cos}\,M$	m^x_{44}	$-m^x_{45}\,\mathrm{Cos}\,M$
15	—	$m^y_{43}\,\mathrm{Cos}\,N\,\mathrm{Sin}\,M$	$m^y_{43}\,\mathrm{Cos}\,N\,\mathrm{Cos}\,M$	$-m^y_{44}\,\mathrm{Cos}\,N$	$m^y_{45}\,\mathrm{Cos}\,N\,\mathrm{Cos}\,M$
16	X_{31}	$-X_{32}\,\mathrm{Cos}\,M$	$X_{32}\,\mathrm{Sin}\,M$	—	—
17	$-Y_{31}\,\mathrm{Cos}\,M$	$Y_{32}\,\mathrm{Cos}^2 M + F_{33}\,\mathrm{Sin}^2 M$	$(F_{33}-Y_{32})\,\mathrm{Cos}\,M \cdot \mathrm{Sin}\,M$	$-F_{34}\,\mathrm{Sin}\,M$	$F_{35}\,\mathrm{Cos}\,M\,\mathrm{Sin}\,M$
18	$Y_{31}\,\mathrm{Sin}\,M$	$(F_{33}-Y_{32})\,\mathrm{Cos}\,M \cdot \mathrm{Sin}\,M$	$Y_{32}\,\mathrm{Sin}^2 M + F_{33}\,\mathrm{Cos}^2 M$	$-F_{34}\,\mathrm{Cos}\,M$	$F_{35}\,\mathrm{Cos}^2 M$
19	—	$-m^x_{33}\,\mathrm{Sin}\,M$	$-m^x_{33}\,\mathrm{Cos}\,M$	m^x_{34}	$-m^x_{35}\,\mathrm{Cos}\,M$
20	—	$m^y_{33}\,\mathrm{Cos}\,M\,\mathrm{Sin}\,M$	$m^y_{33}\,\mathrm{Cos}^2 M$	$-m^y_{34}\,\mathrm{Cos}\,M$	$m^y_{35}\,\mathrm{Cos}^2 M$
	6	7	8	9	10

11	X_{11}				
12	$-Y_{11}\ \mathrm{Cos}\ N$	$Y_{12}\ \mathrm{Cos}^2\ N$ $+F_{13}\ \mathrm{Sin}^2\ N$	Symmetrical		
13	$-Y_{11}\ \mathrm{Sin}\ N$	$(Y_{12}-F_{13})\ \mathrm{Cos}\ N$ $\cdot \mathrm{Sin}\ N$	$Y_{12}\ \mathrm{Sin}^2\ N$ $+F_{13}\ \mathrm{Cos}^2\ N$		
14	—	$-m^x_{13}\ \mathrm{Sin}\ N$	$m^x_{13}\ \mathrm{Cos}\ N$	m^x_{14}	
15	—	$m^y_{13}\ \mathrm{Cos}\ N\ \mathrm{Sin}\ N$	$-m^y_{13}\ \mathrm{Cos}^2\ N$	$-m^y_{14}\ \mathrm{Cos}\ N$	$m^y_{15}\ \mathrm{Cos}^2\ N$
16	X_{21}	$-X_{22}\ \mathrm{Cos}\ N$	$-X_{22}\ \mathrm{Sin}\ N$	—	—
17	$-Y_{21}\ \mathrm{Cos}\ M$	$Y_{22}\ \mathrm{Cos}\ N\ \mathrm{Cos}\ M$ $-F_{23}\ \mathrm{Sin}\ N\ \mathrm{Sin}\ M$	$Y_{22}\ \mathrm{Cos}\ M\ \mathrm{Sin}\ N$ $+F_{23}\ \mathrm{Cos}\ N\ \mathrm{Sin}\ M$	$F_{24}\ \mathrm{Sin}\ M$	$-F_{25}\ \mathrm{Cos}\ N\ \mathrm{Sin}\ M$
18	$Y_{21}\ \mathrm{Sin}\ M$	$-Y_{22}\ \mathrm{Cos}\ N\ \mathrm{Sin}\ M$ $-F_{23}\ \mathrm{Cos}\ M\ \mathrm{Sin}\ N$	$-Y_{22}\ \mathrm{Sin}\ N\ \mathrm{Sin}\ M$ $+F_{23}\ \mathrm{Cos}\ N\ \mathrm{Cos}\ M$	$F_{24}\ \mathrm{Cos}\ M$	$-F_{25}\ \mathrm{Cos}\ N\ \mathrm{Cos}\ M$
19	—	$-m^x_{23}\ \mathrm{Sin}\ N$	$m^x_{23}\ \mathrm{Cos}\ N$	m^x_{24}	$-m^x_{25}\ \mathrm{Cos}\ N$
20	—	$m^y_{23}\ \mathrm{Cos}\ M\ \mathrm{Sin}\ N$	$-m^y_{23}\ \mathrm{Cos}\ N\ \mathrm{Cos}\ M$	$-m^y_{24}\ \mathrm{Cos}\ M$	$m^y_{25}\ \mathrm{Cos}\ N\ \mathrm{Cos}\ M$
	11	12	13	14	15

16	X_{11}				
17	$X_{11}\ \mathrm{Cos}\ M$	$Y_{12}\ \mathrm{Cos}^2\ M$ $+F_{13}\ \mathrm{Sin}^2\ M$	Symmetrical		
18	$-Y_{11}\ \mathrm{Sin\ M}$	$(F_{13}-Y_{12})\ \mathrm{Cos}\ M$ $\cdot \mathrm{Sin}\ M$	$Y_{12}\ \mathrm{Sin}^2\ M$ $+F_{13}\ \mathrm{Cos}^2\ M$		
19	—	$-m^x_{13}\ \mathrm{Sin}\ M$	$-m^x_{13}\ \mathrm{Cos}\ M$	m^x_{14}	
20	—	$-m^y_{13}\ \mathrm{Cos}\ M\ \mathrm{Sin}\ M$	$-m^y_{13}\ \mathrm{Cos}^2\ M$	$m^y_{14}\ \mathrm{Cos}\ M$	$m^y_{15}\ \mathrm{Cos}^2\ M$
	16	17	18	19	20

Table 6

The substitution of the following values in Table 5 will yield cylindrical shell element stiffness matrix.

$$F_{13} = (4k^4+4+2.8k^2-0.8\mu k^2)\, L/a\, k^3$$
$$F_{23} = (-4k^4+2-2.8k^2+0.8\mu k^2)\, L/a\, k^3$$
$$F_{33} = (2k^4-4-2.8k^2+0.8\mu k^2)\, L/a\, k^3$$
$$F_{43} = (-2k^4-2+2.8k^2-0.8\mu k^2)\, L/a\, k^3$$
$$F_{24} = (2k^2+0.2-0.2\mu)\, L/k$$
$$F_{34} = (-k^2+0.2+0.8\mu)\, L/k$$
$$F_{44} = (k^2-0.2+0.2\mu)\, L/k$$
$$F_{25} = (1-0.2k^2-0.8\mu k^2)\, L/k^2$$
$$F_{35} = (-2-0.2k^2+0.2\mu k^2)\, L/k^2$$
$$F_{45} = (-1+0.2k^2-0.2\mu k^2)\, L/k^2$$

$$m^x_{13} = (-2k^2-0.2-0.8\mu)\, L/k \qquad m^y_{13} = (2/k^2+0.2+0.8\mu)\, L$$
$$m^x_{23} = (-2k^2-0.2+0.2\mu)\, L/k \qquad m^y_{23} = (1/k^2-0.2-0.8\mu)\, L$$
$$m^x_{33} = (-k^2+0.2+0.8\mu)\, L/k \qquad m^y_{33} = (2/k^2+0.2-0.2\mu)\, L$$
$$m^x_{43} = (-k^2+0.2-0.2\mu)\, L/k \qquad m^y_{43} = (1/k^2-0.2+0.2\mu)\, L$$
$$m^x_{14} = (4-4\mu+20k^2)\, a\, L/15\, k \qquad m^y_{14} = -\mu\, a\, L$$
$$m^x_{24} = (-1+\mu+10k^2)\, a\, L/15\, k \qquad m^y_{24} = 0$$
$$m^x_{34} = (-4+4\mu+10k^2)\, a\, L/15\, k \qquad m^y_{34} = 0$$
$$m^x_{44} = (1-\mu+5k^2)\, a\, L/15\, k \qquad m^y_{44} = 0$$
$$m^y_{15} = (20+4k^2-4\mu k^2)\, a\, L/15\, k$$
$$m^x_{25} = 0 \qquad m^y_{25} = (10-4k^2+4\mu k^2)\, a\, L/15\, k$$
$$m^x_{35} = 0 \qquad m^y_{35} = (10-k^2+\mu k^2)\, a\, L/15\, k$$
$$m^x_{45} = 0 \qquad m^y_{45} = (5+k^2-\mu k^2)\, a\, L/15\, k$$

$$X_{11} = \left[\frac{1}{3k}+\frac{(1-\mu)k}{6}\right] D_1 \quad : \quad Y_{11} = \left[\frac{\mu}{4}+\frac{(1-\mu)}{8}\right] D_1$$
$$X_{21} = \left[\frac{1}{6k}-\frac{(1-\mu)k}{6}\right] D_1 \quad : \quad Y_{21} = \left[-\frac{\mu}{4}+\frac{(1-\mu)}{8}\right] D_1$$
$$X_{31} = \left[-\frac{1}{3k}+\frac{(1-\mu)k}{12}\right] D_1 : \quad Y_{31} = -Y_{21}$$
$$X_{41} = \left[-\frac{1}{6k}-\frac{(1-\mu)k}{12}\right] D_1 : \quad Y_{41} = -Y_{11}$$
$$X_{12} = Y_{11} \quad : \quad Y_{12} = \left[\frac{k}{3}+\frac{(1-\mu)}{6k}\right] D_1$$
$$X_{22} = -Y_{21} \quad : \quad Y_{22} = \left[-\frac{k}{3}+\frac{(1-\mu)}{12k}\right] D_1$$
$$X_{32} = Y_{21} \quad : \quad Y_{32} = \left[\frac{k}{6}-\frac{(1-\mu)}{6k}\right] D_1$$
$$X_{42} = -Y_{21} \quad : \quad Y_{42} = \left[-\frac{k}{6}-\frac{(1-\mu)}{12k}\right] D_1$$

Here,
$D_1 = E\,h/(1-\mu^2)$ — $k = b/a$, ratio of the sides
$D_2 = E\,h^3/12\,(1-\mu^2)$ — $L = D_2/a$
μ = Poisson's ratio — a = Length of Element along the "Y" axis
E = Young's modulus — b = Length of Element along the "X" axis
h = Thickness of the shell

Table 7

$X_{11} = 0$

$Y_{11} = 0$

$X_{21} = 0$

$Y_{21} = 0$

$X_{31} = 0$

$Y_{31} = -Y_{21}$

$X_{41} = 0$

$Y_{41} = -Y_{11}$

$Y_{12} = \dfrac{a\,h}{6\,b}\,\sigma_x^i$

$X_{22} = -Y_{21}$

$Y_{22} = \dfrac{a\,h}{12\,b}\,\sigma_x^i$

$X_{32} = Y_{21}$

$Y_{32} = -\dfrac{a\,h}{6\,b}\,\sigma_x^i$

$X_{42} = -Y_{11}$

$Y_{42} = -\dfrac{a\,h}{12\,b}\,\sigma_x^i$

$F_{13} = 276\,A$

$m_{13}^x = -33\,a\,A$

$m_{13}^y = 21\,b\,A$

$F_{23} = 102\,A$

$m_{23}^x = 19.5\,a\,A$

$m_{23}^y = 10.5\,b\,A$

$F_{33} = -276\,A$

$m_{33}^x = 33\,a\,A$

$m_{33}^y = 21\,b\,A$

$F_{43} = -102\,A$

$m_{43}^x = -19.5\,a\,A$

$m_{43}^y = 10.5\,b\,A$

$m_{14}^x = 6\,a^2\,A$

$m_{14}^y = 0$

$F_{24} = -19.5\,a\,A$

$m_{24}^x = -4.5\,a^2\,A$

$m_{24}^y = 0$

$F_{34} = 33\,a\,A$

$m_{34}^x = -6\,a^2\,A$

$m_{34}^y = 0$

$F_{44} = 19.5\,a\,A$

$m_{44}^x = 4.5\,a^2\,A$

$m_{44}^y = 0$

$m_{15}^y = 28\,b^2\,A$

$F_{25} = 10.5\,b\,A$

$m_{25}^x = 0$

$m_{25}^y = 14\,b^2\,A$

$F_{35} = -21\,b\,A$

$m_{35}^x = 0$

$m_{35}^y = -7\,b^2\,A$

$F_{45} = -10.5\,b\,A$

$m_{45}^x = 0$

$m_{45}^y = -3.5\,b^2\,A$

Here $A = \dfrac{h\,a\,\sigma_x^i}{630\,b}$

References

1. TIMOSHENKO, S.: Theory of Elastic stability. McGraw-Hill Book Co., Inc., New York, 1936.
2. MELOSH, R. J.: Basis for Derivation of Matrices for the Direct Stiffness Method. AIAA Journal, Vol. 1, July 1963, pp. 1631–1637.
3. ZIENKIEWICZ, O.C. and CHEUNG, Y. K.: The Finite Element Method in structural and continuum mechanics. McGraw-Hill, 1967.
4. TEZCAN, S. S.: Discussion of Simplified Formulation of Stiffness Matrices by Peter M. Wright, proceedings, paper 3478, April 1963, Journal of Structural Division, ASCE, Dec. 1963, pp. 445–449.
5. KAPUR, K. K. and HARTZ, B. J.: Stability of Plates using the Finite Element Method. Journal of the Engineering Mechanics Division ASCE. April 1966, pp. 177–195.
6. GALLAGHER, R. H., GELLATLY, R. A., PADLOG, J., and MALLET, R. H.: A Discrete Element. Procedure of Thin-Shell Instability Analysis. AIAA Journal, Vol. 5. January 1967, pp. 138–145.
7. HRENNIKOFF, A., MATHEW, C. I., and RAJAN SEN: Stability of Plates Using Rectangular Bar Cells. Publication pending by I.A.B.S.E.

Summary

This paper presents the finite element matrix displacement approach to the stability analysis of shells in general, and to the cylindrical shells in particular. The buckling of deep cylindrical shells is herein investigated considering the membrane and flexural stiffnesses. The stiffness and stability matrices for a rectangular shell element are presented in an explicit form. The critical loads of cylindrical shells have herein been determined using sophisticated Eigenvalue programs. The results obtained are compared with the theoretical solutions to demonstrate the convergence characteristics.

Résumé

Ce travail présente la méthode de la matrice de déplacements basée sur les éléments finis pour l'analyse de stabilité de coques en général et de coques cylindriques minces en particulier. Le voilement de coques cylindriques minces est examiné en tenant compte des rigidités de la membrane et à la flexion. Les matrices de rigidité et de stabilité pour un élément de coque rectangulaire sont présentées en forme explicite. Les charges critiques de coques cylindriques ont été déterminées en utilisant des programmes compliqués de valeurs propres. Les résultats obtenus sont comparés aux solutions théoriques pour en démontrer les caractéristiques concordantes.

Zusammenfassung

Die vorliegende Arbeit befasst sich mit der endlichen Elemente-Matrix-Verschiebungsnäherung zur Stabilitätsanalyse von Schalen im allgemeinen und von zylindrischen Schalen im besonderen. Die Beulung tiefer zylindrischer Schalen ist hierbei inbegriffen, unter Berücksichtigung der Membran- und Biegesteifigkeiten. Die Steifigkeits- und Stabilitätsmatrizen für ein rechteckiges Schalenelement werden in expliziter Form dargelegt. Die kritischen Belastungen zylindrischer Schalen wurden unter Benutzung komplexer Eigenwertprogramme bestimmt. Die erhaltenen Resultate werden mit den theoretischen Lösungen zum Zwecke der Übereinstimmung verglichen.

Dynamic Analysis of Frameworks by Frequency Dependent Stiffness Matrix Approach

Analyse dynamique de poutres à treillis à l'aide de matrices de rigidité dépendant de la fréquence

Dynamische Analyse von Fachwerken durch Näherungen mit frequenzabhängigen Steifigkeitsmatrizen

BÜLENT ÖVÜNÇ
Ph. D., Professor of Civil Engineering
University of Southwestern Louisiana, U.S.A.

Introduction

The dynamic analysis of the multi-element systems has been treated by considering the mass of the system lumped at the joints; the constituent elements are assumed to be massless springs. Natural frequencies and normal modes are obtained by solving characteristic values and characteristic vectors from the determinant function of a singular dynamic matrix either by analytical methods [1], [2], [3], [4] or by numerical methods [4], [5], [6]. The dynamics of frames with nonuniform elastic elements have been investigated by dividing each nonuniform element into uniform subelements [5]. A solution method for an element with continuously varying cross section has been given [7], [8]. In the lumped mass idealization concentrated masses are placed at the joints or nodal points in the directions of the assumed element degrees of freedoms. They are calculated by assuming that the material within the mean locations on either side of the specified displacement behaves like a rigid body while the remainder of the element does not participate in the motion. Therefore the dynamic couplings between the element displacements are excluded. An equivalent mass matrix has been derived in order to include the dynamic couplings between the element displacements [9], [10], [11]. The frequency dependent mass and stiffness matrices for a bar element have been obtained by assuming the displacements be given by a series in ascending powers of the natural circular frequency [11], [12]. Hermitian polynomials are used for

the approximation of the deformations of structural elements such as beams, plates. In the case of plane frame systems, the establishment of the elastic stiffness matrix and of the mass matrix is straightforward [13]. The classical Bernoulli-Euler theory of flexural vibration has been recognized as inadequate for higher modes [14]. The literature of vibration problems based on the TIMOSHENKO's beam theory [15] is voluminous [16], [17], [18], [19]. A general formulation of dynamic matrix and computational procedures [20] have been presented, and the dynamic stiffness coefficients are derived as nondimensional parameters corresponding to the effects of rotatory inertia, and of shear and bending deformation [21], but still the masses are considered as lumped at the joints. By dropping the appropriate parameter, the stiffness coefficients can be applied to a problem with various considerations of Timoshenko's theory, Rayleigh theory, bending and shear, and of Bernoulli-Euler theory. The usual engineering practice to neglect the secondary effects, such as rotatory inertia and transverse shear, in calculating the natural frequencies may be justified to some extent for slender beams, at best for few first modes. In this case, the influence of secondary effects is small. In short beams, particularly for higher modes, the secondary effects become more important. Experimental investigations [22], [23] have shown that the experimental frequencies are lower than the frequencies obtained from refined beam theories, the discrepancies between theory and experiment are rather small. Recent [24] work, on the shear constant of short beams involved in the Timoshenko equation, yielded values to the shear constant as high as 0.870 instead of the original value of 2/3 proposed by Timoshenko in the case of rectangular cross section. Starting from three-dimensional equations of equilibrium of the theory of elasticity and introducing approximate simplifying assumptions, one dimensional theory of wave propagation has been deduced [25]. The equations governing the transverse vibrations of beams have been formulated starting from representative physical assumptions such as zero transverse direct strains and complete freedom to axial displacement [26]. Introducing a suitable expression for axial displacement distribution and using the Kantorovich form of Rayleigh-Ritz procedure simpler equations to various order of approximation have been obtained. The well known elementary beam equation and the Timoshenko theory correspond to some special cases in this formulation.

A new approach is derived for the analysis of systems under dynamic loading. This approach eliminates the concept of lumping the masses of the members at the joints. The masses are assumed to be continuously attached to the member as they are. If a concentrated mass exists on the system, its point of application is considered as a joint of the system. Therefore the inertia forces due to concentrated masses are taken into account as inertial joint forces. The stiffness matrices of the members are obtained considering the inertia forces of the masses of the members and are combined by means of code numbers in order to generate the structure stiffness matrix. The

matrix equation of motion consists of an inertia force term of the concentrated masses, if any, plus a stiffness term being equal to the externally applied dynamic forces plus a term due to fixed end reactions of the members. The natural frequencies are obtained by setting the left side of the matrix equation of motion to zero. Once the natural frequencies have been determined, one natural frequency at a time is introduced into the equations of motion to determine the modal shape corresponding to the natural frequency considered. The member end forces are obtained from the product of member stiffness matrix by the member end displacements and rotations corresponding to one natural frequency at a time.

Procedure of Analysis

A right-handed cartezian coordinate axes system related to the members is selected such that the element centerline is taken as the y axis, while the major and minor principal intertia axes of the cross section constitute the x and z axes respectively. These axes are called "member axes" and are referred to a general stationary $X\ Y\ Z$ cartesian coordinate axes system called "common axes system" Fig. 1. The joint translations and forces acting on the member are

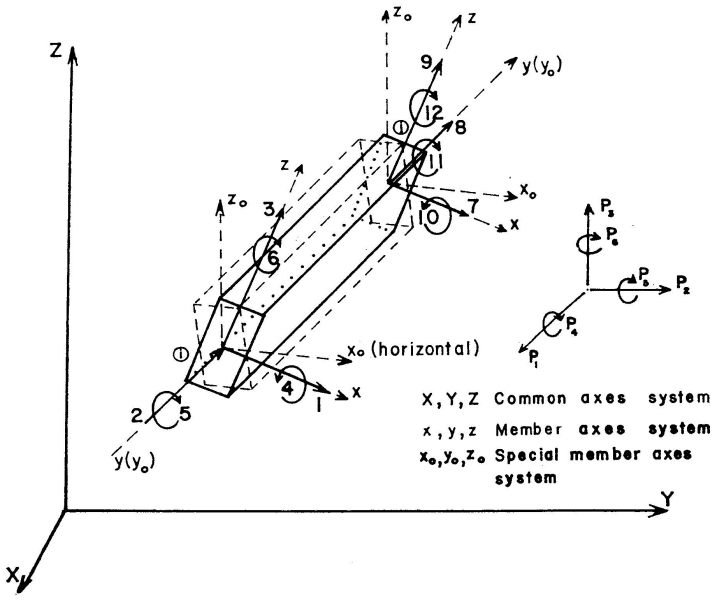

Fig. 1. Coordinate Axes System and Member Freedoms.

positive along the positive directions of the coordinate axes, while the positive directions of the joint rotations and the moments are determined in accordance with the right hand screw rule (Fig. 1). It is assumed that the material is homogeneous and isotropic, the stresses remain within the elastic limites of the material, the strains and the displacements are infinitesimal. The Ber-

noulli-Euler hypothesis for the deflection of the bars such that a plane cross section perpendicular to the centerline of the bar before the deformations remains plane and perpendicular to the centerline after the deformations. The damping is neglected.

The frequency dependent stiffness matrix is derived first for member with uniform cross section subjected to uncoupled deformations such as axial displacements, torsional rotations, and bending in two orthogonal planes. A similar derivation is applied to the member with nonuniform cross section. The effect of rotatory inertia and the transverse shear can be taken into account without any difficulty.

Member with Uniform Cross Section

The frequency dependent member stiffness matrix is derived separately for uncoupled displacements and rotations then they are combined.

Member Subjected to Axial Deformation

The axial displacement function of a bar member subjected to a free vibration is given by

$$d_y = Y(y) f(t) \tag{1}$$

where
$$Y(y) = C_1 \cos \alpha y + C_2 \sin \alpha y \tag{2}$$

and
$$f(t) = A \cos wt + B \sin wt. \tag{3}$$

If the part $Y(y)$ of the axial displacements related with the position y is resolved into its components Y_2 and Y_8 due to d_2 and d_8, respectively (Fig. 1), the Eq. (2) can be written as

$$\begin{Bmatrix} Y_2 \\ Y_8 \end{Bmatrix}^T = (\cos \alpha y \ \ \sin \alpha y) \begin{bmatrix} C_{11} & C_{12} \\ C_{21} & C_{22} \end{bmatrix}. \tag{4}$$

The integration constants $\begin{Bmatrix} C_{11} \\ C_{21} \end{Bmatrix}$ and $\begin{Bmatrix} C_{12} \\ C_{22} \end{Bmatrix}$ are to be determined from the boundary conditions imposed to the displacements Y_2 and Y_8 at an arbitrary time t after the vibration has started. The integration constants A and B are to be determined from the initial conditions of the vibration at time t equal to zero.

Setting the boundary conditions on Y_2 and Y_8 such as:

$$\begin{aligned} &\text{for } Y_2\text{:} \quad \text{at } y=0 \quad Y_2=d_2, \quad \text{at } y=L \quad Y_2=0, \\ &\text{for } Y_8\text{:} \quad \text{at } y=0 \quad Y_8=0, \quad \text{at } Y=L \quad Y_8=d_8, \end{aligned} \tag{5}$$

Introducing the boundary conditions (Eq. (5)) into the Eq. (4) one has

$$[A][C] = [D], \tag{6}$$

where

$$[A] = \begin{bmatrix} 1 & 0 \\ \cos\alpha L & \sin\alpha L \end{bmatrix}, \quad [C] = \begin{bmatrix} C_{11} & C_{12} \\ C_{21} & C_{22} \end{bmatrix} \text{ and } [D] = \begin{bmatrix} d_2 & 0 \\ 0 & d_8 \end{bmatrix}. \tag{7}$$

If the Eq. (6) is premultiplied by $[A]^{-1}$, one has

$$[C] = [A]^{-1}[D]. \tag{8}$$

Replacing $[C]$ in Eq. (4)

$$\begin{Bmatrix} Y_2 \\ Y_8 \end{Bmatrix}^T = \{F_y\}^T [A]^{-1}[D], \tag{9}$$

where $$\{F_y\}^T = (\cos\alpha y \ \ \sin\alpha y)$$

and $$[A]^{-1} = \begin{bmatrix} 1 & 0 \\ -\dfrac{\cos\alpha L}{\sin\alpha L} & \dfrac{1}{\sin\alpha L} \end{bmatrix}. \tag{10}$$

The part of the internal force P related with the position y is

$$P = A E \frac{dY}{dy} = A E (-C_1 \sin\alpha y + C_2 \cos\alpha y), \tag{11}$$

where A is the cross sectional area and E the Young's Modulus.

The member end reactions at $y = 0$ and $y = L$ due to d_2 and d_8 can be written from Eq. (11) as follows.

$$[P] = [H][C], \tag{12}$$

where

$$[P] = \begin{bmatrix} P_{11} & P_{12} \\ P_{21} & P_{22} \end{bmatrix} \text{ and } [H] = A E \alpha \begin{bmatrix} 0 & -1 \\ -\sin\alpha L & \cos\alpha L \end{bmatrix}. \tag{13}$$

If the matrix $[C]$ from Eq. (8) is replaced into the Eq. (12) one has,

$$[P] = [H][A]^{-1}[D]. \tag{14}$$

The member end reactions matrix $[P]$ is the frequency dependent member stiffness matrix $[k]$ when the diagonal displacements matrix $[D]$ is set to be a unit matrix $[U]$; therefore from Eq. (14) one has

$$[k] = [H][A]^{-1}. \tag{15}$$

The expanded form of the frequency dependent member stiffness matrix is:

$$[k] = A E \alpha \begin{bmatrix} \dfrac{1}{\tan\alpha L} & -\dfrac{1}{\sin\alpha L} \\ -\dfrac{1}{\sin\alpha L} & \dfrac{1}{\tan\alpha L} \end{bmatrix}.$$

Member Subjected to Torsional Rotation

The twist angle function of a member subjected to a free vibration is given by

$$\theta = \phi(y) f(t), \tag{16}$$

where

$$\phi(y) = C_1 \cos \alpha y + C_2 \sin \alpha y, \tag{17}$$

$$f(t) = A \cos wt + B \sin wt. \tag{18}$$

If it is noticed that the similarity of twist angle function θ (Eq. (16)) with the axial displacement function d_y (Eq. (1)) and the stress strain relations in both cases, the frequency dependent member stiffness matrix of a member subjected to a torsional rotation can be written easily from the frequency dependent member stiffness matrix of a member subjected to an axial displacement by simply replacing AE axial force rigidity term by GJ torsional rigidity term. Thus the frequency dependent member stiffness matrix under a torsional rotation can be written from Eq. (15) as

$$[k] = GJ\alpha \begin{bmatrix} \dfrac{1}{\tan \alpha L} & -\dfrac{1}{\sin \alpha L} \\ -\dfrac{1}{\sin \alpha L} & \dfrac{1}{\tan \alpha L} \end{bmatrix}. \tag{19}$$

Member Subjected to Bending in YZ Plane

The deflection function of a member subjected to a free vibration is given by

$$d_z = Z(y) f(t), \tag{20}$$

where

$$Z(y) = C_1 \sin \alpha y + C_2 \cos \alpha y + C_3 \sinh \alpha y + C_4 \cosh \alpha y \tag{21}$$

and

$$f(t) = A \cos wt + B \sin wt. \tag{22}$$

If the part $Z(y)$ of the deflection related with the position y is resolved into its components Z_3, Z_4, Z_9 and Z_{10} due to d_3, d_4, d_9 and d_{10}, respectively, the Eq. (21) can be written as

$$\begin{Bmatrix} Z_3 \\ Z_4 \\ Z_9 \\ Z_{10} \end{Bmatrix}^T = (\sin \alpha y \ \cos \alpha y \ \sinh \alpha y \ \cosh \alpha y) \begin{bmatrix} C_{11} & C_{12} & C_{13} & C_{14} \\ C_{21} & C_{22} & C_{23} & C_{24} \\ C_{31} & C_{32} & C_{33} & C_{34} \\ C_{41} & C_{42} & C_{43} & C_{44} \end{bmatrix}. \tag{23}$$

The integration constants

$$\begin{Bmatrix} C_{11} \\ C_{21} \\ C_{31} \\ C_{41} \end{Bmatrix}, \quad \begin{Bmatrix} C_{12} \\ C_{22} \\ C_{32} \\ C_{42} \end{Bmatrix}, \quad \begin{Bmatrix} C_{13} \\ C_{23} \\ C_{33} \\ C_{43} \end{Bmatrix} \quad \text{and} \quad \begin{Bmatrix} C_{14} \\ C_{24} \\ C_{34} \\ C_{44} \end{Bmatrix},$$

are to be determined from the boundary conditions imposed to the displacements and rotations d_3, d_4, d_9 and d_{10} at an arbitrary time t after the vibration has started. The integration constants A and B are to be determined from the initial conditions of the vibration at time t equals zero.

Setting the boundary conditions on Z_3, Z_4, Z_9 and Z_{10} such as

$$\begin{aligned}
&\text{for } Z_3 \quad \text{at } y=0 \quad Z_3 = d_3, \ \frac{dZ_3}{dy}=0, \quad \text{at } y=L \quad Z_3 = 0, \ \frac{dZ_3}{dy}=0,\\
&\text{for } Z_4 \quad \text{at } y=0 \quad Z_4 = 0, \ \frac{dZ_4}{dy}=d_4, \quad \text{at } y=L \quad Z_4 = 0, \ \frac{dZ_4}{dy}=0,\\
&\text{for } Z_9 \quad \text{at } y=0 \quad Z_9 = 0, \ \frac{dZ_9}{dy}=0, \quad \text{at } y=L \quad Z_9 = d_9, \ \frac{dZ_9}{dy}=0,\\
&\text{for } Z_{10} \quad \text{at } y=0 \quad Z_{10}=0, \ \frac{dZ_{10}}{dy}=0, \quad \text{at } y=L \quad Z_{10}=0, \ \frac{dZ_{10}}{dy}=d_{10}.
\end{aligned} \tag{24}$$

Introducing the boundary conditions (Eq. (24)) into the Eq. (23), one has

$$[A][C]=[D], \tag{25}$$

where

$$[A]=\begin{bmatrix} 0 & 1 & 0 & 1 \\ \alpha & 0 & \alpha & 0 \\ \sin\alpha L & \cos\alpha L & \sinh\alpha L & \cosh\alpha L \\ \alpha\cos\alpha L & -\alpha\sin\alpha L & \alpha\cosh\alpha L & \alpha\sinh\alpha L \end{bmatrix},$$

$$[C]=\begin{bmatrix} C_{11} & C_{12} & C_{13} & C_{14} \\ C_{21} & C_{22} & C_{23} & C_{24} \\ C_{31} & C_{32} & C_{33} & C_{34} \\ C_{41} & C_{42} & C_{43} & C_{44} \end{bmatrix} \text{ and } [D]=\begin{bmatrix} d_3 & 0 & 0 & 0 \\ 0 & d_4 & 0 & 0 \\ 0 & 0 & d_9 & 0 \\ 0 & 0 & 0 & d_{10} \end{bmatrix}. \tag{26}$$

If the Eq. (25) is premultiplied by $[A]^{-1}$, one has

$$[C]=[A]^{-1}(D]. \tag{27}$$

Replacing $[C]$ into Eq. (23)

$$\begin{Bmatrix} Z_3 \\ Z_4 \\ Z_9 \\ Z_{10} \end{Bmatrix}^T = \{F_y\}^T[A]^{-1}[D], \tag{28}$$

where

$$\{F_y\}^T=(\sin\alpha y \ \cos\alpha y \ \sinh\alpha y \ \cosh\alpha y). \tag{29}$$

The part of the internal shear force V and bending moment M related with the position y are:

$$V=-EI_x\frac{d^3Z}{dy^3}=-EI_x\alpha^3[-C_1\cos\alpha y+C_2\sin\alpha y+C_3\cosh\alpha y+C_4\sinh\alpha y],$$

and (30)

$$M=-EI_x\frac{d^2Z}{dy^2}=-EI_x\alpha[-C_1\sin\alpha y-C_2\cos\alpha y+C_3\sinh\alpha y+C_4\cosh\alpha y]. \tag{31}$$

The member end reactions V and M at $y=0$ and $y=L$ due to d_3, d_4, d_9 and d_{10} can be written from Eqs. (30) and (31) as follows

$$\begin{bmatrix} P_{11} & P_{12} & P_{13} & P_{14} \\ P_{21} & P_{22} & P_{23} & P_{24} \\ P_{31} & P_{32} & P_{33} & P_{34} \\ P_{41} & P_{42} & P_{43} & P_{44} \end{bmatrix} = E I_x \alpha^2 \begin{bmatrix} -\alpha & 0 & \alpha & 0 \\ 0 & 1 & 0 & -1 \\ \alpha\cos\alpha L & -\alpha\sin\alpha L & -\alpha\cosh\alpha L & -\alpha\sinh\alpha L \\ -\sin\alpha L & -\cos\alpha L & \sinh\alpha L & \cosh\alpha L \end{bmatrix} \begin{bmatrix} C_{11} & C_{12} & C_{13} & C_{14} \\ C_{21} & C_{22} & C_{23} & C_{24} \\ C_{31} & C_{32} & C_{33} & C_{34} \\ C_{41} & C_{42} & C_{43} & C_{44} \end{bmatrix}$$

or putting in matric equation form,

$$[P] = [H][C], \tag{32}$$

where

$$[P] = \begin{bmatrix} P_{11} & P_{12} & P_{13} & P_{14} \\ P_{21} & P_{22} & P_{23} & P_{24} \\ P_{31} & P_{32} & P_{33} & P_{34} \\ P_{41} & P_{42} & P_{43} & P_{44} \end{bmatrix}$$

and

$$[H] = E I_x \alpha^2 \begin{bmatrix} -\alpha & 0 & \alpha & 0 \\ 0 & 1 & 0 & -1 \\ \alpha\cos\alpha L & -\alpha\sin\alpha L & -\alpha\cosh\alpha L & -\alpha\sinh\alpha L \\ -\sin\alpha L & \cos\alpha L & \sinh\alpha L & \cosh\alpha L \end{bmatrix}.$$

If the matrix $[C]$ from Eq. (27) is replaced into Eq. (32) one has

$$[P] = [H][A]^{-1}[D]. \tag{33}$$

The member end reactions matrix $[P]$ is the frequency dependent member stiffness matrix $[k]$ when the diagonal displacements and rotations matrix $[D]$ is set to be a unit matrix $[U]$. Therefore from Eq. (33) one has,

$$[k] = [H][A]^{-1}. \tag{34}$$

The expanded form of the frequency dependent member stiffness matrix is,

$$[k] = \frac{\alpha E I_x}{\Delta} \begin{bmatrix} \alpha^2(\cos\alpha L\sinh\alpha L+\sin\alpha L\cosh\alpha L) & \alpha\sin\alpha L\sinh\alpha L & -\alpha^2(\sin\alpha L+\sinh\alpha L) & -\alpha(\cos\alpha L-\cosh\alpha L) \\ & \sin\alpha L\cosh\alpha L-\cos\alpha L\sinh\alpha L & \alpha(\cos\alpha L-\cosh\alpha L) & -(\sin\alpha L-\sinh\alpha L) \\ & \text{symmetric} & \alpha^2(\cos\alpha L\sinh\alpha L+\sin\alpha L\cosh\alpha L) & -\alpha\sin\alpha L\sinh\alpha L \\ & & & \sin\alpha L\cosh\alpha L-\cos\alpha L\sinh\alpha L \end{bmatrix}, \tag{35}$$

where

$$\Delta = 1-\cos\alpha L\cosh\alpha L.$$

Member Subjected to Bending in XZ Plane

The derivation of the frequency dependent member stiffness matrix under bending in the XZ plane is the same as bending in the YZ plane except that the moment of inertia, I_x, with respect to the x axis has to be replaced by the moment of inertia I_z with respect to the z axis. Therefore the bending stiffness matrix for bending in the XZ plane can be written as

$$[k] = \frac{\alpha E I_z}{\Delta} \begin{bmatrix} \alpha^2(\cos\alpha L \sinh\alpha L + \sin\alpha L \cosh\alpha L) & \alpha \sin\alpha L \sinh\alpha L \\ & \sin\alpha L \cosh\alpha L - \cos\alpha L \sinh\alpha L \\ \text{symmetric} & \end{bmatrix}$$

$$\begin{bmatrix} -\alpha^2(\sin\alpha L + \sinh\alpha L) & -\alpha(\cos\alpha L - \cosh\alpha L) \\ \alpha(\cos\alpha L - \cosh\alpha L) & -(\sin\alpha L - \sinh\alpha L) \\ \alpha^2(\cos\alpha L \sinh\alpha L + \sin\alpha L \cosh\alpha L) & -\alpha \sin\alpha L \sinh\alpha L \\ & \sin\alpha L \cosh\alpha L - \cos\alpha L \sinh\alpha L \end{bmatrix}, \quad (36)$$

where $$\Delta = 1 - \cos\alpha L \cosh\alpha L.$$

The frequency dependent member stiffness matrix $[k]$ for all the member end freedoms is obtained by combining the $[k]$ matrices for the axial displacement (Eq. (15)), the torsional rotation (Eq. (19)) and the bending in two planes (Eqs. (35), (36)).

Member with Nonuniform Cross Section

The variation of the area A, the moment of inertia I of a member with nonuniform cross section is assumed as

$$A = (ny+m), \quad I_x = I_z = (ny+m)^3, \quad J_x = I_x/2. \quad (37)$$

The coefficients n and m are determined from the section properties at both ends of the member.

Member Subjected to Axial Deformation

It can be noticed that the equation of motion of an element subjected to axial deformation,

$$E\frac{\delta^2 dy}{\delta x^2} - \frac{\rho}{g}\frac{\delta^2 dy}{\delta t^2} = 0 \quad (38)$$

is independent of the cross section area A. Therefore the equations from Eq. (1) to Eq. (10) of uniform cross section case remain valid also for this case.

The part of the internal force P related with the position y is

$$P = EA\frac{dY}{dy} = E\alpha(ny+m)(-C_1\sin\alpha y + C_2\cos\alpha y). \quad (39)$$

The member end reactions at $y=0$ and $y=L$ due to d_2 and d_8 can be written from Eq. (39)

$$[P] = [H][C], \tag{40}$$

where

$$[P] = \begin{bmatrix} P_{11} & P_{12} \\ P_{21} & P_{22} \end{bmatrix} \text{ and } [H] = E\alpha \begin{bmatrix} 0 & -m \\ -(nL+m)\sin\alpha L & (nL+m)\cos\alpha L \end{bmatrix}. \tag{41}$$

If the matrix $[C]$ from Eq. (8) is replaced into the Eq. (40), one has,

$$[P] = [H][A]^{-1}[D]. \tag{42}$$

The member end reactions matrix $[P]$ is the frequency dependent member stiffness matrix when the diagonal displacements matrix $[D]$ is set to be a unit matrix $[U]$. Therefore from Eq. (42) one has

$$[k] = [H][A]^{-1}. \tag{43}$$

The expanded form of the frequency dependent member stiffness matrix is

$$[k] = E\alpha \begin{bmatrix} \dfrac{m}{\tan\alpha L} & -\dfrac{m}{\sin\alpha L} \\ -\dfrac{nL+m}{\sin\alpha L} & \dfrac{nL+m}{\tan\alpha L} \end{bmatrix}.$$

Member Subjected to Torsional Rotation

In this case the frequency dependent member stiffness matrix, $[k]$, can be written easily if the analogy with the member subjected to axial deformation is considered. Therefore the expanded form of the frequency dependent member stiffness matrix is,

$$[k] = \frac{G\alpha}{2} \begin{bmatrix} \dfrac{m^3}{\tan\alpha L} & -\dfrac{m^3}{\sin\alpha L} \\ -\dfrac{(nL+m)^3}{\sin\alpha L} & \dfrac{(nL+m)^3}{\tan\alpha L} \end{bmatrix}. \tag{44}$$

Member Subjected to Bending in YZ Plane

The differential equation of the motion of a member subjected to bending in the YZ plane is given by,

$$E\frac{\delta^2}{\delta y^2}\left[I_x \frac{\delta^2 d_z}{\delta y^2}\right] = -\frac{A\rho}{g}\frac{\delta^2 d_z}{\delta t^2}. \tag{45}$$

The deflection d_z is a function of the position y and the time t but can be expressed in separable variables form such as

$$d_z = Z(y)f(t). \tag{46}$$

Therefore the differential equation of motion (Eq. (45)) can be written as follows.

$$E\frac{d^2}{dy^2}\left[I_x\frac{d^2Z(y)}{dy^2}\right]=\frac{A\rho}{g}w^2Z(y). \tag{47}$$

Introducing the corresponding functions of the area A, the moment of inertia I_x in Eq. (47) and simplifying one obtains

$$(ny+m)^2\frac{d^4Z}{dy^4}+6n(ny+m)\frac{d^3Z}{dy^3}+6n^2\frac{d^2Z}{dy^2}-\frac{2\rho w^2}{g}Z=0. \tag{48}$$

The above fourth order linear differential equation with variable coefficients is equivalent to a pair of second order linear differential equations such as:

$$(ny+m)\frac{d^2Z}{dy^2}+2n\frac{dZ}{dy}+k_0^2Z=0 \tag{49}$$

and

$$(ny+m)\frac{d^2Z}{dy^2}+2n\frac{dZ}{dy}-k_0^2Z=0, \tag{50}$$

where

$$k_0^4=\frac{2\rho w^2}{Eg}.$$

The general solution of Eq. (48) is a linear combination of the general solutions of Eq. (49) and (50). To solve the last two equations the variables are changed as follows

$$S=(ny+m)^{1/2}Z,$$
$$s=(ny+m)^{1/2}$$

and the Eqs. (49) and (50) become

$$\frac{d^2S}{ds^2}+\frac{1}{s}\frac{dS}{ds}+\left(4k^2-\frac{1}{s^2}\right)S=0, \tag{51}$$

$$\frac{d^2S}{ds^2}+\frac{1}{s}\frac{dS}{ds}-\left(4k^2-\frac{1}{s^2}\right)S=0, \tag{52}$$

where

$$k=k_0/n.$$

Eqs. (51) and (52) are, respectively, a Bessel's equation, and a modified Bessel's equation of order one. Their general solutions are, respectively.

$$S=C_1J_1(2ks)+C_2Y_1(2ks), \tag{53}$$

$$S=C_3I_1(2ks)+C_4K_1(2ks), \tag{54}$$

where J_1 and Y_1 are the Bessel function of the first and second kind, respectively, of order one, and I_1 and K_1 are the modified Bessel functions of the first and second kind, respectively, of order one.

Adding the solutions (Eqs. (53) and (54)) and returning to the variables y and $Z(y)$, the general solution of the Eq. (48) is obtained in the form

$$\begin{aligned}Z(y)=(ny+m)^{-1/2}\{&C_1J_1[2k(ny+m)^{1/2}]+C_2Y_1[2k(ny+m)^{1/2}]\\&+C_3I_1[2k(ny+m)^{1/2}]+C_4K_1[2k(ny+m)^{1/2}]\}.\end{aligned} \tag{55}$$

If the part $Z(y)$ of the deflection related with the position y is resolved into its components Z_3, Z_4, Z_9, and Z_{10} due to d_3, d_4, d_9 and d_{10}, respectively, the Eq. (55) can be written as

$$\begin{Bmatrix} Z_3 \\ Z_4 \\ Z_9 \\ Z_{10} \end{Bmatrix}^T = (n\,y+m)^{-1/2}\{J_1[2\,k\,(n\,y+m)^{1/2}]\,Y_1[2\,k\,(n\,y+m)^{1/2}]\,I_1[2\,k\,(n\,y+m)^{1/2}]$$
$$K_1[2\,k\,(n\,y+m)^{1/2}]\}\begin{bmatrix} C_{11} & C_{12} & C_{13} & C_{14} \\ C_{21} & C_{22} & C_{23} & C_{24} \\ C_{31} & C_{32} & C_{33} & C_{34} \\ C_{41} & C_{42} & C_{43} & C_{44} \end{bmatrix}. \tag{56}$$

The integration constants,

$$\begin{Bmatrix} C_{11} \\ C_{21} \\ C_{31} \\ C_{41} \end{Bmatrix}, \quad \begin{Bmatrix} C_{12} \\ C_{22} \\ C_{32} \\ C_{42} \end{Bmatrix}, \quad \begin{Bmatrix} C_{13} \\ C_{23} \\ C_{33} \\ C_{43} \end{Bmatrix} \quad \text{and} \quad \begin{Bmatrix} C_{14} \\ C_{24} \\ C_{34} \\ C_{44} \end{Bmatrix}$$

are to be determined from the boundary conditions imposed to the displacements and rotations d_3, d_4, d_9 and d_{10} at an arbitrary time t after the vibration has started.

Setting the boundary conditions on Z_3, Z_4, Z_9 and Z_{10} such as:

$$\begin{aligned}
&\text{for } Z_3 \quad \text{at } y=0 \quad Z_3 = d_3, \ \frac{dZ_3}{dy}=0, \quad \text{at } y=L \quad Z_3=0, \ \frac{dZ_3}{dy}=0,\\
&\text{for } Z_4 \quad \text{at } y=0 \quad Z_4 = 0, \ \frac{dZ_4}{dy}=d_4, \quad \text{at } y=L \quad Z_4=0, \ \frac{dZ_4}{dy}=0,\\
&\text{for } Z_9 \quad \text{at } y=0 \quad Z_9 = 0, \ \frac{dZ_9}{dy}=0, \quad \text{at } y=L \quad Z_9=d_9, \ \frac{dZ_9}{dy}=0,\\
&\text{for } Z_{10} \quad \text{at } y=0 \quad Z_{10}=0, \ \frac{dZ_{10}}{dy}=0, \quad \text{at } y=L \quad Z_{10}=0, \ \frac{dZ_{10}}{dy}=d_{10}.
\end{aligned} \tag{57}$$

Introducing the boundary conditions (Eq. (57)) into the Eq. (56) the matrix $[C]$ is solved as

$$[C] = [A]^{-1}[D], \tag{58}$$

where $[A]^{-1}$ is obtained from Eq. (57) and $[D]$ is the diagonal matrix of the member ends displacements and rotations.

Replacing $[C]$ into Eq. (56) one has:

$$\begin{Bmatrix} Z_3 \\ Z_4 \\ Z_9 \\ Z_{10} \end{Bmatrix}^T = \{F_y\}^T[A]^{-1}[D], \tag{59}$$

where $\{F_y\}^T = (n\,y+m)^{-1/2}\{J_1[2\,k\,(n\,y+m)^{1/2}]\,Y_1[2\,k\,(n\,y+m)^{1/2}]$
$I_1[2\,k\,(n\,y+m)^{1/2}]\,K_1[2\,k\,(n\,y+m)^{1/2}]\}$.

The part of the internal shear force V and bending moment M related with the position y are:

$$V = -E\,I_x\frac{d^3\,Z}{dy^3} \tag{60}$$

and

$$M = -E\,I_x\frac{d^2\,Z}{dy^2}. \tag{61}$$

The member end reactions V and M at $y=0$ and $y=L$ due to d_3, d_4, d_9 and d_{10} can be written from Eqs. (60) and (61), in matrix form as

$$[P] = [H][C], \tag{62}$$

where the matrix $[H]$ is obtained from Eqs. (60) and (61) for $y=0$ and $y=L$ and the matrix $[P]$ is formed by the end reactions for the corresponding boundary conditions.

If the matrix $[C]$ from Eq. (58) is replaced into Eq. (62) one has

$$[P] = [H][A]^{-1}[D]. \tag{63}$$

The member end reactions matrix $[P]$ is the frequency dependent member stiffness matrix $[k]$ when the diagonal displacements and rotations matrix $[D]$ is set to be a unit matrix $[U]$. Therefore from Eq. (63) one has

$$[k] = [H][A]^{-1}. \tag{64}$$

Member Subjected to Bending in XZ Plane

The derivation of the frequency dependent member stiffness matrix under the bending in the XZ plane is the same as the bending in the YZ plane except that the moment of inertia I_x with respect to the x axis has to be replaced by the moment of inertia I_z with respect to the z axis.

The frequency dependent member stiffness matrix $[k]$ for all the member end freedoms is obtained by combining the $[k]$ matrices for axial displacement, torsional rotation and bending in two orthogonal planes.

Secondary Effects

All the effects which are negligible in the usual engineering practices are considered as secondary effects. The secondary effects may become important in some certain cases. For beams with small slenderness ratio, short beams, the effects of transverse shear and the rotatory inertia moments become important. For the systems with large deformations, the influence of axial force on the frequencies of the transverse vibrations of the elements are in noticeable order.

The Effect of Transverse Shear and Rotatory Inertia

In the cases of lumped mass matrix and the equivalent mass matrix analyses, the effect of transverse shear and rotatory inertia can be easily taken into account by adding a factor to the member stiffness matrix and to the mass matrix.

In the case of the frequency dependent stiffness matrix analysis, if the Timoshenko's theory is considered for a beam with uniform cross section, the differential equations of the motion can be expressed as:

$$E I \frac{\delta^4 Z}{\delta y^4} + \frac{\rho A}{g} \frac{\delta^2 Z}{\delta t^2} - \frac{I \rho}{g}\left(1 + \frac{E}{k' G}\right) \frac{\delta^4 Z}{\delta y^2 \delta t^2} + \frac{I \rho^2}{g^2 k' G} \frac{\delta^4 Z}{\delta t^4} = 0 \tag{65}$$

and

$$E I \frac{\delta^4 \Psi}{\delta y^4} + \frac{\rho A}{g} \frac{\delta^2 \Psi}{\delta t^2} - \frac{I \rho}{g}\left(1 + \frac{E}{k' G}\right) \frac{\delta^4 \Psi}{\delta y^2 \delta t^2} + \frac{I \rho^2}{g^2 k' G} \frac{\delta^4 \Psi}{\delta t^4} = 0, \tag{66}$$

where Ψ is the slope of the deflected configuration under the bending without the effect of transverse shear, k' is the ratio of the average shear stress on a section to the product of the shear modulus and shear strain at the neutral axis of the member.

The integrations of the Eqs. (65) and (66) yield

$$Z = C_1 \cos \alpha y + C_2 \sin \alpha y + C_3 \cos h \beta y + C_4 \sin h \beta y, \tag{67}$$

$$\Psi = C_1' \cos \alpha y + C_2' \sin \alpha y + C_3' \cos h \beta y + C_4' \sin h \beta y, \tag{68}$$

where C_1, C_2, C_3 and C_4 are the independent integration constants. The integration constants C_1', C_2', C_3' and C_4' are not independent and can be expressed in terms of C_1, C_2, C_3 and C_4.

A derivation similar to the case without the effect of transverse shear and rotatory inertia can be performed. If Z and Ψ are resolved to their components Z_3, Z_4, Z_9, Z_{10} and Ψ_3, Ψ_4, Ψ_9, Ψ_{10}, respectively, and if the boundary conditions and the relationship between C_i' and C_i

$$[C'] = [Q][C] \tag{69}$$

are taken into account, the components of Z and Ψ can be written as

$$\begin{Bmatrix} Z_3 \\ Z_4 \\ Z_9 \\ Z_{10} \end{Bmatrix}^T = \{F\}^T [A]^{-1} [D] \tag{70}$$

and

$$\begin{Bmatrix} \Psi_3 \\ \Psi_4 \\ \Psi_9 \\ \Psi_{10} \end{Bmatrix}^T = \{F\}^T [Q] [A]^{-1} [D], \tag{71}$$

where $\{F\}^T = (\cos\alpha y \ \sin\alpha y \ \cosh\beta y \ \sinh\beta y)$.

$[A]$ = the matrix obtained by introducing the boundary conditions in Eq. (67).

$[D]$ = the diagonal matrix of the member ends displacements and rotations.

The part of the internal shear force V and the bending moment M with the position y are

$$M = -E I \frac{\delta \Psi}{\delta y}, \tag{72}$$

$$V = k' G A \left(\frac{\delta Z}{\delta y} - \Psi\right). \tag{73}$$

The member end reactions V and M at $y=0$ and $y=L$ due to d_3, d_4, d_9 and d_{10} can be written from Eqs. (72) and (73) as follows

$$[P] = [H][A]^{-1}[D], \tag{74}$$

where $[H]$ is the matrix obtained from the boundary values of Eqs. (72), (73) and for $y=0$ and $y=L$.

The member end reactions matrix $[P]$ is the frequency dependent member stiffness matrix $[k]$ when the diagonal displacements and rotations matrix $[D]$ is set to be a unit matrix $[U]$. Therefore from Eq. (74), one has

$$[k] = [H][A]^{-1}. \tag{75}$$

Conclusion

The frequency dependent stiffness matrix is derived for members in space with uniform and with nonuniform cross section. The error involved by considering the lumping of the masses of the members at the joints of the system are eliminated. The concentrated masses existing on the system, if any, are duly taken into account. The effect of the rotatory inertia and the transverse shear are also considered. The lumped mass or the equivalent mass matrix solution require the division of the elements into sub-elements in order to obtain a close approximation in the natural frequencies especially for higher modes. It is not necessary to divide the elements into sub-elements to refine the approximation in the natural frequencies of any mode, either for uniform nor for nonuniform cross section elements, since the natural frequencies obtained by frequency dependent stiffness matrix approach are independent of the division of the elements into sub-elements. The lumped mass or the equivalent mass matrix solutions for continuous system furnish as many natural frequencies as the number of unknowns. The frequency dependent stiffness matrix furnishes an infinity number of natural frequencies.

References

1. ROGERS, G. L.: Dynamics of Framed Structures. John Wiley & Sons, New York, 1959.
2. RUBENSTEIN, M. F., and HURTY, W. C.: Dynamics of Structures. Prentice-Hall, Englewood Cliffs, New Jersey, 1964.
3. PESTEL, E. C., and LECKIE, F. A.: Matrix Methods in Elastomechanics. McGraw-Hill, New York, 1963.
4. BIGGS, J. M.: Introduction to Structural Dynamics. McGraw-Hill, New York, 1964.
5. CHENG, F. Y.: Dynamics of Frames with Nonuniform Elastic Members. Journal of the Structural Division, ASCE, Vol. 94, No. ST 10, October 1968, pp. 2411–2428.
6. CAKIROGLU, A., and OZMEN, G.: Numerical Integration of Forced Vibration Equations. Journal of the Structural Division, ASCE, Vol. 94, No. EM 3, June 1968, pp. 711–729.
7. HOUSNER, G. W., and KEIGHTLEY, W. O.: Vibrations of Linearly Tapered Beams. Transactions ASME, Vol. 128 (1963), Part I, pp. 1020–1048.
8. VOLTERRA, E., and ZACHMANOGLU, E. C.: Dynamics of Vibrations. Merrill Books, Inc., Columbus, Ohio, 1965.
9. ARCHER, J. S.: Consistent Mass Matrix for Distributed Mass Systems. Journal of the Structural Division, ASCE, Vol. 89, No. ST 4, August 1963, pp. 161–168.
10. ARCHER, J. S.: Consistent Matrix Formulation for Structural Analysis Using Finite Element Techniques. Journal of AIAA, Vol. 3, No. 11, October 1965, pp. 1910–1918.
11. PRZEMIENIECKI, J. S.: Theory of Matrix Structural Analysis. McGraw-Hill, New York, 1968.
12. PRZEMIENIECKI, J. S.: Quadratic Matrix Equations for Determining Vibration Modes and Frequencies of Continuous Elastic Systems. Proc. Conf. Matrix Method in Structural Mechanics, Wright-Patterson Air Force Base, Ohio, October 26–28, 1965, AFFDL-TR 60–80, 1966.
13. PESTEL, E. C.: Dynamic Stiffness Matrix Formulation by Means of Hermitian Polynomials. Proc. Conf. Matrix Methods in Structural Mechanics, Wright-Patterson Air Force Base, Ohio, October 26–28, 1965, AFFDL-TR 60–80, 1966, pp. 479–502.
14. CLOUGH, R. W.: On the Importance of Higher Modes of Vibration in the Earthquake Response of a Tall Building. Bulletin of the Seismological Society of America, Vol. 45, 1955, pp. 289–301.
15. TIMOSHENKO, S. P.: Vibration Problems in Engineering. D. Van Nostrand Co., New York, 1955.
16. GAINES, J. H., and VOLTERRA, E.: Transverse Vibrations of Cantilever Bars of Variable Cross Sections. The Journal of the Acoustical Society of America, Vol. 39, No. 4, 1966, pp. 674–679.
17. HUANG, T. C.: The Effect of Rotatory Inertia and of Shear Deformation on the Frequency and Normal Mode Equations of Uniform Beam with Simple End Conditions. Journal of Applied Mechanics, Vol. 28, No. 4, 1961, pp. 578–584.
18. LEE, H. C., and BISSHOPP, K. E.: Application of Integral Equations to the Flexural Vibration of a Wedge with Rotatory Inertia and Shear. Journal of the Franklin Institute, Vol. 277, No. 4, 1964, pp. 327–336.
19. RISSONE, R. F., WILLIAMS, J. J.: Vibrations of Nonuniform Cantilever Beams. The Engineer, September 1965, pp. 497–506.
20. WANG, C. K.: Matrix Methods of Structural Analysis. International Textbook Co., Scranton, Pa., 1970.
21. CHENG, F. Y.: Vibrations of Timoshenko Beams and Frameworks. Journal of the Structural Division, ASCE, Vol. 96, No. ST 3, March 1970, pp. 551–571.

22. Traill-Nash, R. W., and Collar, A. R.: The Effect of Shear Flexibility and Rotatory Inertia on the Bending Vibrations of Beams. Quarterly Journal of Mechanics and Applied Mathematics, Vol. 6, 1953, pp. 186–222.
23. Kordes, E. D., and Kruszewski, E. T.: Experimental Investigations on the Vibrations of a Built-up Rectangular Beam. TN 3618, 1956, NACA.
24. Cowper, G. R.: The Shear Coefficient in Timoshenko Beam Theory. Journal of Applied Mechanics, Vol. 33, June 1966, pp. 335–340.
25. Medick, M. A.: One Dimensional Theories of Wave Propagation and Vibrations in Elastic Bars of Rectangular Cross Section. Journal of Applied Mechanics, Vol. 33, September 1966, pp. 439–495.
26. Krishna Murty, A. V.: Vibrations of Short Beams. Journal of AIAA Vol. 8, No. 1, January 1970, pp. 34–38.

Summary

A new approach has been derived for the analysis of the systems under dynamic loading. This approach eliminates the concept of lumping the masses of the elements at the joints. The masses are assumed to be continuously attached to the elements as they are. If a concentrated mass exists on the system, its point of application is considered as a joint of the system. Therefore the inertia forces due to the concentrated masses are taken into account as inertial joint forces. It is assumed that the material is homogeneous and isotropic, also the Hooke's law and Bernoulli-Euler hypothesis are valid. The damping is neglected. The frequency dependent mass matrix approach does not require the division of the elements into sub-elements in order to refine the approximation in natural frequencies, especially for higher modes, and furnishes an infinity number of natural frequencies.

Résumé

Une nouvelle méthode de solution pour le calcul de systèmes sous charges dynamiques a été élaborée. Les charges y sont reparties selon leur distribution véritable sur l'élément. Le point d'application d'une charge concentrée est considéré comme nœud du système. Par là, les forces d'inertie provenant des charges concentrées sont introduites dans le calcul comme forces d'inertie de nœud. On suppose un matériau homogène et isotrope, de même sont valables la loi de Hooke et l'hypothèse Bernoulli-Euler. L'amortissement est négligé. La méthode de la matrice de masse dépendant de la fréquence ne demande pas la subdivision des éléments pour améliorer l'approximation des oscillations propres, surtout pour des types plus compliqués. Elle fournit, d'autre part, un nombre infini d'oscillations propres.

Zusammenfassung

Eine neue Lösungsmethode wurde zur Berechnung von Systemen unter dynamischen Lasten entwickelt. Die Lasten werden in ihrer wirklichen Verteilung über das Element angenommen. Der Angriffspunkt einer konzentrierten Last wird als Knoten des Systems betrachtet. Dadurch kann man die von konzentrierten Lasten herrührenden Trägheitskräfte als Knotenträgheitskräfte in die Berechnung einführen. Es wird ein homogen-isotropes Material angenommen; ebenso soll das Hookesche Gesetz und die Euler-Bernoulli-Hypothese gültig sein. Die Dämpfung wird vernachlässigt. Die Methode der frequenzabhängigen Massmatrizen erfordert keine Unterteilung der Elemente in Subelemente, um die Approximation der Eigenschwingungen zu verbessern (besonders für komplizierte Schwingungstypen) und liefert eine unbegrenzte Zahl von Eigenschwingungen.

Stability of Load Bearing Trapezoidal Diaphragms

Stabilité d'entretoises trapézoidales sous charges

Stabilität trapezförmiger belasteter Querträger

K. C. ROCKEY
M.Sc., Ph.D., C.Eng., F.I.C.E., M.I. Mech.E. Professor of Civil and Structural Engineering, University College, Cardiff, U.K.

M. A. EL-GAALY
M.S.E., D.Sc., M.ASCE
Research Fellow, Civil and Structural Engineering Department, University College, Cardiff, U.K.

1. Introduction

In box girders, diaphragms are employed to transfer the vertical shear force carried by the webs to the supports. The stress distribution which occurs in load bearing diaphragms is complex and varies with the inclination of the webs and the position of the bearing pads. In order to be able to design such diaphragms it is necessary to know the loads at which the diaphragm will buckle either locally or in an overall mode. A survey of the existing literature shows that little information is available regarding the overall buckling of trapezoidal diaphragms.

A finite element study has therefore been carried out to determine the stress distribution which occurs in both rectangular and trapezoidal diaphragms and to determine the applied load at which overall buckling of the diaphragms will occur. In the present paper the overall buckling load of unstiffened trapezoidal and rectangular diaphragms has been determined for different geometric properties of the diaphragms and for varying position and length of the supporting pads. It is fully appreciated that most large diaphragms are stiffened and in a forthcoming paper, the buckling of orthogonally stiffened diaphragms will be dealt with.

2. Method of Analysis

Since the finite element method of analysis which has been used in the present study has been reported elsewhere [1]–[4] full details of the method

will not be given here. In the present study a constant strain plane stress triangular element having 6 degrees of freedom [1], [5], [6], [7] was used to evaluate the inplane stresses, and in the buckling analysis a non-conforming triangular element with 9 degrees of freedom [7]–[10] was used. Fig. 1 shows a typical finite element idealization as used in the present study.

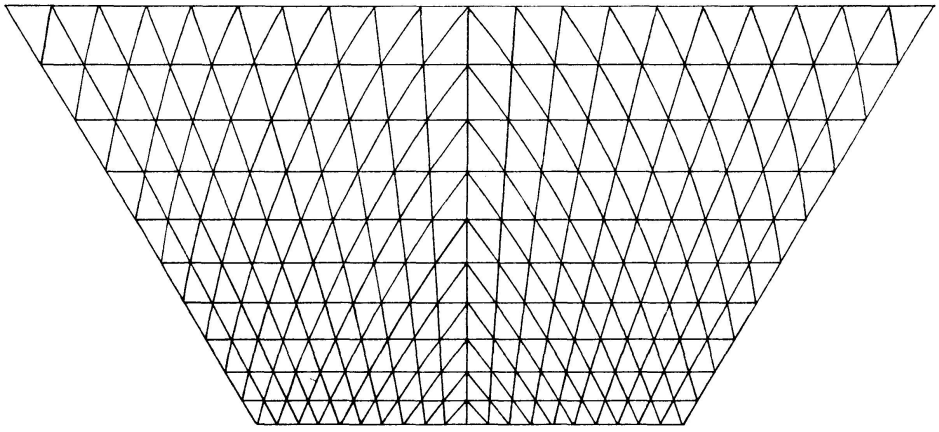

Fig. 1. A Typical Finite Element Idealization.

In what follows it is assumed that the diaphragm is composed of a homogeneous and isotropic material. Fig. 2 shows a typical trapezoidal diaphragm supported on two bearings. The parameters which influence the stress distribu-

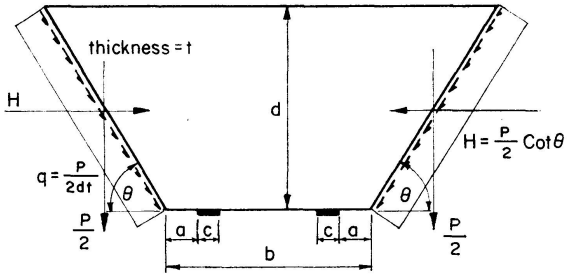

Fig. 2. Dimensions of a Typical Diaphragm.

tion and the buckling load are: the inclination of the webs (θ), the width to depth ratio of the diaphragm (b/d), the position and length of the bearings as defined by the parameters a/b and c/b, respectively. It has been assumed that the load is transmitted from the webs to the diaphragm by a uniform shear applied along the sides of the diaphragm. Two support conditions have been assumed, in the first, it is assumed that the load bearings are rigid in the vertical direction but do not prevent lateral movement, and in the second case (hereafter referred to as fixed supports) it is assumed that both horizontal and vertical displacements are prevented along the length of the bearings.

3. Results and Discussion

The study involved an examination of how the buckling load of the diaphragm varies with the following parameters:

1. The angle of slope of the web, θ.
2. The relative position of the supporting pads, a/b.
3. The relative width of the supporting pads, c/b.
4. The diaphragm aspect ratio, b/d.

3.1. Reactions

The distribution of the reaction forces will be seen to vary with the position of the pads and the results for six representative cases are shown in Fig. 3. The stress distribution in a diaphragm is effected by two actions which vary with the position and length of the bearings. First, when the bearing pads are "in set" as shown in Fig. 4a, there will be an overhanging moment which

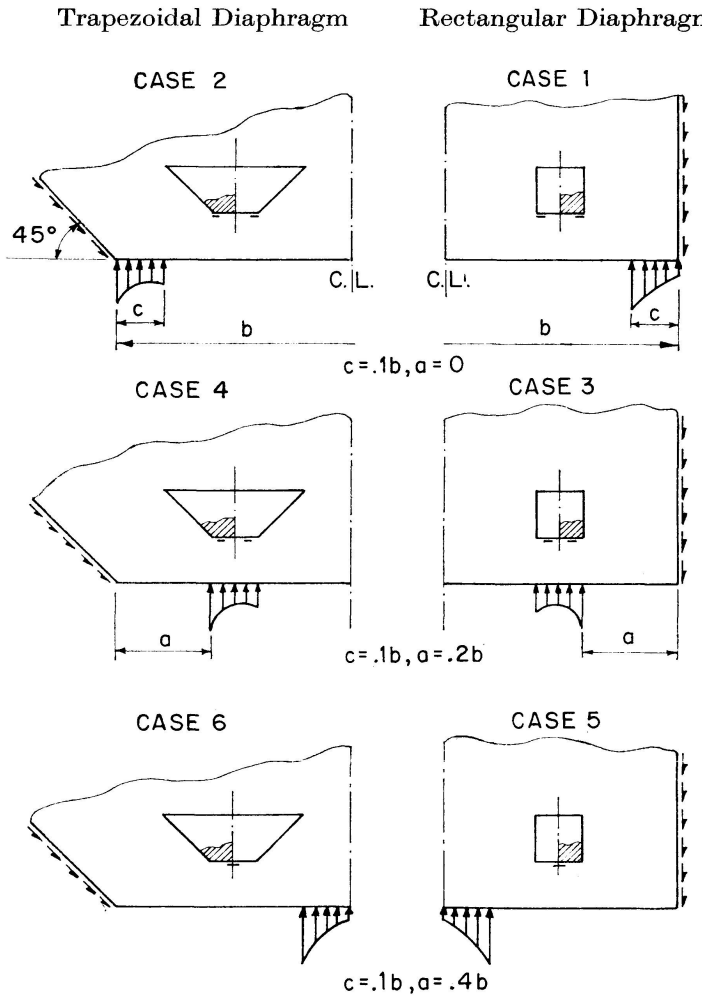

Fig. 3. Variation of the Distribution of the Reaction Forces with a Change in the Position of the Bearings, the Width of all the Bearings Being Constant ($= 0.1$ b) Diaphragms, $b/d = 1$.

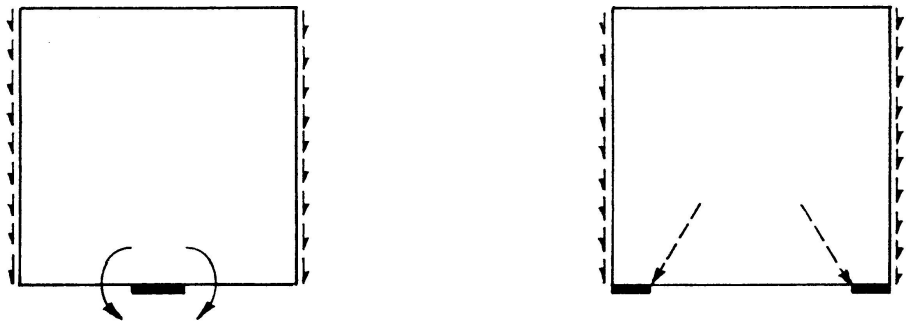

a) Overhanging Moment b) Arching Effect

Fig. 4. Overhanging Moment and Arching Effect.

becomes especially significant in the case of trapezoidal diaphragms. The second is an internal arching action as shown in Fig. 4b. Due to the arching effect the reactions must be larger at the inner edges of the pads whereas due to the overhanging moments, the reactions will be larger at the outer edges. In case 1, which is that of a rectangular diaphragm with a pad adjacent to the web, it will be noted from Fig. 3 that in the absence of any overhanging moment, the reactions are larger at the inner edges of the bearing pads and decrease gradually toward the outer edges. In cases 2, 3 and 4 due to the presence of both the arching effect and the overhanging moment the reactions are now larger at the two edges of the supporting pads. Finally, in the case of a central single pad, cases 5 and 6, due to the presence of a significant overhanging moment and the absence of any arching effect, the reactions are now very large at the outer edges of the pad and the variation of the reactions across the pad is quite rapid. Fig. 5 shows how the distribution of the reaction

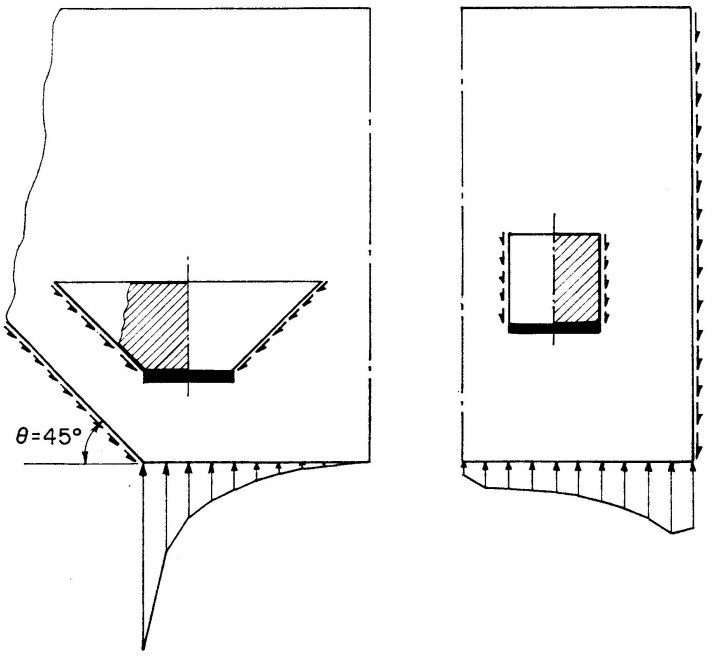

Fig. 5. Distribution of the Reaction Forces for a Continuous Supporting Pad ($c = b$).

forces varies when the supporting pad is continuous over the bottom width of the diaphragm, ($c = b$). In the case of the trapezoidal diaphragm the influence of the overhanging moment is shown to be significant.

3.2. Stresses

A diaphragm acts as a deep beam and therefore the simple theory of flexure cannot be used to determine the stress distribution within the diaphragm. Using a plane stress method of analysis, stress contours, of σ_x, σ_y and τ_{xy}, have been obtained for the 8 representative cases examined in Figs. 3 and 5, and are shown in Figs. 6, 7, 8 and 9. The stress values given were obtained when the diaphragm had the following dimensions and material properties: width (b) = 100″ (2450 mm), depth (d) = 100″ (2450 mm), thickness (t) = 0.125″ (3.175 mm), load (P) = 200 kips (90.72 tons), Young's modulus (E) = 29,000 ksi (2039 t/cm^2), and Poisson's ratio (μ) = 0.3.

3.2a. Stresses in the x-Direction σ_x

It will be seen that in all cases the horizontal stresses (σ_x) which are set up in the trapezoidal diaphragms are much larger than those occurring in the rectangular diaphragms due to the larger overhanging moment and the horizontal component of the shear. It will also be noted that the position of the supporting pads affects the magnitude of these stresses, since by moving the supporting pads toward the edges, the overhanging moment is reduced. Comparison between the values of σ_x obtained using the finite element method with values obtained using the elementary beam theory shows reasonable similarity for high aspect ratio b/d, see Fig. 10.

3.2b. Stresses in the y-Direction σ_y

These stresses are localized near the applied edge loads and the reactions, where they can reach very high values. As will be seen from Figs. 6, 7 and 8, the magnitude of σ_y does not vary significantly with the position of the supporting pad or the slope of the web, but does vary markedly with the width of the supporting pad, as shown in Fig. 9. It should be noted that these stresses do not decrease linearly with the increase in the width of the supporting pad, because of the concentration of the reaction forces near the edges of the supporting pad. In Fig. 11, the stress distribution of σ_y at the critical section (the edge of the supporting pad) is shown for three values of the c/b ratio.

3.2c. Shear Stresses τ_{xy}

In the neighbourhood of a concentrated load, localized shear stresses are always present and this is clearly shown in Figs. 6, 7 and 8. These very high local shear stresses occur in the same region as the high σ_y and σ_x values and clearly the stability of diaphragms in the neighbourhood of support bearings

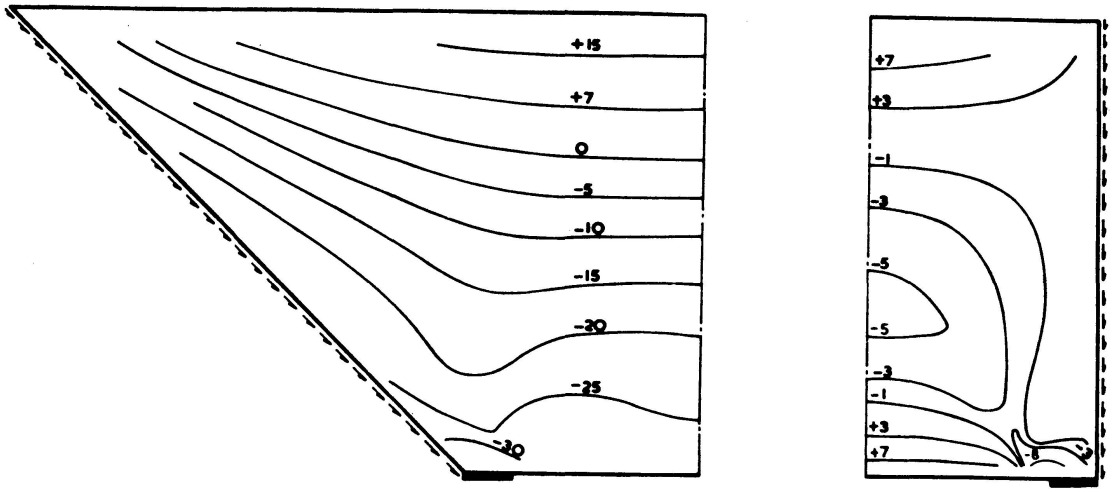

Stresses in the x-direction σ_x

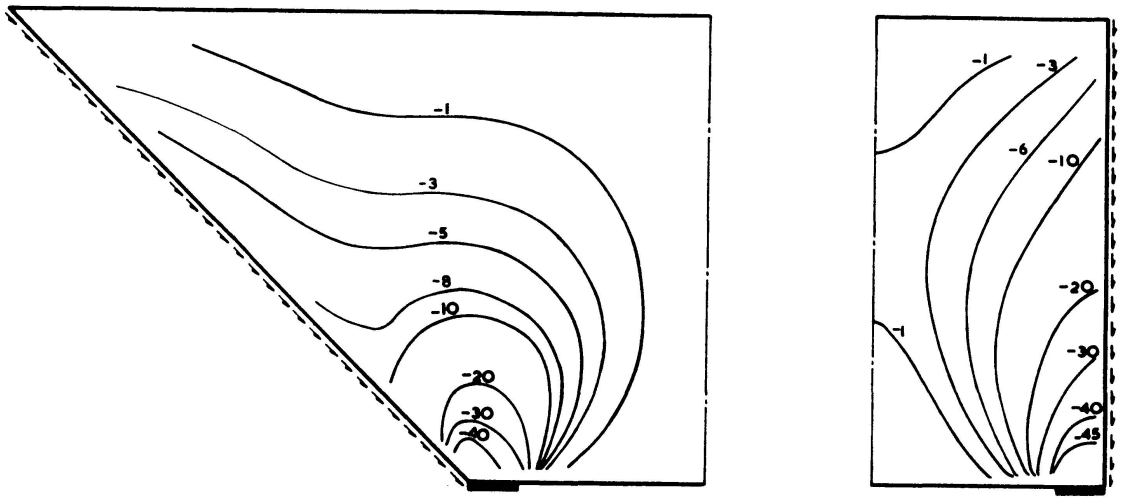

Stresses in the y-direction σ_y

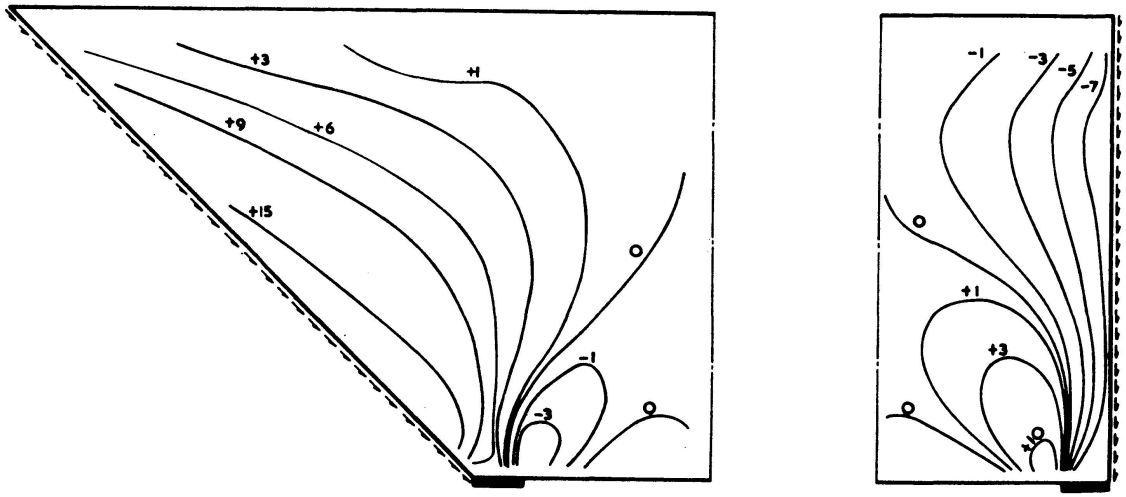

Shear stresses τ_{xy}

Fig. 6. Stresses σ_x, σ_y and τ_{xy} (Ksi).

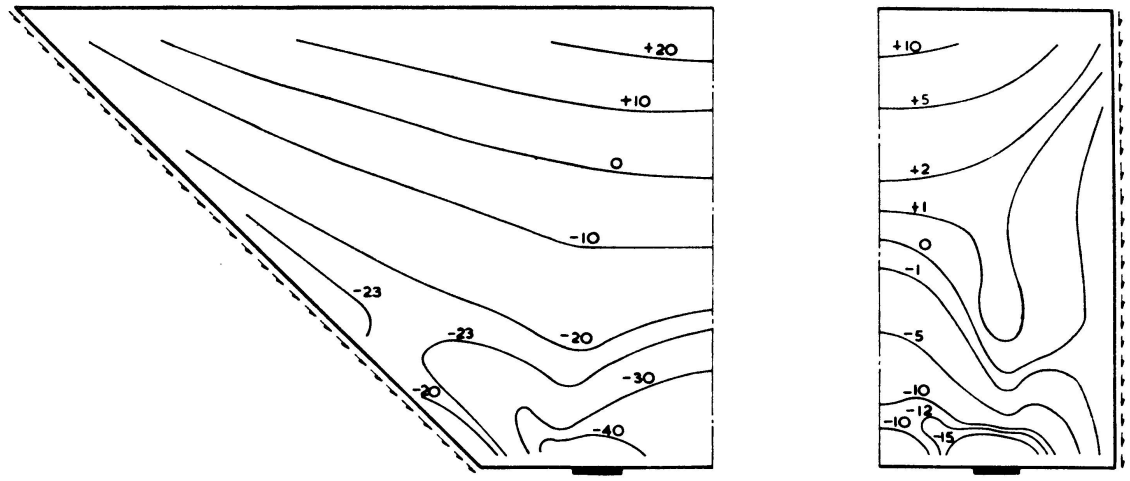

Stresses in the x-direction σ_x

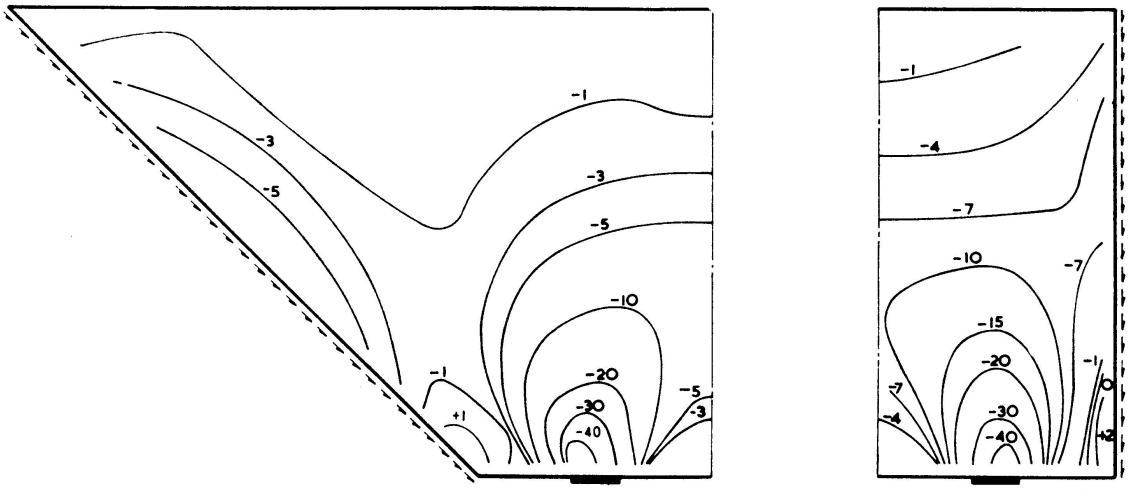

Stresses in the y-direction σ_y

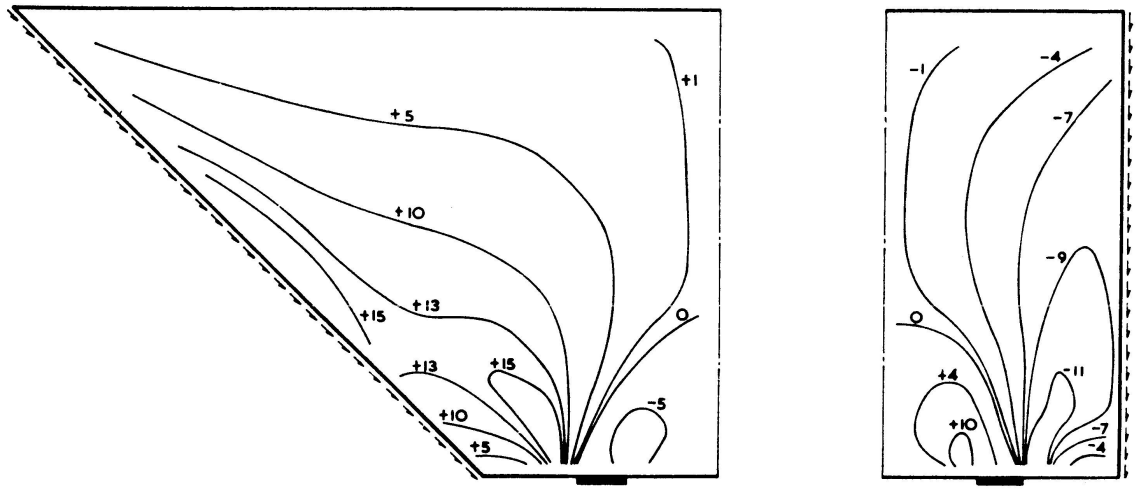

Shear stresses τ_{xy}

Fig. 7. Stresses σ_x, σ_y and τ_{xy} (Ksi).

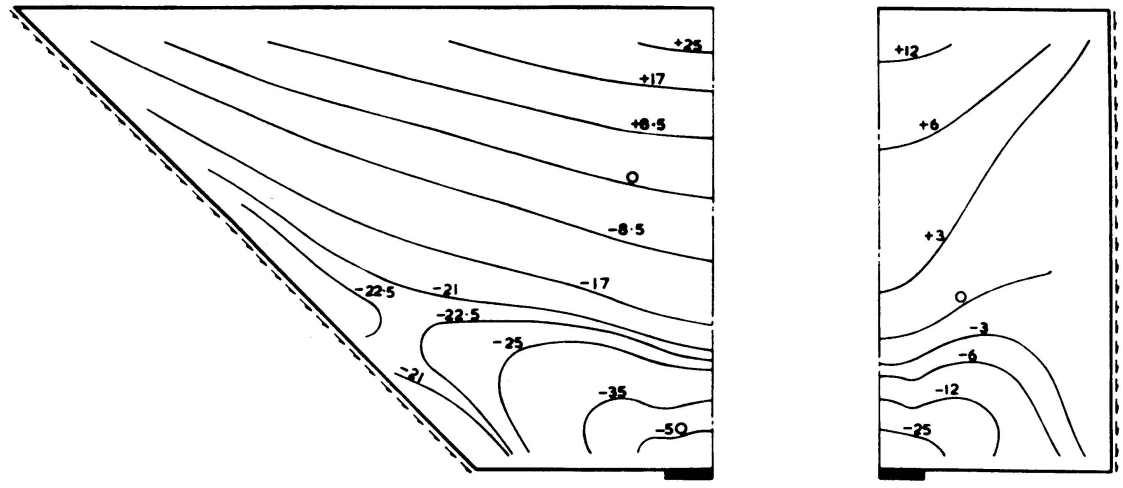

Stresses in the x-direction σ_x

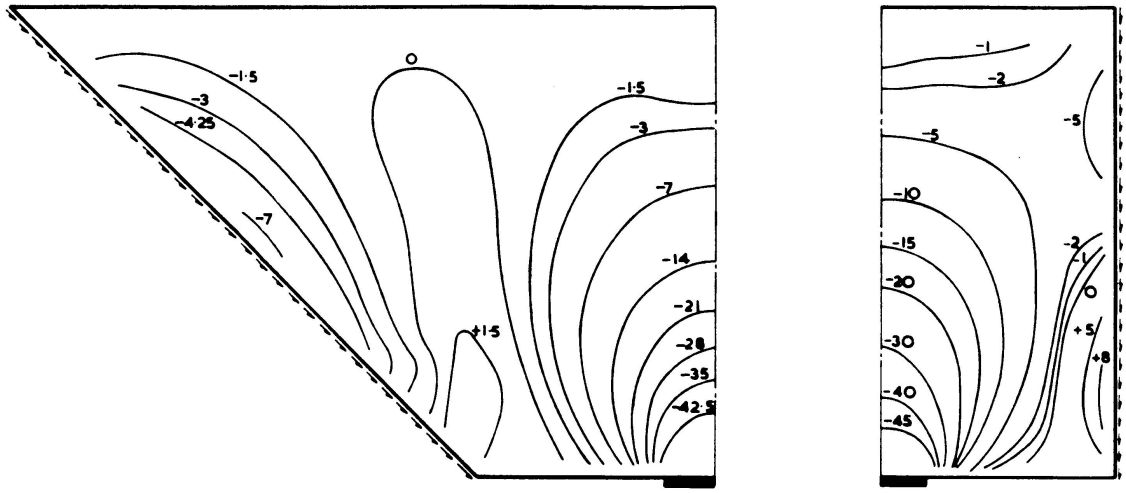

Stresses in the y-direction σ_y

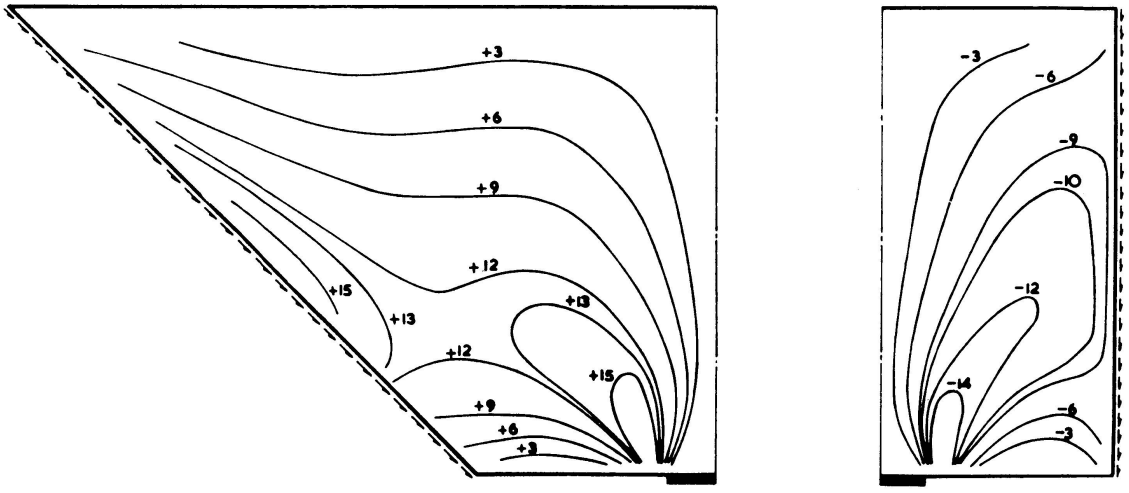

Shear stresses τ_{xy}

Fig. 8. Stresses σ_x, σ_y and τ_{xy} (Ksi).

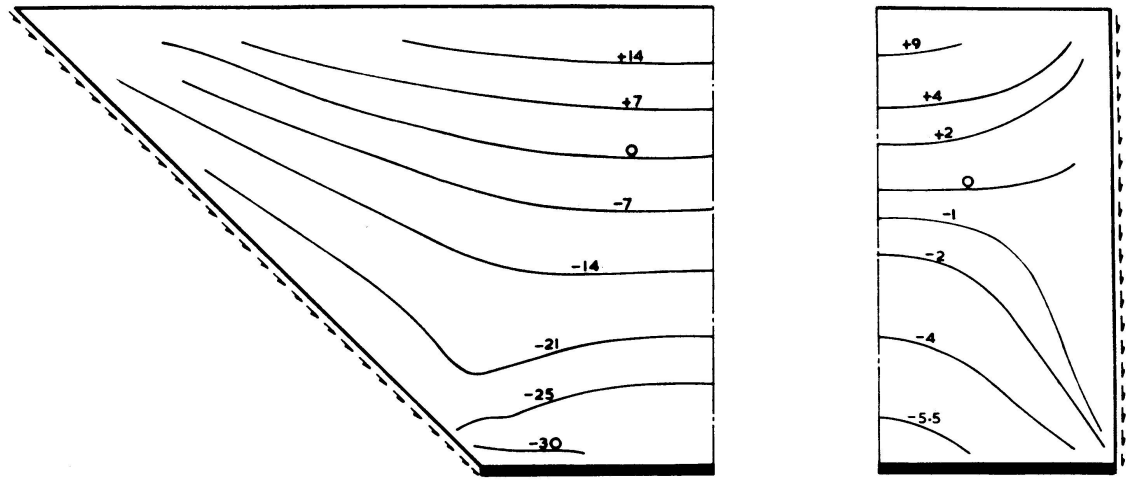

Stresses in the x-direction σ_x

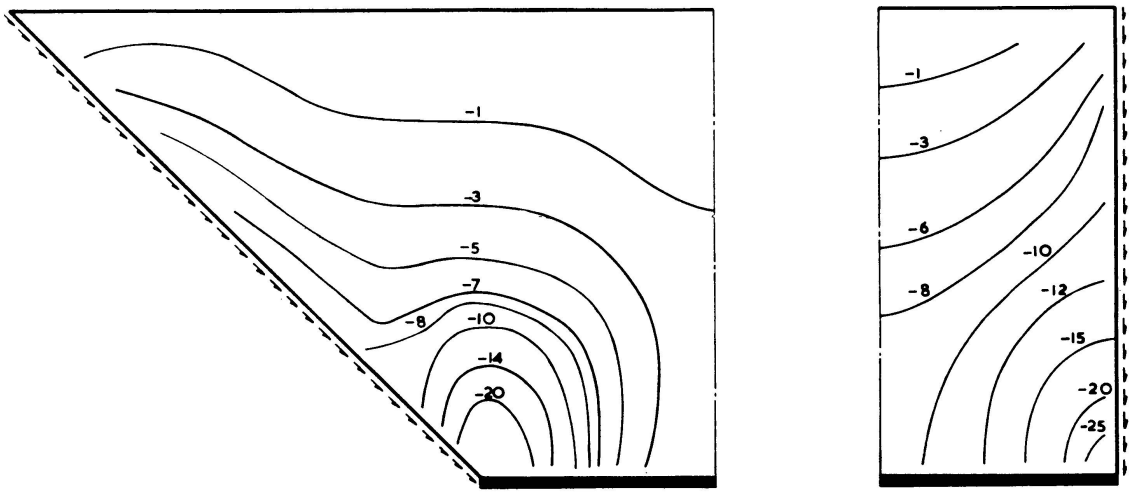

Stresses in the y-direction σ_y

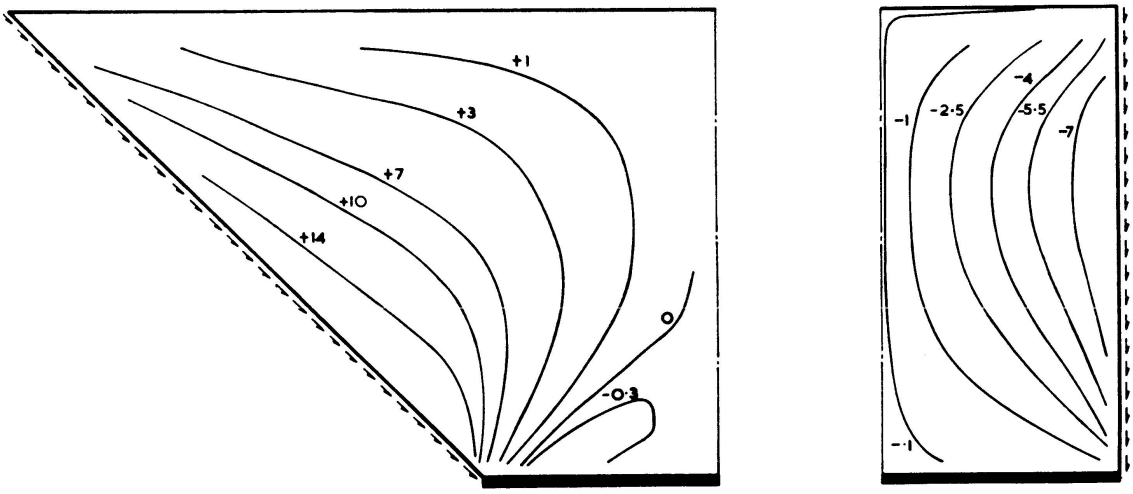

Shear stresses τ_{xy}

Fig. 9. Stresses σ_x, σ_y and τ_{xy} (Ksi).

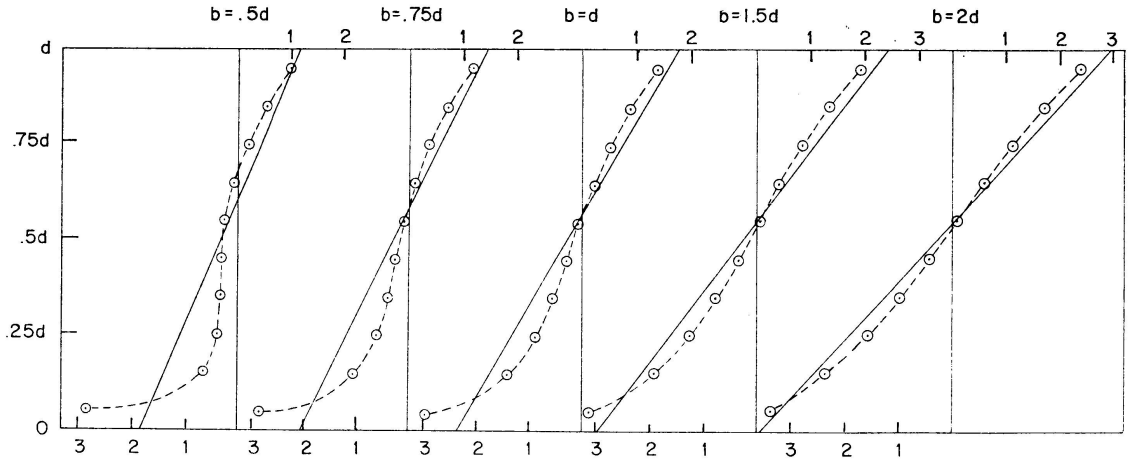

Central Supporting Pad ($c = 0.2b$, $a = 0.4b$) $\theta = 60°$

Fig. 10. Stresses σ_x Across the Depth at the Edge of the Supporting Pad – Comparison with Elementary Beam Theory.

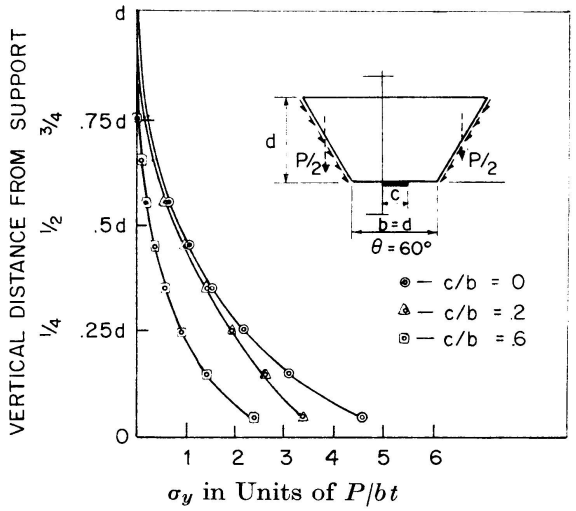

Fig. 11. Stress Distribution of σ_y at Critical Section.

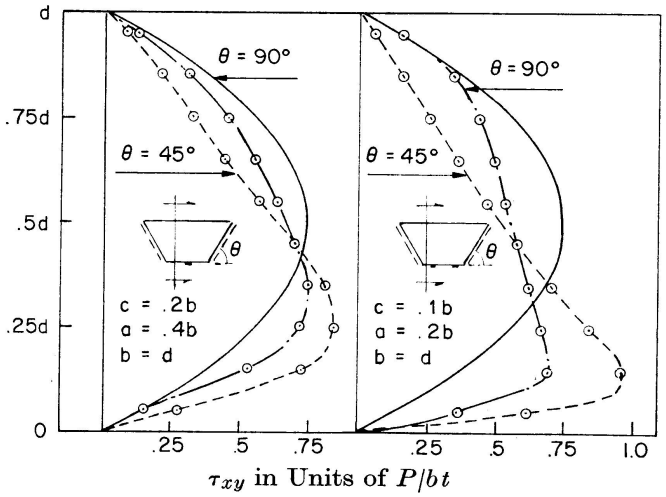

Fig. 12. Shear Stress Distribution Across the Depth.

needs special attention. Fig. 12 shows the shear stress distribution which occurs at a section midway between the outer edge of the supporting pad and the bottom corner of the diaphragm, for four representative cases. It will be noted that this shear stress distribution differs radically from the conventional parabolic form, the shear stresses in the lower portion being significantly greater than those acting in the upper portion of the diaphragm. Finally, one has to notice the localized shear stresses of opposite sign in the vicinity of the inner edges of the supporting pads, these stresses are induced since the total shear force between the inner edges of the pads is equal to zero.

3.3. Fixed Supports

The effect of preventing any horizontal movement along the length of the supporting pad has been examined. The σ_x, σ_y and τ_{xy} stress distributions which occur at representative sections are shown in Fig. 13, together with the corresponding stress distributions, which occur when horizontal movement along the length of the supporting pad is permitted (moveable supports). Clearly, the horizontal reactive forces at the two supports must be equal in magnitude and opposite in direction, and they induce localized tensile horizontal stresses (σ_x) between the inner edges of the supporting pads and additional localized compressive horizontal stresses outside the outer edges of the supports, as shown in Fig. 13. The effect on σ_y and τ_{xy} is also localized near the supports and is not as significant as the effect on σ_x.

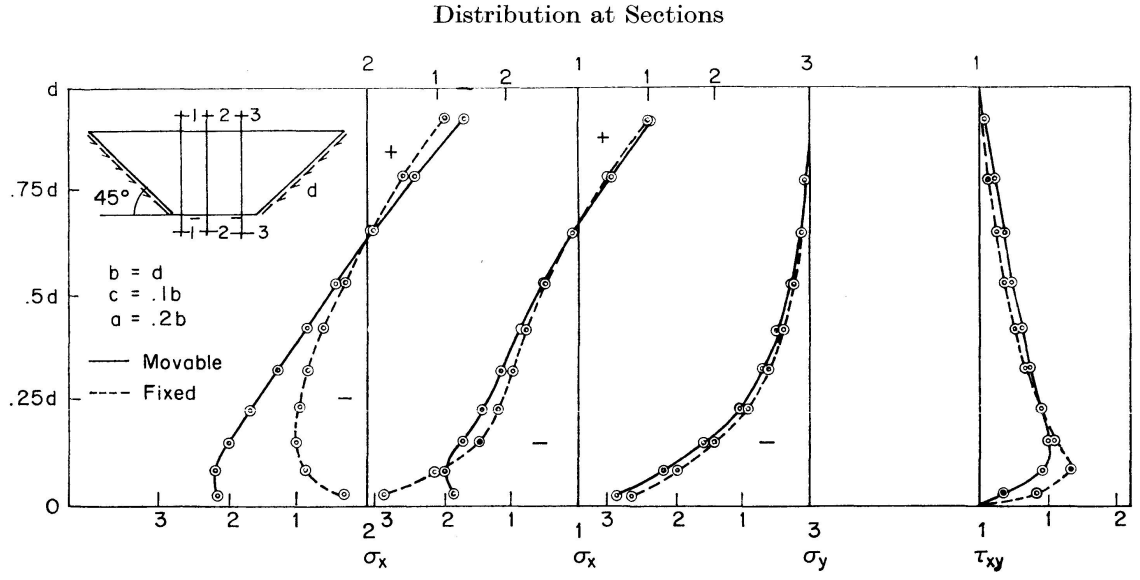

Fig. 13. The Effect of Preventing any Horizontal Movement Along the Length of the Supporting Pad on the σ_x, σ_y and τ_{xy} Stress Distributions.

3.4. General

In most practical cases the depth of the diaphragm (d) is comparable to its width (b), and hence the simple theory of flexure is not applicable. Consequently, the finite difference or the finite element method has to be used to solve the plane stress problem. In both methods difficulties will arise where steep stress gradient exists, hence the results obtained from both methods in the vicinity of concentrated loads (or reactions) are not dependable unless a very fine mesh is employed.

Fortunately, the stresses are linear functions of the term $\frac{P}{b\,t}$, thus the values given in this paper can be used for other values of P, b and t provided that the corresponding values of the parameters θ, a/b, c/b and b/d are identical.

3.5. Overall Buckling of Plane Simply Supported Diaphragms

In this section the buckling of a plane, unreinforced, trapezoidal diaphragm simply supported along its boundary will be considered.

Earlier work [11] on the buckling of rectangular web plates subjected to inplane patch loading has shown that the buckling load P_{cr} can be expressed by Eq. (1)

$$\frac{P_{cr}}{b\,t} = K \frac{\pi^2 E}{12\,(1-\mu^2)} \left(\frac{t}{d}\right)^2, \tag{1}$$

in which the non-dimensional parameter K is a function of the aspect ratio b/d and the width of the patch load c/b, see Fig. 14. Although the curves presented in Fig. 14 are not strictly applicable to the present problem, one would expect rather similar behaviour.

The overall buckling load P_{cr} for the trapezoidal diaphragm can be expressed

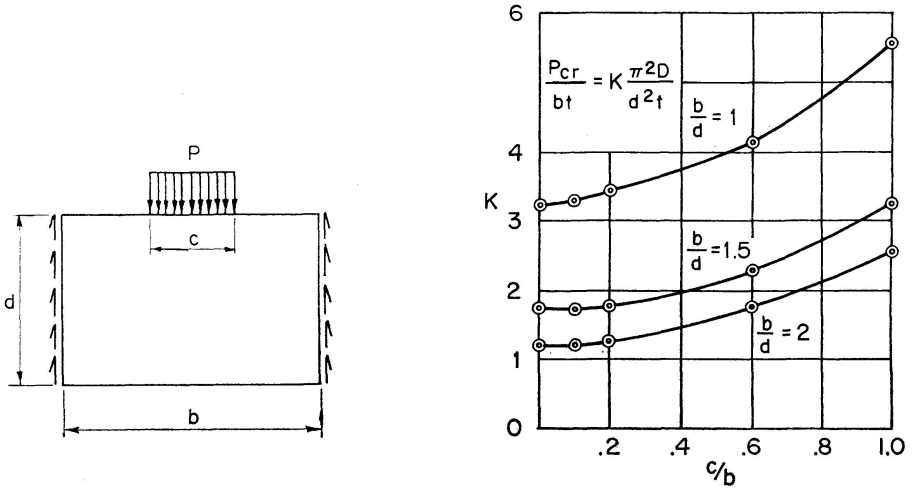

Fig. 14. Buckling Load Coefficient for Rectangular Web Plates Subjected to In-Plane Patch Loading (Reference 11).

in a similar form by Eq. (2)

$$\frac{P_{cr}}{dt} = K \frac{\pi^2 E}{12\,(1-\mu)^2}\left(\frac{t}{d}\right)^2, \tag{2}$$

in which the non-dimensional parameter K is a function of θ, a/b, c/b and b/d. Fig. 15 gives the results obtained for a diaphragm having an aspect ratio $b/d = 1.0$ and which is supported on non-yielding bearings of width $c = 0.1\,b$. The diaphragm is assumed to be simply supported on all four edges and to be subjected to a uniformly applied shear load along its "vertical" boundaries.

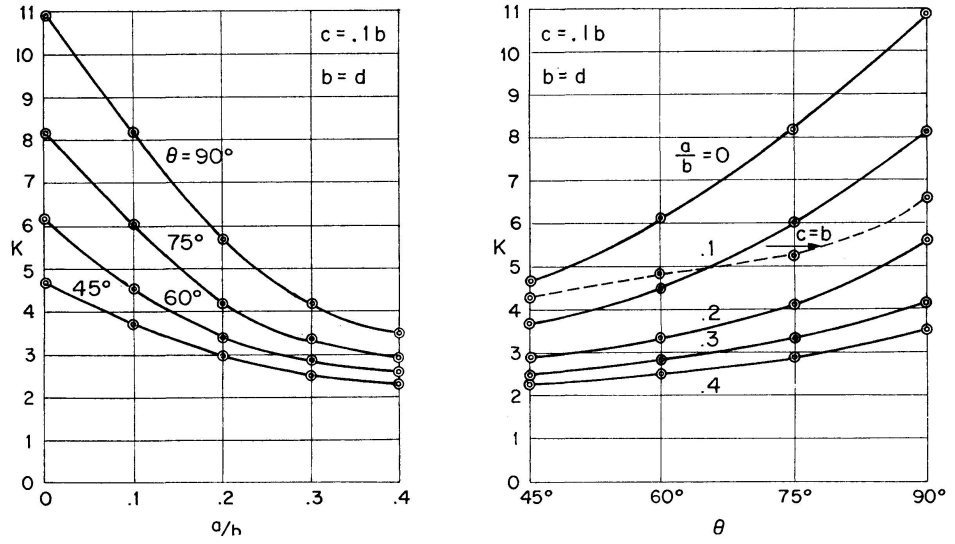

Fig. 15. Buckling Load Coefficient for Various a/b and θ Values ($b = d$, $c = 0.1b$).

It will be noted that the buckling coefficient K varies significantly with the angle of inclination θ of the sloping face, the reduction in values of the buckling coefficient K, with decreasing values of θ is due to the greater horizontal stresses induced into the web by the inclined forces. It will also be noted that the buckling coefficient K decreases as the pads are moved towards the centre of the panel. It will be recalled that the horizontal compressive stresses increase when the pads are moved away from the corners due to the influence of the overhanging moments. The effect of the position of the supporting pad on K is seen to be of increasing significance with increasing values of θ and is a maximum when $\theta = 90°$, since in this case the overhanging moment depends only on the position of the supporting pad. For smaller values of θ, a big overhanging moment as well as a horizontal component H are present even for $a/b = 0$, hence, increasing a/b will only increase the already existing moment and the decrease in K is therefore more gradual.

The dotted curve, in Fig. 15, is for the case of a continuous support along the bottom edge of the diaphragm. For high values of θ, the overhanging moment is small and consequently the reaction concentration near the edges

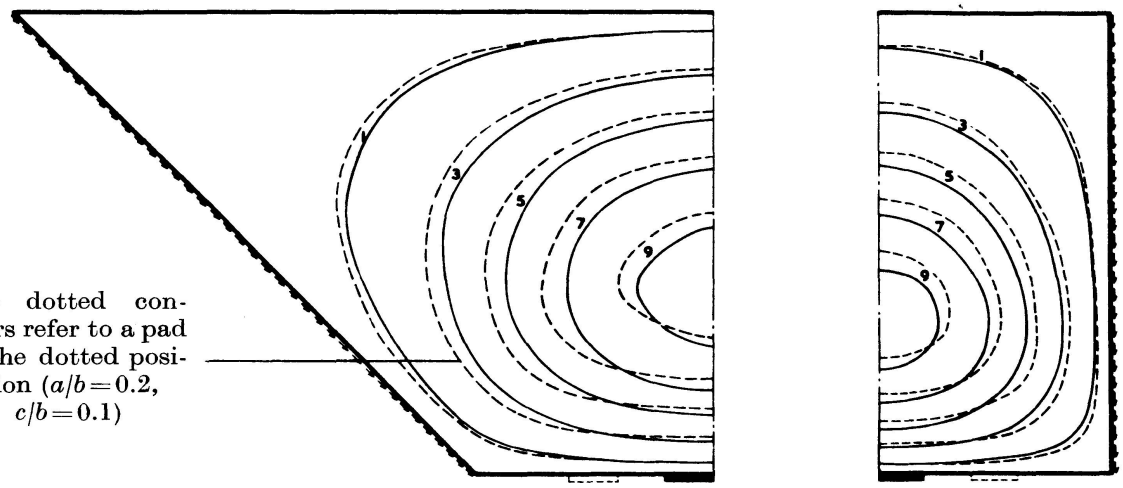

Supporting pads at $a/b=0.4$ and $c/b=0.2$

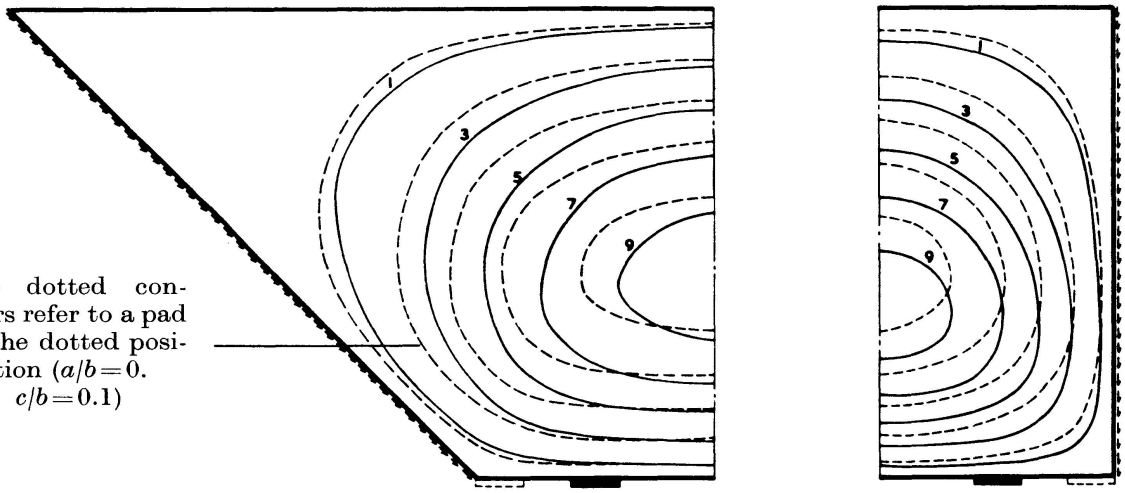

Supporting pads at $a/b=0.2$ and $c/b=0.1$

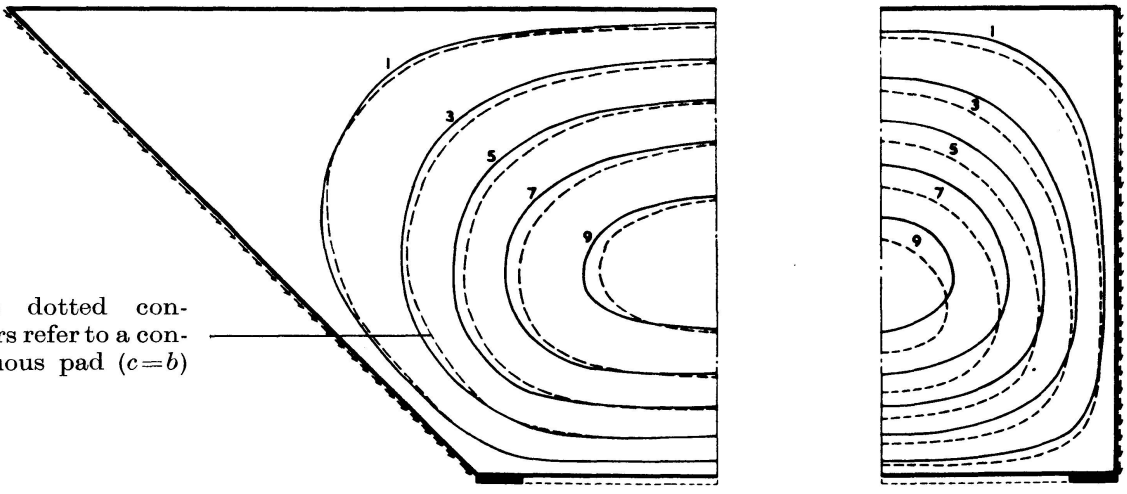

Supporting pads at $a/b=0$ and $c/b=0.1$

Fig. 16. Buckling Modes.

is relatively small and the buckling load is somewhere between the values for $a/b = 0.1$ and 0.2, however, for small values of θ the reaction concentration near the edges is higher and the buckling load is between the values for $a/b = 0$ and 0.1.

The buckling modes for six representative cases are shown in Fig. 16. In all cases it will be noted that there is a single half-wave buckling mode and that the crest of the half wave is nearer to the mid-depth position for lower values of θ due to the presence of the horizontal force H which elevates the position of the neutral axis. As mentioned before, there is an arching effect between the inner edges of the supporting pads which creates tensile stresses in the lower portion of the diaphragm which reduces the compressive stresses from the overhanging moment and the horizontal force. Therefore, the crest of the half wave moves upward by moving the supporting pads outward.

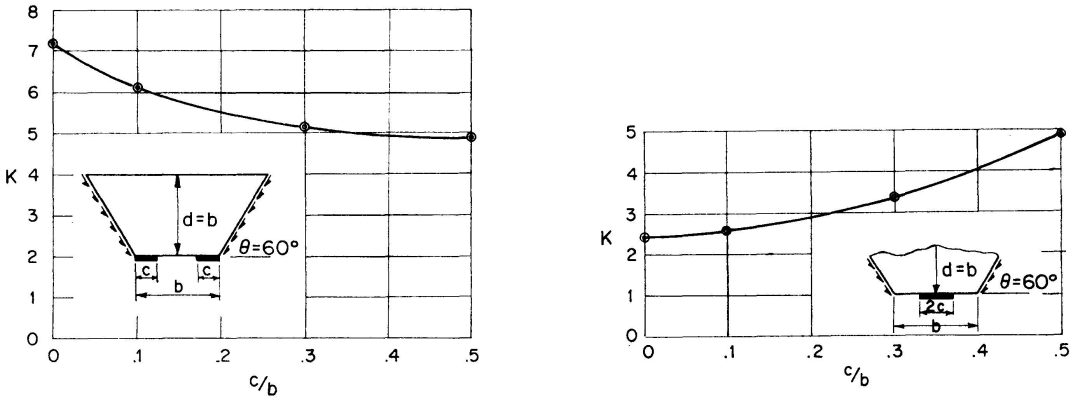

Fig. 17. Buckling Load Coefficient for Various c/b Values ($b = d$, $\theta = 60°$).

Fig. 17 shows how the buckling load of a trapezoidal diaphragm varies with the width of the supporting pad. In the case of two edge supporting pads, the buckling load is decreased by increasing the width of the pad. This is because the high values of the vertical stress σ_y, now act further away from the supported edges and in addition there will be less arching effect and consequently greater compression in the lower portion of the diaphragm. Meanwhile for a central supporting pad, the buckling load increases by increasing the width of the pad. The reason for this is obvious, since a wider supporting pad results in a smaller overhanging moment with a corresponding reduction in the horizontal stress σ_x whilst there is also a reduction in the vertical stress σ_y.

Finally, fig. 18 shows how the buckling coefficient K varies with the aspect ratio b/d for a representative case, in which the webs are inclined at 60° and the central pad has a width of $0.2b$. It will be noted that the relationship between the buckling coefficient K and the aspect ratio b/d is of a form very similar to that encountered in the compressive buckling of rectangular plates.

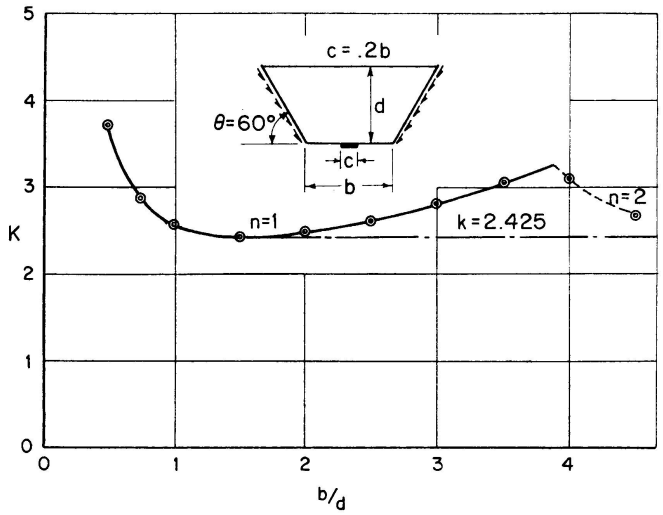

Fig. 18. Buckling Load Coefficient for Various b/d Values ($\theta = 60°$, $c/b = 0.2$, $a/b = 0.4$).

4. Conclusions

When the depth of the diaphragm is comparable to its width, the simple theory of flexure cannot be applied to determine the stress distribution within the area of the diaphragm. Moreover, the simple theory of flexure takes no account of the normal stresses in the y-direction, σ_y. In the present paper the stress distribution has been obtained, using the finite element method of analysis, for several representative cases. It has been found that the stress distribution varies with the inclination of the webs, the position and width of the supporting pads, and the aspect ratio of the diaphragm.

The overall buckling load has been determined for different geometric properties of the diaphragms and for varying position and length of the supporting pads, again using the finite element method of analysis. The buckling load has been expressed in the usual form for specifying critical loadings on flat plates. The non-dimensional buckling parameter K has been given as a function of θ, a/b, c/b and b/d.

Notation

a Distance between the bottom corner of the diaphragm and the outer edge of the supporting pad (see Fig. 2).
b Width of the bottom edge of the diaphragm.
c Width of the supporting pad.
d Depth of the diaphragm.
E Young's modulus of elasticity.
K Non-dimensional buckling coefficient.
P Applied total vertical load.

P_{cr} Critical buckling load.
t Thickness of the diaphragm.
θ Angle of inclination of the web.
μ Poisson's ratio.
σ_x Normal stresses in the horizontal direction.
σ_y Normal stresses in the vertical direction.
τ_{xy} Shear stresses.

References

1. Turner, M. J., Clough, R. W., Martin, H. C. and Topp, L. J.: Stiffness and Deflection Analyses of Complex Structures. Journal of Aeronautical Sciences, Vol. 23, No. 9, September, 1956, p. 805.
2. Clough, R. W.: The Finite Element Method in Plane Stress Analysis. 2nd Conference on Electronic Computation, Pittsburgh, Pa. Sept. 8–9, 1960. Sponsored by the ASCE.
3. Kapur, K. K., and Hartz, B. J.: Stability of Plates Using the Finite Element Method. Proc. ASCE, Jour. of Eng. Mech. Div., Vol. 92. No. EM 2, April 1966, pp. 177–195.
4. Bagchi, D. K.: Large Deflection and Stability of Structural Members using the Finite Element Method. Ph. D., thesis, University College, Cardiff, 1969.
5. Clough, R. W.: The Finite Element Method in Structural Mechanics. Stress Analysis, edited by O. C. Zienkiewicz and G. S. Holister. Jon Wiley & Sons Ltd., London-New York-Sydney, 1965.
6. Argyris, J. H.: Recent Advances in Matrix Methods of Structural Analysis. Pergamon Press, Oxford, 1964.
7. Zienkiewicz, O. C.: The Finite Element Method in Structural and Continuum Mechanics. McGraw-Hill, London, 1967.
8. Bazeley, G. P., Cheung, Y. K., Irons, B. M. and Zienkiewicz, O. C.: Triangular Elements in Plate Bending – Conforming and Non-Conforming Solutions. Matrix Methods in Structural Mechanics, Proceedings of the Conference held at Wright-Patterson Air Force Base, Ohio 1965 (Editor J. S. Przemieniecki).
9. Clough, R. W. and Tocher, J. L.: Finite Element Stiffness Matrices for Analysis of Plate Bending. The same book as Reference 8.
10. Argyris, J. H.: Matrix Displacement Analysis of Anisotropic Shells by Triangular Elements. J. of the Royal Aeronautical Society, Vol. 69, Nov. 1965.
11. Rockey, K. C., and Bagchi, D. K.: Buckling of Plate Girders Webs under Partial Edge Loadings. Int. J. Mech. Sci. Pergamon Press 1970, Vol. 12, pp. 61–76.

Summary

In this paper, the finite element method of analysis has been used to determine the stress distribution which occurs in both rectangular and trapezoidal diaphragms and to determine the applied load at which overall buckling of the diaphragms will occur. Stress contours have been given for various representative cases and the effect of the geometric properties of the

diaphragms and the position and length of the supporting pads has been examined. The buckling load has been expressed in the usual form for specifying critical loadings on flat plates and the non-dimensional buckling coefficient K has been given as a function of the parameters involved.

Résumé

La méthode des éléments finis a été utilisée pour déterminer la distribution des tensions dans les entretoises transversales, rectangulaires ou trapézoidales et la charge de voilement. On examine la distribution des tensions pour différents cas ainsi que l'influence des dimensions des entretoises et de la disposition et de la longueur des dalles d'appuis. La charge de voilement est exprimée sous la forme usuelle pour les charges critiques des plaques minces. Le coefficient de voilement K non-dimensionnel est donné en fonction des paramètres impliqués.

Zusammenfassung

Die Methode der finiten Elemente wurde verwendet, um die Spannungsverteilung, welche in rechteckigen und trapezförmigen Querträgern auftritt, sowie die kritische Beullast zu bestimmen. Die Spannungsverteilung wird für verschiedene repräsentative Fälle angegeben. Der Einfluss der geometrischen Abmessungen der Querwände sowie verschiedener Anordnungen und Längen der Auflagerplatten wurde ebenfalls untersucht. Die Beullast ist in der gleichen Form wie bei dünnen Platten ausgedrückt, und der dimensionslose Beulwert K wird in Funktion der verwendeten Parameter angegeben.

Finite Element Analysis of Skew Vault Bridges

Analyse de ponts en arc biais à l'aide des éléments finis

Berechnung schiefer Bogenbrücken mittels der finiten Elemente

R. G. SISODIYA
Ph. D., MEIC, Assistant Prfessor of Civil Engineering,
McGill University, Montreal, Quebec, Canada

Y. K. CHEUNG
Ph. D., MICE, Professor of Civil Engineering, The University of Calgary

A. GHALI
Ph. D., MASCE, Professor of Civil Engineering, The University of Calgary

Introduction

In the past vault bridges such as in Fig. 1 have been analyzed approximately by treating them as arch beams. The approximation involved may not be acceptable when the bridge is skew or when the bridge width is of the same order as the span. In such cases a spatial structural analysis is necessary and the finite element method is used here for this purpose.

SABIR and ASHWELL [1] analyzed the rectilinear bridge in Fig. 1 by finite element method using rectangular plate bending element for the slab and cylindrical shell element for the vault. Their analysis assumed that the slab rests on the crown of the vault, and the interaction between the deck and the vault is of only vertical forces along the crown. This assumption is valid only for special cases.

A parallelogram shell element developed in References 2 and 3 is used in the present analysis. The stiffness of this element is a combination of the bending stiffness developed by DAWE [4] and in-plane stiffness derived [2], [3] specially for bridge analysis. The latter refers to a high order in-plane element which includes in-plane rotations as nodal parameters and is used in the present analysis because of its superior accuracy over the standard bilinear parallelogram element.

The examples analyzed in the present paper are for rectilinear and skew

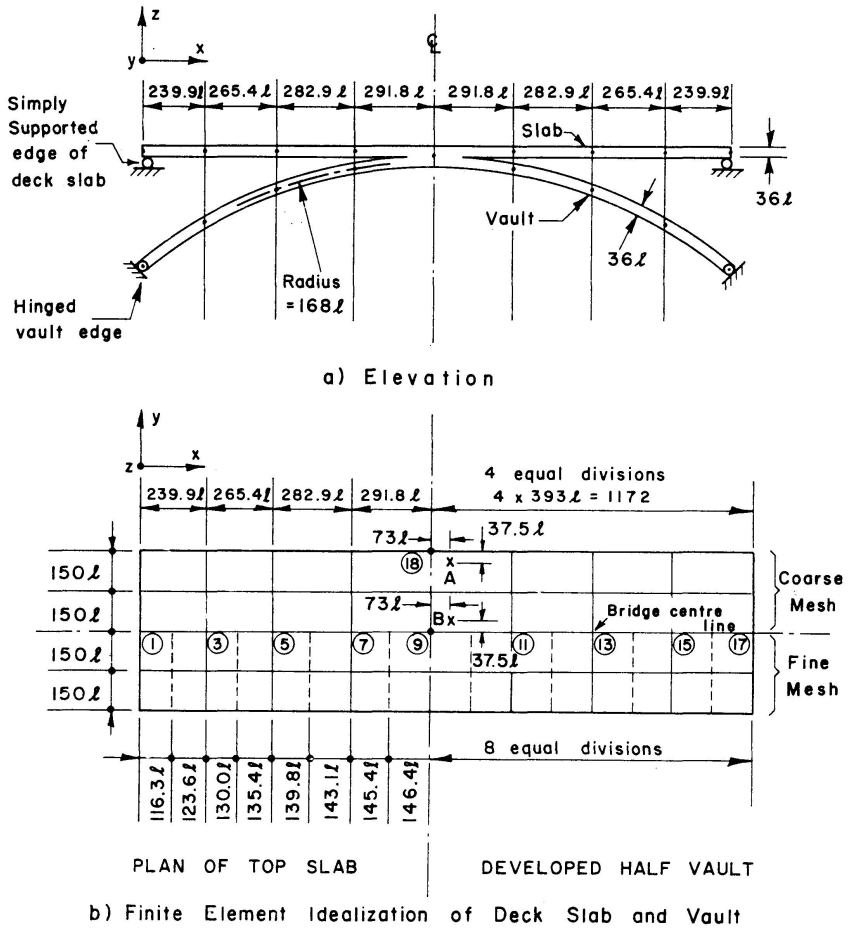

Fig. 1. Bridge No. 1 Analyzed in Example 1 (Sabir and Ashwell's Bridge).

bridges made up of a vault, a slab deck and interconnecting walls or columns with monolithic joints (Fig. 2). The computer program used is also capable of analyzing bridges for which the vault or the deck are of box girder or slab-beam construction.

Method of Analysis

The paralelogram element used has the following nodal parameters at its corners (Fig. 3): w, θ_x and θ_y (for bending) and u, v, $\theta_z = (\partial v/\partial x)$ (for in-plane displacements). The displacement function used to derive the in-plane stiffness are given below for easy reference:

$$\begin{Bmatrix} u \\ v \end{Bmatrix} = \sum_{i=1}^{4} \begin{bmatrix} f_1 & f_4 & f_5 \\ 0 & f_2 & f_3 \end{bmatrix}_i \begin{Bmatrix} u \\ v \\ \theta_z \end{Bmatrix}_i ,$$

where

$$f_{1i} = \tfrac{1}{4}(1+\xi\,\xi_i)(1+\eta\,\eta_i),$$
$$f_{2i} = \tfrac{1}{2}(2+\xi\,\xi_i-\xi^2)f_{1i},$$
$$f_{3i} = -\tfrac{1}{4}a\,\xi_i(1-\xi^2)f_{1i},$$

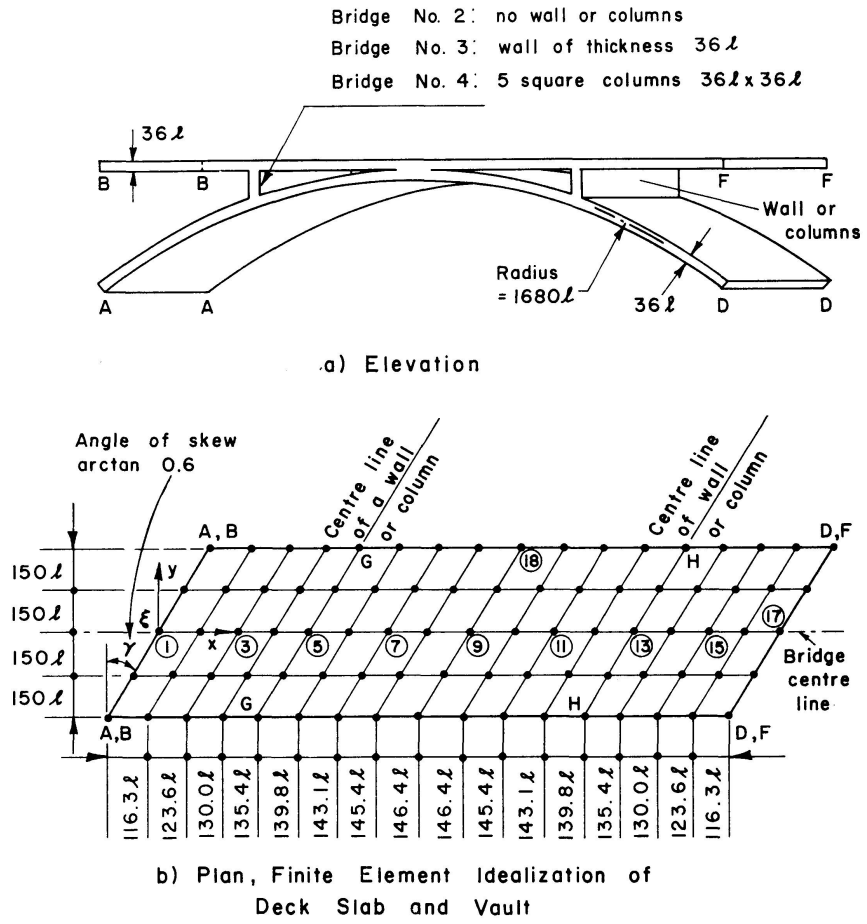

Fig. 2. Skew Bridges Nos. 2, 3 and 4 Analyzed in Example 2.

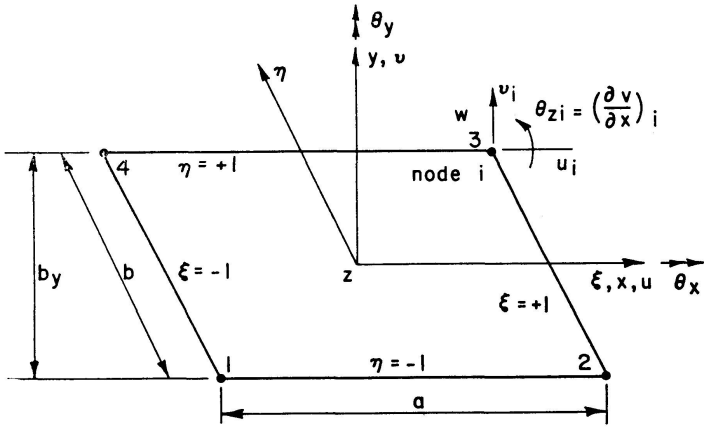

Fig. 3. An In-Plane Stiffness Parallelogram Element.

$$f_{4i} = \frac{3}{8a} b_y \xi_i \eta_i (1-\xi^2)(1-\eta^2),$$

$$f_{5i} = -\frac{1}{16} b_y \eta_i (1-\eta^2)(1-2\xi\xi_i-3\xi^2).$$

The quantities a and b_y and the co-ordinates x, y, ξ and η are defined in Fig. 3.

For beams or columns (if any) a standard beam element [5] is used with three translations and three rotations at each end. For beams monolithic with the deck slab the 12 displacements are taken at "eccentric" nodes on the centroid of the beams, and these are then transformed to nodes in the middle surface of the slab (assuming rigid connection). In the examples discussed below, Poisson's ratio is considered equal to 0.2.

Example 1: Rectilinear Bridge

The bridge analyzed by Sabir and Ashwell (Bridge No. 1, Fig. 1) is symmetrical in structure and loading, and thus their assumption that only vertical forces exist between the slab and the vault at the crown is correct, even if the two are monolithically connected. Sabir and Ashwell carried out the analysis for a vertical concentrated load P at points 9 and 18, Fig. 1b, using a 12×12 mesh for the deck and an 8×8 mesh for the vault. Their results are used for checking the present analyses, in which both a coarse mesh and a fine mesh idealization (Fig. 1b) are used.

Since the displacement functions of the plane stress element are not balanced in the x and y directions, a study was made to determine the effect of this by running two identical coarse mesh solutions with the elements' axes interchanged. The results shown in Fig. 4 indicate that the general behaviour

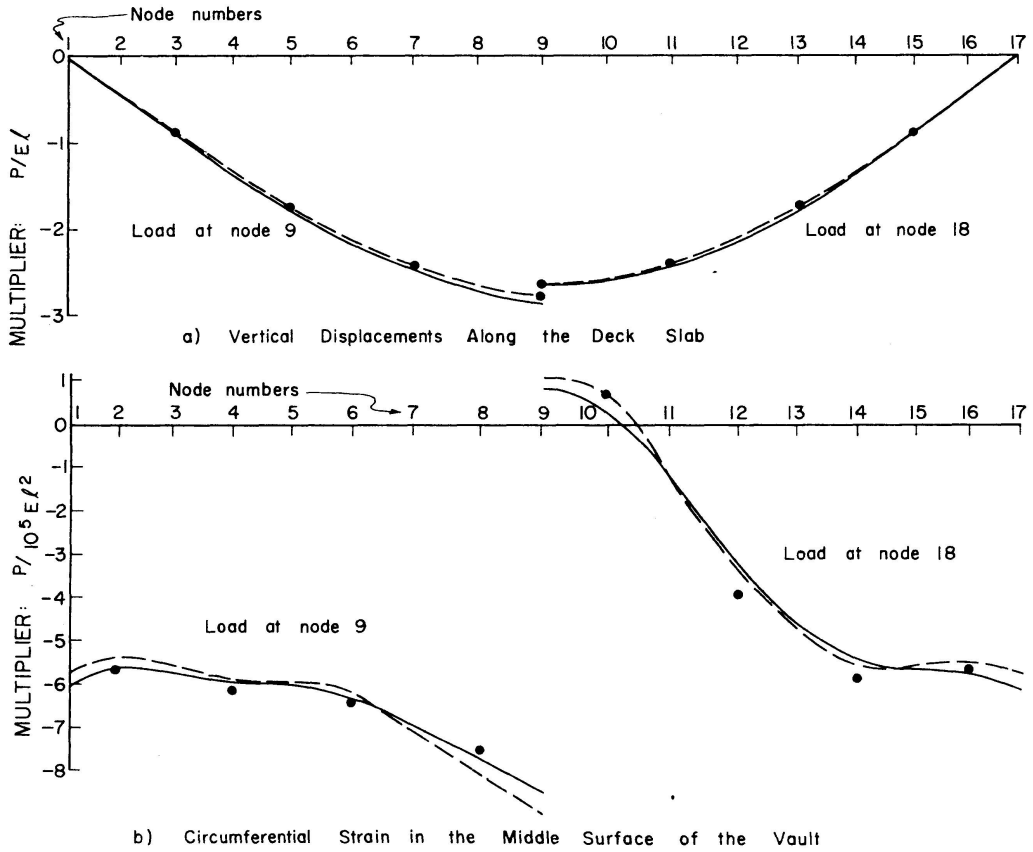

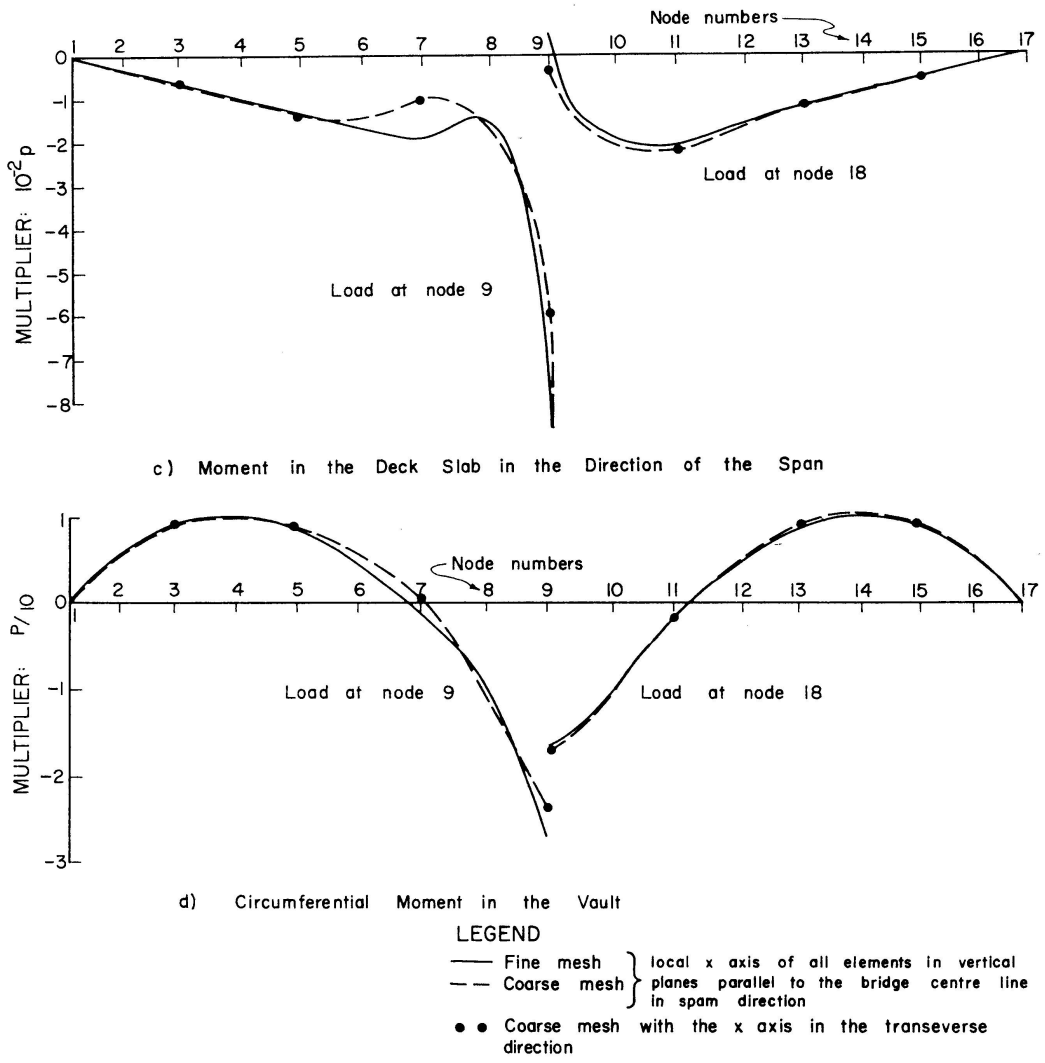

Fig. 4. Variation of Vertical Displacement, Strain and Moment Along the Centre Line of Bridge in Fig. 1.

Table 1. Comparison of Results of Analysis of the Bridge No. 1 in Fig. 1

	Multiplier	Point	Load at Node 18			Load at Node 9		
			Ref. [1]	Present Analysis		Ref. [1]	Present Analysis	
				Coarse Mesh	Fine Mesh		Coarse Mesh	Fine Mesh
Deflections	$-\frac{P}{10^2 El}$	1	531	506	525	—	253	263
		2	—	253	263	290	275	285
Circumferential Forces	$-\frac{P}{10^4 l}$	A	100	84	91	—	8	6
		B	—	4	6	37	27	31
Circumferential Bending Moment	$-\frac{P}{10^3}$	A	281	257	262	—	145	148
		B	—	158	152	176	157	166

of the bridge is unaltered. For this reason, in all the subsequent analyses the local x-axis of the elements will always be in a vertical plane parallel to the direction of span.

The results given in Reference [1] are in agreement with the present analysis (Table 1). The moments and stresses in the present analysis are calculated at the nodes and the centre of the element sides respectively, these are then plotted in graphs from which the results in Table 1 are deduced. The values of the moments and forces quoted from Reference [1] are the "maximum" mid-element values; these are assumed here to represent Sabir and Ashwell's results at points A and B.

Example 2: Skew Bridge

Three skew bridges are analyzed; they have the same plan and elevation shown in Fig. 2. The Bridge No. 2 has no connection between the deck slab and vault along lines GG and HH; in Bridge No. 3 vertical walls are provided along these lines and in Bridge No. 4 each wall is replaced by 5 vertical square columns ($36l \times 36l$). The conditions of support at the ends of the deck slab

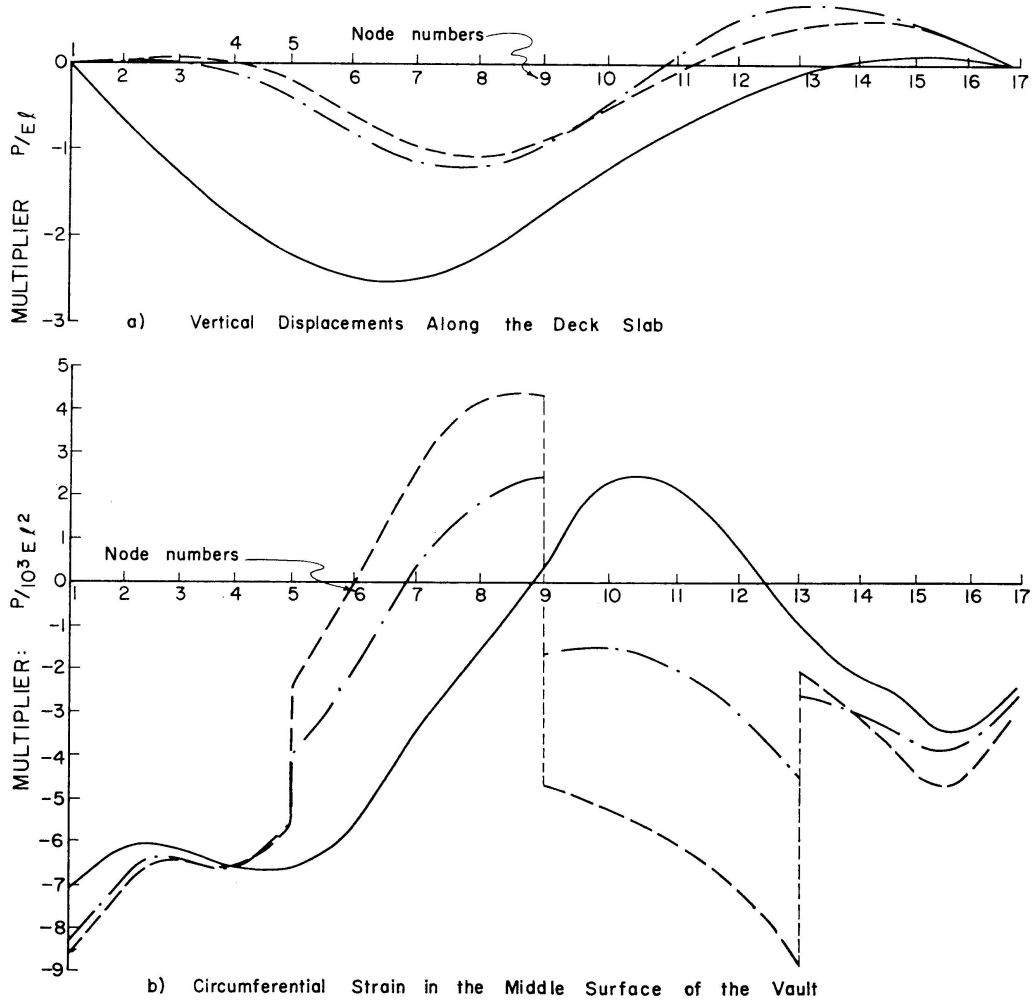

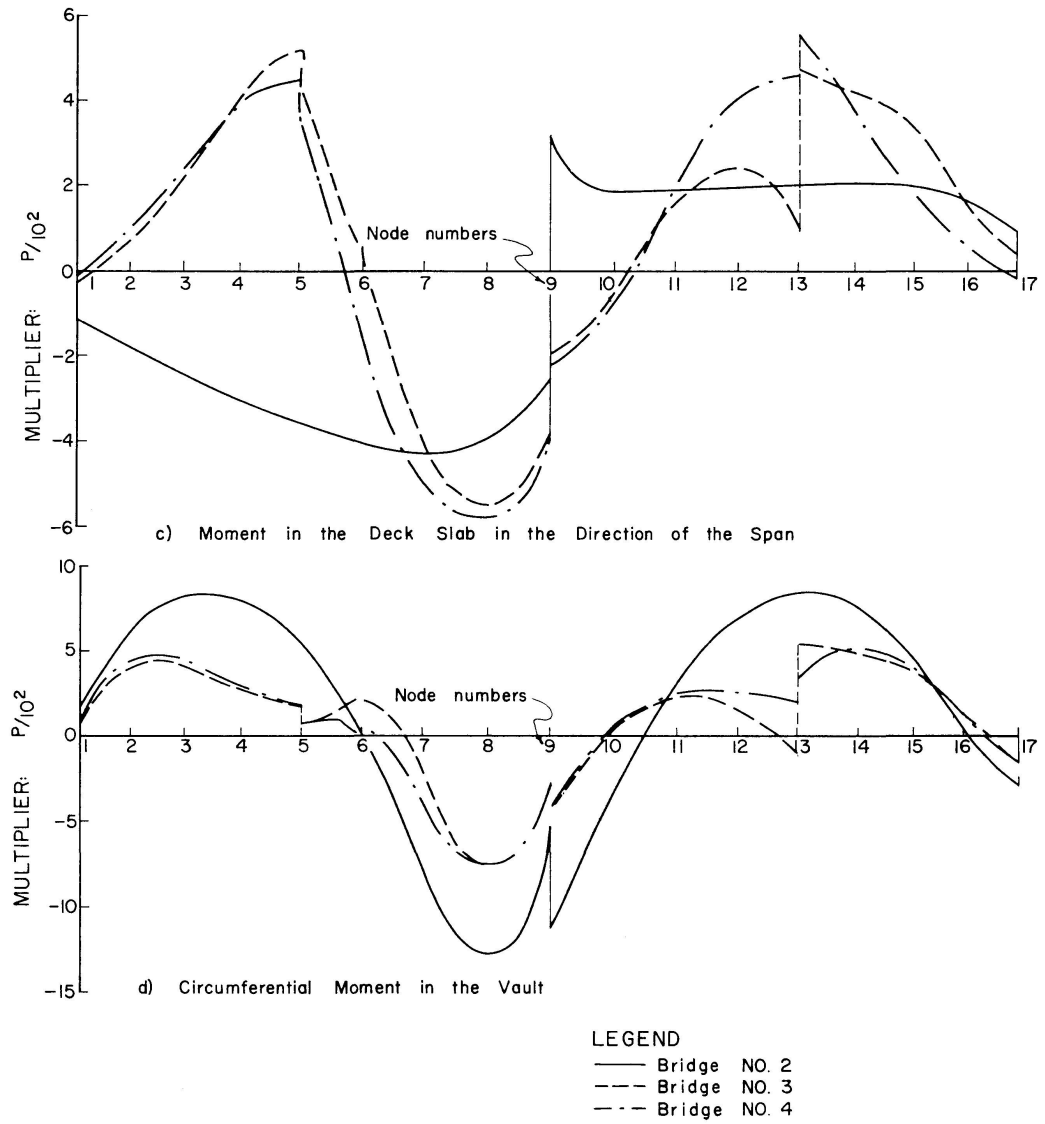

Fig. 5. Variation of Vertical Displacement, Strain and Moment Along the Centre Line of Bridge in Fig. 2.

and the vault are the same as in Example 1. The three skew bridges are analyzed for a concentrated load P at node 18. The finite element idealization of the deck slab is indicated in Fig. 2b; this figure also represents the projection of the mesh division in the vault which divides the vaults into equal elements. Each of the two walls in Bridge No. 3 is divided into 4 elements by vertical lines joining the nodes in the deck slab and the vault.

Fig. 5 shows the variation of vertical displacements, moments and strains along the centre line of the deck slab and vaults of the three bridges. Comparison of the results of Bridges No. 1 and No. 2, which are identical except for the skew angle, for the same case of loading shows totally different values. Thus an analysis in which the skew effect is properly accounted for is essential for this type of bridges.

The effect of shew is further studied for the dead loading. Bridge No. 3

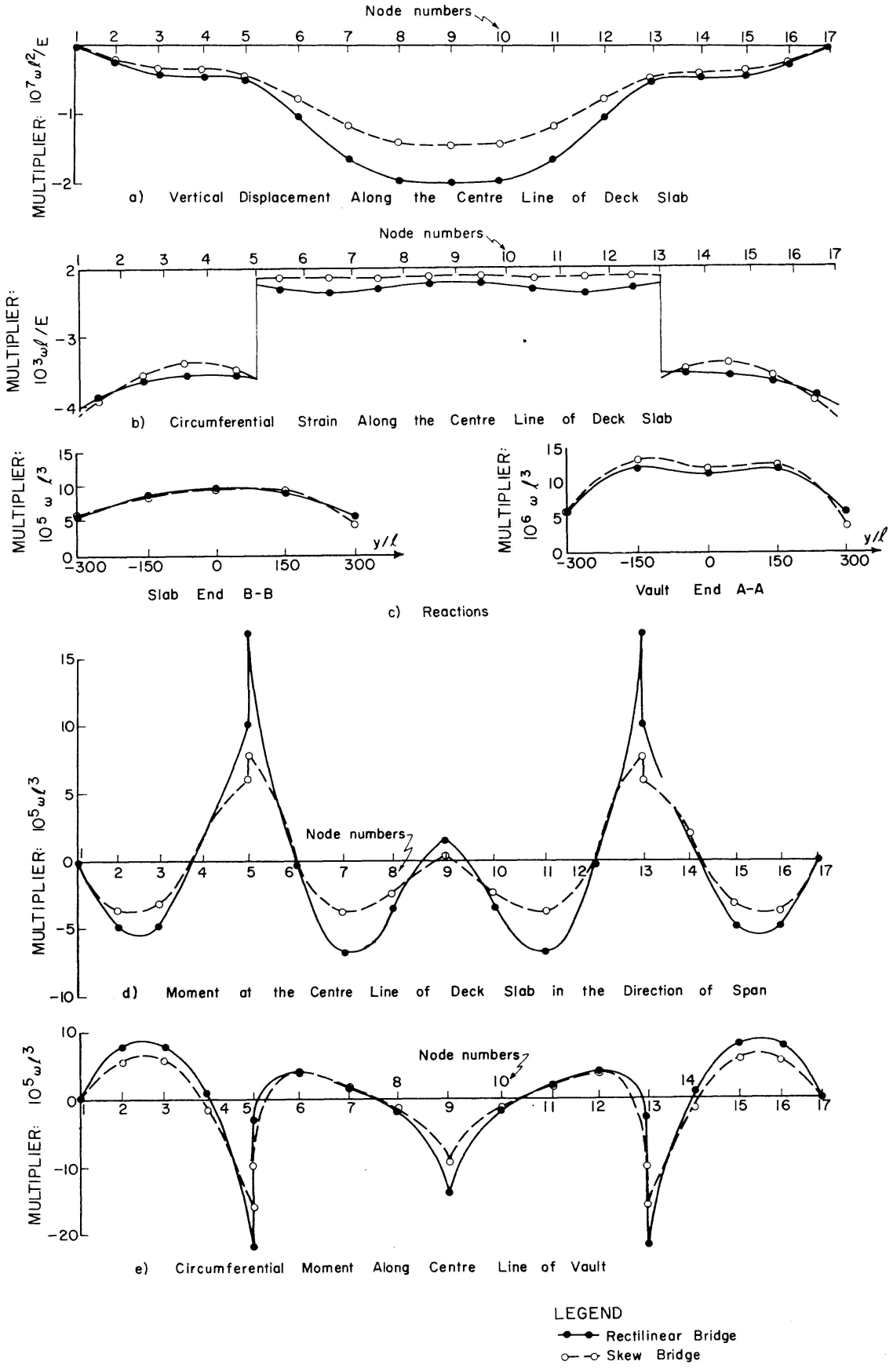

Fig. 6. Dead Load Effects on a Rectilinear and Skew Bridge (See Fig. 2).

and an identical bridge but with the skew angle $\gamma = 0$ (Bridge No. 5) are analyzed for the dead loading, which is represented for each element by 4 equal vertical forces at its corners. The results are shown in Fig. 6, which includes the reactions at the supports in addition to the vertical displacements, strains and moments considered in Fig. 5.

Compilation and execution time for complete analyses for one loading case CDC/6400 computer using KRONOS operating system compiler FTN with optimization level 1 is 90 and 110 seconds, respectively. Execution time is increased by about 5 seconds for each additional load case.

Conclusions

The finite element analysis described can be used economically for skew vault bridges. The accuracy of the method is verified for a rectilinear bridge by comparison with published results. The results of examples analyzed show the drastic effect of the angle of skew, thus demonstrating the necessity of an appropriate spatial structural analysis.

Notations

$a, b. b_y$	dimensions of a parallelogram element (see Fig. 3).
E	Young's modulus.
i	integer.
l	length parameter.
P	concentrated vertical point load.
u, v, w	translations in x, y and z directions respectively.
x, y, z	axes.
γ	skew angle defined in Fig. 5b.
θ	rotation which can be represented by a vector along any of the axes x, y, and z.
ξ, η	dimensionless co-ordinates in a parallelogram element (see Fig. 3).
ω	specific weight.

Acknowledgement

Financial support of this research provided by the National Research Council of Canada is gratefully acknowledged.

References

1. A. B. Sabir and D. G. Ashwell: Finite Element Analysis of a Broad Arch Bridge with a Slab Deck. Development in Bridge Design and Construction, Cardiff, Great Britain, 29 March – 2 April, 1971.

2. R. G. Sisodiya, Y. K. Cheung, and A. Ghali: New Finite Elements with Application to Box Girder Bridges. Proceedings I.C.E., London Paper No. 7479.
3. R. G. Sisodiya: Finite Element Analysis of Box Girder Bridges. Ph. D. thesis, The University of Calgary, Calgary, Alberta, Canada, 1971.
4. D. J. Dawe: Parallelogramic Elements in the Solution of Rhombic Cantilever Plate Problems. Journal of Strain Analysis, Vol. 1, No. 3, 1966.
5. A. Ghali and A. M. Neville: Structural Analysis – A Unified Classical and Matrix Approach. International Textbook Co., Scranton, Pennsylvania, 1972, p. 79.

Summary

The finite element method is used to analyse skew bridges composed of a vault and a horizontal deck connected by walls or columns. A parallelogram element combining in-plane and plate bending stiffnesses is used. The in-plane element stiffness is derived (in a earlier publication) particularly for use in bridge design and is proved to lead to accurate results with small number of elements. The analysis is applied to rectilinear and skew bridges and the effect of the skew angle is discussed.

Résumé

La méthode des éléments finis est utilisée pour analyser des ponts biais composés d'un arc et d'une dalle de chaussée horizontale, liés entre eux par des parois ou des piles. On travaille avec un élément ayant la forme d'un parallèlogramme qui combine la rigidité dans le plan et la rigidité de flexion. La rigidité dans le plan des éléments a été traitée spécialement (voir la publication antérieure) pour l'application dans la construction de ponts. On a démontré qu'elle mêne, même avec un petit nombre d'éléments, à de très bons résultats. L'analyse est appliquée à des ponts droits et biais et l'effet de l'inclinaison est discutée.

Zusammenfassung

Die Methode der endlichen Elemente wird verwendet, um schiefe Brücken, deren Bögen durch Wände oder Stützen mit der Fahrbahn verbunden sind, zu berechnen. Es wird ein parallelogrammförmiges Element, das Scheiben- und Plattensteifigkeit kombiniert, verwendet. Die Scheibenelementsteifigkeit wurde speziell für die Anwendung im Brückenbau (in einer früheren Publikation) entwickelt; es wurde bewiesen, dass sie bereits bei einer kleinen Anzahl von Elementen zu genauen Resultaten führt. Die Berechnung wurde an geraden und schiefen Brücken durchgeführt, und der Einfluss der Schiefe wird diskutiert.